Spring 5-14-2021

INVESTIGATIONS OF GEOCHEMICAL VARIATIONS WITH DEPTH AT THE FIRST 15 DRILL SITES ON MARS ANALYZED BY THE CHEMCAM INSTRUMENT ONBOARD THE CURIOSITY ROVER AND SUPPORTED BY LABORATORY STUDIES AND ANALOG RESEARCH AT THE VALLE GRANDE PALEOLAKE, VALLES CALDERA, NEW MEXICO, USA

Ryan S. Jackson

Ryan Jackson
Candidate

Earth and Planetary Sciences
Department

This dissertation is approved, and it is acceptable in quality and form for publication:

Approved by the Dissertation Committee:

Dr. Horton Newsom, Chairperson

Dr. Roger Wiens

Dr. Laura Crossey

Dr. Adrian Brearley

INVESTIGATIONS OF GEOCHEMICAL VARIATIONS WITH DEPTH AT THE FIRST 15 DRILL SITES ON MARS ANALYZED BY THE CHEMCAM INSTRUMENT ONBOARD THE CURIOSITY ROVER AND SUPPORTED BY LABORATORY STUDIES AND ANALOG RESEARCH AT THE VALLE GRANDE PALEOLAKE, VALLES CALDERA, NEW MEXICO, USA

by

RYAN JACKSON

B.S., Geology, Eastern New Mexico University, 2012
M.S., Earth and Planetary Sciences, University of New Mexico, 2016

DISSERTATION

Submitted in Partial Fulfillment of the
Requirements for the Degree of

Doctor of Philosophy
Earth and Planetary Sciences

The University of New Mexico
Albuquerque, New Mexico

May 2021

DEDICATION

Dedicated to the three people I could always depend on – my wife, father, and mother.

ACKNOWLEDGEMENTS

Funding for this dissertation was provided in part by NASA's Mars Exploration Program, the Mars Science Laboratory project, as well as teaching assistantships and scholarships from the Department of Earth and Planetary Sciences at the University of New Mexico.

This research would have been impossible without all of the talented people involved in designing, launching, and operating the Curiosity rover and I am grateful for their hard work and dedication. I am also thankful for the support, encouragement, and guidance of the members of my committee, Horton Newsom, Roger Wiens, Laura Crossey, and Adrian Brearley. I am especially thankful for Roger Wiens taking a chance to hire me as a Post-Baccalaureate researcher at Los Alamos National Laboratory and then providing aid and guidance ever since.

I would like to thank my parents, Cindy and Dale Jackson, and my grandparents, Roy and Trudy Marsh, for their unending support, bottomless supply of belief, and willingness to humor me when I spoke endlessly about highly technical issues. I am thankful for my friends who have continued to show me support and friendship even as I became increasingly anti-social.

Finally, I would like to thank my wonderful wife for believing in me and encouraging me throughout this entire process.

INVESTIGATIONS OF GEOCHEMICAL VARIATIONS WITH DEPTH AT THE FIRST 15 DRILL SITES ON MARS ANALYZED BY THE CHEMCAM INSTRUMENT ONBOARD THE CURIOSITY ROVER AND SUPPORTED BY LABORATORY STUDIES AND ANALOG RESEARCH AT THE VALLE GRANDE PALEOLAKE, VALLES CALDERA, NEW MEXICO USA

By

Ryan Steele Jackson

B.S., Geology, Eastern New Mexico University, 2012
M.S., Earth and Planetary Sciences, University of New Mexico, 2016
Ph.D., Earth and Planetary Sciences, University of New Mexico, 2021

ABSTRACT

The ChemCam instrument collected a wealth of data during the first 15 drill campaigns and on the distribution of trace elements at Yellowknife Bay, Mars. The drill sites investigation showed that most sites were geochemically homogenous down the depth of the drill hole. Two sites in the Stimson formation contained a vertical gradient of decreasing silica down > 3 cm. This gradient may be the result of groundwater flow and is likely recent, within 2.3 Ma. The trace element research was grounded with an analog study at the Valle Grande paleolake in New Mexico. We observed progressive alteration in the minerology and trace elements as the surrounding rhyolites were eroded into lake sediments. This was applied to Yellowknife Bay; where minimal geochemical changes were observed between the sedimentary rocks and float rocks assumed to represent the source material. However, retention of Li does suggest some in-situ clay formation.

.

TABLES OF CONTENTS

PREFACE

Mars holds a special interest to scientists and general public alike due to the possibility that it once had a more Earth-like environment. This interest is bolstered by the evidence collected from orbit and from landers and rovers sent to the planet's surface. Since landing on Mars in 2012, the Curiosity Rover has discovered ample evidence for a geologic history involving water, including evidence for rivers and lakes (Grotzinger et al., 2014; Grotzinger et al., 2015). However, the details of that history are still being uncovered and discussed. In addition, there is evidence for a few distinct occurrences of diagenesis at Gale Crater, including the deposition of Ca-sulfate veins and substantial alteration of sediments (Frydenvang et al., 2017; Nachon et al., 2017; Yen et al., 2017). In order to better understand these results, it is necessary to delve deeper into the massive amount of data collected by the Curiosity Rover so far at Gale Crater.

The unique nature of the ChemCam instrument onboard the Mars Science Laboratory provides an exciting opportunity to investigate these sites in detail. The ChemCam instrument contains a Laser Induced Breakdown Spectroscopy (LIBS) instrument and a Remote Micro Imager (RMI). The LIBS technique functions by firing a laser at the target of interest, vaporizing a small amount of the material and forming plasma. The plasma emits light at characteristic wavelengths, which are analyzed by the spectrometers onboard the rover to provide a chemical composition (Cremers & Knight, 2006; Maurice et al., 2012; Wiens et al., 2012). The LIBS technique allows ChemCam to collect geochemical analyses up to 7 m from the rover, while also collecting data at several points at each target analyzed in a line scan or raster (Wiens et al., 2013). ChemCam is also capable of collecting

multiple targets during each day of rover operations. This has resulted in ChemCam sampling > 2,500 geologic targets (each with multiple observation points) and collecting > 820,000 individual spectra. The ChemCam laser has a small footprint (~400 μm in diameter), allowing differentiation between sediments and diagenetic features, as well as accurately sampling powdered materials such as soils and drill cuttings. In addition, the laser pulses fired by ChemCam are capable of clearing dust off rocks in as few as five shots, allowing for relatively uncontaminated analyses by the subsequent shots.

However, the ChemCam instrument also comes with some unique challenges. The LIBS technique has become more popular for a variety of research applications in the earth sciences (Galbács, 2015; Qiao, 2015), but ChemCam is the first use of the LIBS technique for planetary exploration. This requires a certain amount of experimentation to determine the optimal methods to use the instrument, especially when analyzing novel materials. For example, the ability of the ChemCam instrument to remove dust becomes a liability when analyzing thin piles of drill cuttings on top of solid rock, as it is quite easy for the LIBS shots to blast through the drill cuttings and begin to sample the rock underneath. In addition, generating a plasma on a variety of materials with differing physical properties can create complications (Cremers & Knight, 2006), especially when interrogating small variations in the data, as was done in much of this research. This dissertation takes advantage of these unique capabilities while also taking pains to understand and work around the difficulties inherent with the technique.

This dissertation has four chapters. Chapter 1 investigates some of the challenges found when using LIBS for this research. It is focused on limiting errors and finding useful

ways to correct or to work around these issues. This chapter consists of studies that have a variety of presentation and publishing histories. Sections 2 and 3 are included in the supplementary information for a paper based on Chapter 2 that is intended to be submitted to *Icarus*. These sections have only been presented within the ChemCam science team. Section 4 is recent work that has not been presented elsewhere, and Section 5 is based on work that was presented at the 2019 Lunar and Planetary Science Conference.

Chapter 2 is based on a series of research projects that were presented at the 2015, 2016, and 2018 Lunar and Planetary Science Conferences and the 2017 GSA Cordilleran section meeting. In addition, it is currently being prepared for submission to Icarus; this process requires presentations to the ChemCam team and the general Curiosity Rover science team. The chapter investigates the first 15 drill holes on Mars and analyzes them for chemical heterogeneity with depth. This research revealed one location, which shows evidence of recent diagenesis of the sediments. This possibility was then investigated as thoroughly as possible given the nature of the data, and a geochemical plausibility model was developed to understand the potential geologic processes investigated.

Chapter 3 is based on research that was presented at the 2016 Geological Society of America meeting. The foundation for this research was established in my 2016 Master's thesis. It is an investigation of source to sink geochemical variations in the Valle Grande paleolake in Valles Caldera, New Mexico, USA, which is a closed basin surrounded by volcanic rocks. This makes it a good analog for Gale Crater, the Curiosity Rover's landing site. The site has been well researched and has had a large amount of data collected there. This includes a drill core of the lake sediment, which allowed for chemical variations to be

observed as the climatic conditions at this site varied, while the source material largely stayed the same.

The foundations of Chapter 4 were presented at the 2017 Geological Society of America meeting and at various meetings within the ChemCam science team. This is an investigation of the source to sink changes in the trace elements observed at Yellowknife Bay, Gale Crater, Mars, the first lacustrine environment encountered by the rover. This research was intended as a follow up to both the original geologic investigations by the science team and to the improvements made to ChemCam's ability to detect and quantify trace elements. As ChemCam is best able to analyze highly mobile trace elements, it was hoped that this capability would improve the understanding of the relatively limited amount of weathering that occurred to the Yellowknife Bay sediments.

The Mars Science Laboratory (MSL) team is made up of hundreds of members, which necessitates collaborative research. Numerous scientists and engineers were involved in everything from the designing, building, and calibration of the instruments to the day-to-day operation of those instruments on Mars. The planning process, in the short and long term, is a collaborative endeavor that determined what material was analyzed, how much was analyzed, and the time available for the analyses. The drilling process, especially, is a complicated endeavor, and it was the input of many people that determined how many sites were drilled and how long the rover would stay to analyze the byproducts (drill hole wall and drill cuttings). These decisions had a large impact on the nature of the materials in this research. However, the majority of this work was produced by me, and I am the lead author on all manuscripts.

CHAPTER 1: Laboratory and in-situ studies of ChemCam analysis of powdered and related materials

1. Introduction

The Curiosity Rover drilled 15 sites on Mars before a drill fault took the drill temporarily out of operation. The resulting fix changed the drilling process and thus the sites after this occurrence were excluded from this study. These sites were the subject of an investigation into geochemical changes in the first ~6 cm beneath the martian surface by the ChemCam instrument. In order to adequately characterize the geochemical data at the drill sites, it was necessary to investigate the possible complications that could affect the interpretation. First, as the Laser Induced Breakdown Spectroscopy (LIBS) technique can "dig" through material, it was necessary to investigate how many shots it takes to "dig" through the fines produced by the drilling process. Second, it was uncovered in previous laboratory experiments that K_2O is often underreported in powdered materials by ChemCam, and this behavior would have to be understood in order to determine K_2O in the drill sites investigation. Third, in the high-silica Stimson formation, the geochemical signature of the dust was found to continue in the measurements of the surface after five shots, the point at which it was originally thought that all dust would be vaporized or blown away. This phenomenon was investigated to see if it was possibly connected to a form of geochemical alteration or if the dust signature continued further and contaminated the surface observation points. Finally, it was hoped that the Sr abundance in the Ca-sulfate veins could be used to provide insights into the geologic his

tory of the sites. This necessitated the investigation to take account of the effects that the optical properties of crystalline gypsum and other Ca sulfates may have on the detection of trace elements in those materials.

Data in this research came from two sources, the ChemCam instrument onboard the Curiosity rover currently exploring Mars and the ChemCam engineering model at Los Alamos National Laboratory. ChemCam consists of a Laser Induced Breakdown Spectroscopy (LIBS) instrument which allows for ~400 µm diameter chemical analyses from 1.5 m to 7.0 m away, as well as a panchromatic Remote Micro Imager (RMI) for context (Maurice et al., 2012; Wiens et al., 2012). At each point ChemCam fires multiple laser shots and records an emission spectrum for each shot (Wiens et al., 2012). The elemental detections from the LIBS spectra are reported in terms of the abundances of SiO_2, TiO_2, Al_2O_3, FeO_T, MgO, CaO, Na_2O, and K_2O. The abundances are quantified by using a calibration method which uses both a Partial-Least Squares (PLS1) training algorithm and Independent Component Analysis (Clegg et al., 2009; Clegg et al., 2017; Forni et al., 2013; Wiens et al., 2013). Li, Rb, Sr, and Ba are calibrated through a univariate calibration method which measures the changes in peak area for a single peak per element against a large set of standards. Each peak was selected for stability and least interference from the peaks of other elements (Ollila et al., 2014; Payré et al., 2017). The LIBS technique vaporizes a small amount of material with each laser shot, so that successive shots penetrate deeper into the material. By analyzing successive spectra, one can observe how the composition of the material changes with depth on a scale of microns, in rocks, and millimeters, in loose material. In loose sediment, such as the tailings and dump pile, the LIBS shots can “dig”

through the material into the rock underneath, even in sequences of only 30 shots per point (Lanza et al., 2015). The ChemCam engineering model is identical to the instrument on the Mars rover. The samples reported in this research were collected at a standoff distance of 3 m and either under ambient conditions or simulated Martian conditions of 7 Torr pressure and a CO_2 atmosphere.

2. Determining the number of ChemCam shots needed to analyze the tailings and dump piles without contamination from the substrate

It had been observed that ChemCam analyses "dig" through the tailings and dump piles (fines created by the drilling process), so we investigated the number of shots it typically takes to "dig" through the tailings (Lanza et al., 2015). For each tailing pile we compared the reported composition of the first shot, the first three shots averaged together, the first five shots averaged together, and the first ten shots averaged together. The above groupings of data were then plotted against the distribution of silica (Fig. 1.1) and CaO for the drill sites in the Murray and the Stimson (Fig. 1.2).

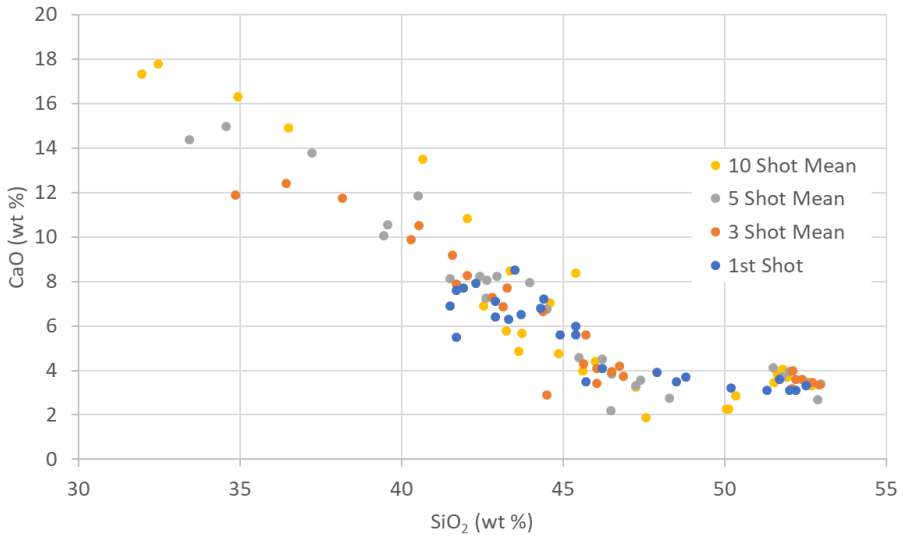

Figure 1.1: Composition of the points in the drill tailings at the Oudam, Marimba, Quela, and Sebina drill sites in the Murray formation. The points are presented as the first shot at each point, the average of the first three shots, the average of the first five shots, and the average of the first 10 shots.

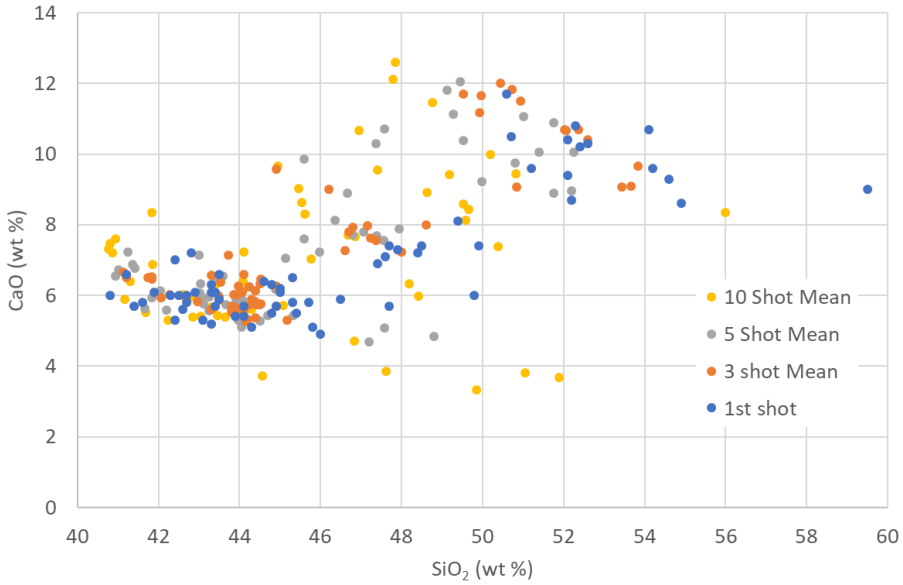

Figure 1.2: Distribution of CaO and SiO_2 of the LIBS points in the drill tailings at the Big Sky, Greenhorn, Lubango, and Okoruso drill sites in Stimson formation. The points are presented as the first shot at each point, the average of the first three shots, the average of the first five shots, and the average of the first 10 shots.

We Investigated the Oudam, Marimba, Quela, and Sebina drill sites in the Murray formation as a "best case" scenario due to the minimal geochemical variation observed at those sites, and we investigated Stimson drill sites as a "worst case" scenario due to the variation observed at those sites (Chapter 2). We only used drill tailings, as these are typically thicker and spatially more coherent, allowing for more thorough investigation. Using dump piles – the material collected by the drill assemblage then dumped back on the surface – would likely have led to overly conservative estimations of the number of shots in the powdered material.

In the Middle Murray drill tailings, the averages all followed the same anticorrelation between CaO and SiO_2, but as LIBS points included more shots on the average, they started to show high CaO values. The higher CaO values seen in averages with more points suggests

that the shots were “drilling” through the tailings and incorporating material from Ca-sulfate veins beneath the tailings. In the Stimson drill tailings, we saw a greater spread in CaO values as we averaged a greater number of shots into each point in the tailings. However, there was also slightly more spread in the silica concentration between the one shot and three shot averages with the data on the first shot showing slightly more spread.

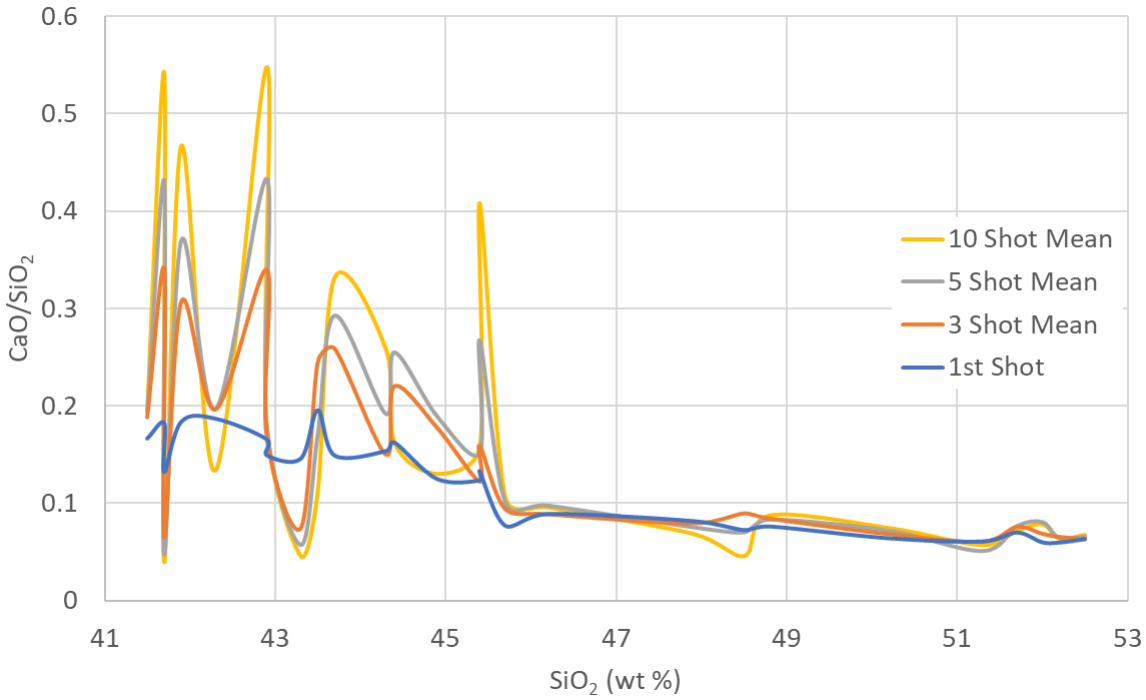

Figure 1.3: The ratio of CaO to SiO_2 (wt%) plotted against SiO_2 (wt%) for the points in the drill tailings of the Oudam, Marimba, Quela, and Sebina drill sites .

These results were then verified through a separate method. We collected the first shot and the average composition of the first three, five, and ten shots for the Oudam, Marimba, Quela, and Sebina sites. Then we computed the ratio of CaO to SiO_2 to check for the influence of Ca-sulfate veins beneath the drill tailings. The results were plotted against SiO_2 abundance so that we could see what occurred at different SiO_2 amounts (Fig. 1.3). This resulted in all four methods having roughly equal results at values above 46% SiO_2, but different results below that. At lower silica abundances, there were higher peaks in the ratio

values for the averages with a greater number of shots. The trend of greater variation with more shots averaged suggests that more CaO, possibly from Ca-sulfate veins, was being incorporated with each shot. The first shot showed the least amount of contamination, but the three-shot average had much less contamination than the other two averages.

If the drill tailings were a well-mixed representation of the average composition of the drill holes and all the shots were in the tailings, then we would expect less variation with a greater number of shots averaged. As the amount of variation seen in the averages tends to increase with a greater number of shots included in the averages, it seems reasonable to assume that the shots were "drilling" through the tailings into the rock underneath. The average of the first three shots was chosen to minimize the amount of underlying material included into the reported tailings and dump pile compositions while also preventing an anomalous composition at a single point from affecting the reported composition at that point. Using only the first shot was also decided to be unfeasible, because air-fall dust could contaminate the piles, but the first shot should remove that material.

3. K_2O Anomaly in Powdered materials

We first investigated the behavior of K_2O at the different drill sites by calculating ratios of the average K_2O abundances of the tailings to the average K_2O abundances of the drill hole wall, as these data types came from roughly the same location (0 to 2 cm below the surface) within the drill site. We only used drill sites with little indication of geochemical changes in depth. The K_2O content seemed to be depleted in the tailings at some sites, especially more in mudstones than in sandstones (Fig. 1.4).

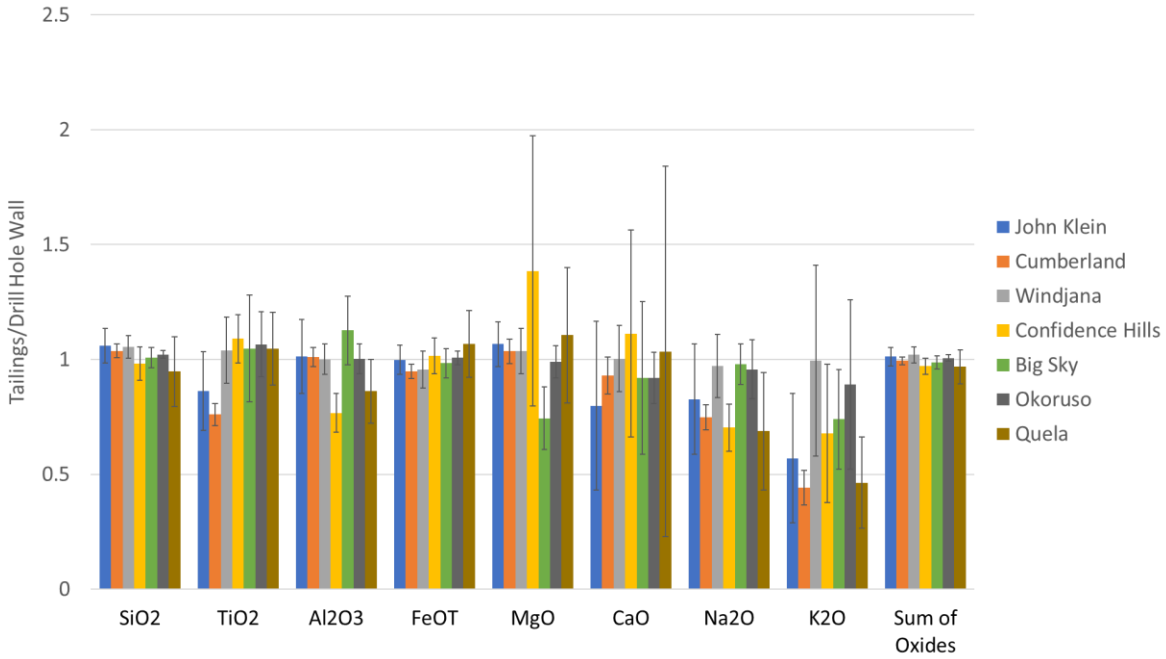

Figure 1.4: Ratio of average values of tailings to average value of the drill hole wall. Tailings represent material from the surface to < 2 cm of depth down the drill sites, and the drill hole wall data comes from < 1.5 cm of depth at the drill sites. This allows for a comparison of the composition by ChemCam of the same rocks as a solid and as powdered materials.

We also investigated the behavior of K_2O using powdered standards of andesine and lepidolite as analogs of the drill tailings. These powders were sieved to different grain sizes denoted on the graphs in Figure 1.5. The "Lepidolite_pellet" sample should represent the whole rock analyses of that standard. We were unable to obtain a pellet sample of andesine for a whole rock analysis using the LIBS instrument as the pellet was no longer available. However, the andesine standard has a reported K_2O content of 0.21 weight %. For reference, 75-100% of the rover drill tailings were less than 1 mm in diameter and 30-90% were less than 150 microns in diameter, as reported by the MSL engineering team (Anderson et al., 2012).

Figure 1.4 displays the K_2O abundances reported by calibrated LIBS observations using the ChemCam engineering model. Both Figures 1.4 and 1.5 show a lower estimated K_2O in the powdered sample compared to the whole rock; this lower value does not seem

to be related to total emission, i.e., the strength of the signal collected by the light emitted by the plasma generated by the laser. Unfortunately, the lack of a clear trend prevents a correction for K_2O based on a relationship with total emission, as was originally hoped. Thus, K_2O was found to be an unreliable oxide for studies that involve powdered and solid materials.

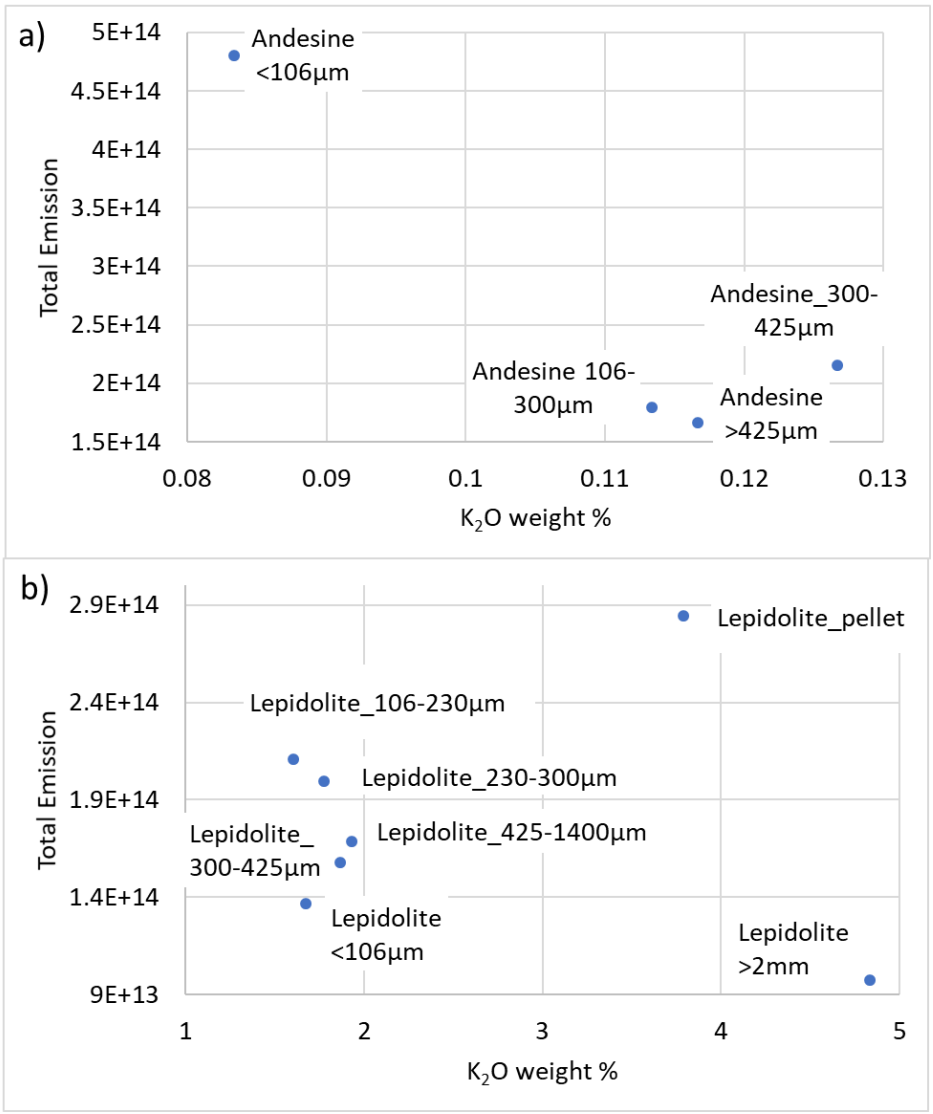

Figure 1.5: Behavior of reported K_2O abundance and total emission from LIBS observations using the ChemCam Los Alamos National Laboratory engineering unit for a) andesine and b) lepidolite standards sieved to different sizes.

4. Dust coatings and possible porous surfaces in the high silica surfaces

It was found that, on average, in the single shot data in the high silica Stimson formation, there was an increase in silica from shot #5 to shot #10 or #15 (Fig. 1.6). This resembles a continuation in the dust signal after the first five shots when the dust is thought to have been removed, due to the lower silica composition of the dust (Wiens et al., 2013). The trend of increasing silica may result in some high silica Stimson targets having lower silica than reported by ChemCam. This increase in silica with shot number was investigated by collecting the single shot data for the high silica Stimson targets and averaging each shot together across all targets: all the first shots averaged together, then all the second shots averaged together, and so on through the 30^{th} shots collected at each point. In addition, due to the large data sets used in these calculations, the standard deviation of the mean was calculated to estimate the accuracy of the mean (McKillup & Dyar, 2010). The average of each shot in the high silica stimson showed in an increase in silica from 59.0±0.4 % at shot #6 to 60.8±0.4 % at shot #20 (Fig. 1.6a). However, not every point exhibited the pattern of extended increase in silica. Therefore, each ChemCam observation point was evaluated separately to find points, which strongly matched the pattern observed in Figure 1.6a. The selection of the ChemCam observation points with this characteristic was done, with the requirement that the silica composition continued to increase from the dust composition after shot #5 and leveled off at some point between shot #10 and shot #20. The single shot data was averaged together in the same manner as discussed above and showed a more significant increase in silica from 61.6±0.9 % at shot #6 to 67.8±1.0 % at shot #20 (Fig. 1.6b). This result contrasts with the baseline Stimson points

where the single shot data were averaged in the same manner as the high silica targets and the silica abundances leveled out after shot #5 (Fig. 1.6c). The baseline Stimson points with the single shots averaged in this way gave a silica abundance of 45.2±0.1 % at shot #6 and 45.7±0.1 % at shot #20 and 45.9±0.1 % at shot #30. At the baseline sites, silica also continued to increase after the dust should have been removed; however, the magnitude was much less, and the values did not level off after shot #15 or #20.The average of the "best examples" was distinct from the average of all high silica Stimson data. While the first shot in the dust was nearly identical, the "best examples" leveled out at ~68 wt% SiO_2, compared to 60.8 wt% for all points in the high silica Stimson. The change from shot #5 to shot #15 was much greater, 7.4 wt% SiO_2 for the best examples, compared to just 2.3 wt% for all the data.

The continuation of the dust signal after shot #5 may be due to several possibilities. One is that it takes more than the first five shots to remove all of the dust; this effect would not have been observed previously, because the contrast between dust and the high silica Stimson sediment was greater here than at other locations. Another possibility is that the diagenetic silica at the Stimson formation (Frydenvang et al., 2017) variably coats the sediments, and this effect was more prominent at the surface. In this instance, the laser pulse could sample a variety of different geochemical components. At this location, these include possible remnant baseline Stimson, altered Stimson, silica coatings, as well as Ca-sulfate material, all of which could have an effect on the silica abundances measured. In addition, plasma coupling effects cannot be ruled out (Cremers & Knight, 2006), and an in-depth investigation of the individual spectra at these locations should be conducted in the

future, especially for the spectra highlighted as the best examples. In addition, it could be helpful to broaden this research to compare the results on the high silica Stimson with other geologic units with compositions distinct from martian global dust. A good starting place for this comparison could be the Kimberley (Rice et al., 2017) or LIBS points completely on diagenetic features,

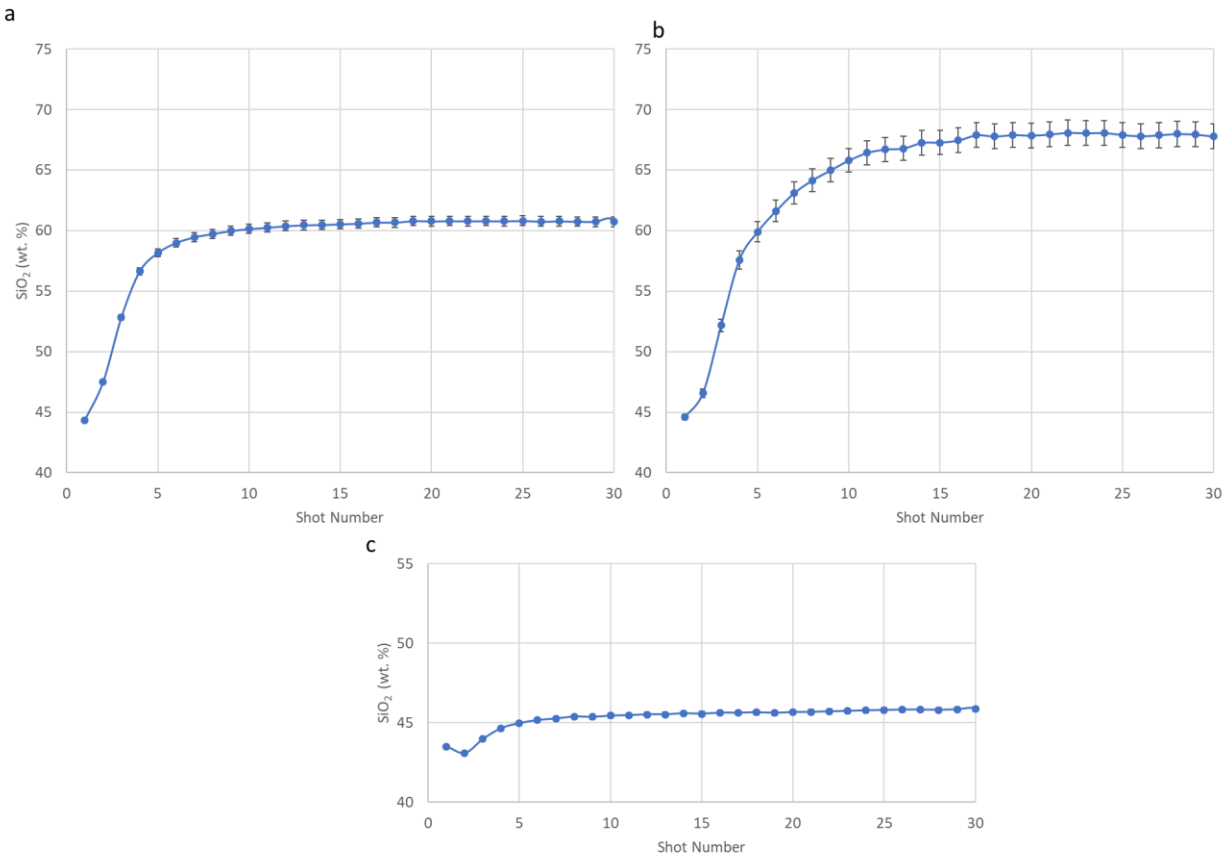

Figure 1.6: Plotting the average SiO_2 abundance at each individual shot across points in the high silica Stimson and Baseline Stimson; in order to observe an increasing silica gradient after the dust should have been removed by the ChemCam laser. a) average SiO_2 values for single shot data at each shot for all targets in the high silica Stimson, b) average SiO_2 values for single shot data at each shot for the targets for the best examples of this trend in the high silica Stimson, c) average SiO_2 values for single shot data at each shot for all targets in the baseline Stimson. All error values are standard deviation of the mean.

for example Ca-sulfate veins. To best understand this occurrence, it would be important to conduct laboratory studies using ChemCam engineering models and analogs of martian dust and the high silica Stimson sandstones to understand exactly what is interacting, for

example, an interaction between dust and rock or plasma effects, as well as determine nature of the interaction.

5. Strontium in the Ca-sulfate veins

The behavior of Sr in Ca-sulfate veins is of interest because Sr^{2+} can substitute for Ca^{2+} in the structure of Ca-sulfates. Strontium, Mg, Na, and K will precipitate in gypsum at differing rates based on temperature, concentration in the solution, and growth rate of the crystal (Lu, Meyers, & Hanson, 2002). However, the Sr abundance in Ca sulfates is the least influenced by the presence of fluid and solid inclusions in the mineral (Kushnir, 1980). These observations suggests that the ChemCam Sr/Ca ratio could be useful for determining information on the environments in which the veins were deposited, notably the Ca-sulfate veins sampled by the rover, since entering Yellowknife Bay and throughout the Murray formation (Nachon et al., 2014; Nachon et al., 2017). In addition, Ca-sulfate cements have been detected in the Murray formation (Baker et al., 2019), which provides another material for comparison of the behavior of Sr.

We used the ratio of Sr to Ca to normalize the Sr abundance to the amount of Ca in the observation. ChemCam observation of veins may include dust or sediment. These materials still contained CaO (< 10 weight %) and an unknown amount of Sr, which might bias the measurements of Ca sulfates though likely not by much; however, the ratio of Sr/CaO provides the simplest way to investigate substitution of Ca by Sr in Ca sulfates. We observed considerable variation in the Sr/Ca ratio at each geologic unit, but the values in the veins were usually all on the low end of values seen at each elevation by comparison of the veins and the bedrock units (Fig. 1.7).

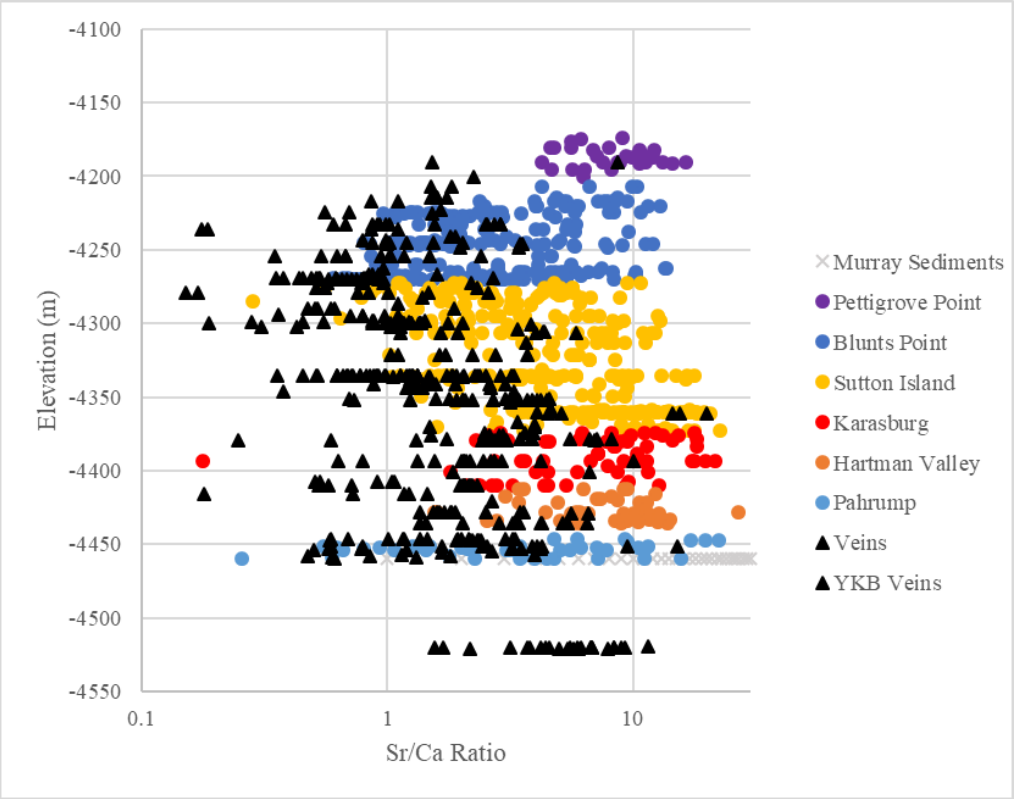

Figure 1.7: Variation in the Sr (ppm) to Ca (wt. %) ratio with elevation across the Murray Formation for Ca-sulfate veins and cements (triangles and colored circles, respectively). Stratigraphy in the Murray formation is divided into geologic members which are color coded for the cement data. Veins are placed according to elevation, so their geologic members can be determined by the color of the surrounding bedrock data. Higher ratios suggest deposition from a more saline fluid.

Previous research has shown that Ca sulfates can suffer from poor laser coupling with the ChemCam instrument on Earth (Wiens et al., 2012). We checked the laser coupling by comparing the modeled Sr abundances from the ChemCam trace element calibration for a set of gypsum standards to the laboratory reported Sr abundances (Fig 1.8). The standards used in this study include gypsum standards obtained from Brammers and geologic standards collected from the Society Cliffs Formation (Bylot Supergroup, northern Baffin Island, Canada). All these standards and their characterization by the ChemCam instrument have been extensively discussed elsewhere; it is important to note that the Sr calibration method used ~400 standards consisting of a large range of rock types (Clegg et al., 2009;

Kah et al., 2001; Ollila et al., 2014; Payré et al., 2017; Wiens et al., 2013). The ChemCam calibration did not agree with the laboratory results for Sr. Standards with lower Sr abundances, on average, were overestimated, and standards with higher Sr abundances, on average, were underestimated. However, each standard was sampled five times by the ChemCam engineering model at Los Alamos, and many standards had a large amount of variation with some standards having nearly as much variation in those five measurements as the variation between standards. This resulted in some standards being both overestimated and underestimated at times.

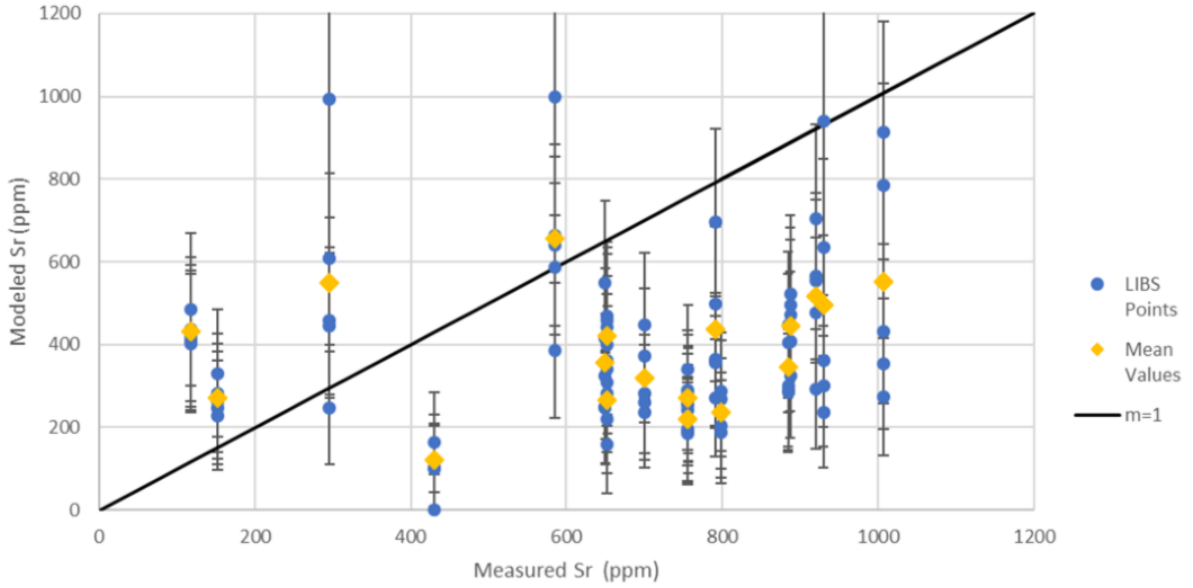

Figure 1.8: Sr abundances of Ca-sulfate standards compared to Sr determined by the whole rock ChemCam calibration [8 & 9]. Blue dots are single LIBS points on each standard and the error bars are root mean square errors for each. The yellow triangles are the average of the five points on each standard. The black line shows the 1:1 correlation.

We investigated the variability of the spectra of the standards by calculating the standard deviation of the signal intensity at every wavelength across the 30 laser shots fired at each observation point. This value was then normalized by the mean signal intensity so that the standards could be compared with each other. The standards containing gypsum or

other Ca-sulfate material had much greater variation than the basalts standards, which are thought of as analogs to 'typical' martian sediments. Together, Figures 1.8 and 1.9 suggest that the unique optical properties of crystalline gypsum create a problem for analysis by the LIBS technique. These laboratory results, along with the variation and low values observed on Mars, suggest that the current trace element calibration is insufficient for Sr in Ca-sulfate veins. In addition, it seems unlikely that it will be possible to develop a vein-centered calibration method due to the poor coupling with gypsum standards on Earth.

6. Conclusion

The initial part of this project was undertaken to evaluate possible complications when using the ChemCam LIBS technique. As a result of the energetic nature of the LIBS laser pules, special care must be taken when analyzing drill fines or other thin powders on top of solid rocks; however, by using only the first three shots on those piles, it is possible to conduct a successful analysis. In addition, I identified three instances where further work is needed. The K_2O anomaly should be further investigated to determine if a correction for data in powdered material is possible, but it is important to note that most of the research on the drill byproducts can be done without K_2O. The silica signal seen in the shot-to-shot data on the high silica Stimson warrants a more in-depth study that time did not allow here. Future studies should delve deeper into the data collected on Mars as well as include laboratory studies to understand the pattern observed. Finally, it would be beneficial if Sr in Ca-sulfate veins could be accurately quantified; however, due to the laser's poor coupling with Ca-sulfate standards on Earth, this may not be possible.

CHAPTER 2: ChemCam investigation of the Curiosity rover drill sites, drill holes, and drill fines through sol 1497; evidence of surface-correlated chemical variations

1. Introduction

The Curiosity Rover has a 1.9 m long robotic arm, at the end of which is a turret housing the Sample Acquisition, Processing, and Handling Subsystem (SA/SPaH), responsible for collecting rock samples for delivery to the internal instruments (Grotzinger et al., 2012). The SA/SPaH subsystem has three components: the Dust Removal Tool (DRT), a spinning wire brush which partially removes dust from surfaces for APXS and MAHLI observations and two systems involved in the processing of materials for the internal instruments, The Powder Acquisition Drill System (PADS) and the Collection and Handling for Interior Martian Rock Analysis (CHIMRA). The PADS is composed of a rotary-percussive drill and a collection tube. Due to the design of this tool, material is not collected until after the drill reaches a depth of ~2 cm into the bedrock, when the end of the collection tube descends below the surface, into the hole. The resulting holes are 1.6 cm in diameter and 5 - 6.5 cm deep. Material produced by drilling is transferred to the CHIMRA, which is responsible for sorting and delivery of the material to the internal instruments – CheMin and the Sample Analysis on Mars (SAM) instrument (Anderson et al., 2012). After Mars solar day, or "Sol" 1500, the CHIMRA could not be used due to failure of the drill feed (Fig. 2.1b); this also changed the drilling procedures for sites drilled after this failure. CheMin is a powder X-ray diffraction (XRD) instrument with a detection limit generally ~ 3 wt. % for crystalline phases, a relative accuracy of ±15 %, and relative precision of ±10 % (Blake et al., 2012).

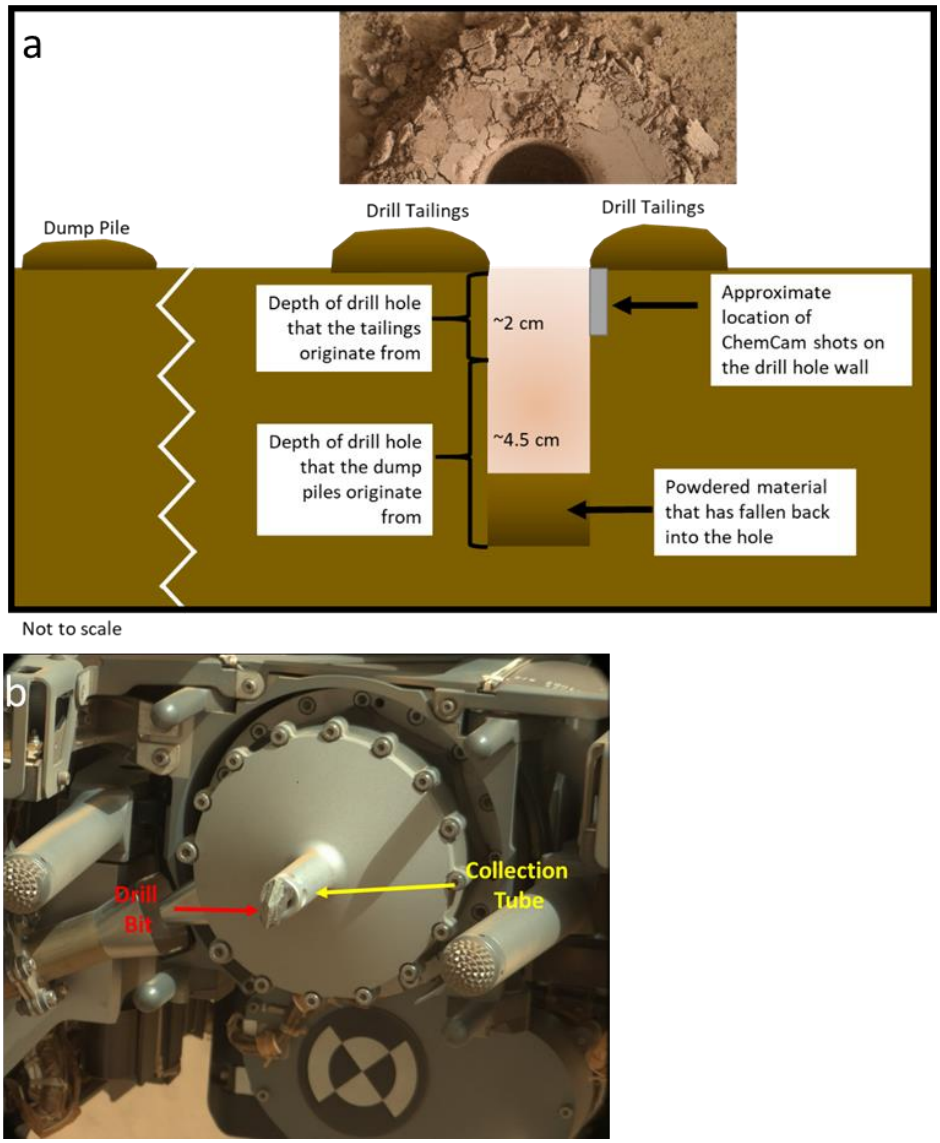

Figure 2.1: a) Schematic of the drill site showing the locations within the hole where the drill tailings (material not ingested by the sampling system) and dump pile material (material processed in the SA-SPaH system) originated. Also shown is the location on the drill hole wall where ChemCam is able to target. The drill tailings accumulate at the surface around the drill hole as can be seen in the MAHLI image of the Quela drill site above the schematic (NASA/JPL-Caltech/MSSS). The dump pile is taken up by the rover and dumped near the drill site or carried by the rover before being dumped at a new location. b) MastCam image of the drill bit after the Cumberland sample was drilled (NASA/JPL-Caltech/MSSS). The diameter of the drill bit is 1.6 cm and the collection tube is 1.4 cm.

In some cases, CheMin can report minerals in concentrations below 3% (e.g. Rampe et al., 2017a; Yen et al., 2017; Bristow et al., 2018). In addition, CheMin is also able to identify phyllosilicates, including clays (Blake et al., 2012). SAM consists of three instruments: a quadrupole mass spectrometer, a tunable laser spectrometer, and a six-column gas

chromatograph (Mahaffy et al., 2012). The SAM instrument has provided information about water content, organics, and other volatiles as well as some age constraints from cosmogenic nuclides at some of the drill sites (e.g. Ming et al., 2014; Farley et al., 2014; Martin et al., 2017).

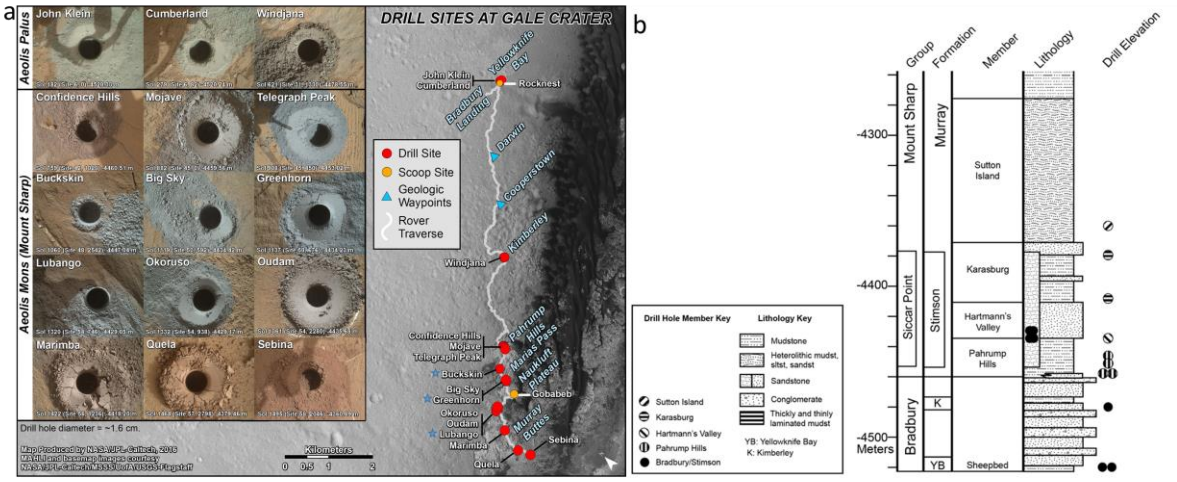

Figure 2.2: a) All fifteen drill holes discussed in the paper with pertinent information; as well as the location of each drill site along the rover traverse. The high-silica group which consists of Buckskin, Greenhorn, and Lubango are marked with a blue star. b) Stratigraphy of the portions of Gale Crater explored so far by the Curiosity rover with locations of each drill site marked. Modified from MSL sedimentology and stratigraphy working group.

Previous research has demonstrated that the drill tailings, which are created during the initial drilling process, are distinct from the dump pile, which is composed of material collected by the drilling system and left over from delivery to the internal instruments (Anderson et al., 2012, Jackson et al., 2016). Drill tailings are from the top ~2 cm of the drill hole while the dump piles are from material collected by the SA/SPaH and overwhelmingly come from below ~2 cm (Fig. 2.1a). These materials are analyzed by ChemCam and APXS in addition to sampling the surface of the drill sites before drilling. ChemCam can also directly target the drill hole wall with the LIBS system, but only to a depth of typically < 1.5 cm.

Table 2.1: Published CheMin data on the drill sites in this report, modified from the sources indicated.

Samples	Windjana	Confidence Hills	Mojave _2	Telegraph Peak	Buckskin	Oudam	Marimba	Quela	Sebina	Big Sky	Greenhorn	Lubango	Okoruso
Formation	Kimberley				Murray						Stimson		
Locality/ Member	Dillenger	Pahrump Hills			Marias Pass	Hartmann's Valley	Karasburg		Sutton Island				
Sol Drilled	621	759	882	910	1062	1361	1422	1464	1495	1119	1137	1320	1332
Sanidine	21	5		5.2	3.4		2.4±0.6	2.3±0.5	1.4±0.4				
Augite	20	6.4	2.2										
Pigeonite	11	5.3	4.6	4.2						17.0	1.6	1.6	13.5
Orthopyroxene		2.1		3.4		5.3±0.9	0.7±0.6	2.7±0.7	2.8±0.4	8.4	2.7	2.8	7.2
Plagioclase	3	20.4	23.5	27.1	17.1	27.8±0.5[c]	14.0±0.9[c]	13.5±0.7[c]	10.7±0.4[c]	36.5	14.7	11.7	27.2
K-feldspar										1.1			1.9
Olivine	det?[a]	1.2[b]	0.2[b]	1.1[b]									
Magnetite	12	3.0	3.0	8.2	2.8					10.3	6.1	3	11.2
Hematite	0.6	6.8	3.0	1.1		13.9±0.4	6.4±0.4	7.1±0.4	6.9±0.2	3.0	2.1	0.6	0.7
Quartz		0.7	0.8	0.9		0.7±0.1	Detected	Detected	Detected	1.4	0.8	0.9	0.9
Cristobalite				7.3	2.4								
Tridymite					13.6								
Pyrrhotite	0.3												
Akaganeite	0.2												
Anhydrite	0.4				0.7					1.2	5.6	3.3	0.5
Bassanite	0.5										1.4	2.4	0.8
Gypsum												0.6	
Ca-Sulfates*						6.3±0.3	7.0±0.6	5.5±0.4	7.4±0.6				
Jarosite	det?	1.1	3.1	1.5			Detected	Detected	Detected				
Fluorapatite		1.3	1.8	1.9						1.1			1
Opal-CT				10.9	6								
Clay Minerals**	10	7.6[c]	4.7[c]			3±1	28±5	16±3	19±4				
Amorphous Component	15	39.2±15	53	27.2±15	54	43±20	40±20	52±25	51±25	20±10	65±20	73±20	35±15
Reference	Treiman et al., 2016	Rampe et al., 2017					Bristow et al., 2018				Yen et al., 2017		

a: Enstatite
b: Forsterite
c: Andesine

* Ca-sulfates reported as the sum of Gypsum, Anhydrite, and Basanite

**Clay minerals alternatively reported as Phyllosilicates or Smectite/Illite

Beginning at Yellowknife Bay (Grotzinger et al., 2013) up through Sol 1500, the rover drilled fifteen sites which are shown in Fig. 2.2; CheMin mineralogy is reported in Table 2.1. The first two drill sites, John Klein and Cumberland, were both in the Sheepbed Mudstone in the Yellowknife Bay formation. The Yellowknife Bay formation was determined to have formed in a lacustrine environment that had a neutral pH and contained relatively fresh water (Grotzinger et al., 2014; Vaniman et al., 2014). The Sheepbed mudstone is the lowest explored stratigraphic unit in the formation and has evidence for diagenetic materials, notably Ca-sulfate veins (Nachon et al., 2014) and Mg-rich ridges (McLennan et al., 2014; Leveille et al., 2014). The geologic context of the different drill sites has been described in various papers by the Curiosity science team.

After leaving Yellowknife Bay, the next location that Curiosity drilled was Windjana in the Kimberly formation. The Kimberley is a prograding, fluvio-deltaic system thought to predate the sedimentary Mount Sharp deposits; the likely source of the sediments is an alkali feldspar protolith (Rice et al., 2017; Treiman et al., 2016; Le Deit et al., 2016). After deposition, the Kimberley experienced several stages of diagenesis resulting in Ca-sulfate veins, manganese oxide fracture fills (Lanza et al., 2015), and resistant nodules. Windjana is in the Dillinger member of the Kimberly (Fig. 2.3), which is an eolian sandstone, while the rest of the Kimberly is characterized by fluvial sandstones. The Dillinger member is geochemically distinct from the fluvial sandstones, so it is not likely a reworking of those sandstones (Le Deit et al., 2016).

After leaving the Bradbury group the rover entered the Murray formation, the lowest exposed strata of the Mount Sharp group (Fig. 2.3). This formation consists of a ~350

m thick sequence of fine-grained laminated mudstone with some interfingered sandstone; it is interpreted to be the result of mostly lacustrine environments. The Pahrump Hills section was the first section of the Mount Sharp group (Fig. 2.2) encountered by the Curiosity rover (Grotzinger et al., 2015). The team's preferred interpretation of the Pahrump Hills setting is deposition in relatively fresh lake waters. However, the chemistry and mineralogy could also be consistent with sediment deposition in lake waters with variable pH and Eh (Hurowitz et al., 2017). After lithification, at least one episode of acidic groundwater was apparently involved in diagenesis along fractures (Rampe et al., 2017a). The rover drilled at three sites in the Pahrump Hills and the mineralogy results are reported in Table 2.1. About 13 m up section from Confidence Hills, the rover drilled at the Buckskin drill site. At Buckskin, no phyllosilicates were detected; the site was notable for containing 13.6% tridymite. This observation was interpreted as representing the first in-situ detection of silicic volcanism products in sediments on Mars (Morris et al., 2016). After exploring the Stimson sandstone (see below) the rover re-entered the Murray formation and drilled at another four sites, Oudam, Marimba, Quela, and Sebina. At these sites, feldspars and phyllosilicates make up most of the crystalline weight of each sample, with hematite and Ca-sulfates being the next most common crystalline phases, followed by mafic igneous minerals (Rampe et al., 2017b).

Draping over the eroded surface of the Murray formation, sloping down from Mt. Sharp, is the Stimson sandstone (Fig. 2.2) which is the youngest stratigraphic unit that the Curiosity rover has explored so far. The sandstone is of an eolian origin based on the presence of wind ripples and grain characteristics (Banham et al., 2018). In the lower

portion of the formation, light-toned fracture-related halos were observed, interpreted as regions of late aqueous alteration and high-silica deposition. This alteration represents one of the youngest hydrogeologic events known at Gale Crater (Frydenvang et al., 2017; Yen et al. 2017). There were four drill sites in the Stimson (Table 2.1); two, Big Sky and Okoruso, in the baseline Stimson and two more, Greenhorn and Lubango, in the high-silica halos.

The various ChemCam observations at the drill sites at Yellowknife Bay have been studied to compare the original surface, the walls of the holes, the tailings, and the dump piles in order to understand the homogeneity of the material that was drilled and its surroundings. These two drill holes (Fig. 2.4) showed very little geochemical variation down the depth of the hole; however, at John Klein there was a variation in the amount of CaO between the top and bottom of the drill site. The variation in CaO at John Klein was most likely due to a heterogeneous distribution of Ca-sulfate veins throughout the hole which was corroborated by MAHLI imagery of the drill hole walls. This observed variation in chemical composition indicates that spatial variation of the geochemical components at the drill sites can be determined by investigating the drilling byproducts. (Jackson et al., 2016). The study of these types of ChemCam observations was extended to the subsequent 13 drill holes in the units described above to similarly investigate if there are any geochemical changes with depth at these sites.

2. Methods

ChemCam consists of a Laser Induced Breakdown Spectroscopy (LIBS) instrument which allows for ~400 µm diameter chemical analyses from 1.5 m to 7.0 m away, as well as a panchromatic Remote Micro Imager (RMI) for context (Maurice et al., 2012; Wiens et al.,

2012). ChemCam analyses are planned and organized by individual sequences (which have a unique target name), usually consisting of a line-scan or grid raster pattern of observation points. At each point ChemCam fires multiple laser shots and records an emission spectrum for each shot. In this study, 5-10 different points in a line or grid raster pattern were analyzed per named target sequence (Wiens et al., 2012). The elemental detections from the LIBS spectra are reported in terms of the abundances of SiO_2, TiO_2, Al_2O_3, FeO_T, MgO, CaO, Na_2O, and K_2O; data for Li, Rb, Sr, and Ba are provided in Appendix C. The abundances are quantified by using a calibration method which uses both a Partial-Least Squares (PLS1) training algorithm and Independent Component Analysis (Clegg et al., 2009; Wiens et al., 2013; Forni et al., 2013; Clegg et al., 2017). The LIBS technique vaporizes a small amount of material with each laser shot, so that successive shots penetrate deeper into the material. By analyzing successive spectra one can observe how the composition of the material changes with depth on a scale of microns in rocks and millimeters in loose material. In loose sediment, such as the tailings and dump pile, the LIBS shots can "dig" through the material into the rock underneath even in sequences of only 30 shots per point (Lanza et al., 2015). This effect was dealt with during data processing, described below.

ChemCam data are usually processed and reported in two ways: as an average for each point, which ignores the first five laser shots (typically out of 30 or 50). This procedure involves creating an averaged spectrum which is analyzed via the calibration method discussed above. In normal bedrock targets the first five shots can contain a signature of surficial dust, not present on fresh drill hole targets, drill tailings, or dump piles. The other method is use of single shot data where the spectrum generated by each individual shot is

analyzed by the calibration method separately. The former has a much less noisy average spectra but does not reveal variations among the 30 shots that might occur in tailings or dump piles. In this paper, the averaged data processing was used for targets on the surface of the drill sites and on the drill hole walls, while the data for the first three single shots were collected and averaged at each point in the tailings and dump piles. Only the first three shots were used in the drill tailings and dump piles to try to exclude as much of the underlying rock in those analyses, but it may not be possible in all cases to prevent some sampling of the underlying rock in the analyses of drill fines (Chapter 1).

Table 2.2: Number of ChemCam observation points used to compute each average.

Samples	John Klein	Cumber-land	Wind-jana	Confidence Hills	Mojave_2	Telegraph Peak	Buck skin	Oudam	Marimba	Quela	Sebina
Surface	26	74	26	---	8	3	13	9	20	10	10
Drill Hole	10	4	26	10	---	23	10	---	10	19	9
Tailings	17	16	18	15	10	---	5	1	---	5	---
Dump Pile	10	15	9	3	4	3	---	5	3	---	---

Samples	Big Sky	Greenhorn	Lubango	Okoruso
Surface	5	15	10	19
Drill Hole	10	19	19	3
Tailings	5	5	9	20
Dump Pile	---	5	5	15

All points were reviewed to ensure the accurate targeting of the laser and only points validated for delivery to the Planetary Data Science Node were used to ensure data quality. The number of points used in each average are given in Table 2.2. Points were then separated into four categories based on the documented observational intention: Surface, Drill Hole Wall, Drill Tailings, and Dump Pile. During the review, it was noted if a point was inadvertently targeted outside of the observation's intended category – for example a point intended to be on the tailings instead landing on the surface – and that point was moved

into the correct category. Then the mean values and the standard deviations of the observation points for each category at each site were calculated.

Unfortunately, it was determined that K_2O abundances are underestimated in powdered materials compared to solid materials. This was verified in laboratory experiments on Earth and therefore in this paper the K_2O abundance is not reported. For other elements besides K_2O, powdered materials (tailings and dump piles) can be compared to solid materials (drill site surfaces and the drill hole walls). Fortunately, alkali behavior can still be inferred through the behavior of Na_2O (Chapter 1).

3. Results

Figure 2.4 displays the variation between the mean oxide abundances for each element at each drill site, including the Sheepbed sites reported in Jackson et al. (2016). Table 2.3 lists the average abundances and the standard deviations of the ChemCam points for each oxide within each data type. Here we present the results for the subsequent drill sites in successive order.

Looking at the Windjana plot, it does not show much variation between the surface, drill hole wall, tailings, and dump pile, with each oxide having small standard deviations and all the mean oxide values falling within one standard deviation of the mean of the points for each data type. In Table 2.4, the percent change from the mean composition of the surface is displayed for the other three data types; however, as stated previously for Windjana all these changes fall within one standard deviation from the mean surface composition.

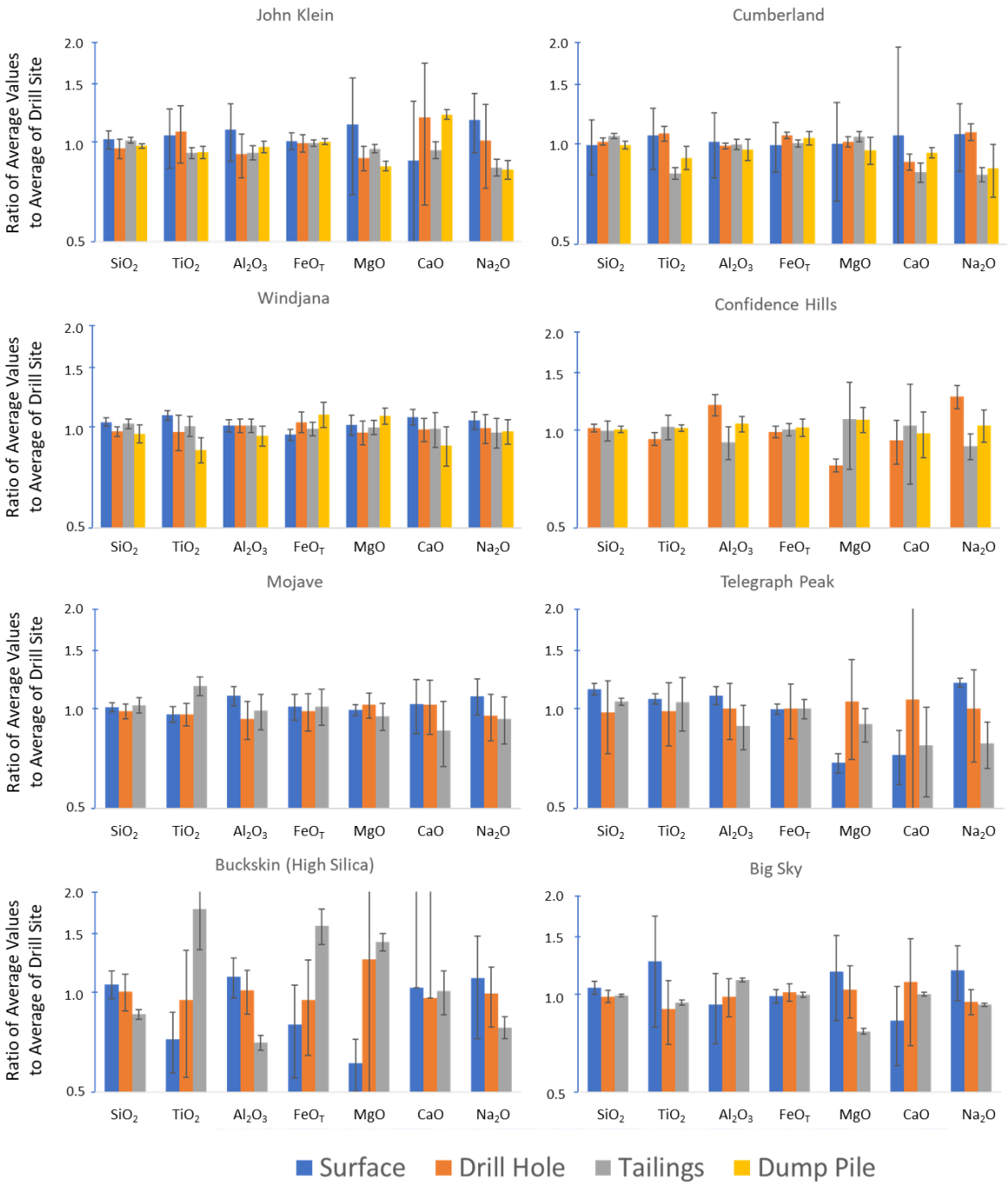
John Klein
Cumberland
Windjana
Confidence Hills
Mojave
Telegraph Peak
Buckskin (High Silica)
Big Sky
Ratio of Average Values to Average of Drill Site
2.0
1.5
1.0
0.5
SiO2
TiO2
Al2O3
FeOT
MgO
CaO
Na2O
Surface
Drill Hole
Tailings
Dump Pile

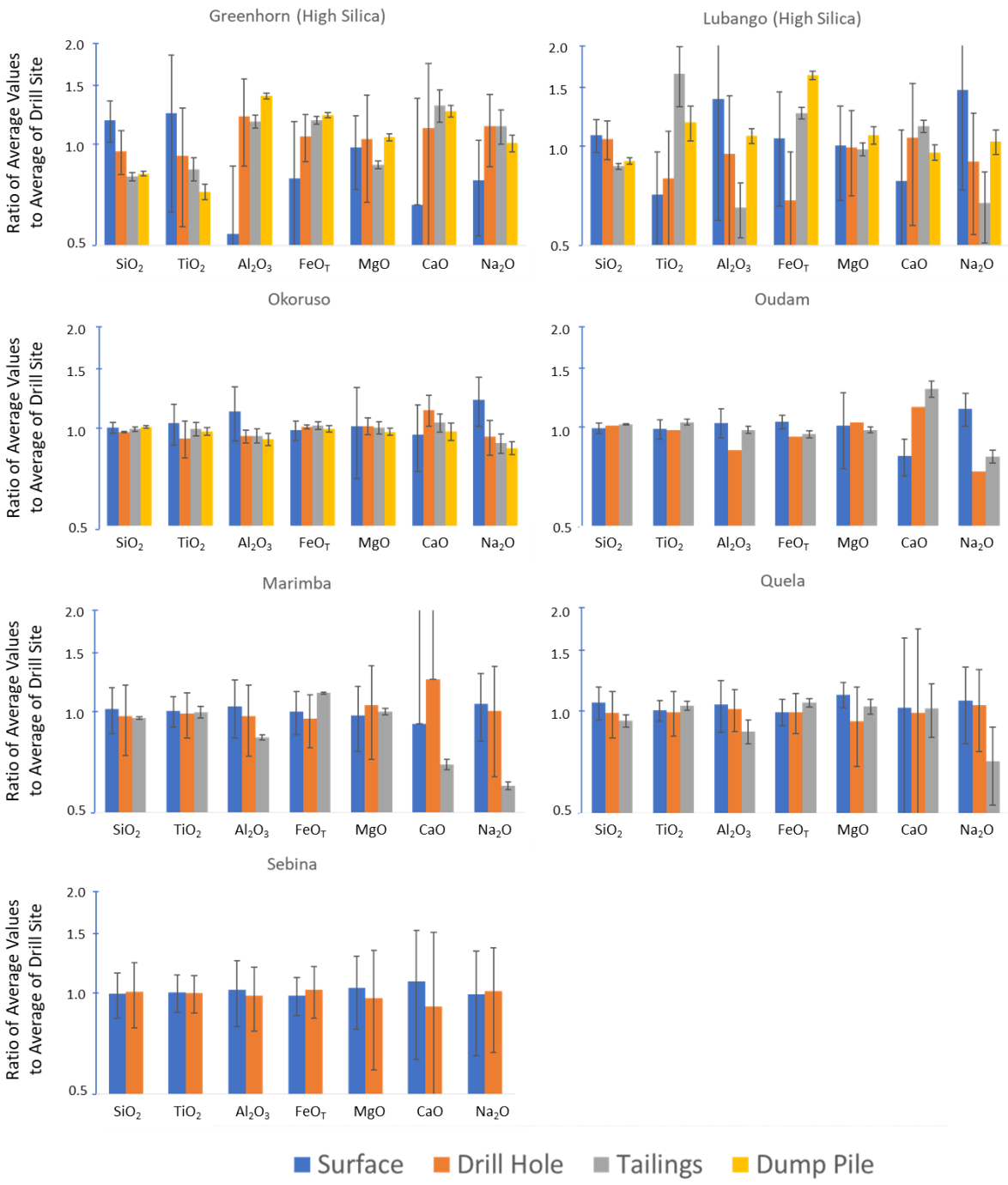

Figure 2.3: Average compositions for each data type normalized to the average of all data for each point present at each drill site. Error bars show one standard deviation of the data set normalized to the average of all data at that drill site. Graphs are in semi-log format. The three high-silica sites are noted as such in their titles. It was not always possible to collect each data category at every drill site.

Table 2.3: Average value and standard deviations for surface, drill hole wall, tailings, and dump pile for every drill site.

Samples	John Klein	Cumberland	Windjana	Confidence Hills	Mojave_ 2	Telegraph Peak	Buckskin	Oudam	Marimba	Quela	Sebina	Big Sky	Greenhorn	Lubango	Okoruso
Surface															
SiO_2	47.3±3.0	45.2±8.4	44.8±1.3	---	51.5±1.6	51.4±2.1	67.9±8.0	51.1±1.8	49.3±7.7	48.5±5.4	41.8±6.5	43.9±2.0	68.0±9.6	63.2±7.3	44.0±1.7
TiO_2	0.9±0.2	1.0±0.2	0.9±0.03	---	0.9±0.1	1.2±0.04	2.6±0.6	1.0±0.1	0.9±0.1	0.9±0.1	0.8±0.1	1.3±0.5	2.0±1.0	1.3±0.5	1.0±0.1
Al_2O_3	10.1±2.0	9.3±2.1	7.4±0.3	---	16.4±1.1	12.5±0.8	9.9±1.4	10.3±1.0	9.5±1.9	9.9±1.7	8.9±2.0	10.4±2.5	2.7±1.6	8.1±4.6	11.5±2.1
FeO_T	19.2±1.1	19.1±3.2	18.0±0.7	---	15.8±1.4	18.7±0.7	6.2±3.8	20.0±0.9	18.4±2.7	19.0±1.7	15.7±2.0	19.4±0.9	11.7±5.6	11.2±4.2	20.0±1.3
MgO	10.8±4.1	8.1±2.6	9.6±0.7	---	4.8±0.2	2.5±0.2	2.3±1.2	5.5±1.4	4.1±0.9	4.3±0.4	3.6±0.9	8.2±2.4	2.6±0.6	3.4±1.1	7.3±2.2
CaO	5.3±2.7	6.8±5.6	4.8±0.3	---	5.3±1.0	5.4±1.0	3.9±4.7	2.3±0.3	5.4±6.5	8.1±4.9	13.7±5.7	6.2±1.7	5.5±5.9	7.7±3.3	5.6±1.3
Na_2O	2.9±0.6	2.8±0.7	1.3±0.1	---	3.3±0.4	3.1±0.1	2.3±0.8	2.4±0.3	2.2±0.5	2.2±0.6	1.6±0.6	2.8±0.5	1.3±0.4	2.6±1.3	2.9±0.5
Drill Hole															
SiO_2	44.5±3.1	46.2±1.1	41.9±1.4	49.5±1.4	---	43.6±10.9	64.7±8.2	---	46.9±11.1	45.2±7.0	42.5±9.4	41.1±1.8	55.0±8.2	61.6±8.2	42.7±0.2
TiO_2	0.9±1.0	1.01±0.1	0.8±0.1	1.0±0.04	---	1.1±0.2	3.4±1.4	---	0.9±0.1	0.9±0.1	0.8±0.1	0.9±0.2	1.5±0.6	1.5±0.6	0.9±0.1
Al_2O_3	8.5±1.3	9.1±0.2	7.4±0.3	12.8±1.0	---	11.5±2.2	9.0±1.4	---	8.8±2.1	9.5±1.3	8.6±1.8	11.0±1.5	6.0±1.7	5.5±2.8	9.7±0.4
FeO_T	19.0±1.1	20.4±0.4	19.6±1.4	19.9±0.8	---	18.8±3.6	7.4±2.4	---	17.5±3.1	19.0±2.5	16.3±2.9	19.9±1.3	15.7±2.5	7.3±2.9	20.5±0.3
MgO	8.6±0.7	8.2±0.3	9.2±0.8	3.6±0.2	---	3.9±1.3	4.7±4.6	---	4.4±1.4	3.6±0.9	3.3±1.3	7.2±1.3	2.8±1.0	3.4±1.0	7.3±0.4
CaO	7.1±3.3	5.7±0.3	4.4±0.4	4.0±0.6	---	7.9±7.3	3.7±5.9	---	7.4±8.6	7.8±5.9	11.5±7.6	8.2±3.0	9.3±5.1	10.5±4.8	6.6±0.7
Na_2O	2.5±0.7	2.9±0.2	1.2±0.1	2.7±0.2	---	2.6±0.8	2.0±0.4	---	2.0±0.7	2.1±0.6	1.7±0.6	2.2±0.2	1.9±0.5	1.6±0.6	2.2±0.3
Tailings															
SiO_2	47.1±1.0	47.9±0.9	44.3±1.4	48.6±3.5	50.1±2.6	---	55.2±1.9	52.07*	---	42.8±1.8	---	41.5±0.4	46.2±1.4	50.9±1.0	43.7±0.7
TiO_2	0.8±0.03	0.8±0.03	0.8±0.1	1.1±0.1	0.9±0.1	---	6.5±1.6	0.94*	---	0.9±0.03	---	1.0±0.02	1.4±0.1	3.0±0.6	0.9±0.04
Al_2O_3	8.6±0.4	9.2±0.3	7.4±0.4	9.8±1.1	14.0±1.8	---	6.2±0.3	8.5*	---	8.2±0.7	---	12.3±0.2	5.8±0.3	3.8±0.7	9.7±0.5
FeO_T	18.9±0.4	19.4±0.5	18.8±0.9	20.2±0.9	15.3±2.0	---	12.4±1.5	17.97*	---	20.3±0.6	---	19.6±0.3	17.4±0.5	13.3±0.5	20.6±0.6
MgO	9.1±0.3	8.5±0.3	9.5±0.5	5.0±1.5	5.0±0.4	---	5.4±0.3	5.63*	---	4.0±0.2	---	5.4±0.1	2.3±0.1	3.4±0.2	7.2±0.3

CaO	9.0±5.03	5.3±0.4	4.4±0.5	4.4±1.5	5.3±1.0	---	3.9±0.6	3.17*	---	8.1±1.5	---	7.5±0.1	10.9±1.2	11.3±0.5	6.1±0.4
Na_2O	2.1±0.1	2.2±0.1	1.2±0.1	1.9±0.2	2.9±0.5	---	1.6±0.1	1.56*	---	1.5±0.4	---	2.2±0.02	1.9±0.2	1.2±0.3	2.2±0.1
Dump Pile															
SiO_2	45.3±0.7	45.2±1.2	41.4±2.6	49.1±1.1	52.3±2.6	47.0±1.1	---	52.5±0.3	46.2±0.4	---	---	---	47.2±0.7	52.9±1.1	44.3±0.5
TiO_2	0.8±0.03	0.9±0.1	0.7±0.1	1.1±0.02	1.1±0.1	1.2±0.2	---	1.0±0.02	0.9±0.04	---	---	---	1.2±0.1	2.2±0.3	0.9±0.02
Al_2O_3	9.0±0.4	8.8±0.7	6.9±0.5	11.2±0.6	14.8±1.8	10.2±1.6	---	9.8±0.2	7.6±0.1	---	---	---	6.9±0.2	6.3±0.3	9.5±0.4
FeO_T	19.1±0.4	20.1±0.9	20.7±1.8	20.6±1.3	15.9±2.0	18.8±1.3	---	18.3±0.5	20.8±0.1	---	---	---	18.1±0.3	17.3±0.5	20.2±0.5
MgO	8.1±0.3	7.7±0.7	10.3±0.6	4.9±0.5	4.6±0.4	3.3±0.4	---	5.4±0.1	4.2±0.1	---	---	---	2.8±0.1	3.7±0.2	7.0±0.2
CaO	7.3±0.2	6.03±0.2	4.0±0.5	4.2±0.7	4.4±1.0	5.8±1.7	---	3.6±0.2	4.1±0.2	---	---	---	10.4±0.4	9.5±0.5	5.7±0.3
Na_2O	2.0±0.1	2.2±0.4	1.2±0.1	2.2±0.3	2.8±0.5	2.1±0.3	---	1.7±0.1	1.2±0.03	---	---	---	1.7±0.1	1.8±0.2	2.1±0.1

*Only one point in the Oudam Tailings

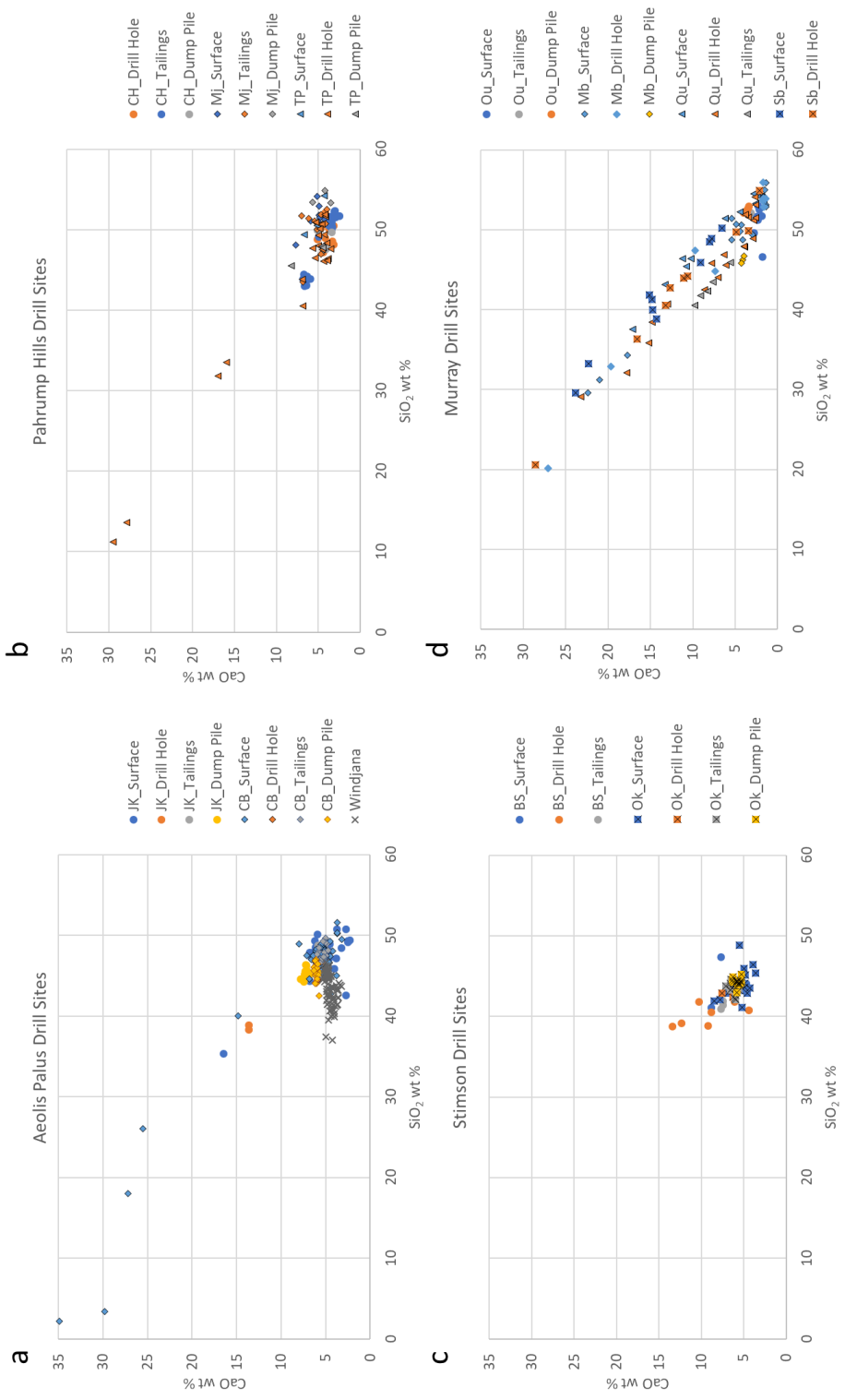

Figure 2.4: Scatter plots of SiO_2 and CaO for the baseline drill sites (all drill sites except Buckskin, Greenhorn, and Lubango). JK = John Klein, CB = Cumberland, CH= Confidence Hills, Mj = Mojave, TP = Telegraph Peak, BS = Big Sky, Gh = Greenhorn, Lb = Lubango, Ok = Okoruso, Ou = Oudam, Mb = Marimba, Sb = Sebina.

Table 2.4: Percent change of drilling products relative to the average surface. Confidence Hills was omitted due to lacking any “Surface” data.

Samples	John Klein	Cumber-land	Windjana	Mojave_2	Telegraph Peak	Buck skin	Oudam	Marimba	Quela	Sebina	Big Sky	Green horn	Lubango	Okoruso
Drill Hole														
SiO_2	-6.10	-4.30	-6.35	---	-15.08	-2.78	---	-4.74	-6.77	1.68	-6.24	-19.10	-2.66	-2.87
TiO_2	2.79	2.81	-10.80	---	-8.01	36.73	---	-1.67	-1.33	-0.65	-28.83	-25.15	11.94	-9.77
Al_2O_3	-15.71	-13.33	-0.10	---	-8.52	-10.54	---	-6.77	-3.34	-3.94	5.59	123.78	-31.81	-15.54
FeO_T	-1.38	6.64	8.99	---	0.33	2.67	---	-4.77	-0.06	3.87	2.73	33.57	-35.13	2.50
MgO	-20.71	17.14	-4.80	---	53.26	79.13	---	7.13	-16.40	-6.68	-11.71	6.14	-1.01	-0.02
CaO	34.63	-5.42	-8.34	---	46.96	-10.91	---	35.48	-3.51	-16.00	31.35	68.72	35.18	18.23
Na_2O	-13.21	-15.63	-5.26	---	-16.35	-11.12	---	-5.06	-3.19	2.43	-19.75	44.79	-39.12	-22.39
Tailings														
SiO_2	-0.51	-0.74	-1.16	-2.72	---	-17.07	1.98	---	-11.73	---	-5.48	-32.03	-19.53	-0.75
TiO_2	-11.37	-21.81	-7.24	-0.20	---	157.45	-0.93	---	3.26	---	-25.44	-31.68	131.79	-3.80
Al_2O_3	-14.64	-12.40	0.01	-14.84	---	-37.76	-17.39	---	-16.75	---	18.88	115.80	-52.97	-15.29
FeO_T	-1.52	1.01	4.14	-3.21	---	72.13	-9.97	---	6.65	---	1.00	48.72	18.90	3.20
MgO	-15.38	21.34	-1.41	3.56	---	102.05	2.01	---	-7.60	---	-34.31	-11.05	-2.45	-1.08
CaO	7.48	-12.05	-7.99	-0.47	---	-6.72	40.39	---	-0.25	---	20.69	97.45	46.33	8.61
Na_2O	-28.21	-36.98	-7.89	-12.82	---	-29.65	-35.11	---	-33.46	---	-21.40	45.16	-54.38	-25.75
Dump Pile														
SiO_2	-4.42	-6.46	-7.62	1.54	-8.41	---	2.76	-6.09	---	---	---	-30.65	-16.39	0.59
TiO_2	-10.92	-12.88	-21.09	21.38	-1.94	---	4.95	-0.62	---	---	---	-41.46	65.41	-5.35
Al_2O_3	-11.16	-15.41	-6.72	-9.77	-18.88	---	-4.82	-19.34	---	---	---	157.04	-22.58	-17.34
FeO_T	-0.41	4.56	14.94	0.26	0.24	---	-8.30	13.44	---	---	---	54.01	54.55	1.10
MgO	-25.00	10.54	6.58	-4.32	30.70	---	-3.06	2.38	---	---	---	7.46	7.56	-3.88
CaO	37.52	0.56	-17.68	-16.59	7.25	---	59.61	-24.22	---	---	---	89.68	22.22	2.07
Na_2O	-29.18	-34.24	-7.25	-14.61	-34.25	---	-28.13	-43.03	---	---	---	28.88	-30.22	-28.11

Three sites at Pahrump Hills – Confidence Hills, Mojave, and Telegraph Peak – show no variation between the surface, drill hole wall, and tailings. The latter two of these sites are notable though because they were targeted using manual z-stack focus techniques, so the team was not able to sequence as many observation points (Maurice et al., 2016). Unlike at Yellowknife Bay or sites in Stimson or further up in Murray, Ca-sulfates are uncommon within the data for the drill sites and were only sampled at the visible veins on the drill hole wall at Telegraph Peak, which was targeted multiple times by ChemCam to be able to sample the vein (Fig. 2.5b & Fig. 2.6). The multiple attempts to sample the veins at Telegraph Peak likely account for the large standard deviations and percent change in CaO in the Telegraph Peak data (Fig. 2.4 & Table 2.4).

Buckskin was drilled to investigate the mineralogy associated with the high silica discovered by ChemCam (Frydenvang et al., 2017) at Marias Pass (the region within which the Buckskin hole was drilled). The SiO_2 abundance is 17% lower in the tailings compared to the surface (Table 2.4) and is also lower than the drill hole wall region targeted by ChemCam. Figure 2.4 shows that TiO_2 and FeO_T have higher mean values in the tailings than at the surface, while Al_2O_3 has lower values in the tailings than at the surface. The surface and the drill hole wall have larger standard deviations than what has been seen before, especially the MgO observed on the drill hole wall (Table 2.3, Fig. 2.4). Unfortunately, Buckskin's dump pile was not sampled by ChemCam.

Of the four drill sites in the Stimson formation, the two baseline sites were chosen to avoid visible light-toned veins or haloes. Big Sky and Okoruso show little variation with depth, while of the high-silica sites, Lubango seems to show greater variation than

Greenhorn. At Lubango, TiO_2 and CaO abundances are greater in the tailings than in the dump pile, and Al_2O_3, FeO_T, and possibly Na_2O are lower in the tailings than in the dump pile. Greenhorn displays similar relationships, but these are less evident (Fig. 2.4). The percent change calculations clearly show that despite their similarities, not all elements behave similarly between Greenhorn and Lubango, most notably Al_2O_3 (Table 2.4).

The last four drill sites covered in this paper are in the Murray formation, above Pahrump Hills. Oudam is the stratigraphically lowest site of the four, near the base of the Hartmann's Valley Member. Oudam had only one usable point in the tailings, but for most of the oxides it is very close in value to the dump pile. The dump pile and possibly tailings are richer in CaO than the surface values and comparatively depleted in Na_2O. Marimba and Quela are at the bottom and top of the Karasburg member, respectively (Fig. 2.3). Marimba has greater CaO and possibly Na_2O at the surface and drill hole wall than in the dump pile. At both sites, but especially at Quela, the CaO concentrations have greater variations than seen at Oudam or most of the Pahrump Hills sites. Sebina only had useable data on the surface and drill hole wall, the compositions of which are nearly identical. (Fig. 2.4 and Table 2.4).

APXS and ChemCam data were compared to investigate differences due to the scale of the instruments' footprints, 15 mm for APXS (Campbell et al., 2014; VonBommel et al., 2016) and ~400 µm diameter spots arranged in various rasters for ChemCam. For the most part, there was not a sizable difference between the results of the two instruments; the greatest differences are at Buckskin and Lubango. These sites were characterized by high-silica abundances and spatial variations in silica abundances of up to 15 wt. % over 10 – 30

centimeters, suggesting either that the differences are due to precise sampling location and geometry or due to different instrumental responses in the high-silica material.

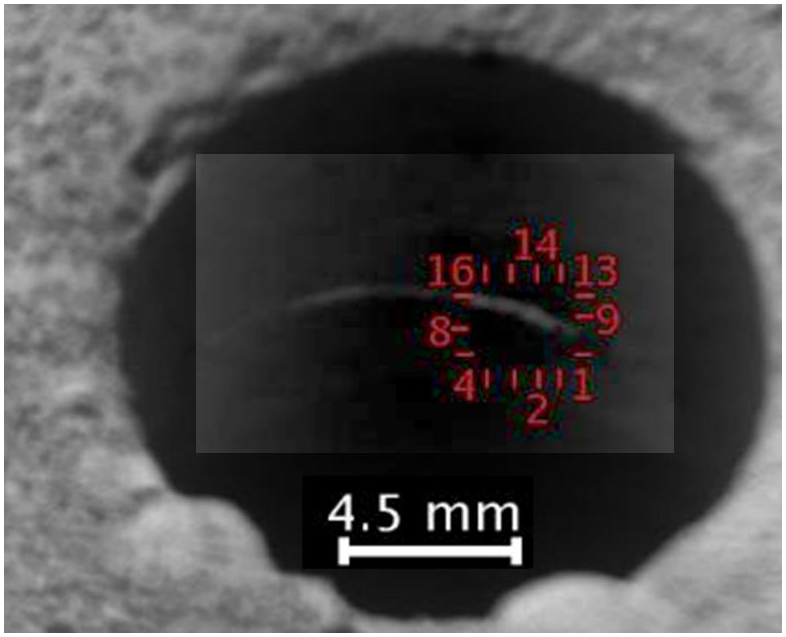

Figure 2.5: Remote Micro-Imager image of the Telegraph Peak drill hole, with the location of the last ChemCam sequence taken on the drill hole wall. The Ca-sulfate vein is prominently located within the ChemCam raster. The contrast of the center of the image has been enhanced to make the vein more visible.

4. Discussion

The drill sites can be divided into a “High-Silica” group consisting of Buckskin, Greenhorn, and Lubango and a “Baseline” group which is made up of the rest of the drill sites. High-silica sites were observed in Murray but, besides Buckskin, they were not drilled (Yen et al., 2017).

4.1 Baseline Sites

The baseline sites (Fig. 2.5) are all characterized by an anti-correlation between CaO and silica; this is due to variable sampling of silicate sediments and diagenetic Ca-sulfate veins and possibly Ca-sulfate cement. The silica-CaO anticorrelation becomes more pronounced as the rover progressed up Mount Sharp. The data from the sites on the crater

floor (Bradbury Group) are divided between points entirely on silicate sediments, a few points on or mostly on Ca-sulfate veins, and some points in the tailings and dump piles between the two extremes showing a mix of Ca-sulfates and those same silicate sediments in the drill fines. The only exception is Windjana which completely lacked evidence of Ca-sulfates in the ChemCam data. The Pahrump Hills sites were also mostly devoid of Ca-sulfates except for Telegraph Peak. While these sediments are higher in silica than John Klein and Cumberland, they display a similar relationship between silica and CaO. The sites higher in the Murray formation show a much more pronounced trend, indicating much more consistent mixing in the tailings and dump piles between silicate sediments and Ca sulfates. While the baseline Stimson sites – Big Sky and Okoruso – do have the same trend seen at the other locations, it is much less pronounced due to the smaller variation in both CaO and silica (Fig. 2.5).

Calcium sulfates may exist in two forms at these locations, either veins which would typically be visible at the hand sample scale, or cements where the Ca sulfates would be invisible to the naked eye (Baker et al., 2019). The lack of mixing between silica and CaO in the Surface and Drill Hole data indicates that Ca sulfates do not likely exist as a cement at John Klein, Cumberland, Windjana or at Pahrump Hills. Calcium-sulfate cements are much more likely at sites Oudam through Sebina due to the clear mixing trend between CaO and silica which is present in many of the points on the surface and drill hole wall (Fig. 2.5d). The Stimson sites may display an analogous trend as seen in Fig. 2.5d, but the trend ends earlier at ~40% silica and ~14% CaO (Fig. 2.5c). It is possible that this represents the presence of limited Ca-sulfate cements, but the cements would have to be much less common than

what was seen at the later Murray sites. The silica-CaO trend is the dominant geochemical trend at the baseline sites with few changes observed with depth in other elements (Fig. 2.4). There is no evidence of any surface enrichments in any of the elements.

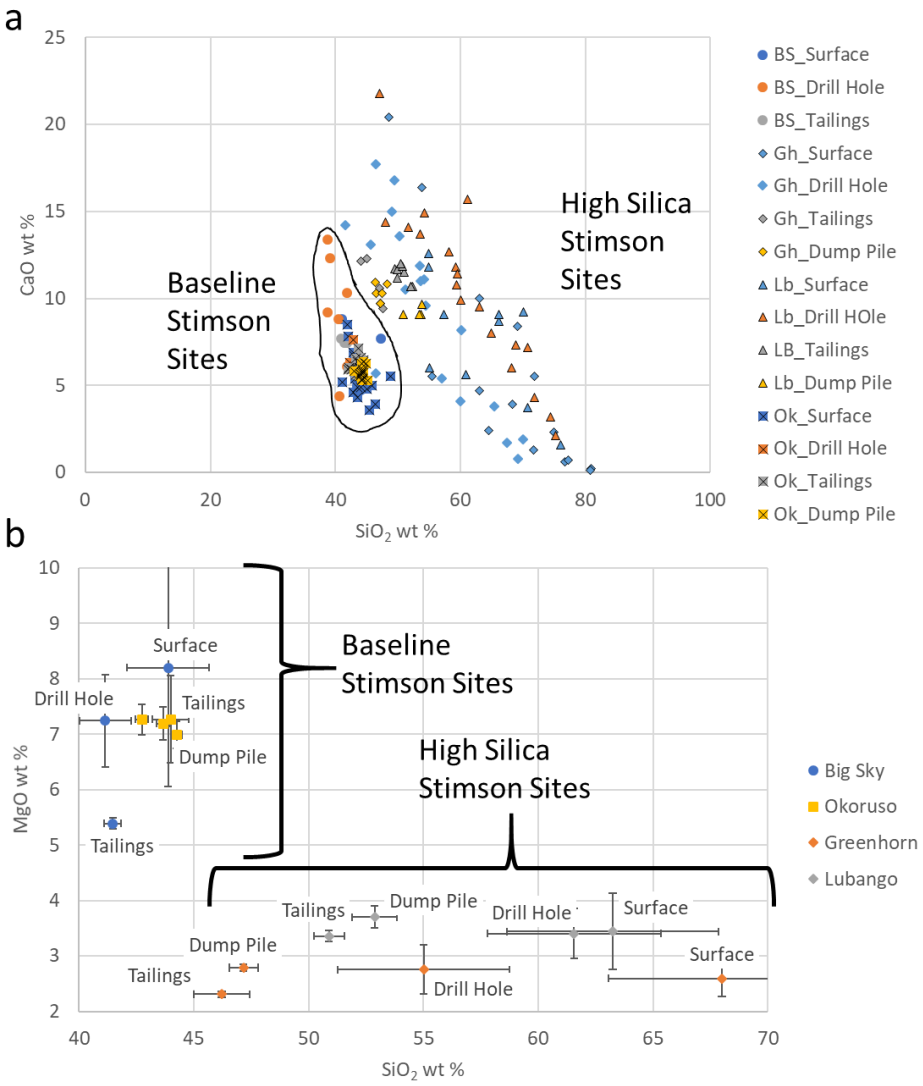

Figure 2.6: a) Scatter graph of SiO_2 and CaO for all Stimson sites. The enclosed points are the baseline sites shown in Figure 2.5c. Captions are provided in Figure 2.5. b) Scatter graph of SiO_2 and MgO for all Stimson sites using the same data as Figure 2.4. Points in the upper left are baseline Stimson and points on the bottom of the graph are the high-silica Stimson. Error bars display two standard deviations of the mean $\left(\frac{\sigma}{\sqrt{\sum N}}\right)$ (McKillup and Dyar, 2010).

4.2 High-Silica Sites

4.2.1 ChemCam Results at Greenhorn and Lubango

Fig. 2.7a displays the silica-CaO anticorrelation for the baseline and high-silica Stimson sites, which are not only enriched in silica, but also have much more variable CaO than the baseline sites. The broad CaO-SiO_2 trend passes above and to the right (higher SiO_2 and CaO) of the Baseline Stimson points, suggesting variable enrichment in both CaO and silica. Calcium-sulfate veins were observed at the high-silica locations, which explains the higher CaO values seen at these sites (Frydenvang et al., 2017; Yen et al., 2017). The trend in CaO vs. silica does not follow a tight linear relationship in this case like it did for locations discussed earlier. Instead, the trend is broader and less defined; Greenhorn and Lubango data have a Pearson correlation coefficient of -0.77 compared to -0.96 for sites Oudam through Sebina (Pearson coefficients are between -1.0 and 1.0 with 0 indicating no correlation). It is clear that other processes besides Ca-sulfate precipitation have affected the geochemical relationships here.

The high-silica Stimson sites can be easily differentiated from the baseline sites based on enrichment in silica and concurrent reductions in most other elements. The exceptions are CaO, discussed above, and TiO_2, which increases along with silica. The difference is perhaps most clearly seen in a plot of MgO vs. silica where the high-silica sites are not only more enriched in silica but are also lower in MgO with less variation in MgO abundance (Fig. 2.7b). The reasons for these trends have been discussed elsewhere (Frydenvang et al., 2017; Yen et al., 2017).

Unique to this investigation, we see that the high-silica sites in the Stimson show a decrease in the silica abundance systematically with depth (Fig. 2.7b, bottom part of the plot). At both of these high-silica drill sites, SiO_2 is highest at the surface, followed by the drill-hole walls (analyses extend < 2 cm below the surface). The tailings and dump piles are the lowest in SiO_2. The tailings can represent a mixture of material from the surface to ~2 cm beneath the drill site. Likewise, the dump pile samples depths > 2 cm and is most diagnostic of the materials delivered to SAM and CheMin (Fig. 2.1). This suggests that the high silica present at these sites decreases over the 6.5 cm depth of the drill hole in the ChemCam data.

4.2.2 APXS Results at Greenhorn and Lubango

Given the apparent compositional trend observed by ChemCam from the surface to material from the lowest part of the drill hole, we turn to APXS to see if its results are consistent with ChemCam's. While APXS does not make observations down the drill hole wall, it makes observations of all of the other materials that ChemCam does—the pre-drilled surface, the tailings, and the dump pile. The silica abundances for the APXS results on the Greenhorn and Lubango materials are presented in Figure 2.8.

A key detail must be recognized for the APXS comparisons between surface, tailings, and dump pile: dust contamination can lower the measured SiO_2 abundances for the surface, while the recently produced tailings and dump piles are not influenced by dust. APXS analyses that have been brushed by the DRT are still contaminated by global martian dust. Based on a study of the effect of dust on APXS measurements, dust coverage can result in measured silica abundances up to ~6.5 wt. % lower than actual surface

compositions (Schmidt et al. 2018). The method estimates the remaining dust coverage based on MAHLI images, corrects each element using the average value of the APXS-derived martian dust composition, and renormalizes the composition to a total of 100% (Schmidt et al. 2018). The study estimated the Buckskin DRT surface to be ~21% dust covered, the Greenhorn DRT surface to be ~29%, and Lubango to be 25% dust covered. However, the study was unable to produce a systematic correction of the contamination from the dust on rocks in the Stimson formation due to chemical variation in the rocks and possibly in the dust (Schmidt et al., 2018).

We attempted to provide a possible range of dust-free compositions by performing a series of deconvolution calculations (Table 2.5). We used the maximum and minimum dust composition values for each major element reported in Schmidt et al. (2018). The details of the deconvolution calculations are included in the supplementary materials (Appendix B). The result gives a range in silica of 67 – 78 wt.% at Buckskin, 61 – 66 wt.% at Greenhorn, and 57 – 59 wt.% at Lubango (Fig. 2.8 & Table 2.5). These estimates are sensitive to errors in the dust composition, as well as to measurement errors of dust coverage and thickness (see Appendix B). This correction gives a range of silica abundances for the Greenhorn surface ~1-6 wt. % above the values for the tailings (Table 2.5 & Fig. 2.8); however, this does not match the amount of change between surface and tailings (~15-20 wt. %) seen in the ChemCam data (Fig. 2.7b). The correction does not do the same for the Lubango data (Fig. 2.8); however, the APXS surface target is ~6 cm further from the center of the fracture than the drill hole. Over this distance, the silica likely decreased enough for the sequence to not be a fair representation of the composition at the surface of the drill

site (see Frydenvang et al. 2017 for more information on SiO_2 gradients from the centers of fractures). It seems likely that when accounting for dust in the surface measurements and for the different location of the Lubango surface measurement by APXS, the APXS results are consistent with a higher surface abundance of SiO_2 than the tailings and dump piles. The APXS data also show a decrease in silica from tailings to dump piles which the ChemCam data does not show, but there may be a reasonable explanation. ChemCam may have blasted through the dump pile in less than three shots and incorporated the material beneath. However, dump pile average composition determined from just the first shot at each LIBS point increases the silica abundance at both Greenhorn and Lubango dump piles by ~1.5 weight percent.

Table 2.5: Results of deconvolution-dust correction calculations for high-silica APXS DRT targets. The results are not renormalized to 100%.

APXS target	Buckskin_DRT_raster1		Buckskin_DRT_raster2		Greenhorn_DRT		Lubango_DRT[2]	
Dust coverage[1]	21.2±1.8		21.2±1.8		29.4±0.8		25.1	
	Min	Max	Min	Max	Min	Max	Min	Max
SiO_2	67.2	70.4	74.3	77.5	60.9	65.9	58.2	62.2
Al_2O_3	6.2	6.3	5.3	5.4	3.9	4.1	4.6	4.8
MgO	3.2	4.3	1.4	2.5	2.2	3.8	1.5	2.9
CaO	3.3	4.6	2	3.3	3.9	6	5.1	6.8
Na_2O	2.2	2.5	1.9	2.2	2.3	2.8	2.6	3.0
SO_3	8.3	8.8	2.6	6.8	10.9	11.6	11.4	12.0

[1]The dust composition range and the fraction of dust coverage comes from Schmidt et al. (2018).
[2]Standard deviation is not reported for Lubango because only one method out of the three attempted of dust coverage estimation was successful; the dust coverage reported is the results from that one method

Another possibility is that the ChemCam results are affected by an alteration coating on the sediment grains exposed in the tailings and dump pile. It is likely that if diagenetic silica was added to form the halos precipitated silica would have coated the sediment grains

(e.g., Blatt, 1992). David et al. (submitted) demonstrated that for loose material made up of coated grains < 500 µm, but not larger grains, the ChemCam analyses are biased towards the composition of the alteration coating over the composition of the sediment. The dump pile data for both the Lubango and Greenhorn sites are in the post-sieve piles which have grain sizes limited to < 150 µm.

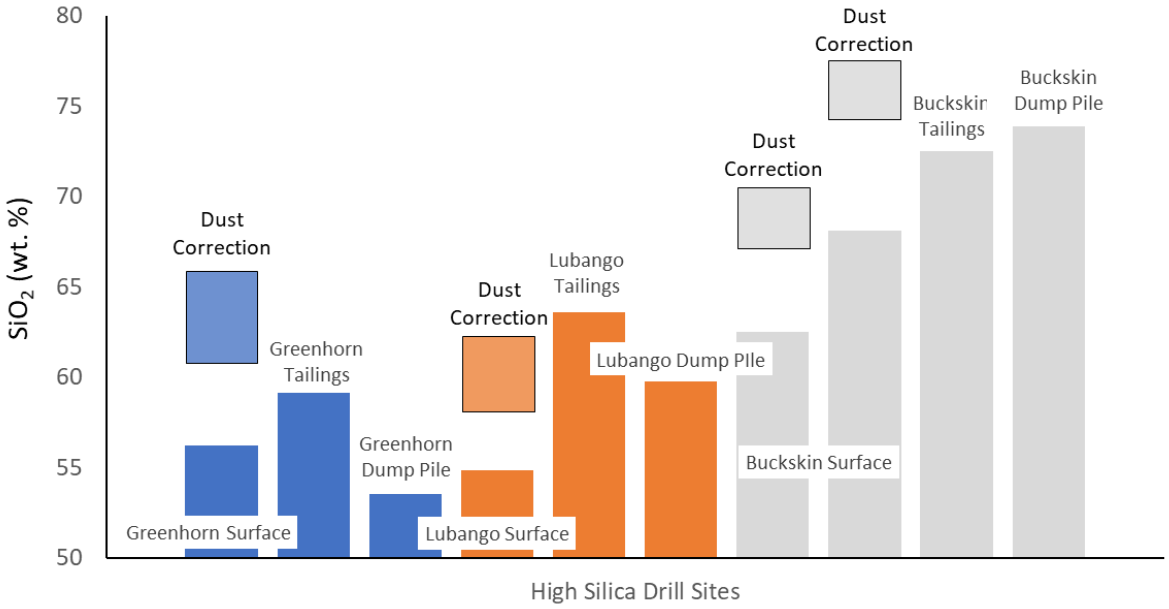

Figure 2.7: Distribution of APXS analyses on high-silica drill sites, tailings, and dump piles. The Lubango Surface target was approximately 6 cm's further from the fracture than the drill hole and has lower silica in part due to the horizontal silica gradient described in Frydenvang et al. (2017). The Buckskin surface target with lower silica sampled a vein, which explains the lower value. The light-toned boxes above the surface values represent the potential range of dust corrections (Table 2.5).

In contrast the drill tailings are less constrained, with more coarse-grained material: 10-70% > 150 µm and up to 25% > 1 mm (Anderson et al., 2012). The distribution of grain sizes between the tailings and dump piles suggests that at Greenhorn and Lubango, the SiO_2 abundances in the dump piles are higher in the ChemCam data than they would be in a bulk chemical analysis (like the APXS data) while the drill tailings data would be less influenced by any potential surface coatings. As such, the silica abundances in the dump piles are likely lower than what was shown in Figure 2.7 and Table 2.3. This would continue the silica

gradient lower in the drill hole and have the ChemCam data more consistent with the APXS results for the dump piles (Fig. 2.8).

4.2.3 Buckskin Results

Buckskin, which is in the Murray formation, had unfortunately fewer points collected by ChemCam as would have been preferred, considering the apparently complex nature of the site in addition the dump pile was not sampled. There is a decrease from the surface and drill hole wall to the tailings, but unlike the high-silica Stimson sites, there is also an inverse correlation between silica and MgO (Pearson Correlation coefficient of -0.6 in data with the two points on veins removed). The anticorrelation results in the tailings having higher MgO than the surface (Fig. 2.9a). This anti-correlation was not observed at the Stimson sites. In addition, unlike the Stimson sites, there is very little difference in the silica abundance between the surface and drill hole wall. The CaO abundaces in the tailings plot very close to the points with low CaO values in the surface and drill hole wall which suggests that veins make up little of the total volume of the Buckskin site. (Fig. 2.9b).

The APXS data for Buckskin do not match well with the ChemCam results, as the former shows less evidence for change with depth, since the dump pile is slightly higher in silica than the tailings (Fig. 2.8). Even with the potential correction to dust-free surface compositions (Fig. 2.8), it is not completely clear that the surface composition is higher in silica, 72.5 wt % in the tailings compared to ~67-78 wt. % for the corrected surface values of both Buckskin rasters. The high silica at Buckskin was interpreted to be from the deposition of a layer of material from silica-rich volcanism (Morris et al., 2016), potentially over a broad area, whereas high silica at Greenhorn and Lubango is thought to be the result of localized

fluid interaction (Frydenvang et al., 2017; Yen et al., 2017). It then seems reasonable that Buckskin would have different trends with depth than Greenhorn & Lubango. The ChemCam and APXS data show some variation between the surface, drill hole wall, tailings, and dump pile at Buckskin, but it does not appear to be a decreasing silica gradient like at Greenhorn and Lubango.

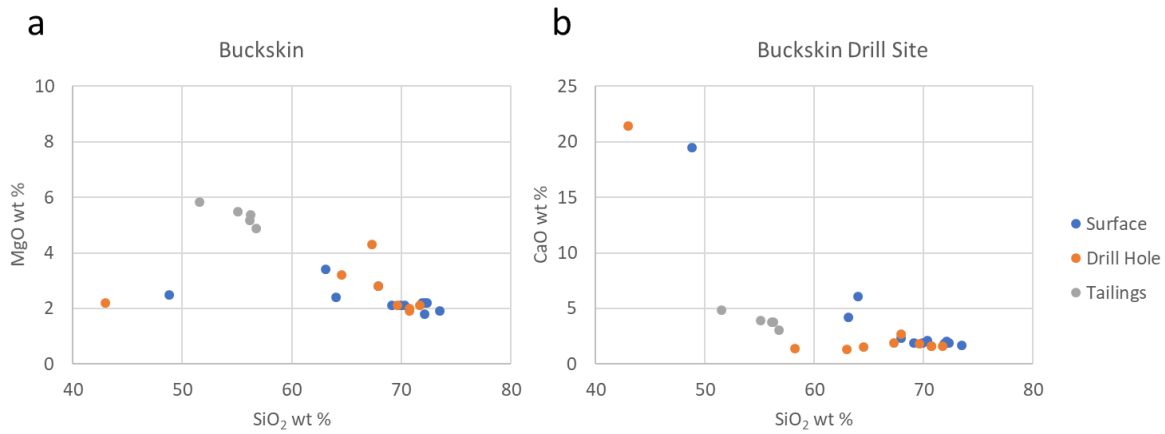

Figure 2.8: Chemical variation from observations on the surface, drill hole wall, and drill tailings at the Buckskin drill site a) Scatter plot for SiO_2 and MgO, b) Scatter plot for SiO_2 and CaO.

4.2.4 Formation of a Vertical Gradient of Silica at Greenhorn and Lubango

Both the Greenhorn and Lubango drill holes appear to have been drilled starting (at the surface) in a very localized region of high alteration and moving (lower down) to a region of lower alteration. One possibility is that paleo fluids moved along both vertical fractures (visible in the images) and also horizontal fractures—ones that resulted in and defined the current surface due to structural weakness. Visually, the images show the tone of the surface (Frydenvang et al., 2017) changing toward the vertical fracture, while the alteration along the horizontal direction is not observed in the present-day landscape.

A serious drawback of this hypothesis is that there is no evidence for alteration along horizontal fractures. The bedding planes are not parallel to the surface, which makes

such a fracture quite unlikely. For this explanation to work, the same scenario must have been the case at both Greenhorn and Lubango. A coincidental episode of alteration parallel to the surface is far less likely to have occurred at both locations.

Alternatively, the results at these two drill sites may indicate a systematic gradient in silica enrichment toward the surface at these fracture-alteration zones. This scenario requires us to consider the nature of the surface of Mars, which is dynamic over long enough time scales. It is well accepted that the Stimson and Murray formations are undergoing deflation. Stimson unconformably overlies the Murray which is thought to have been buried (Banham et al., 2018) along with the Bradbury Group, including Yellowknife Bay (Grotzinger et al., 2015). At the latter location, the Cumberland drill hole has an exposure age of 78±30 Ma (Farley et al., 2014), representing the time interval that the sampled material has been exposed near the surface. The exposure resulted from wind-driven retreat of a small scarp several meters away. From this result, they estimated a rate of scarp retreat of ~0.75 m/Ma but noted that this rate could be episodic (Farley et al., 2014); it must be noted that this is a rate for scarp retreat, not for deflation of a flat surface. Golombek et al. (2014) interpreted the eolian erosion rates over the last 100 Ma on Mars to be ~0.5 – 1.5 mm/Ma (which is also thought to be the long-term average over the last 3 Ga). Flat areas like the Stimson are thought to have slower erosion rates than craters (Williams et al., 2020).

Continuous surface deflation suggests that surface enrichment of silica may be a continuous or frequent process, keeping pace with deflation. It would require that relatively small amounts of groundwater were still active near the surface recently. Cycles of recharge

and evaporation would dissolve silica lower in the sediment. As the water moved upwards it would deposit the silica close to the surface as it evaporated. There is a high amount of amorphous material at the Greenhorn and Lubango drill sites, 65% and 73% by weight respectively; in addition, the amorphous-component composition, inferred from the combination of CheMin and APXS measurements, consists mostly of amorphous silica (Yen et al., 2017), supporting this scenario.

Continuous surface-silica enrichment is not necessary, the effect could occur cyclically, keeping pace with the long-term surface deflation rate. The Martian climate is controlled in part by the planet's eccentricity and obliquity cycles (Murray et al., 1973; Laskar et al., 2004). The variation in obliquity is quite extreme, with a maximal value of 82°, and it likely exceeded 60° in the last billion years (Laskar et al., 2004). These variations in insolation likely resulted in a Martian near-equatorial ice age 2.3-0.4 Ma (Head et al., 2003). A Martian obliquity of greater than 45° would result in year-round stability of ice at the equator (Richardson & Wilson, 2002). Equatorial surface ice associated with obliquity cycles may have recharged a small volume of groundwater. Given the elevation gradients on the slopes of Mt. Sharp, the region near the base of Mt. Sharp would be one of the more likely locations for groundwater to have reached the surface.

Based on a reasonable estimate of the surface deflation rate of a relatively flat surface at Greenhorn and Lubango (from Golombek et al. 2014 and discussed above), we might expect erosion of only 0.2 – 3.5 mm in the time since the last period of possible year-round ice in Gale Crater. A silica gradient would need to exist over these ~3.5 mm plus at least the top three cm of the drill holes, as observed by Curiosity. If there was enough

groundwater to produce a silica gradient over this near-surface distance during the last obliquity cycle, it would have been preserved to the present day.

4.2.5 Potential Analogs and Geological Interpretations

The silica gradient seen at the surface of the high silica Stimson sites could be akin to the formation of silcrete in the arid interior of Australia and in the Kalihari desert (e.g., Twidale and Milnes, 1983; Milnes and Twidale, 1983; Taylor and Eggleton, 2017), but on a more localized scale. Terrestrial silcretes are typically characterized by > 90% SiO_2; Australian silcretes are also characterized by factor-of-two enrichments in TiO_2 relative to surrounding basalts due to the leaching of most other elements (Taylor and Eggleton, 2017). Similar enrichments were reported by Frydenvang et al. (2017). However, as the surface silica gradient at Greenhorn and Lubango are thought to be very recent, we prefer the model of groundwater adding silica rather than the leaching process more typical of silcretes.

Other evidence for post-deposition fluids besides the Ca-sulfate veins may be the polygonal structures in the Siccar Point point group, to which the Stimson formation belongs (Kronyak et al., 2019). These features have morphologies consistent with shrinkage-cracks from dehydration and suggest cycles of wetting and drying. The sequence of events that formed these polygonal features are suggested to have begun with the deposition of the aeolian sand that makes up the Stimson formation. Then groundwaters from below the Stimson-Murray contact are proposed to have intruded into the sand, causing either the local water table to rise, or capillary wicking brought the water up to the surface. This would have established the current surface when dry sand eroded away, but wetted sand resisted

erosion. Multiple cycles of fluid recharge and evaporation are invoked in this scenario (Kronyak et al., 2019). This process could also explain the vertical gradient in silica composition. During an early cycle, the diagenetic silica would have been delivered through the shrinkage cracks. Then the cycles of recharge and evaporation would dissolve silica lower in the sediment. As the water moved upwards it would deposit the silica closer to the surface as it evaporated.

4.2.6 Amounts of Groundwater Needed for Surface Silica Enrichment

Here we attempt to understand the amount of groundwater necessary for the establishment of a silica gradient. The concept is to understand whether a reasonably small amount of groundwater could result in the observed surface chemical alteration—a quantity of groundwater that could have flowed and evaporated during the last obliquity cycle. Previous work (e.g. Fraeman et al., 2020) have posited that groundwater flow affecting Mount Sharp could consist of either local flow from higher up on Mount Sharp as well as regional flow from the southern highlands and flow recharged at the northern crater rim which flowed deep under the crater and back up at the crater floor. As the groundwater flow put forward in this research is interpreted to be quite recent, we assume that the flow is from higher up on Mount Sharp.

In order to model the amount of water needed to cause this change, we began with the average mineralogy from Greenhorn and Lubango as the target composition. This included an assumed amorphous silica content equal to the total silica reported in the chemistry of the amorphous component but excluded the remainder of the amorphous component (Yen et al., 2017). To determine a starting composition, we assumed that the

proportions of all minerals had stayed the same except for amorphous silica. However, the chemistry of the CheMin mineralogy didn't match exactly the chemistry reported by ChemCam, with the mineralogy resulting in a silica abundance of 71.35 wt. % for the average of Greenhorn and Lubango compared to 65.62 wt. % for the average surface values of the two drill sites. The amorphous silica content was decreased so that the chemistry of the material had ~61 wt. % SiO_2 to be consistent with the degree of change in silica abundance observed at Greenhorn and Lubango from the surface to the bottom of the drill hole (Fig. 2.7b). The mineralogy was then renormalized to 100 %. We assumed that the initial baseline to high-silica Stimson diagenesis had already taken place and limited the scope of the investigation to a late-stage diagenetic event that only mobilized silica.

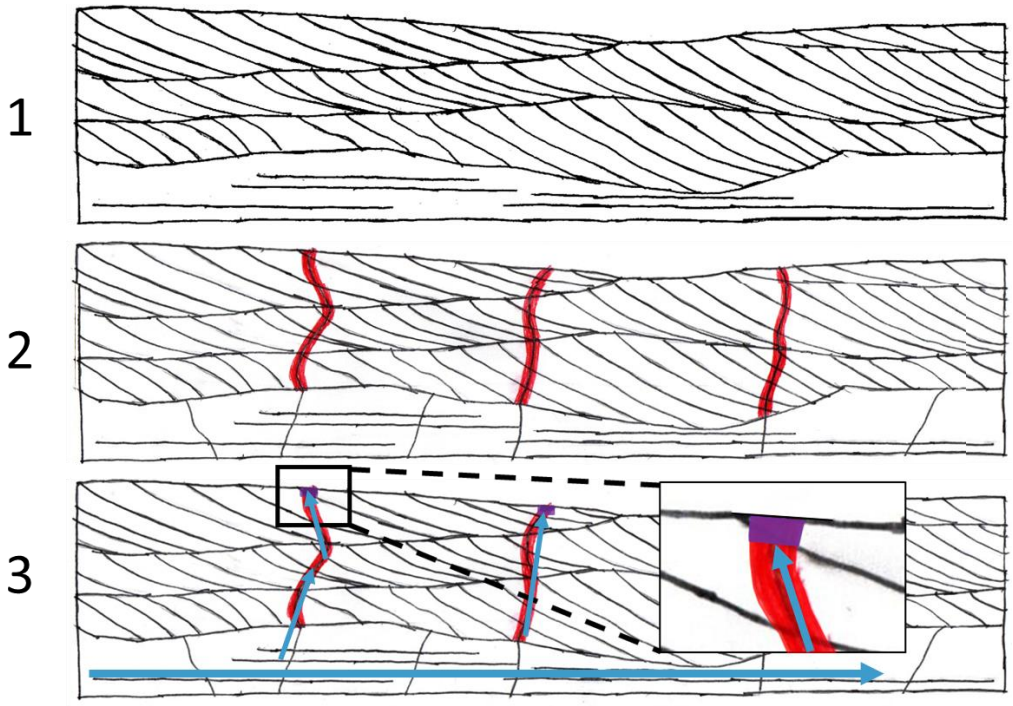

Figure 2.9: Schematic of diagenetic changes that occurred in the High-Silica Stimson. 1) Erosion of Murray surface, eolian deposition, & early diagenesis to 'Baseline' Stimson (e.g. Banham et al., 2018). 2) Emplacement of fractures and high silica alteration along fractures creating the silica haloes (Frydenvang et al., 2017; Yen et al., 2017). 3) Late-stage water flow into Stimson, cooling near the surface, deposition of silica in to 1-3 cm (this paper).

We used PHREEQC to calculate the uppermost amount of silica that could be dissolved in waters at 25°C, 15°C,10°C, and 5°C with the reaction controlled by equilibrium with amorphous silica. Silica solubility decreases with decreasing temperature, so we simply compute the amount of silica that would precipitate as a fluid cooled. We assumed a porosity of 35 % by volume based on previous research on diagenesis in sandstones (Berner, 1980). These waters were cooled to 0°C to calculate the amount of silica that would precipitate. Then we filled a pore volume in a 1 cm^3 sample with water, cooled it and calculated the amount of silica that would precipitate, assuming all precipitation was amorphous silica. This was repeated until there was ~59.7 % amorphous silica in the mineralogy which corresponds to ~70% SiO_2 in the chemical composition. In addition, in each calculation the volume taken up by the newly deposited silica was calculated and that volume subtracted from the initial pore volume. Then the total number of adjusted pore volumes required in the experiments were summed to determine the amount of water necessary per cm^3. This reaction would result in the porosity being decreased to ~9 %. The results are shown in Table 2.6 which has a range from 11.7 mL/cm^3 for water with a starting temperature of 25°C to 67.4 mL/cm^3 for water with a starting temperature of 5°C. Because silica solubility also decreases with decreasing pH we can also consider this mechanism for silica enrichment. At higher pH values it would be possible to dissolve more silica which could be then deposited if the solution moved towards a neutral composition at the surface. A solution with a pH of 10 and temperature of 25°C, could dissolve $3.7x10^{-3}$ mg/L and $5.89x10^{-3}$ mg/L of silica more than a neutral solution in quartz-controlled and amorphous silica-controlled solutions respectively.

Table 2.6: a) The starting and ending chemistry and mineralogy used in the modeling. b) The results and some parameters of the modeling experiment to determine the amount of water needed to create the silica gradient observed in the high-silica Stimson sites. This includes the starting and ending temperatures of the waters modeled, the difference in moles of Si dissolved in the starting temperature water and the end water temperature. The amount of silica in solution at each temperature is controlled by the presence of amorphous silica. The results are shown as the amount of water per cubic centimeter required for the increase in silica from 50 wt. % to 70 wt. %.

a)

	Starting value	End Result	Samples	Starting value	End Result
SiO2	62.46	71.35	Anorthoclase	9.91	7.57
Al2O3	8.56	6.53	Albite	12.62	9.63
TiO2	1.50	1.50	Orthopyroxene	4.69	3.58
FeO	11.93	9.10	Pigeonite	2.73	2.08
MgO	1.05	0.80	Magnetite	7.77	5.93
CaO	6.47	4.94	Hematite	2.31	1.76
Na2O	1.88	1.44	Quartz	1.45	1.11
K2O	0.35	0.35	Anhydrite	7.60	5.80
SO3	6.39	4.88	Bassanite	3.24	2.48
			Gypsum	0.51	0.39
			Amorphous silica	47.16	59.67

b)

Start Temp °C	End Temp °C	Difference in Si dissolved (mol/L)	Estimated Water (mL/cm^3)
25	0	7.84×10^{-4}	11.69
15	0	4.39×10^{-4}	20.93
10	0	2.82×10^{-4}	32.52
5	0	1.36×10^{-4}	67.41

We then attempted to estimate the amount of water necessary for this diagenetic process to occur. We estimated the high silica halos to cover an area of the Stimson between 1% and 7.5% and assumed just the top 1 cm of the high silica sites were altered. This resulted in a minimum value of 1.17×10^6 L/km^2 and a maximum value of 5.06×10^7 L/km^2 with the calculations centering around ~3×10^7 L/km^2. The main contiguous portion of Stimson was determined to have an area of 1.4 km^2 with more sections scattered across

another 17 km^2 (Banham et al., 2018). In addition, we do not know if the high silica halos or similar features related to the same ground water flow are present elsewhere on Mount Sharp beyond the rover's traverse. The total extent of the Stimson and the high silica halos would ultimately determine the total water needed for this scenario. However, if we allowed for only 1000 earth years for this alteration to occur, this would require an average discharge per km^2 of 0.10 L/min for the largest amount of water and 0.06 L/min for the amount of water of the more typical results. Glacial fed springs at Axel Heiberg Island in the Canadian High Arctic have been invoked as potential Martian analogs, and have consistent flow rates of 1.8 – 2.1 L/sec or ~100 L/min (Andersen et al., 2001). These terrestrial values are about three orders of magnitude greater than our calculated martian values.

5. Conclusions

The analysis of the drill sites' surfaces, drill hole walls, tailings, and dump piles provide a unique opportunity to observe compositions at discrete depths in each drill hole. The ChemCam-derived compositions of most of the sites are relatively homogenous down the depth of the drill hole, with some variability due to unequal spatial distribution of Ca-sulfate veins. By contrast, both APXS and ChemCam results are consistent with a decrease in silica abundances with increasing depth at the high-silica Stimson drill sites. The ChemCam data clearly shows a decrease from the surface to the drill hole wall to the tailings. APXS shows the decrease continuing from the tailings to the dump pile, which may have been missed by ChemCam. Looking at the data from both instruments, it is likely that there is a decrease in silica with depth down to at least the upper ~3 cm of the Greenhorn and Lubango drill holes.

The vertical gradient of silica at the high-silica Stimson sites may have been produced by dissolution and precipitation by groundwater. A surface enrichment suggests a recent process, as the surfaces of the Murray and Stimson formations are undergoing deflation over periods of millions of years. Groundwater activity at the surface is currently precluded in Gale by MSL observations including the low relative humidity. However, a small quantity of groundwater may have found its way to the surface during periods of high obliquity, when surface ice is expected to have been present near the equator. An estimate of the quantity of the groundwater required to precipitate amorphous silica at the surface suggests that these quantities are not excessively large. The surface silica enrichments observed here may be analogous to silcrete that can be found in dry climatic regions on Earth.

Besides any specific geological interpretations, the observation of the vertical silica gradient illustrates that by careful analysis and comparison of the drilling byproducts the ChemCam instrument can provide additional geochemical details that may be overlooked otherwise. As the Mars Perseverance rover also has a relatively shallow (~7 cm) drill as part of its sample cache system (Chu, Brown, & Kriechbaum; 2017), these results may prove applicable to this mission and other missions with shallow drilling components. For the most part, surface composition is a good indicator of subsurface chemistry over the ~6.5 cm of depth seen in this study. The only exceptions suggested by these data are locations with spatially varying composition, like the high-silica halos observed in Stimson. The varying composition observed at the surface also seemed to be present with depth.

CHAPTER 3: Investigation of aqueous processes in the Valle Grande paleo-lake, Valles Caldera, New Mexico, USA as a Martian analog

1. Introduction

The Valle Grande paleo-lake was a long-lived mid-Pleistocene lake that was formed by the emplacement of a rhyolite dome damming the East Fork of the Jemez River 552 kya. The lake lasted for at least 180 ky and was 11 km long, up to 5 km wide, and likely reached a depth of at least 125 m (Fawcett et al., 2011; Reneau et al., 2007). It is located within Valles Caldera, USA, in an arid watershed that is compositionally dominated by igneous rocks (Smith & Bailey, 1968; Stix et al., 1995). These characteristics makes the Valle Grande lake a potentially useful analog for Mars (Crumpler et al., 2007) and more specifically for the lacustrine systems observed at the landing site of the Mars Science Laboratory (MSL), Gale Crater (Grotzinger et al., 2014). Although the rocks in the Valle Grande watershed are dominated by rhyolites while the rocks in the Gale Crater watershed are basaltic. The sedimentary rocks deposited in the Gale Crater lake may have experienced a similar series of geochemical processes, beginning with crust formation, exposure to fluid interactions before and after the formation of Gale Crater, alteration during exposure at the surface on the crater rim, fluvial transport into a lake, and the processes of alteration and fluid mobility within the crater lake. Furthermore, the MSL mission is investigating changing climate at Gale Cater as it climbs up the 5 km mound of sediment (Mount Sharp), which contains sedimentary layers that record the changing global Martian climate from the relatively warm and wet Noachian Epoch to the colder and dryer Hesperian Epoch (Anderson & Bell, 2010; Milliken et al., 2010).

The Valle Grande lake sediment was cored in 2004 with 82 m of sediments collected. The drill core was designated VC-3; the sediments recorded three glacial and two interglacial periods from the mid-Pleistocene, referred to as Marine Isotope Stages (MIS). Numerous climate proxies were collected from the drill core, so these climatic periods are well understood (Fawcett et al., 2011). A large suite of elements has previously been quantified through ICP-AES with samples collected at 20 cm intervals down the first 53 m and at 60 cm intervals afterwards (Johnson et al., 2006).

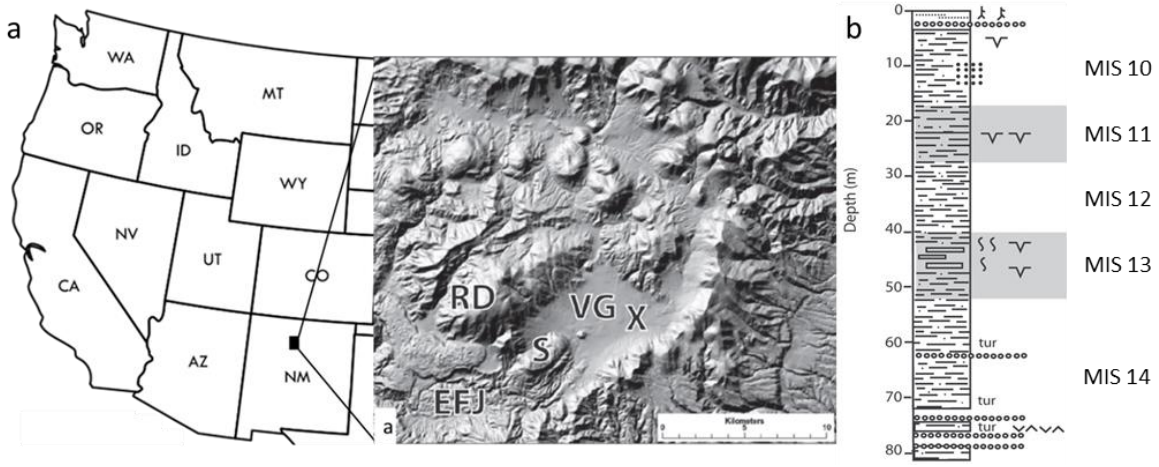

Figure 3.1: a) Map of the western United States showing the location of Valles Caldera and a digital elevation model of Valles Caldera, X marks the location of the VC-3 drill hole, VG is Valle Grande, S is South Mountain rhyolite, RD is Redondo Dome, and EFJ is East Fork of the Jemez River. b) Stratigraphic section taken from the VC-3 drill core from Fawcett et al. (2007). Gray bars represent interglacial stages and white bars represent glacial stages. Standard stratigraphic symbols were used with the addition of circles showing the presence of gravel, "tur" indicating turbidites, and rectangles at ~ 45 m depth representing blocky facies. The Marine Isotope Stages (MIS) are labeled to the right of the strat column.

The interglacial MIS 11 core section is characterized by thickly laminated to thinly bedded sediments and contains a meter-deep mud crack, indicating complete or near complete desiccation of the lake during this time period. The glacial MIS 10, MIS 12, and MIS 14 are characterized by well-laminated sediments. In addition, the pollen assemblage and low total organic carbon indicate relatively cold and wet climates that would have allowed for the formation of a relatively deep lake. MIS 13 is another interglacial stage and

the core from this time period also contains mud cracks indicative of the lake drying during this time due to high temperatures and low precipitation (Fawcett et al., 2011).

2. Methods

2.1 Original Data Collection

Several hand samples were collected from the southern flank of Redondo Peak, Cerro de Medio, and South Mountain which define the north, west, and east boundaries of Valle Grande. Eight samples were collected from the area around Redondo Peak; eight samples were collected from Cerro del Medio, including the two soil samples; and two additional samples were collected from South Mountain. The samples were named from the geologic unit that they were found in, although several samples were float rocks and either could only be named in the broadest sense, e.g., Qvdm for Cerro del Medio samples, or were named for colluvium deposits, e.g., Qc for Redondo Peak samples. The samples from Redondo Peak included Deer Canyon Member rhyolites, Bandelier tuff, and hillside colluvium generated from caldera material. Cerro del Medio and South Mountain material came from the respective rhyolites of those specific rhyolite domes. The geologic units were determined from the Geologic map of Valles Caldera, Jemez Mountains, New Mexico (Goff et al., 2011).

Representative samples of MIS 11 and 12 were also measured and analyzed by X-ray diffraction (XRD) to determine mineralogy using a Rigaku SmartLab instrument. The MIS 11 sample came from a depth of 23.89 m and the MIS 12 sample came from a depth of 31.52 m. The 16 rock samples that were collected from around the Valle Grande watershed were also analyzed by X-ray diffraction. The two samples from the VC-3 drill core and the two

sediment samples from Cerro del Medio were collected for clay analysis. About 1 g of each of these samples was collected and then washed no less than three times with distilled water to remove any salts.

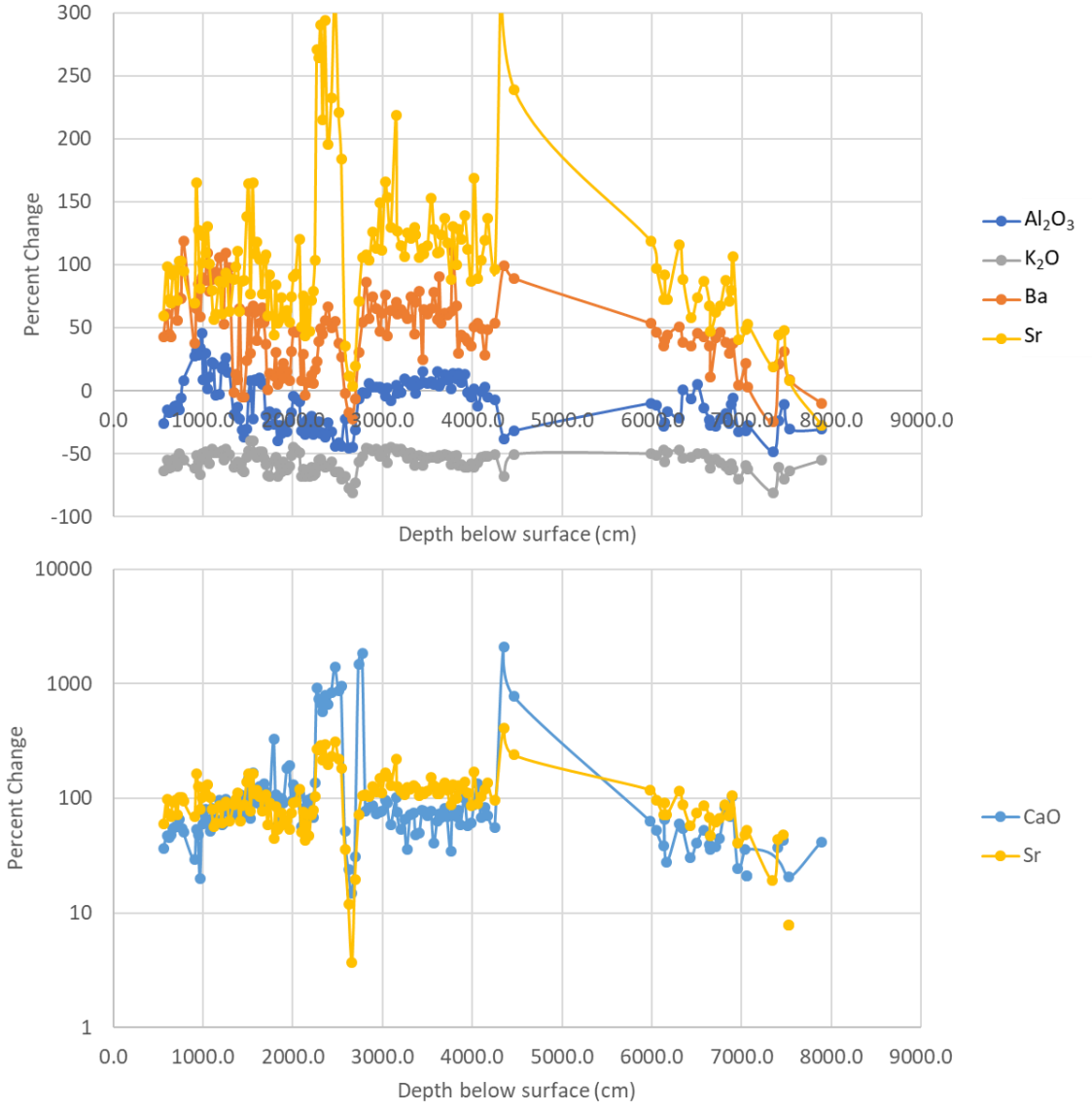

Figure 3.2: Data collected from previous research in the Valle Grande water shed, analytical details can be found in Groff et al. (2007) and Fawcett et al. (2011). a) Graph of the percent change of selected elements compared to a hypothetical "average" protolith that would have washed into the Valle Grande paleo-lake, b) semi-log scale of the percent change of CaO and Sr compared to a hypothetical "average" protolith that would have washed into the Valle Grande paleo-lake.

The two VC-3 core sediment samples were also treated with an anti-flocculant to prevent the clay minerals from clumping together in suspension. The clay-sized sediment

suspended in solution was then dripped onto a glass slide with an eye dropper and left to dry overnight. The four clay samples were run in the XRD four times. The first run was after the slide had dried to observe the clay in the state it was found in the environment. The next run was after the slides were left sitting for at least two days in an airtight container of ethyl glycol; this was done to expand any swelling clays. The last two runs were after the slides were heated at 400˚C for 2 hours and again after being heated a second time at 550˚C for 1-2 hours; this process drives out volatiles and collapses the exchange sites.

2.2. Reviewing Previously Collected Data

We also collected data for continued scrutiny from earlier sources pertaining to the relatively simple and constrained source to sink system defining sediment transport at Valle Grande. These analyses included data from the geologic features surrounding Valle Grande (Goff et al., 2007) and the original data collected from the VC-3 drill core (Fawcett et al., 2011; Johnson et al., 2006). These data were used to calculate an “average” hypothetical protolith that would have washed into the valley, and then to calculate the percent change for each sample collected from VC-3. The major drawback is the lack of consistent trace element data between the two data sets. We were not able to investigate the changes in a wide swath of trace elements, as the data was not available in the research reviewed. We were, however, able to compare the changes in Ba and Sr along the depth of the VC-3 drill core.

3. Results

3.1 Mineralogy

Table 3.7: Qualitative mineralogy from X-ray diffraction separated into the different source regions. The consistently present (in every analysis) phases were present in all samples, the inconsistently present (not in every analysis) phases were present in some of the samples, and the Clays/Phyllosilicates were determined through clay analyses.

	Cerro del Medio	South Mountain	Redondo Peak	VC-3 Sediment
Consistently Present Phases	Sanidine, Albite, Cristobalite	Sanidine, Quartz, Albite, Cristobalite	Albite, Quartz, Sanidine	Quartz, Muscovite, Cristobalite, Albite, Smectite[1]
Inconsistently Present Phases	Tridymite, Anorthite, Orthoclase	Muscovite, Microcline	Microcline, Tridymite, Orthoclase, Epidote, Microcline, Enstatite, Anorthoclase, Zeolite	Microcline, Sanidine, Illite, Pyrophillite, Pyrite
Clays/ Phyllosilicates[1]	Pyrophyllite, Mica Group, Kaolinite, Illite			Kaolinite, Illite-montmorillonite

[1]Clay identification could not be as rigorous as the rest of the minerals.

3.2 Source to Sink Geochemical Changes

Al_2O_3 represents a mostly conserved element with increases and decreases of Al_2O_3 more indicative of changes in other elements and the complications that arise from normalizing the composition to 100 %. Barium and Sr mostly follow the changes seen in Al_2O_3 but with far greater variation and enrichment (Fig. 3.2a). Strontium at ~2360 – 2540 cm depth and at ~4350 cm depth becomes much more enriched; these depths also show large enrichments in CaO and smaller enrichments in Ba (Fig. 3.2b). Additionally, the percent change of K_2O is shown to provide context as to the behavior of alkali elements;

K_2O is consistently depleted in the VC-3 drill core compared to the "average" protolith (Fig. 3.2a).

4. Discussion

4.1 Source to Sink Variations

There is only a short distance of transport (a few km at most) from the igneous features surrounding Valle Grande to the lake. Therefore, only moderate geochemical changes were expected where clays or other alteration phases had formed but rhyolitic minerals also still existed. In Figurue 3.2, Al_2O_3 remained mostly conserved; the enrichments over the protolith alumina composition can be easily explained by the loss of other elements due to leaching and transport, and the depletions are mostly in locations where it is known that a new component was added, such as the precipitation of calcite. K^+ was likely leached from the protolith and then remained in solution and lost to the system (fig. 3.2a). The enrichment of Sr and Ba was likely due to two separate factors. The two elements mostly follow Al_2O_3 but show far greater enrichment, Al_2O_3 is conserved as aluminosilicates are altered into clays (e.g. Goldich, 1938; Middelburg, van der Weijden, & Woittiez, 1988). Barium and Sr in solution are then adsorbed by the clay minerals, becoming enriched (e.g. Fischer & Puchelt, 1969; Fischer et al., 1969). The largest enrichments in these two elements coincide with the large enrichments in CaO (starting at 2350 cm and 4350 cm below the surface as seen Figure 3.2b), which resulted from times when the lake mostly or completely dried up and calcite precipitated. The XRD samples were not collected near the calcite deposition; calcite was identified in Fawcett et al. (2011). Strontium and Ba are divalent ions that can substitute for Ca in the mineral structure of calcite; Sr is more likely to

do this, which is why it becomes more enriched at these locations than Ba does (Fischer & Puchelt, 1969; Fischer et al., 1969).

Many of the source rock minerals occur in the lake sediments; however, sanidine does not seem to be as common in the lake sediment as in the source rocks. In addition, phyllosilicates appear to be more common in these sediments than the source rocks. The XRD results indicate a greater amount and variability of clays, such as kaolinite and illite, in the lake sediments compared to the sediments collected on Cerro del Medio; thus the lacustrine sediments went through an unspecified degree of chemical weathering before they were deposited in the lake. However, the ease of detecting smectite in the X-ray diffraction data (suggesting that the clay minerals became more prominent in the lake sediment data) and the additional clay minerals detected in the Valle Grande lake sediment would suggest that the sediment continued to undergo alteration after being deposited in the lake (Table 3.1).

One source of uncertainty is the degree to which eolian material, such as loess, has been included into the Valle Grande Lake sediment. Dust transport increased during the cold periods in the Pleistocene, and such material can be concentrated in traps formed by topographic obstacles. Additionally, there are large loess deposits in the High Planes of Eastern New Mexico and Colorado, which suggests a large degree of dust transport within the same general region as the Valle Grande paleolake (Tsoar & Pye, 1987). The chemical and mineralogical composition of loess indicates that the starting material was the upper continental crust. In addition, loess has a chemical index of alteration of about 60 which indicates minimal alteration (Gallet et al., 1998). Determining the amount of loess material

is problematic due to a lack of literature on the composition and amount of loess transported to this region, which is coupled by the fact that there are local sources of dust that might provide eolian input as well.

4.2 Martian analog

Valles Caldera has been invoked as a martian analog due to its young age, arid climate – indicating less chemical weathering – and watershed dominated by igneous rocks, (Crumpler et al., 2007). This is supported in this research by the continued presence of igneous minerals in the sediment as much of the lake sediment is composed of physically weathered rhyolites sourced from the nearby volcanic structures. This provides the opportunity to compare the Valle Grande paleolake to the environment found at Gale Crater on Mars, especially the Yellowknife Bay region (Grontzinger et al., 2014) and the Murray formation (Mangold et al., 2019) as both represent Martian paleolakes. The sedimentary rocks within Gale Crater are mostly derived from generally unaltered basalts that range from mud- to sand-sized sediments. There is some evidence for chemical alteration as clay was observed in this locale, although it is not known if this material was formed in-situ or transported to the locale (Grotzinger et al. 2014; Vaniman et al. 2014). In such settings, where a depositional basin is dominated by a specific example of igneous rocks, especially those with minimal chemical weathering, it is useful to understand how fluid mobile elements originating in the source rocks can be concentrated in the sink. Based on the results from Valle Grande, it seems likely that we should expect concentration of alkali earth metals and the loss of alkali metals.

5. Conclusion

The source region around the Valle Grande watershed is dominated by rhyolites characterized by the presence of sanidine, low pressure SiO_2 polymorphs, and albite. The sediment that has formed on the slopes contains kaolinite and illite suggesting alteration of the rhyolites occurs without transportation. The weathered sediments were only transported a few km's a most before being deposited in the lake. The mineralogy of the lake sediment shows the presence of more alteration products such as smectite and illite-montmorillonite clays. This is further supported by the chemistry data that shows the preservation of Al_2O_3, enrichment of Ba and Sr, and the loss of K_2O. Additionally, during times that the lake dried up, resulting in the deposition of calcite, Sr and Ba seem to have been incorporated into the evaporites and become much more enriched. The enrichment was stronger in Sr than Ba.

Valles Caldera with its arid climate has previously been invoked as an analog to igneous dominated watersheds on Mars (Crumpler et al., 2007). As such, this research at Valle Grande could be helpful to understanding the sediments at Gale Crater on Mars. In addition, both Ba and Sr can be detected by the ChemCam instrument on the MSL rover. Enrichments in Ba and Sr could help identify sediments with increases of clay minerals when analyzing silicate sediments and not evaporites, which would then be of interest for analysis by the full suite of instruments onboard the rover. In addition, similar diagenetic processes have been observed during MSL's traverse in Gale Crater (Grotzinger et al., 2015). It would likely be helpful to keep the Valle Grande results in mind as the paleoclimate of Gale continues to be investigated.

CHAPTER 4: Source to sink changes of trace elemental distributions observed at Yellowknife Bay, Gale Crater, Mars

1. Introduction

1.1 Geologic Setting

After landing in Gale Crater, the Curiosity Rover first drove to Yellowknife Bay. It was thought that this was a likely location to find exposed layered sedimentary rocks due to the intersection of three distinct lithologies occurring there. At this site, the rover discovered the ~1.7 m thick Glenelg unit overlying the ~2.0 m thick Gillespie sandstone, which overlies the > 1.5 m thick Sheepbed mudstone (Grotzinger et al., 2014) (Fig. 4.1). These units were all extensively sampled by the ChemCam instrument onboard the rover (Mangold et al., 2015). All units have major element chemistries roughly similar to basalt with little indication of substantial chemical weathering in the source region. Sheepbed is a massively bedded mudstone with diagenetic features consisting of Ca-sulfates veins, raised ridges, and nodules (Grotzinger et al., 2014). Two samples of the Sheepbed were delivered to the CheMin X-ray diffraction mineralogy instrument, which detected ~20% smectite clays and ~1-3% olivine indicating some alteration of primary mafic minerals into Fe/Mg phyllosilicates (Vaniman et al., 2014). The Gillespie sandstone contains Ca-sulfate diagenetic material throughout. The Glenelg member is a cross-stratified sandstone with interbedded siltstone and an unknown “vuggy” material. These strata indicate a relatively cold and arid environment with a hydrologic system that lasted for at least hundreds to tens of thousands of years (Grotzinger et al., 2014).

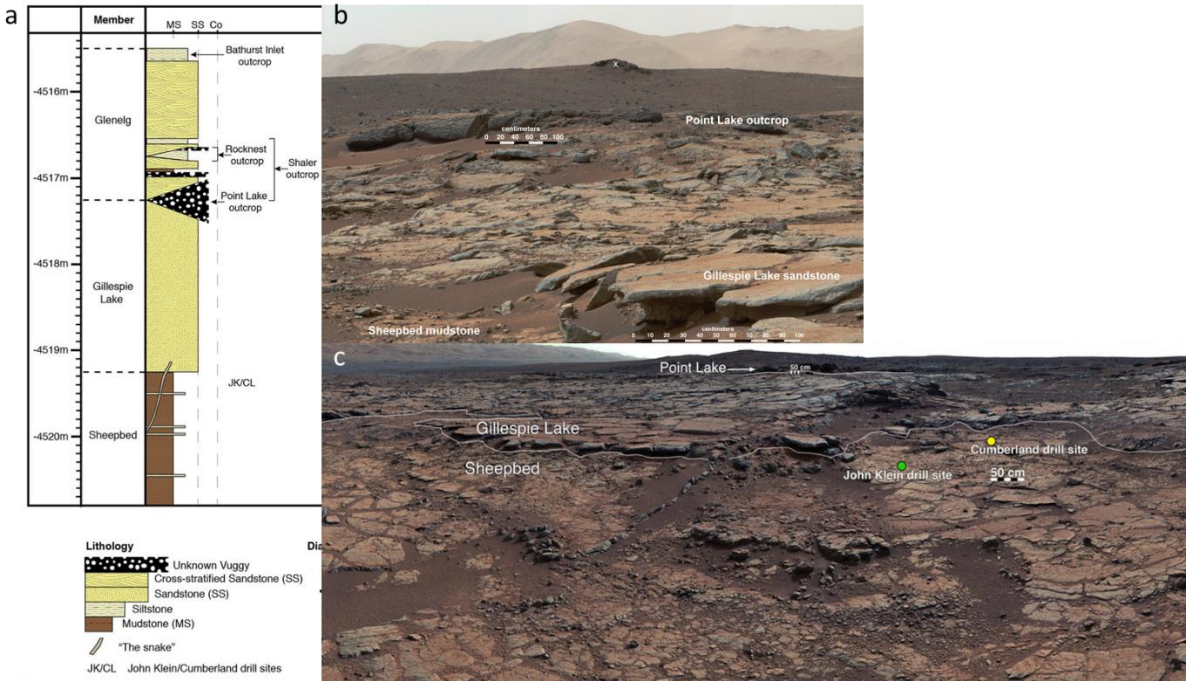

Figure 4.1: a) Stratigraphy of Yellowknife Bay (modified from Grotzinger et al., 2014), b) and c) MastCam images of Yellowknife Bay (the Glenelg member is not visible).

Previous work has identified five geochemical endmembers that have contributed to the sediments within Gale Crater. The sediments in Yellowknife Bay are dominated by contributions from a subalkaline basalt with a composition similar to the Adirondack class basalts observed at Gusev Crater by the Mars Exploration Rover Program (Bedford et al., 2019). The ChemCam instrument has sampled several float rocks that were determined to be aphanitic mafic rocks (Cousin et al., 2017) (Fig. 4.2). These extrusive mafic rocks were also determined to be basalts and trachybasalts, which were derived from a subalkaline basaltic melt that is also consistent with the Adirondack class basalts (Edwards el al., 2017) (Fig. 4.3).

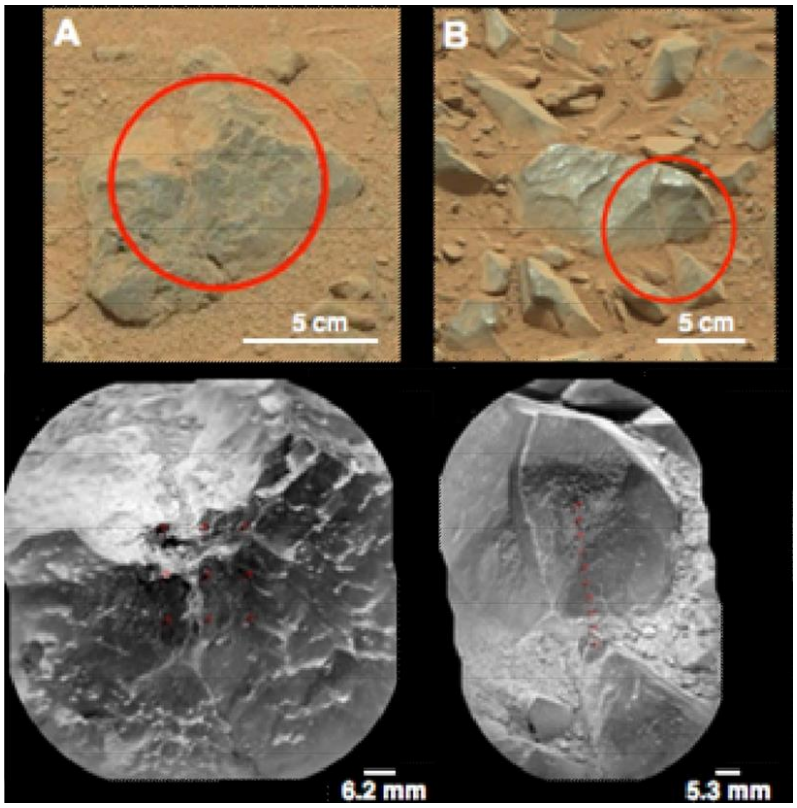

Figure 4.2: MastCam and RMI images of basaltic float rocks, Pisolet and Gunflint, modified from Cousin et al., 2017.

1.2 Trace Element Geochemistry

There have been extensive studies of the behavior of trace elements in terrestrial geologic systems, including during the weathering of basalt. The terrestrial behavior of trace elements on the Earth can be complicated by the presence of organic material and alteration by organisms (Berner, 1980), which is not an issue on Mars. Lithium behaves distinctly from other alkalis and will not significantly substitute for Na^+ or K^+; rather, it tends to substitute with Mg^{2+}, Fe^{2+}, and Al^{3+} in igneous minerals due to similar ionic radii. In clays, lithium may help with charge balance when Mg^{2+} replaces Al^{3+} (Horstman, 1957). Lithium also tends to be enriched in muds whereas in sandstone the abundances are similar to the parent rock (Cocco et al., 1969a). This enrichment is likely due to the incorporation of Li into the mineral structure of autochthonous clays; however, Li is far less likely than other alkalis

to be included into the exchange sites of clays (Horstman, 1957). During the weathering of basalts, Li behaves like other alkalis, becoming more depleted with increasing degrees of weathering, but also showing a stronger affinity for phyllosilicates than other alkalis and substituting with Mg^{2+} for Al^{3+} into the structure of clays (Babechuk, Widdowson, & Kamber, 2014; Das & Krishnaswami, 2007).

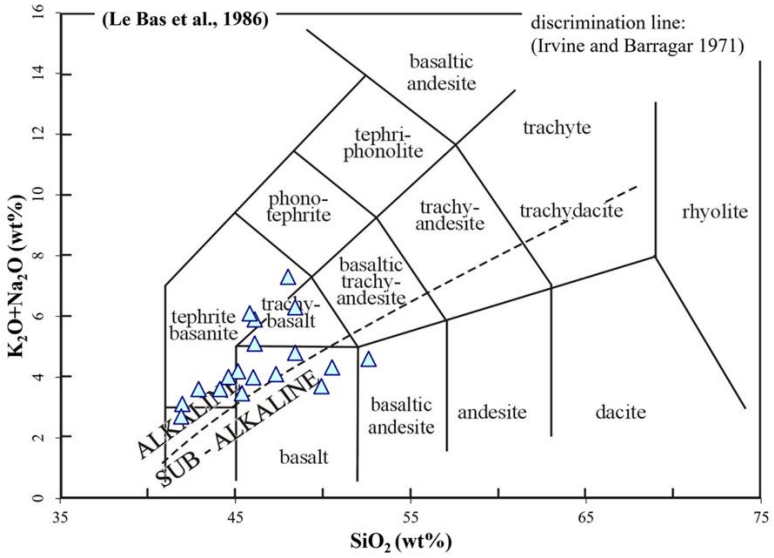

Figure 4.3: Total alkali-silica classification of float rocks used in this study with the two most altered rocks (Ikpiarjuk & Tully, CIA > 45) removed for clarity.

Rubidium has a similar ionic radius to K and is dispersed in K-rich minerals such as K-feldspars. Rubidium is closely related to K during weathering, but adsorption onto clays can play an important role in the later stages of weathering. Adsorption onto clays results in Rb being enriched relative to K in shales, whereas in sandstones Rb will remain in the primary igneous minerals (Cocco et al., 1969b). Rubidium is rapidly lost during weathering of basaltic weathering profiles likely due to its presence in volcanic glass (Eggleton, Foudoulis, & Varkevisser, 1987).

Sr^{2+} substitutes with Ca and K into minerals due to similar ionic radii and charge in the case of Ca. In igneous systems, Sr substitutes for K into K-feldspars and, to a lesser

extent, for Ca into clinopyroxenes and amphiboles. Strontium is closely linked to Ca during the weathering of granites and basalts, which makes it a very mobile element, but it is also more easily exchanged onto clays, compared to Ca (Middelburg, van der Weijden, & Woittiez, 1988). Strontium is very mobile during the early alteration of basalts, which is likely due to its presence in volcanic glass (Eggleton, Foudoulis, & Varkevisser, 1987). During transport and deposition, Sr also follows Ca and other alkali earth metals; these elements decrease in concentration in weathering profiles as the degree of weathering increases. However, when calcite is precipitated, Sr is also incorporated into the carbonate and both elements can become enriched compared to parent basalts (Babechuk, Widdowson, & Kamber, 2014; Das & Krishnaswami, 2007). For this research, another important behavior of Sr is its ready substitution for Ca into Ca-sulfates (Fischer et al., 1969).

2. Methods

The ChemCam instrument consists of a Laser Induced Breakdown Spectroscopy (LIBS) instrument which allows for ~400 μm diameter chemical analyses from 1.5 m to 7.0 m away, as well as a panchromatic Remote Micro Imager (RMI) for context (Maurice et al., 2012; Wiens et al., 2012). ChemCam analyses are planned and organized by individual sequences (which have a unique target name) usually consisting of a line-scan or grid raster pattern of observation points. At each point ChemCam fires multiple laser shots and records an emission spectrum for each shot. In this study, 5-10 different points were typically analyzed per named target sequence (Wiens et al., 2012). The elemental detections from the LIBS spectra are reported in terms of the abundances of SiO_2, TiO_2, Al_2O_3, FeO_T, MgO, CaO, Na_2O, and K_2O. The abundances are quantified by using a calibration method which

uses both a Partial-Least Squares (PLS1) training algorithm and Independent Component Analysis (Clegg et al., 2009; Clegg et al., 2017; Forni et al., 2013; Wiens et al., 2013). Lithium, Rb, Sr, and Ba are calibrated through a univariate calibration method, which measures the changes in peak area for a single peak per element against a large set of standards. Each peak is selected for stability and the least amount of interference from the peaks of other elements (Ollila et al., 2014; Payré et al., 2017). While Ba can be measured this way, most of the spectra in this research had a poor fit for Ba as reported by the ChemCam trace element calibration tool, so it was not used in this research. To ensure quality all targets used in this study were limited to solid rocks, with no drill fines or soils included (Chapter 1 Section 3).

Most elemental data in this research are presented as the element normalized to Al_2O_3 in weight percent; Li, Rb, and Sr were in ppm when ratioed, while all major elements were in weight percent when they were ratioed (e.g. Nesbitt & Wilson, 1992). Aluminum is considered a conserved element and is not thought to be mobilized in any significant amount by water, except in acidic environments (Cronan & Schofield, 1979; Johnson et al., 1981). Elements were normalized to the conserved alumina so that changes in the element of interest would not be affected by changes in other elements, as is the case when looking at concentrations in terms of percentages or parts per million (Nesbitt & Markovics, 1980). In order to determine relationships across a large amount of data (1,174 individual points and averaged spectra in this study), Pearson correlation coefficients were calculated using Microsoft Excel's PEARSON function. In order to compare geochemical changes at the hand sample scale instead of at the grain or mineral crystal scale, the LIBS observation points that made up the rasters for each target were averaged together. Averaging the ChemCam data

by target was necessary due to the small spot size of the ChemCam laser. When calculating the Chemical Index of Alteration (CIA), points that may have diagenetic calcium-sulfate, had to be removed. To do so, points with > 10 % CaO were assumed to contain Ca sulfates and were removed.

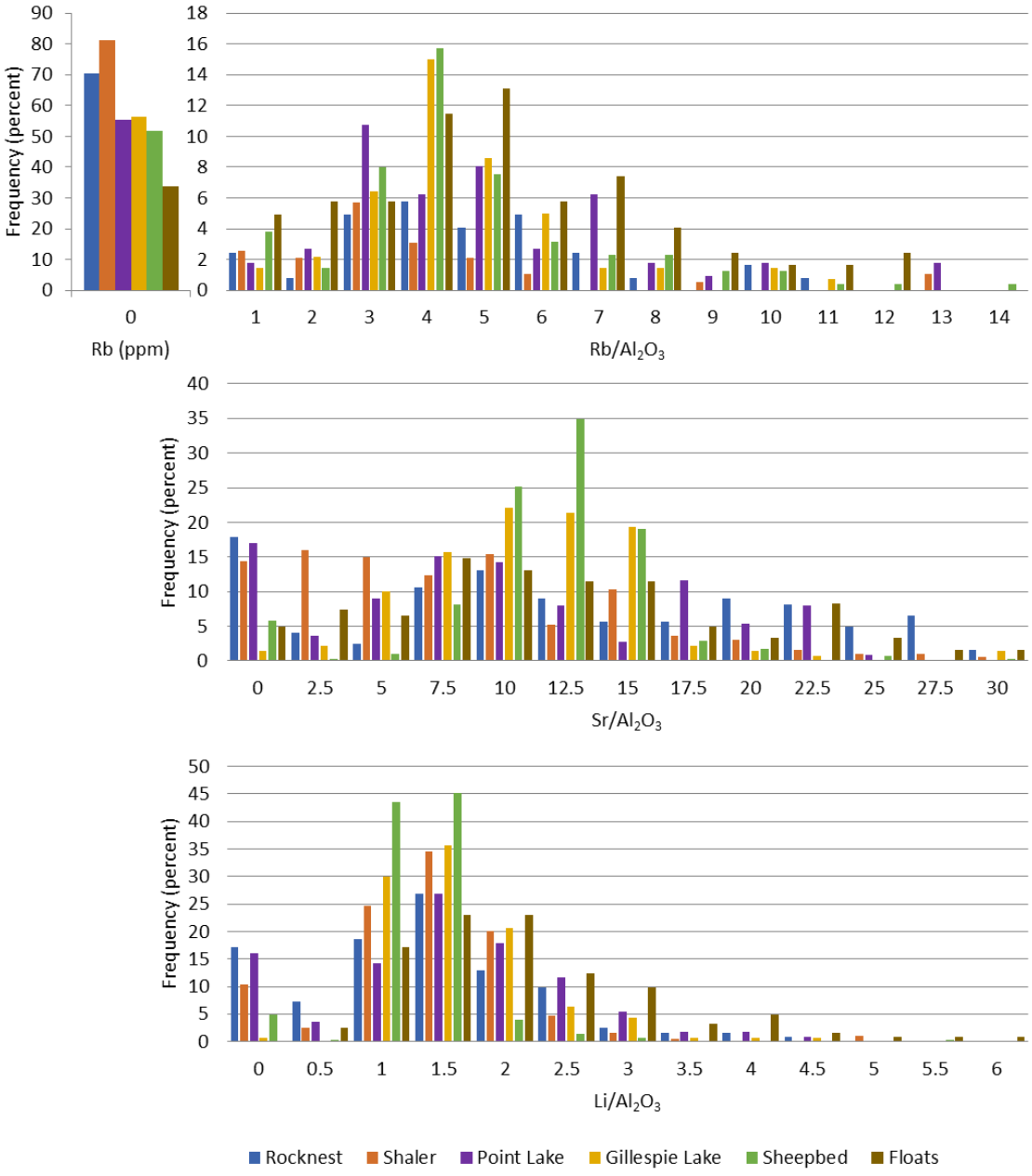

Figure 4.4: Histograms of Rb, Sr, & Li normalized to Al_2O_3 with Ca-sulfates removed. The '0' bin for Rb which represents either poor focus or no detectable Rb was removed and displayed next to the rest of the graph so that all the Rb data could be easily visible.

3. Results

Figure 4.4 displays the distribution of Li/Al_2O_3, Rb/Al_2O_3, and Sr/Al_2O_3. In the Rb graph, the zero bin is separated from the rest of the graph due to the large number of points in that bin in order to make the distribution trends easier to observe. The first two sandstone units have a larger number of analyses with no detectable Rb than Sheepbed or in the float basalts. In the observation points with detectable Rb, the distribution of the floats peak at a ratio value of 5, while Sheepbed and Gillespie peak at 4, and Point Lake peaks at 3.

Rocknest

	Fe/Al	Mg/Al	Ca/Al	Na/Al	K/Al	Li/Al	Rb/Al	Sr/Al	
CIA	-0.12	-0.24	-0.91	0.04	0.04	-0.11	-0.05	0.18	CIA
Fe/Al		-0.03	0.13	0.44	0.09	0.01	-0.19	-0.40	Fe/Al
Mg/Al			0.17	-0.12	-0.28	0.22	0.02	-0.25	Mg/Al
Ca/Al				-0.27	-0.19	0.10	-0.02	-0.11	Ca/Al
Na/Al					0.78	0.24	0.22	-0.06	Na/Al
K/Al						0.28	0.40	0.32	K/Al
Li/Al							0.29	0.24	Li/Al
Rb/Al								0.14	Rb/Al

Shaler

	Fe/Al	Mg/Al	Ca/Al	Na/Al	K/Al	Li/Al	Rb/Al	Sr/Al	
CIA	-0.43	-0.28	-0.95	-0.06	0.20	-0.58	-0.49	0.44	CIA
Fe/Al		0.82	0.41	0.29	-0.24	0.64	0.34	-0.51	Fe/Al
Mg/Al			0.26	0.28	-0.31	0.63	0.16	-0.39	Mg/Al
Ca/Al				-0.08	-0.21	0.60	0.57	-0.40	Ca/Al
Na/Al					0.19	0.19	0.02	0.10	Na/Al
K/Al						0.01	0.66	0.18	K/Al
Li/Al							0.64	-0.38	Li/Al
Rb/Al								-0.17	Rb/Al

Point Lake

	Fe/Al	Mg/Al	Ca/Al	Na/Al	K/Al	Li/Al	Rb/Al	Sr/Al	
CIA	-0.49	-0.45	-0.79	-0.10	0.38	-0.30	-0.36	0.16	CIA
Fe/Al		0.72	0.21	0.15	-0.33	0.50	0.36	-0.55	Fe/Al
Mg/Al			0.28	0.13	-0.31	0.62	0.47	-0.33	Mg/Al
Ca/Al				0.04	-0.33	0.11	0.38	0.10	Ca/Al
Na/Al					0.08	0.01	-0.12	0.27	Na/Al
K/Al						-0.04	-0.01	0.06	K/Al
Li/Al							0.54	-0.30	Li/Al
Rb/Al								-0.17	Rb/Al

Gillespie Lake

	Fe/Al	Mg/Al	Ca/Al	Na/Al	K/Al	Li/Al	Rb/Al	Sr/Al	
CIA	-0.41	-0.25	-0.87	-0.04	0.17	-0.52	0.05	-0.13	CIA
Fe/Al		0.76	0.40	0.10	-0.19	0.64	0.21	-0.15	Fe/Al
Mg/Al			0.25	0.09	-0.26	0.54	0.01	-0.21	Mg/Al
Ca/Al				-0.24	-0.31	0.54	-0.02	0.14	Ca/Al
Na/Al					0.49	-0.26	-0.01	0.06	Na/Al
K/Al						-0.20	0.49	0.08	K/Al
Li/Al							0.23	-0.16	Li/Al
Rb/Al								-0.08	Rb/Al

Sheepbed

	Fe/Al	Mg/Al	Ca/Al	Na/Al	K/Al	Li/Al	Rb/Al	Sr/Al	
CIA	-0.50	-0.12	-0.62	0.05	0.26	-0.50	-0.11	-0.44	CIA
Fe/Al		0.72	0.70	0.41	-0.12	0.64	0.07	0.57	Fe/Al
Mg/Al			0.33	0.32	-0.18	0.50	-0.02	0.25	Mg/Al
Ca/Al				0.08	-0.23	0.60	0.03	0.91	Ca/Al
Na/Al					0.52	0.13	0.10	0.14	Na/Al
K/Al						-0.23	0.28	-0.08	K/Al
Li/Al							0.05	0.46	Li/Al
Rb/Al								0.18	Rb/Al

Figure 4.5: Pearson correlation coefficients for CIA score and the elements: Fe, Mg, Ca, Na, K, Li, Rb, and Sr all normalized with Al_2O_3. The yellow color shows anticorrelations and the blue color shows correlations, the darker the color the stronger the connection. Of important note is the change in Sr from anticorrelated with Fe, Mg, and Ca in Shaler to correlated in Sheepbed.

In the Sr data, the floats show a broad peak that is skewed to the right with the highest at ratio values of 7.5 and 10, but values extend out to 15. Sheepbed values peak at 12.5 while Gillespie Lake also has a broad peak from 10 to 15. Rocknest, Shaler, and Point Lake all have >10 % of their points in the zero bin and fairly broad distributions. Point Lake is the closest to a normal distribution with a peak spread between 7.5 and 10, but it has some evidence of a bimodal distribution with a second peak at 17.5. Shaler points are mostly uniformly distributed from ratio values of 0 to 10. Rocknest values are spread fairly wide across the range of ratio values. In general, the Li values show a much tighter distribution with the float rocks having a peak around values of 1.5 and 2, Sheepbed having a peak at 1 to 1.5, and the rest of the units peaking at a Li/Al_2O_3 ratio of 1.5.

Figure 4.5 displays the Pearson correlation coefficients for Chemical Index of Alteration (CIA) values, the trace elements, and selected major elements with all elements normalized to Al_2O_3. Moving down strata, there is a general trend of more elements becoming anti-correlated with CIA. It is important to note that the correlation of CIA and Ca/Al is likely biased to some degree due to the need to remove many points with high CaO to remove the possible diagenetic Ca and because molar CaO (along with Na_2O and K_2O) are used in the calculation of CIA, although the points with detectable diagenetic Ca-sulfate material did not have a CIA score calculated. There is a positive correlation in Li with Fe and Mg in the sediment across all strata except Rocknest, and there is a correlation between Li and Ca at all strata except Rocknest and Point Lake.

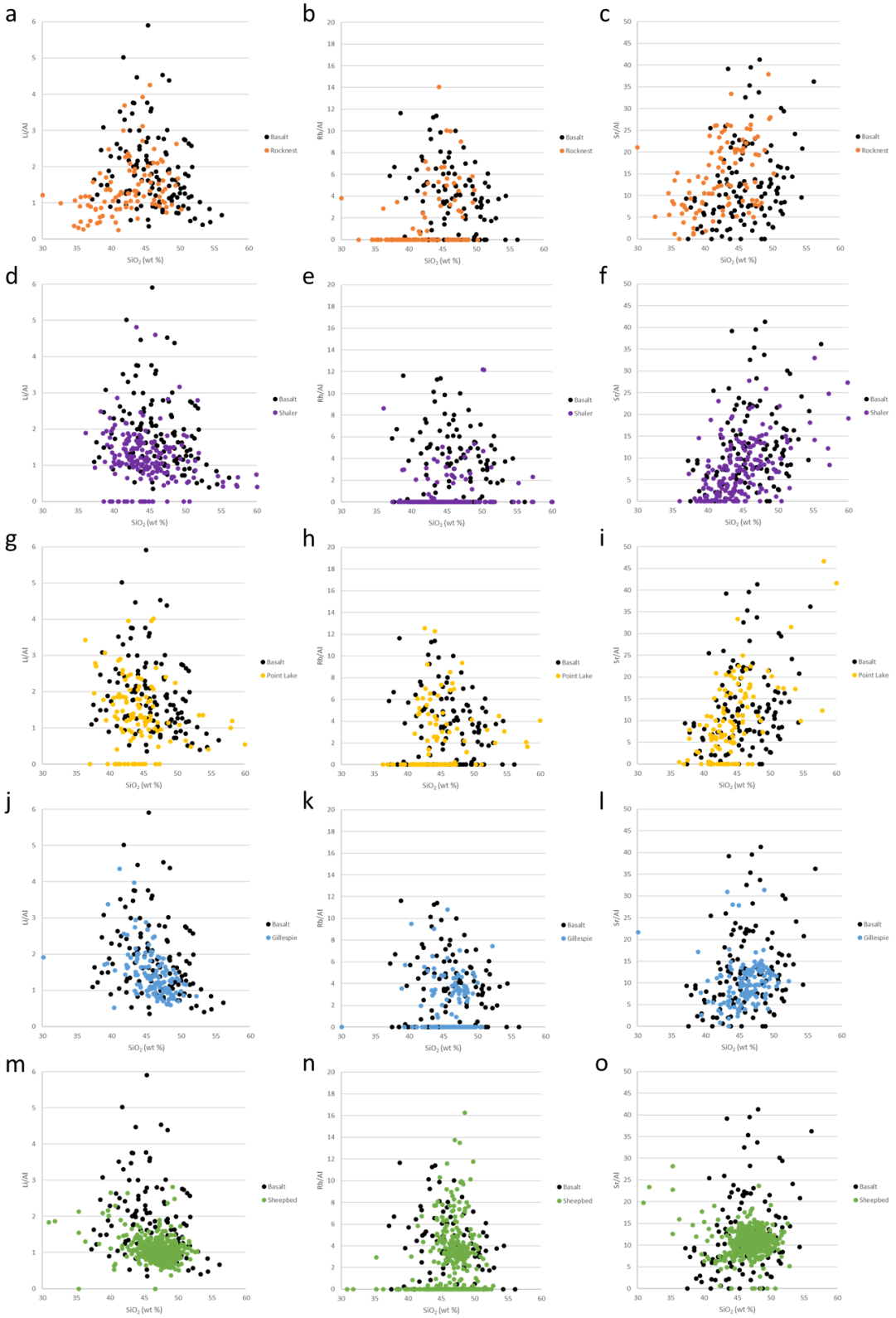

Figure 4.6: Distribution of Li, Rb, and Sr normalized to Al_2O_3 across the five stratigraphic units presented in this research each compared to the distribution seen in the float basalts. a-c) Rocknest, d-f) Shaler, g-i) Point Lake, j-l) Gillespie Lake, m-o) Sheepbed. Abundances are in Appendix E.

Rubidium is typically correlated, at least weakly, with K_20 across most strata, which is consistent with the known behavior of Rb substituting for K in igneous and sedimentary minerals (Cocco et al., 1969b). Rubidium is also correlated, at least weakly (coefficient >0.35), with every element except Na_20 at some point across all the strata, and in different units it is strongly correlated (coefficient >0.5) with CaO (at Shaler and Gillespie) and Li (at Shaler, Point Lake, and Gillespie). Strontium is weakly correlated with CIA and anti-correlated with FeO in Shaler and with FeO in Point Lake. Then, in Sheepbed Sr becomes weakly anti-correlated with CIA and correlated with FeO, as well as CaO and Li.

Figure 4.6 displays Li, Rb, and Sr normalized to Al_2O_3 for each stratigraphic unit at Yellowknife Bay to the float basalts. In the Rocknest data, Li is slightly depleted compared to the basalts (especially at low silica values). There is little difference in Sr between Rocknest and the basalts, and most of the points in Rocknest have Rb below the detection limit. At Shaler the Li ratio values cluster at a value of ~1-1.5, Sr ratio values are mostly below 15 but also show a slight positive trend with SiO_2, most of the points have Rb values below detection. At Point Lake, Li, Rb, and Sr all follow the distribution seen in the basalts to various degrees, although Li and Sr do not have the same range in values as they lack observation points at the higher values seen in the basalts. In addition, the Rb values are often below the detection limit. At Gillespie Lake, the relationships described above continue but Sr/Al_2O_3 values are much more concentrated at values below 15 and Rb/Al_2O_3 values are concentrated at values below ~5. At the Sheepbed mudstone, Li/Al_2O_3 values are concentrated around ~1 and SiO_2 of ~47 wt. % and are mostly absent above a ratio value of 2. Rubidium values mostly follow what was observed in the basalts. Sr/Al_2O_3 mostly cluster

around ~11, but there is a secondary trend at the lower silica values that is anticorrelated to silica and is likely related to the presence of sulfate materials.

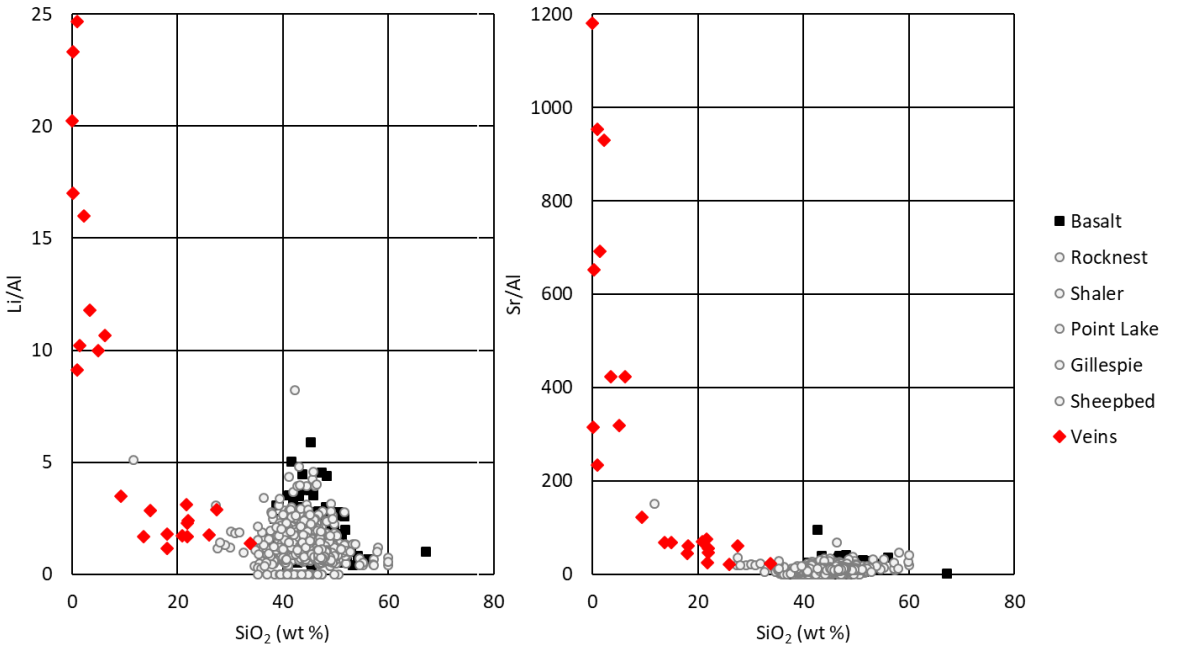

Figure 4.7: Plots of trace elements Li and Sr normalized to Al_2O_3 against silica with values in the veins displayed. Most of the spectra of the points on the veins had poor fits for the Rb univariate curves, so Rb could not be quantified and was not included.

The ChemCam instrument sampled 21 points on Ca-sulfate veins in the Sheepbed unit and one point on veins in both the Gillespie and Point Lake units. Both Li and Sr normalized to Al_2O_3 are enriched over the sediments and float basalts with veins reaching 25 and 120 times the median ratio values, respectively (Fig. 4.7). However, at these low values of Al_2O_3 (< 5 weight percent), it is necessary to also check the behavior of the unnormalized trace elements. This check was done in case the increases seen in Li or Sr are due to lower Al_2O_3 compositions rather than actual enrichments. In the unnormalized data, Li shows a weak correlation with Al_2O_3 in the veins and with the Sheepbed mudstone data. In addition, the Li values in the veins do not become depleted compared to the sediments as seen with Na_2O or other alkalis. Strontium is correlated with Al_2O_3 in the floats and the

sediments as well, but in the veins Sr values are anticorrelated with Al_2O_3 and were strongly enriched at the lowest alumina values (Fig. 4.8).

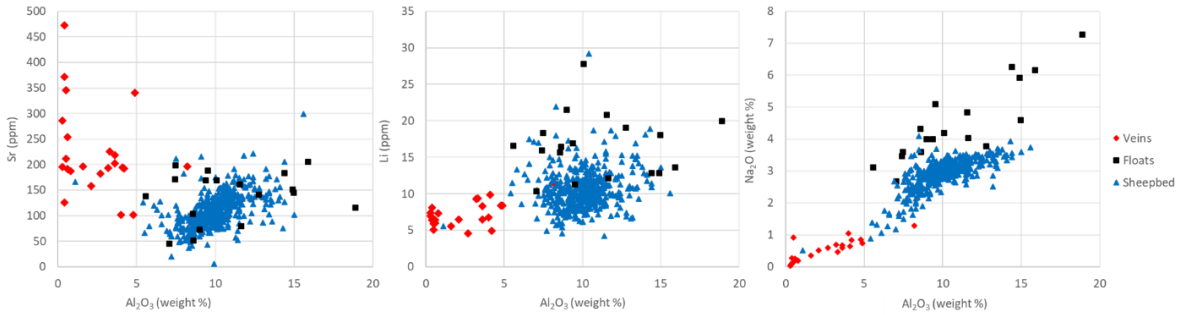

Figure 4.8: Graphs of Sr and Li in ppm against Al_2O_3 in weight % for points in the veins, Sheepbed mudstone, and basaltic float rocks. Values in the floats are averaged for each target.

4. Discussion

Lithium, Rb, and Sr are all mildly and non-uniformly, leached from the basaltic protolith (Fig. 4.4). Lithium is correlated with Fe, Mg, and Ca throughout the Yellowknife Bay units (Fig. 4.5). The results from Figures 4.4 and 4.5 suggest that Li likely remained in lithic fragments from the basalt protolith; Li may be present in trace amounts in clinopyroxene, olivine, or plagioclase (Caciagli et al., 2011).

It also is likely that much of the Rb was lost during early diagenesis due to the amount of points with Rb below the limit of detection in the sedimentary rocks (fig. 4.5). In each unit, half or more of all points have Rb below the limit of detection while only one or two observation points with spectra fit for trace element analyses have points with Li or Sr below the limit of detection. This is a marked increase from the float basalts where less than a third of points have Rb levels below the limit of detection.

Strontium behavior is more complex than what was seen in Li, as evidenced by the switch in correlations between CIA and FeO from Shaler to Sheepbed (fig. 4.5). Early during chemical weathering, Sr was likely mobilized during the breakdown of volcanic glasses then

incorporated into alteration products coating the material. The incorporation of Sr into alteration products would be analogous to the behavior of Ba (which is also an alkali earth metal) during early weathering of basalt (Eggleton, Foudoulis, & Varkevisser, 1987). This stage of weathering is represented by Shaler. Later, Sr was mobilized again from alteration coatings and likely was adsorbed by clays and incorporated into any Ca-sulfates formed during early diagenesis.

In Figure 4.6, trace elements in Rocknest are distributed differently than the rest of the units; Li has a positive correlation with silica at the lowest silica abundances, and Sr has slightly higher values at silica abundaces of ~30 – 40 wt. %. From Shaler through Sheepbed, trace elements begin to behave similarly. Li/Al cluster near a ratio value of ~1. Sr/Al begins with a spread that closely follows what was seen in the basalts, has fewer points with a ratio above 20, and ends with a cluster between ratio values of 10 and 15. The distribution of trace elements in the strata from Shaler through Sheepbed indicate sediments that have compositions similar to the basaltic protoliths.

Later diagenetic events represented by the Ca-sulfate veins play an important role in the behavior of Sr as Sr substitutes for Ca in Ca-sulfate veins (Fig. 4.7). While Li is also enriched in these graphs, Li itself is not enriched in the veins. Instead, the apparent enrichment of Li when normalized to Al_2O_3 is caused by the low abundance of Al_2O_3 in the veins. However, Li is not depleted in the veins like what is observed in Na_2O (Fig. 4.8). This suggests that Li is present within the Ca-sulfate veins, either as a part of solid inclusions – sediment incorporated into the vein material – or fluid inclusions – either remnant diagenetic fluid or pore fluid. Although at the lower values of alumina, the continued

presence of Li suggests fluid inclusions, as solid inclusions would also include aluminosilicates. Sr is enriched over the Sheepbed mudstone both in normalized and unnormalized data (Fig. 4.6 and Fig. 4.8). The Sr enrichment is almost certainly caused by the substitution of Sr^{2+} for Ca^{2+} during the deposition of the Ca-sulfate veins.

5. Conclusion

The lack of changes in trace element composition observed in this research supports the idea of minimal alteration of sediments. The changes observed in the trace element data are consistent with the earliest stages of alteration observed in terrestrial basalts (e.g., Das & Krishnaswami, 2007; Eggleton, Foudoulis, & Varkevisser, 1987; Nesbitt & Wilson, 1992). The three trace elements discussed in this research are three of the most mobile elements and generally are some of the first elements to be liberated from igneous minerals during subaerial weathering (e.g. Eggleton, Foudoulis, & Varkevisser, 1987; Das et al., 2005; Das and Krishnaswami, 2007). In addition, while Li has been depleted in the sediments compared to the float basalts, its continued presence (especially in the Sheepbed mudstone) may suggest some in-situ clay formation as clay formation the most likely way that Li remained in the system, as, unlike Rb and Sr, it is not adsorbed by clays but is incorporated into the structure of clay minerals during formation (Horstman, 1957). The Ca-sulfate diagenetic fluid contained Sr and deposited it along with the veins. This enriched Sr in the veins over the sediments. Additionally, Li was present in the Ca-sulfate veins even as the amount of sediments decreased. The continued presence of Li in veins could be due at times to solid inclusions – sediment grains incorporated into the veins. However, Li remains at about the same abundance in the veins even as alumina becomes nearly absent. This

suggests that the Li present in the veins may also be present in fluid inclusions as if Li was only present in solid inclusion it would decrease along with alumina which must come from solid inclusions. The two likely sources of the fluids are either diagenetic fluid or possibly remnant pore fluids in the sediments.

References

Andersen, D. T., Pollard, W. H., McKay, C. P., & Heldmann, J. (2002). Cold springs in permafrost on Earth and Mars. *Journal of Geophysical Research: Planets*, *107*(E3), 4-1.

Anderson, R. B., & Bell III, J. F. (2010). Geologic mapping and characterization of Gale Crater and implications for its potential as a Mars Science Laboratory landing site. *International Journal of Mars Science and Exploration*, *5*, 76-128.

Anderson, R. C., Jandura, L., Okon, A. B., Sunshine, D., et al. (2012). Collecting samples in Gale Crater, Mars; an overview of the Mars Science Laboratory sample acquisition, sample processing and handling system. Space science reviews, 170(1-4), 57-75.

Babechuk, M. G., Widdowson, M., & Kamber, B. S. (2014). Quantifying chemical weathering intensity and trace element release from two contrasting basalt profiles, Deccan Traps, India. *Chemical Geology*, *363*, 56-75.

Baker, A. M., Ganter, G. E., Nellessen, M. A., Newsom, H. E., et al. (2019). Analysis of Calcium Sulfate-Cemented Sandstones and Veins Along the MSL Traverse, Gale Crater, Mars. *LPI Contributions*, *2089*.

Banham, S. G., Gupta, S., Rubin, D. M., Watkins, J. A., et al. (2018). Ancient Martian aeolian processes and palaeomorphology reconstructed from the Stimson formation on the lower slope of Aeolis Mons, Gale crater, Mars. *Sedimentology*, *65*(4), 993-1042.

Bedford, C. C., Bridges, J. C., Schwenzer, S. P., Wiens, R. C., et al. (2019). Alteration trends and geochemical source region characteristics preserved in the fluviolacustrine sedimentary record of Gale crater, Mars. *Geochimica et Cosmochimica Acta*, *246*, 234-266.

Berner, R. (1980). Early diagenesis, A theoretical approach. *Princeton Series in Geochemistry*, 42-51, 81-89.

Blake, D., Vaniman, D., Achilles, C., Anderson, R., et al. (2012). Characterization and calibration of the CheMin mineralogical instrument on Mars Science Laboratory. *Space Science Reviews*, *170*(1-4), 341-399.

Blatt, H. (1992). *Sedimentary Petrology* (2nd ed.) New York, NY: W. H. Freeman and Company, pg. 129-135.

Bristow, T. F., Rampe, E. B., Achilles, C. N., Blake, D. F., et al. (2018). Clay mineral diversity and abundance in sedimentary rocks of Gale crater, Mars. *Science advances*, *4*(6), eaar3330.

Caciagli, N., Brenan, J. M., McDonough, W. F., & Phinney, D. (2011). Mineral–fluid partitioning of lithium and implications for slab–mantle interaction. *Chemical Geology*, *280*(3-4), 384-398.

Campbell, J. L., King, P. L., Burkemper, L., Berger, et al. (2014). The Mars Science Laboratory APXS calibration target: Comparison of Martian measurements with the terrestrial calibration. Nuclear Instruments and Methods in Physics Research Section B: Beam Interactions with Materials and Atoms, 323, 49-58.

Chu, L. E., Brown, K. M., & Kriechbaum, K. (2017). Mars 2020 sampling and caching subsystem environmental development testing and preliminary results. In *2017 IEEE Aerospace Conference* (pp. 1-10). IEEE.

Clegg, S. M., Sklute, E., Dyar, M. D., Barefield, J. E., & Wiens, R. C. (2009). Multivariate analysis of remote laser-induced breakdown spectroscopy spectra using partial least squares, principal component analysis, and related techniques. Spectrochimica Acta Part B: Atomic Spectroscopy, 64(1), 79-88.

Clegg, S. M., Anderson, R. B., Forni, O., Frydenvang, J., et al. (2017). Sulfur Chemical Analysis and Interpretation with ChemCam on the Curiosity Rover. In LPSC XLIX, p. 2439.

Cocco, G., Fanfana, L., Zanazzi, P. F., Heier, K. S., & Billings, G. K. (1969a). Lithium, in (Wedepohl, G.H., Correns, C. W., Shaw, D. M., Turekian, K. K., Zeman, J.) Handbook of Geochemistry Vol. II-1: Springer-Verlag, New York, NY. sec. 3A, 3D-3K.

Cocco, G., Fanfani, L., Zanazzi, P. F., Heier, K. S., & Billings, G. K. (1969b). Rubidium, in (Wedepohl, G.H., Correns, C. W., Shaw, D. M., Turekian, K. K., Zeman, J.) Handbook of Geochemistry Vol. II-4: Springer-Verlag, New York, NY. sec. 37A, 37D-37K.

Cousin, A., Sautter, V., Payré, V., Forni, O., et al. (2017). Classification of igneous rocks analyzed by ChemCam at Gale crater, Mars. *Icarus*, *288*, 265-283.

Cremers, D. A., & Knight, A. K. (2006). *Laser-Induced Breakdown Spectroscopy*. John Wiley & Sons, Ltd.

Cronan, C. S., & Schofield, C. L. (1979). Aluminum leaching response to acid precipitation: effects on high-elevation watersheds in the northeast. *Science*, *204*(4390), 304-306.

Crumpler, L. S., Aubele, J. C., & Zimbelman, J. R. (2007). Volcanic features of New Mexico analogous to volcanic features on Mars. *The Geology of Mars: Evidence From Earth-Based Analogs*.

Das, A., Krishnaswami, S., Sarin, M. M., & Pande, K. (2005). Chemical weathering in the Krishna Basin and Western Ghats of the Deccan Traps, India: rates of basalt weathering and their controls. Geochimica et Cosmochimica Acta, 69(8), 2067-2084.

Das, A., & Krishnaswami, S. (2007). Elemental geochemistry of river sediments from the Deccan Traps, India: implications to sources of elements and their mobility during basalt–water interaction. *Chemical Geology*, *242*(1), 232-254.

David, G., Meslin, P-Y., Dehouck, E., Gasnault, O., et al. (submitted). Laser-Induced Breakdown Spectroscopy (LIBS) characterization of martian soil analogs to distinguish mixtures and coatings: implications for ChemCam data at Gale crater, Mars.

Edwards, P. H., Bridges, J. C., Wiens, R., Anderson, R., et al. (2017). Basalt–trachybasalt samples in Gale crater, Mars. *Meteoritics & Planetary Science*, *52*(11), 2931-2410.

Eggleton, R. A., Foudoulis, C., & Varkevisser, D. (1987). Weathering of basalt: changes in rock chemistry and mineralogy. *Clays and Clay Minerals*, *35*(3), 161-169.

Farley, K. A., Malespin, C., Mahaffy, P., Grotzinger, J. P., et al. (2014). In situ radiometric and exposure age dating of the Martian surface. *science*, *343*(6169), 1247166.

Fawcett, P.J., Heikoop, J., Goff, F., Anderson, R.S., et al. (2007). Two middle Pleistocene glacial-interglacial cycles from the Valle Grande, Jemez Mountains, northern New Mexico. In *Geology of the Jemez Region II. New Mexico Geological Society 58th Annual Field Conference Guidebook. Socorro: New Mexico Geological Society* (pp. 409-417).

Fawcett, P. J., Werne, J. P., Anderson, R. S., Heikoop, et al. (2011). Extended megadroughts in the southwestern United States during Pleistocene interglacials. *Nature*, *470*(7335), 518-521.

Fischer, K., & Puchelt, H. (1969). Barium, in (Wedepohl, G.H., Correns, C. W., Shaw, D. M., Turekian, K. K., Zeman, J.) Handbook of Geochemistry Vol. II-4: Springer-Verlag, New York, NY. sec. 56A, 56D-56K.

Fischer, K., Stueber, A. M., Faure, G., Wedepohl, K. H., Gieskes, J. M., Veizer, J. (1969). Strontium, in (Wedepohl, G.H., Correns, C. W., Shaw, D. M., Turekian, K. K., Zeman, J.) Handbook of Geochemistry Vol. II-4: Springer-Verlag, New York, NY. sec. 38A, 38D-38K.

Forni, O., Maurice, S., Gasnault, O., Wiens, R. C., et al. (2013). Independent component analysis classification of laser induced breakdown spectroscopy spectra. Spectrochimica Acta Part B: Atomic Spectroscopy, 86, 31-41.

Fraeman, A. A., Johnson, J. R., Arvidson, R. E., Rice, M. S., et al. (2020). Synergistic ground and orbital observations of iron oxides on Mt. Sharp and Vera Rubin ridge. *Journal of Geophysical Research: Planets*, *125*(9), e2019JE006294.

Frydenvang, J., Gasda, P. J., Hurowitz, J. A., Grotzinger, et al. (2017). Diagenetic silica enrichment and late-stage groundwater activity in Gale crater, Mars. Geophysical Research Letters, 44(10), 4716-4724.

Galbács, G. (2015). A critical review of recent progress in analytical laser-induced breakdown spectroscopy. *Analytical and bioanalytical chemistry*, *407*(25), 7537-7562.

Gallet, S., Jahn, B., Lanoë, B.V.V., Dia, A., & Rossello, E. Loess geochemistry and its implications for particle origin and composition of the upper continental crust. *Earth and Planetary Science Letters* 156.3 (1998): 157-172.

Gislason, S. R., Arnorsson, S., & Armannsson, H. (1996). Chemical weathering of basalt in Southwest Iceland; effects of runoff, age of rocks and vegetative/glacial cover. *American Journal of Science*, *296*(8), 837-907.

Goff, F., Warren, R. G., Goff, C. J., Whiteis, J., et al. (2007). Comments on the geology, petrography, and chemistry of rocks within the resurgent dome area, Valles Caldera, New Mexico. In *Geology of the Jemez Region II. New Mexico Geological Society 58th Annual Field Conference Guidebook. Socorro: New Mexico Geological Society* (pp. 354-362).

Goff, F., Gardner, J. N., Reneau, S. L., Kelley, S. A., et al. (2011). *Geologic map of the Valles caldera, Jemez Mountains, New Mexico.* New Mexico Bureau of Geology and Mineral Resources, Geologic Map 79, 1:50,000 scale.

Goldich, S. S. (1938). A study in rock-weathering. *The Journal of Geology*, *46*(1), 17-58.

Golombek, M. P., Warner, N. H., Ganti, V., Lamb, M. P., et al. (2014), Small crater modification on Meridiani Planum and implications for erosion rates and climate change on Mars, J. Geophys. Res. Planets, 119, 2522–2547.

Grotzinger, J. P., Crisp, J., Vasavada, A. R., Anderson, R. C., et al. (2012). Mars Science Laboratory mission and science investigation. Space science reviews, 170(1-4), 5-56.

Grotzinger, J. P., Sumner, D. Y., Kah, L. C., Stack, K., et al. (2014). A habitable fluvio-lacustrine environment at Yellowknife Bay, Gale crater, Mars. *Science*, *343*(6169), 1242777.

Grotzinger, J. P., Gupta, S., Malin, M. C., Rubin, D. M., et al. (2015). Deposition, exhumation, and paleoclimate of an ancient lake deposit, Gale crater, Mars. Science, 350(6257), aac7575.

Head, J. W., Mustard, J. F., Kreslavsky, M. A., Milliken, R. E., & Marchant, D. R. (2003). Recent ice ages on Mars. *Nature*, *426*(6968), 797-802.

Horstman, E. L. (1957). The distribution of lithium, rubidium and caesium in igneous and sedimentary rocks, *Geochim. et Cosmochim. Acta*, 12, 1–28.

Hurowitz, J. A., Grotzinger, J. P., Fischer, W. W., McLennan, S. M., et al. (2017). Redox stratification of an ancient lake in Gale crater, Mars. Science, 356(6341), 6849.

Jackson, R. S., Wiens, R. C., Vaniman, D. T., Beegle, L. W., et al. (2016). ChemCam investigation of the John Klein and Cumberland drill holes and tailings, Gale crater, Mars. Icarus, 277, 330-341.

Johnson, N. M., Driscoll, C. T., Eaton, J. S., Likens, G. E., & McDowell, W. H. (1981). 'Acid rain', dissolved aluminum and chemical weathering at the Hubbard Brook Experimental Forest, New Hampshire. *Geochimica et Cosmochimica Acta*, *45*(9), 1421-1437.

Johnson, C. M., Fawcett, P. J., & Ali, A. (2006). Geochemical indicators of redox conditions as a proxy for Mid-Pleistocene climate change from a lacustrine sediment core, Valles Caldera, New Mexico. *AGUFM*, *2006*, PP51B-1143.

Kah, L. C., Lyons, T. W., & Chesley, J. T. (2001). Geochemistry of a 1.2 Ga carbonate-evaporite succession, northern Baffin and Bylot Islands: implications for Mesoproterozoic marine evolution. *Precambrian Research*, *111*(1-4), 203-234.

Kushnir, J. (1980). The coprecipitation of strontium, magnesium, sodium, potassium and chloride ions with gypsum. An experimental study. *Geochimica et cosmochimica acta*, *44*(10), 1471-1482.

Kronyak, R. E., Kah, L. C., Miklusicak, N. B., Edgett, K. S., Sun, V. Z., Bryk, A. B., & Williams, R. M. E. (2019). Extensive polygonal fracture network in Siccar Point group strata: fracture mechanisms and implications for fluid circulation in Gale crater, Mars. *Journal of Geophysical Research: Planets*, *124*(10), 2613-2634.

Lanza, N. L., Ollila, A. M., Cousin, A., Wiens, R. C., et al. (2015). Understanding the signature of rock coatings in laser-induced breakdown spectroscopy data. Icarus, 249, 62-73.

Laskar, J., Robutel, P., Joutel, F., Gastineau, M., Correia, A. C. M., & Levrard, B. (2004). A long-term numerical solution for the insolation quantities of the Earth. *Astronomy & Astrophysics*, *428*(1), 261-285.

Le Deit, L., Mangold, N., Forni, O., Cousin, A., et al. (2016). The potassic sedimentary rocks in Gale Crater, Mars, as seen by ChemCam on board Curiosity. Journal of Geophysical Research: Planets, 121(5), 784-804.

Léveillé, R. J., Bridges, J., Wiens, R. C., Mangold, N., et al. (2014). Chemistry of fracture-filling raised ridges in Yellowknife Bay, Gale Crater: Window into past aqueous activity and habitability on Mars. *Journal of Geophysical Research: Planets*, *119*(11), 2398-2415.

Lu, F. H., Meyers, W. J., & Hanson, G. N. (2002). Trace elements and environmental significance of Messinian gypsum deposits, the Nijar Basin, southeastern Spain. *Chemical Geology*, *192*(3-4), 149-161.

Mahaffy, P. R., Webster, C. R., Cabane, M., Conrad, et al. (2012). The sample analysis at Mars investigation and instrument suite. *Space Science Reviews*, *170*(1-4), 401-478.

Mangold, N., Forni, O., Dromart, G., Stack, K., et al. (2015). Chemical variations in Yellowknife Bay formation sedimentary rocks analyzed by ChemCam on board the Curiosity rover on Mars. Journal of Geophysical Research: Planets.

Mangold, N., Dehouck, E., Fedo, C., Forni, O., et al. (2019). Chemical alteration of fine-grained sedimentary rocks at Gale crater. *Icarus*, *321*, 619-631.

Martin, P. E., Farley, K. A., Baker, M. B., Malespin, C. A., et al. (2017). A two-setp K-Ar experiment on Mars: dating the diagenetic formation of jarosite from Amazonian groundwaters. Journal of Geophysical Research: Planets.

Maurice, S., Wiens, R. C., Saccoccio, M., Barraclough, B., et al. (2012). The ChemCam instrument suite on the Mars Science Laboratory (MSL) rover: science objectives and mast unit description. Space science reviews, 170(1-4), 95-166.

Maurice, S., Clegg, S. M., Wiens, R. C., Gasnault, O., et al. (2016). ChemCam activities and discoveries during the nominal mission of the Mars Science Laboratory in Gale crater, Mars. *Journal of Analytical Atomic Spectrometry*, *31*(4), 863-889.

McKillup, S., & Dyar, M. D. (2010). Working from samples: data, populations, and statistics. In *Geostatistics explained: an introductory guide for earth scientists* (pp. 66-84). Cambridge University Press.

McLennan, S. M., Anderson, R. B., Bell, J. F., Bridges, J. C., et al. (2014). Elemental geochemistry of sedimentary rocks at Yellowknife Bay, Gale crater, Mars. *science*, *343*(6169).

Middelburg, J. J., van der Weijden, C. H., & Woittiez, J. R. (1988). Chemical processes affecting the mobility of major, minor and trace elements during weathering of granitic rocks. *Chemical Geology*, *68*(3), 253-273.

Milliken, R. E., K. Edgett, J. Grotzinger, and B. J. Thomson (2010), Paleoclimate of Mars as captured by the stratigraphic record in Gale Crater, *Geophysical Research Letters*, 37, L04201.

Milnes, A. R., & Twidale, C. R. (1983). An overview of silicification in Cainozoic landscapes of arid central and southern Australia. *Soil Research*, *21*(4), 387-410.Ming, D. W., Archer, P. D., Glavin, D. P., Eigenbrode, J. L., et al. (2014). Volatile and organic compositions of sedimentary rocks in Yellowknife Bay, Gale Crater, Mars. *Science*, *343*(6169), 1245267.

Morris, R. V., Vaniman, D. T., Blake, D. F., Gellert, R., et al. (2016). Silicic volcanism on Mars evidenced by tridymite in high-SiO2 sedimentary rock at Gale crater. Proceedings of the National Academy of Sciences, 113(26), 7071-7076.

Murray, B. C., Ward, W. R., & Yeung, S. C. (1973). Periodic insolation variations on Mars. *Science*, *180*(4086), 638-640.

Nachon, M., Clegg, S. M., Mangold, N., Schröder, S., et al. (2014). Calcium sulfate veins characterized by ChemCam/Curiosity at Gale crater, Mars. Journal of Geophysical Research: Planets, 119(9), 1991-2016.

Nachon, M., Mangold, N., Forni, O., Kah, L. C., et al. (2017). Chemistry of diagenetic features analyzed by ChemCam at Pahrump Hills, Gale crater, Mars. *Icarus*, *281*, 121-136.

Nesbitt, H. W., & Markovics, G. (1980). Chemical processes affecting alkalis and alkaline earths during continental weathering. *Geochimica et Cosmochimica Acta*, *44*(11), 1659-1666.

Nesbitt, H. W., & Wilson, R. E. (1992). Recent chemical weathering of basalts. *American Journal of Science*, *292*(10), 740-777.

Ollila, A. M., Newsom, H. E., Clark, B., Wiens, R. C., et al. (2014). Trace element geochemistry (Li, Ba, Sr, and Rb) using Curiosity's ChemCam: early results for Gale crater from Bradbury landing site to Rocknest. *Journal of Geophysical Research: Planets*, *119*(1), 255-285.

Payré, V., Fabre, C., Cousin, A., Sautter, V., et al. (2017). Alkali trace elements in Gale crater, Mars, with ChemCam: Calibration update and geological implications. *Journal of Geophysical Research: Planets*, *122*(3), 650-679.

Qiao, S., Ding, Y., Tian, D., Yao, L., & Yang, G. (2015). A review of laser-induced breakdown spectroscopy for analysis of geological materials. *Applied Spectroscopy Reviews*, *50*(1), 1-26.

Rampe, E. B., Ming, D. W., Blake, D. F., Bristow, T. F., et al. (2017a). Mineralogy of an ancient lacustrine mudstone succession from the Murray formation, Gale crater, Mars. Earth and Planetary Science Letters, 471, 172-185.

Rampe, E. B., Ming, D. W., Grotzinger, J.P., Morris, R. V., et al. (2017b). Mineral trends in early Hesperian lacustrine mudstone at Gale Crater, Mars. In: LPSC XLVIII, p. 2543.

Reneau, S.L., Drakos, P.G., & Katzman, D. (2007). Post-Resurgence Lakes in the Valles Caldera, New Mexico. In *Geology of the Jemez Region II. New Mexico Geological Society 58th Annual Field Conference Guidebook. Socorro: New Mexico Geological Society* (pp. 354-362).

Richardson, M. I., & Wilson, R. J. (2002). Investigation of the nature and stability of the Martian seasonal water cycle with a general circulation model. *Journal of Geophysical Research: Planets*, *107*(E5), 7-1.

Rice, M. S., Gupta, S., Treiman, A. H., Stack, K. M., et al. (2017). Geologic overview of the Mars Science Laboratory rover mission at the Kimberley, Gale crater, Mars. Journal of Geophysical Research: Planets, 122(1), 2-20.

Schmidt, M. E., Perrett, G. M., Bray, S. L., Bradley, N. J., et al. (2018). Dusty Rocks in Gale Crater: assessing areal coverage and separating dust and rock contributions in APXS analyses. *Journal of Geophysical Research: Planets*, *123*(7), 1649-1673.

Smith, R. L., & Bailey, R. A. (1968). Resurgent cauldrons. *Geological Society of America Memoirs*, *116*, 613-662.

Stix, J., Layne, G. D., & Spell, T. L. (1995). The behavior of light lithophile and halogen elements in felsic magma: geochemistry of the post-caldera Valles Rhyolites, Jemez

Mountains Volcanic Field, New Mexico. *Journal of volcanology and geothermal research*, *67*(1-3), 61-77.

Taylor, G., & Eggleton, R. A. (2017) Silcrete: an Australian perspective. Aus. J. Earth. Sci. 64, 987-1016, doi:10.1080/08120099.2017.1318167.

Treiman, A. H., Bish, D. L., Vaniman, D. T., Chipera, S. J., et al. (2016). Mineralogy, provenance, and diagenesis of a potassic basaltic sandstone on Mars: CheMin X-ray diffraction of the Windjana sample (Kimberley area, Gale Crater). Journal of Geophysical Research: Planets, 121(1), 75-106.

Tsoar, H., & K. Pye. Dust transport and the question of desert loess formation. *Sedimentology* 34.1 (1987): 139-153.

Twidale, C. R., & Milnes, A. R. (1983). Aspects of the distribution and disintegration of siliceous duricrusts in arid Australia. *Geol. Mijnbouw*, *62*, 373-382.

Vaniman, D. T., Bish, D. L., Ming, D. W., Bristow, T. F., et al. (2014). Mineralogy of a mudstone at Yellowknife Bay, Gale crater, Mars. *Science*, 1243480.

VanBommel, S. J., Gellert, R., Berger, J. A., Campbell, J. L., et al. (2016). Deconvolution of distinct lithology chemistry through oversampling with the Mars Science Laboratory Alpha Particle X-ray Spectrometer. *X-Ray Spectrometry*, *45*(3), 155-161.

Wiens, R. C., Maurice, S., Barraclough, B., Saccoccio, et al. (2012). The ChemCam instrument suite on the Mars Science Laboratory (MSL) rover: Body unit and combined system tests. Space science reviews, 170(1-4), 167-227.

Wiens, R. C., Maurice, S., Lasue, J., Forni, O., et al. (2013). Pre-flight calibration and initial data processing for the ChemCam laser-induced breakdown spectroscopy instrument on the Mars Science Laboratory rover. Spectrochimica Acta Part B: Atomic Spectroscopy, 82, 1-27.

Williams, J., Day, M., Chojnacki, M., & Rice, M. (2020). Scarp orientation in regions of active aeolian erosion on Mars. Icarus, 335, 113384.

Yen, A. S., Ming, D. W., Vaniman, D. T., Gellert, R., et al. (2017). Multiple stages of aqueous alteration along fractures in mudstone and sandstone strata in Gale Crater, Mars. Earth and Planetary Science Letters, 471, 186-198.

Appendix A

Spectra for Ca-Sulfate veins

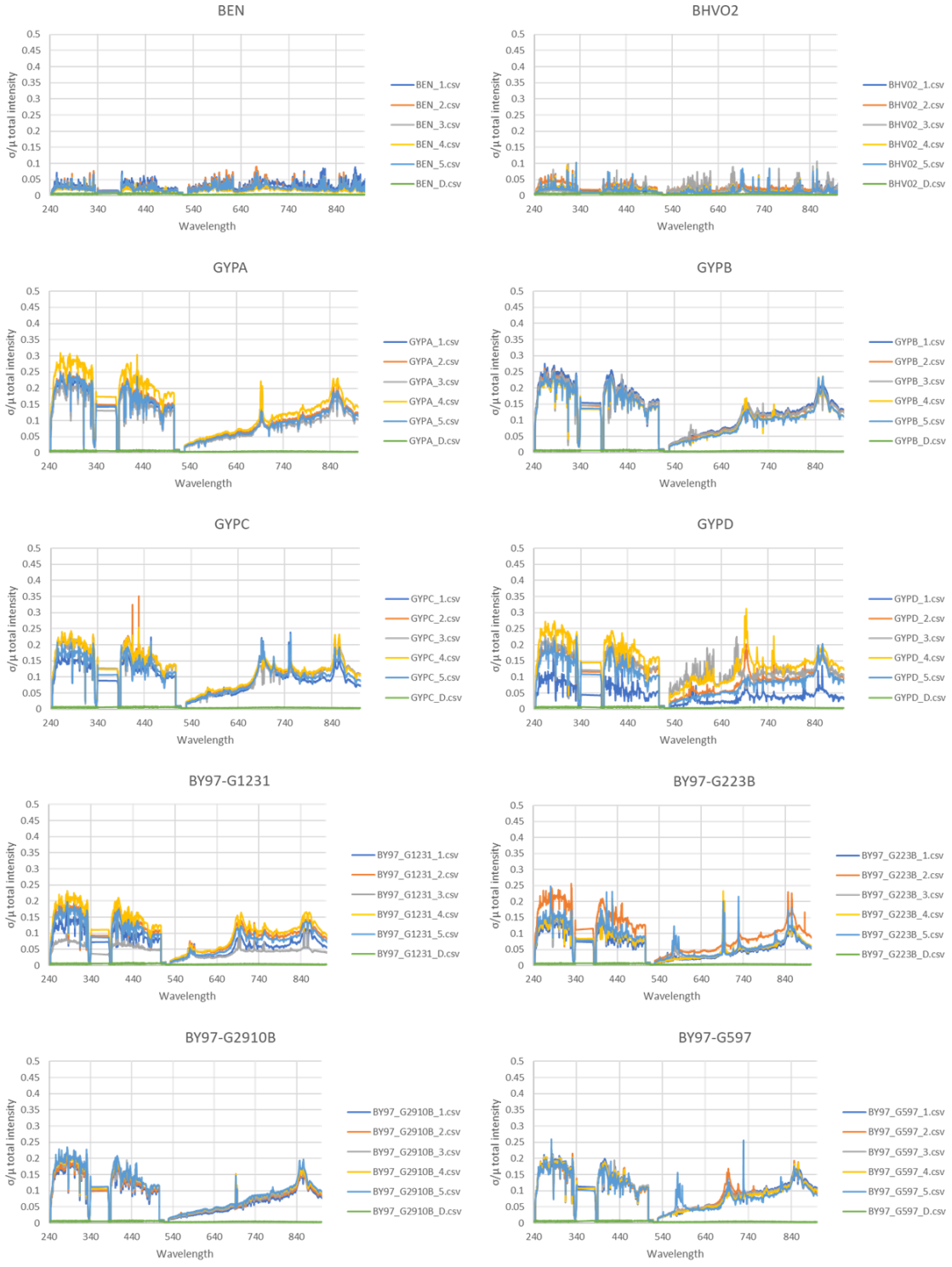

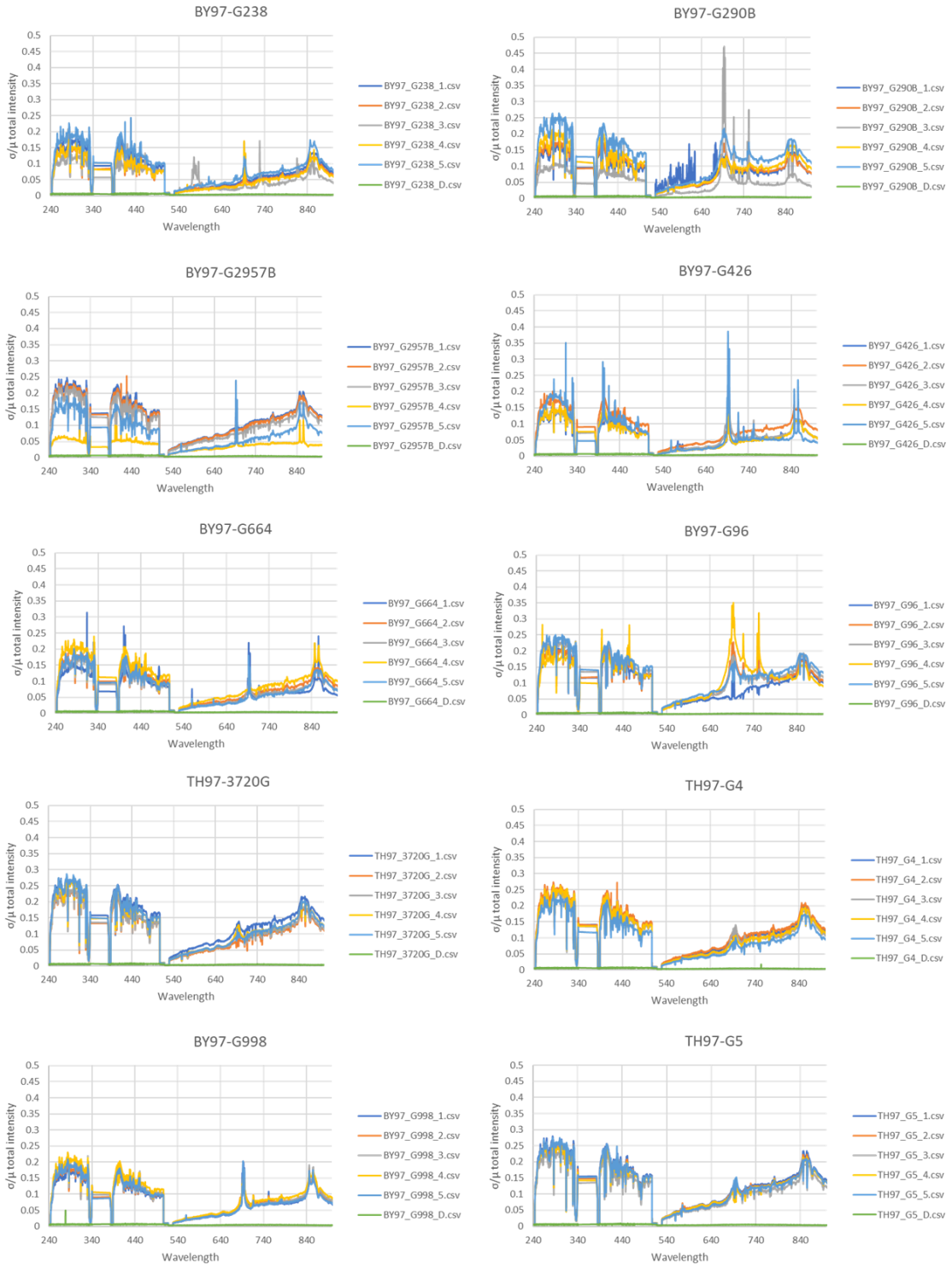

The standard deviation of signal intensity divided by the mean of the intensity across 50 LIBS shots on each point for four standards. BEN and BHVO2 are basalt standards, analogous to whole rock samples on Mars, GYPA, GYPB, GYPC, and GYPD ARE gypsum standards from Brammers, the remaining samples are Ca sulfates from Bylot Supergroup, northern Baffin Island, Canada (Kah et al., 2001).

Appendix B

Relevant APXS Results to the ChemCam investigation of the drill sites

A.1 Comparairson of APXS and ChemCam oxide abundances

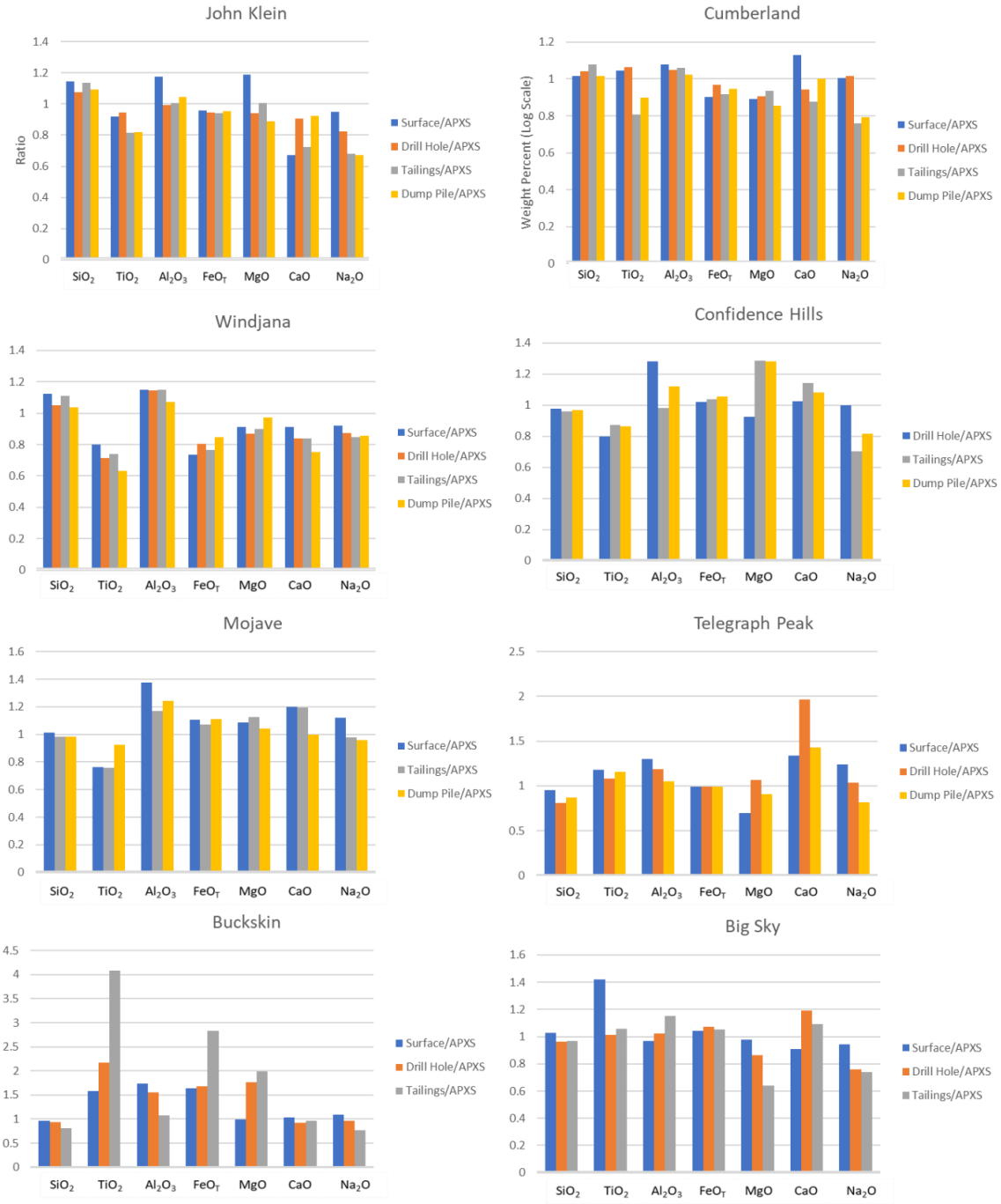

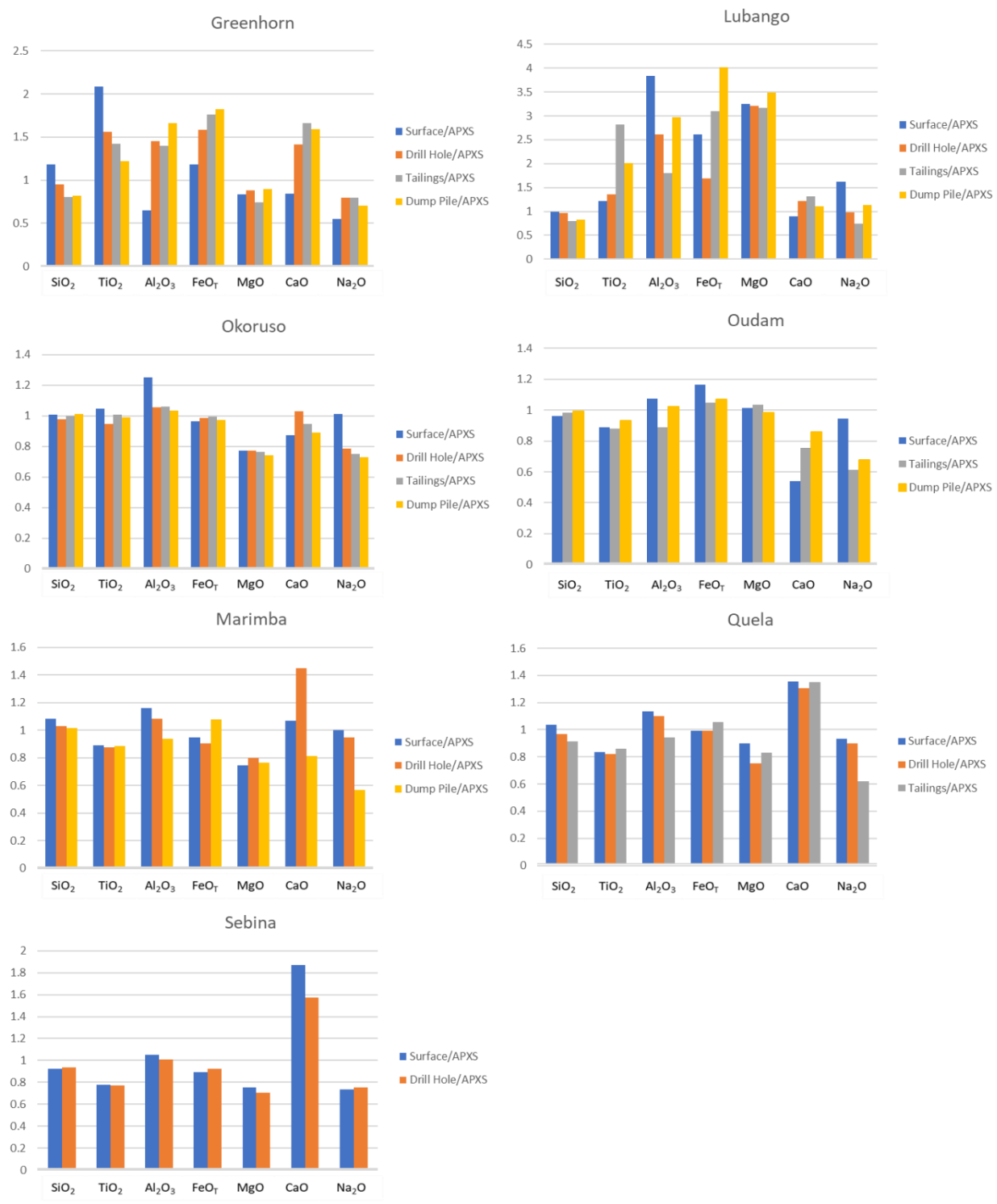

Figure S9: Ratios of the ChemCam compositions for surface, drill hole, tailings, and dump piles to the averaged values reported by APXS for each drill site. APXS dump pile data was excluded to avoid contamination from substrate.

ChemCam data were compared to APXS data collected at each drill site. Oxide abundances were averaged at each drill site, with APXS data averaged into one set which includes both surface and drill fines and ChemCam data averaged by target types described above. The average for each target type was then ratioed against the APXS average to determine if APXS data varied systematically against ChemCam data.

The ratios of averaged ChemCam data types (drill site surface, drill hole wall, tailings, and dump piles) for each site to the average APXS value at those sites fall mostly between 0.75 and 1.25 with 82 out of the 350 oxide ratios falling outside that range. There are no ratios below 0.5, but there are instances of ratio values above 2 indicating the ChemCam means are more than twice that of the APXS means. These all occur at the Buckskin, Greenhorn, and Lubango sites but occur with every data type. Buckskin has high values for TiO_2 and FeO_T (to a lesser extent) in the tailings. Lubango shows greater disparity for Al_2O_3 for the surface values and FeO_T in the dump pile, but APXS has ~3 times higher ratios for MgO across all data types, and for the dump pile Al_2O_3 and tailings FeO_T. Greenhorn only has Surface TiO_2 with a ratio greater than 2. As all three sites are high silica sites with known difficulties in quantifying TiO_2, these differences are likely due to instrumental uncertainty, not geologic changes.

A.2 APXS Dust Deconvolution

In order to estimate the range of compositions of the dust free surfaces for the high-silica drill sites, we used a deconvolution calculation using the fraction of dust coverage and range of dust composition from Schmidt et al. (2018). The equation used is given below:

$$(1 - A)x + AB_{elem} = C_{elem}$$

A is the fraction of the surface that is dust covered, B is the APXS dust composition for the element in question, and C is the APXS reported composition at the drill site for the element in question. The equation is then solved for x to give the dust-free composition for the element in question. In the paper, we reported the composition for each element at the endmembers of the possible range in composition of the Martian global dust.

Table S1, below, shows the results of the normalization calculations displaying the results using the average of the martian dust composition and the range of values that result from running the equations on the high and low end of the range for each oxide. The normalized results from the high and low end calculations were not shown in the paper because there is no reason to assume all the oxides are at the lowest value or all the oxides are at the highest values. It seems more likely that some oxides would be on the high end of the range while others would be at the low end of their range, and as normalization is influnced by all the elements the results from normalization can be nonsensical at times. This can be seen in the normalized “maximum” silica abundances which are all lower than the normalized “minimum” silica abundances. This is due to the high totals of the Maximum Value Results for each APXS target (ranging from ~103% to ~109%).

Table S8: This table shows the results of the dust correction for the high-silica APXS targets. APXS modeled dust composition and range was reported by Schmidt et al. (2018).

APXS Targets	SiO_2	TiO_2	Al_2O_3	FeO	MgO	CaO	Na_2O	K_2O	P_2O_5	SO_3	Cl	MnO
Buckskin_DRT_raster1	62.51	1.48	6.84	4.96	4.88	4.90	2.36	0.80	1.22	8.77	0.88	0.12
Buckskin_DRT_raster2	68.09	1.51	6.09	4.40	3.45	3.87	2.15	0.82	1.32	7.21	0.71	0.08
Greenhorn_DRT	56.23	1.00	5.48	9.43	4.77	5.98	2.53	0.44	1.24	10.78	1.54	0.09
Lubango_DRT	54.86	0.91	5.78	9.82	3.90	6.57	2.67	0.43	1.06	11.20	2.15	0.10

	SiO_2	TiO_2	Al_2O_3	FeO	MgO	CaO	Na_2O	K_2O	P_2O_5	SO_3	Cl	MnO
APXS Modeled Dust	39	0.9	9	16	9	8	2.4	0.54	0.9	9.5	1.2	0.3
Range	+6		+2		+2	+3	+0.6	+0.08	+0.6	+1	+0.2	
	-6	n.c.1	-1	n.c.	-2	-2	-0.6	-0.1	-0.3	-0.8	-0.2	n.c.

Average Value Results[2]

Not Normalized	SiO_2	TiO_2	Al_2O_3	FeO	MgO	CaO	Na_2O	K_2O	P_2O_5	SO_3	Cl	MnO
Buckskin_DRT_raster1	68.84	1.48	6.26	4.96	3.77	4.07	2.35	0.87	1.31	8.57	0.79	0.12
Buckskin_DRT_raster2	75.92	1.51	5.31	4.40	1.96	2.76	2.08	0.90	1.43	6.59	0.58	0.08
Greenhorn_DRT	63.41	1.00	4.01	9.43	3.01	5.14	2.58	0.40	1.38	11.31	1.68	0.09
Lubango_DRT	57.48	0.91	5.25	9.82	3.06	6.33	2.71	0.41	1.09	11.48	2.31	0.10

Normalized[5]	SiO_2	TiO_2	Al_2O_3	FeO	MgO	CaO	Na_2O	K_2O
Buckskin_DRT_raster1	66.34	1.43	6.03	4.78	3.63	3.92	2.26	0.84
Buckskin_DRT_raster2	73.08	1.45	5.11	4.24	1.88	2.66	2.00	0.86
Greenhorn_DRT	60.94	0.96	3.86	9.06	2.89	4.94	2.48	0.38
Lubango_DRT	56.67	0.90	5.17	9.68	3.01	6.24	2.68	0.41

Minimum Value Results[3]

Not Normalized	SiO_2	TiO_2	Al_2O_3	FeO	MgO	CaO	Na_2O	K_2O	P_2O_5	SO_3	Cl	MnO
Buckskin_DRT_raster1	67.22	1.48	6.21	4.96	3.23	3.26	2.19	0.85	1.14	8.30	0.74	0.12
Buckskin_DRT_raster2	74.30	1.51	5.25	4.40	1.42	1.95	1.92	0.87	1.27	6.32	0.50	0.08
Greenhorn_DRT	60.91	1.00	3.93	9.43	2.18	3.89	2.33	0.37	1.13	10.90	1.56	0.09
Lubango_DRT	56.49	0.91	5.21	9.82	2.72	5.84	2.62	0.40	0.99	11.32	2.26	0.10

Normalized	SiO_2	TiO_2	Al_2O_3	FeO	MgO	CaO	Na_2O	K_2O
Buckskin_DRT_raster1	67.16	1.48	6.20	4.96	3.23	3.26	2.19	0.85
Buckskin_DRT_raster2	74.17	1.51	5.24	4.39	1.42	1.95	1.92	0.87
Greenhorn_DRT	61.95	1.02	4.00	9.59	2.21	3.96	2.37	0.37
Lubango_DRT	56.97	0.92	5.26	9.90	2.75	5.89	2.64	0.40

Maximum Value Results[4]

Not Normalized	SiO_2	TiO_2	Al_2O_3	FeO	MgO	CaO	Na_2O	K_2O	P_2O_5	SO_3	Cl	MnO
Buckskin_DRT_raster1	70.45	1.48	6.34	4.96	4.31	4.60	2.51	0.90	1.39	8.79	0.85	0.12
Buckskin_DRT_raster2	77.53	1.51	5.39	4.40	2.49	3.30	2.24	0.92	1.51	6.81	0.63	0.08
Greenhorn_DRT	65.90	1.00	4.14	9.43	3.84	5.97	2.83	0.44	1.51	11.65	1.76	0.09
Lubango_DRT	58.48	0.91	5.30	9.82	3.39	6.66	2.81	0.43	1.14	11.61	2.34	0.10

Normalized	SiO_2	TiO_2	Al_2O_3	FeO	MgO	CaO	Na_2O	K_2O
Buckskin_DRT_raster1	65.79	1.38	5.92	4.63	4.02	4.30	2.34	0.84
Buckskin_DRT_raster2	72.33	1.41	5.03	4.10	2.33	3.08	2.09	0.86
Greenhorn_DRT	60.37	0.92	3.79	8.64	3.52	5.47	2.60	0.40
Lubango_DRT	56.52	0.88	5.12	9.49	3.27	6.44	2.72	0.41

[1]n.c. indicates that the element was not corrected in the dust free composition and the range is not reported here.
[2]The Average Value Results use the average values of the APXS modeled dust composition.
[3]The Minimum Value Results report the lowest values of the dust correction deconvolution calculation which uses the maximum values from the APXS modeled dust composition.
[4]The Maximum Value Results report the highest values of the dust correction deconvolution calculation which uses the minimum values from the APXS modeled dust composition.
[5]Normalized values show the values normalized to a total of 100%; this includes trace element data (not shown).

Appendix C

Chapter 2 Data Tables

John Klein

Target	SiO_2	TiO_2	Al_2O_3	FeO_T	MgO	CaO	Na_2O	Li ppm	Rb ppm	Sr ppm	Ba ppm	Distance m	Spectrum Total
Surface													
John_Klein_CCAM_new	47.1	1.1	14.3	21.3	7.4	4.6	3.9	18.9	n.d.	75.6	n.d.	5.4083	4.01E+14
John_Klein_CCAM_new	49.1	0.6	10.4	21.3	15.1	2.5	3.3	29.2	n.d.	103.7	n.d.	5.4083	3.53E+14
John_Klein_CCAM_new	50.7	0.6	10.0	20.5	18.3	2.7	3.0	14	n.d.	n.d.	n.d.	5.4083	3.83E+14
John_Klein_CCAM_new	50.1	0.8	13.1	19.7	10.4	5.9	3.5	6.6	n.d.	113.1	n.d.	5.4083	3.94E+14
John_Klein_CCAM_new	48.9	0.9	11.4	19.6	8.2	4.5	2.7	4.2	19.5	52.6	156.8	5.44466	5.74E+13
John_Klein_RP2	48.5	1.0	10.8	18.1	8.3	6.1	3.1	10.8	32.4	129.3	n.d.	3.50969	8.44E+14
John_Klein_RP2	50.7	0.8	8.7	18.6	14.8	3.7	2.3	8.9	n.d.	98.2	n.d.	3.50969	5.68E+14
John_Klein_RP2	47.0	1.2	10.7	19.6	8.2	5.6	3.2	9.7	38.4	135.9	n.d.	3.50969	1.09E+15
John_Klein_RP2	44.3	1.1	9.6	20.0	8.0	6.8	3.3	16.3	n.d.	72.6	n.d.	3.50969	1.06E+15
John_Klein_RP2	49.3	0.9	12.3	18.8	7.9	6.2	3.2	12.5	n.d.	105.2	n.d.	3.52743	5.55E+14
John_Klein_RP2	47.1	0.8	7.2	19.1	16.5	3.8	1.7	9.7	n.d.	59.8	n.d.	3.52743	5.05E+14
John_Klein_RP2	48.3	1.0	11.3	18.3	8.6	5.8	3.1	11.3	33.6	119.6	n.d.	3.52743	7.86E+14
John_Klein_RP2	47.5	1.1	11.3	19.3	7.9	6.0	3.0	11	40.8	178.9	n.d.	3.52743	9.37E+14
John_Klein_RP2	45.4		11.5	19.6	8.2	6.3	3.0	12.3	n.d.	98.8	n.d.	3.54415	7.59E+14
John_Klein_RP3	45.8	1.0	7.6	19.2	11.7	4.0	2.4	10.7	n.d.	110.3	n.d.	2.98539	9.24E+14
John_Klein_RP3	47.0	1.1	12.4	18.5	7.0	6.3	3.4	9.5	18.5	221.6	n.d.	2.98539	9.61E+14
John_Klein_RP3	47.2	1.1	11.8	19.0	7.1	6.6	3.3	9.8	28.3	217.9	n.d.	2.98539	1.06E+15
John_Klein_RP3	42.5	0.7	8.3	19.5	18.8	2.7	2.0	21.9	n.d.	37	n.d.	2.98539	5.89E+14

John_Klein_RP3	48.4	0.6	7.2	18.5	18.5	3.2	1.6	17	n.d.	20	n.d.	2.97858	6.11E+14
John_Klein_RP3	49.4	0.6	6.9	19.0	17.4	2.3	2.7	17.1	n.d.	70	n.d.	2.97858	7.70E+14
John_Klein_RP3	35.3	0.8	7.5	15.6	5.9	16.5	1.7	n.d.	n.d.	211.3	n.d.	2.97858	7.68E+14
John_Klein_RP3	47.8	0.9	11.4	17.8	7.6	6.8	3.3	9	9	130.1	n.d.	2.97858	7.29E+14
John_Klein_RP3	47.8	1.0	11.2	18.6	7.2	6.4	3.3	8.9	n.d.	123.4	n.d.	2.99912	7.50E+14
Drilltailings	48.0	1.1	9.4	20.2	8.7	4.6	3.0	8.8	n.d.	101.4	n.d.	2.48239	4.97E+14
Drilltailings	48.3	0.9	8.6	19.8	9.6	5.3	2.8	9.1	50.2	88.4	n.d.	2.48239	5.12E+14
Drilltailings	49.3	0.9	7.9	20.1	13.4	2.5	2.7	10.2	n.d.	99.1	n.d.	2.48239	5.33E+14
Drill Hole													
Drillhole_CCAM	46.0	1.0	9.0	18.8	9.1	5.9	2.9	11.4	30.5	79	n.d.	2.4818	4.15E+14
Drillhole_CCAM	47.0	1.1	9.4	19.6	8.7	5.2	2.9	9.1	n.d.	128	n.d.	2.4818	4.39E+14
Drillhole_CCAM	46.2	1.0	9.2	19.6	8.4	5.3	3.2	7	n.d.	91.5	n.d.	2.47825	4.07E+14
Drillhole_CCAM	45.3	1.2	8.8	20.2	8.3	5.1	3.0	8.7	40.4	118.9	n.d.	2.47825	4.51E+14
Drillhole_CCAM	45.9	1.1	9.6	19.4	8.2	5.2	3.2	6.8	30.2	97.4	n.d.	2.47353	4.10E+14
Drillhole_CCAM	47.4	1.0	10.0	19.3	9.0	5.3	2.9	6.2	n.d.	98.2	n.d.	2.47353	4.39E+14
Drillhole_CCAM	38.8	0.7	5.5	17.6	9.2	13.6	1.4	11.5	n.d.	66	n.d.	2.46942	3.89E+14
Drillhole_CCAM	45.2	0.9	8.4	20.0	9.0	6.2	2.2	9.7	n.d.	85.5	n.d.	2.46942	4.72E+14
Drillhole_CCAM	38.3	0.7	7.0	16.3	6.6	13.6	1.2	8.7	n.d.	102.1	n.d.	2.46942	3.76E+14
Drillhole_CCAM	44.4	0.7	8.3	18.7	9.1	5.9	2.0	8.1	n.d.	52.1	n.d.	2.48595	2.78E+14
Tailings													
Drilltailings	47.7	0.8	8.3	19.5	9.2	5.9	2.1	10.8	n.d.	92.9	n.d.	2.46883	4.14E+14
Drilltailings	46.7	0.8	8.5	19.3	9.0	5.7	1.8	12.3	n.d.	88.9	n.d.	2.46883	3.54E+14
Drilltailings	47.0	0.8	9.0	19.4	9.1	5.5	2.1	8	n.d.	82.1	n.d.	2.46883	4.10E+14
Drilltailings	45.8	0.8	8.8	19.0	9.2	5.5	2.0	8.4	n.d.	90.5	n.d.	2.47707	4.18E+14
Drilltailings	45.6	0.8	7.5	19.0	9.8	5.2	1.9	6.1	26.9	93.4	n.d.	2.47707	3.54E+14
Drilltailings	46.3	0.8	8.6	19.3	8.7	6.0	2.0	8	n.d.	96.1	n.d.	2.47707	3.59E+14
Drilltailings	45.2	0.9	8.0	19.2	8.9	6.6	1.9	14.5	n.d.	89.8	n.d.	2.47589	3.44E+14
Drilltailings_2	47.5	0.7	8.6	18.0	9.3	5.8	2.0	7.4	n.d.	88.9	n.d.	2.48298	4.40E+14
Drilltailings_2	47.8	0.8	8.8	18.4	9.3	5.6	2.1	8.8	n.d.	113.2	n.d.	2.48298	4.45E+14
Drilltailings_2	48.1	0.8	8.9	18.3	8.9	5.5	2.3	4.7	n.d.	104	n.d.	2.48298	4.29E+14

Drilltailings_2	48.2	0.8	8.3	18.7	9.5	5.4	2.1	10.1	n.d.	94.7	n.d.	2.48298	4.40E+14
Drilltailings_2	48.4	0.8	8.2	18.4	9.0	5.1	2.0	9.8	n.d.	94	n.d.	2.47353	3.57E+14
Drill_Tailings	48.7	0.8	9.2	19.3	9.0	5.8	2.2	4.3	n.d.	68.8	n.d.	2.49191	3.44E+14
Drill_Tailings	46.3	0.8	8.7	19.0	9.4	5.6	2.1	9.3	n.d.	84.5	n.d.	2.49191	3.65E+14
Drill_Tailings	47.1	0.8	9.1	19.0	8.8	5.9	2.2	9.4	44.8	97.7	n.d.	2.49191	3.77E+14
Drill_Tailings	47.6	0.8	9.2	19.0	9.2	5.6	2.1	8.7	n.d.	101.5	n.d.	2.49191	3.69E+14
Drill_Tailings	46.6	0.8	9.0	18.9	9.0	6.0	2.1	10.3	40	79.2	n.d.	2.48952	2.85E+14
Dump Pile													
DumpPile	44.8	0.9	8.9	19.2	8.3	7.2	1.9	n.d.	n.d.	n.d.	n.d.	2.48655	6.24E+14
DumpPile	45.6	0.8	8.5	18.7	8.5	7.1	1.9	n.d.	n.d.	n.d.	n.d.	2.48655	4.16E+14
DumpPile	44.5	0.8	9.8	18.8	8.0	7.8	2.1	n.d.	n.d.	n.d.	n.d.	2.48655	3.52E+14
DumpPile	44.2	0.8	9.0	19.7	7.7	7.4	2.1	n.d.	n.d.	n.d.	n.d.	2.48655	2.83E+14
DumpPile	45.1	0.8	9.0	19.5	8.3	6.9	2.1	n.d.	n.d.	n.d.	n.d.	2.48417	2.73E+14
DumpPile	45.1	0.8	8.5	18.6	8.2	7.4	1.8	n.d.	n.d.	n.d.	n.d.	2.48417	1.91E+14
DumpPile	45.5	0.8	9.1	19.2	7.8	7.3	2.2	n.d.	n.d.	n.d.	n.d.	2.48417	1.78E+14
DumpPile	45.0	0.9	8.9	19.2	7.9	7.3	2.1	n.d.	n.d.	n.d.	n.d.	2.48417	1.86E+14
DumpPile	46.3	0.8	9.0	19.0	8.4	7.2	2.0	n.d.	n.d.	n.d.	n.d.	2.48417	1.81E+14
DumpPile	46.3	0.8	9.3	19.6	7.9	7.2	2.2	n.d.	n.d.	n.d.	n.d.	2.48417	1.90E+14

Cumberland

Target	SiO_2	TiO_2	Al_2O_3	FeO_T	MgO	CaO	Na_2O	Li ppm	Rb ppm	Sr ppm	Ba ppm	Spectrum Total
Surface												
Cumberland	47.6	1.1	10.8	19.4	7.3	5.8	3.2	8.2	41.3	126.7	n.d.	5.53E+14
Cumberland	47.8	1.0	8.6	18.8	9.0	5.0	3.0	7.3	n.d.	62.5	n.d.	3.93E+14
Cumberland	46.7	1.0	9.1	18.9	8.3	6.1	3.0	6.9	n.d.	84.5	n.d.	4.97E+14
Cumberland	44.6	1.0	9.8	18.6	8.5	6.8	2.8	11	n.d.	79.4	n.d.	4.45E+14

Cumberland	45.7	1.2	10.9	19.9	7.4	5.6	3.1	9.4	n.d.	130.2	n.d.	5.13E+14
Cumberland	48.4	1.0	9.7	19.9	8.3	5.3	3.1	7.8	n.d.	102.4	n.d.	5.16E+14
Cumberland	48.4	1.1	10.2	20.0	7.4	5.3	3.2	7.2	n.d.	121.5	n.d.	5.04E+14
Cumberland	49.5	0.9	8.0	20.4	11.4	3.2	3.5	8.3	n.d.	n.d.	n.d.	4.86E+14
Cumberland	48.9	1.0	9.3	19.8	10.2	5.0	2.8	8.3	36.3	95.7	n.d.	4.79E+14
Cumberland	47.5	1.0	11.4	19.4	6.6	7.1	3.2	10.1	36.3	138.7	n.d.	5.31E+14
Cumberland	51.6	0.9	8.2	19.9	11.3	3.7	3.5	10.8	1.3	60.5	n.d.	4.23E+14
Cumberland	47.0	1.1	11.0	19.6	7.1	5.9	3.1	7.2	4.8	121.5	n.d.	4.89E+14
Cumberland	47.5	1.1	10.4	20.1	7.7	5.3	3.2	8.9	46.2	108	n.d.	4.29E+14
Cumberland	50.2	0.9	8.2	20.1	12.5	3.7	2.4	7.5	8.4	75.7	n.d.	4.51E+14
Cumberland	46.7	1.1	10.7	20.1	8.2	5.2	2.9	11.9	n.d.	104.2	n.d.	5.06E+14
Cumberland	47.3	1.1	11.1	19.8	7.1	6.2	3.1	9.6	32.4	133.8	n.d.	5.37E+14
Cumberland_CCAM	48.3	1.1	10.7	20.3	7.1	5.7	3.3	10	n.d.	108.7	n.d.	4.40E+14
Cumberland_CCAM	48.4	1.0	10.0	19.2	8.3	5.2	3.2	10.9	n.d.	85.1	n.d.	3.66E+14
Cumberland_CCAM	47.5	1.1	11.5	20.1	7.3	6.4	3.2	11.4	n.d.	129.1	n.d.	4.78E+14
Cumberland_CCAM	46.8	1.1	11.8	20.4	7.8	6.2	3.1	18.7	n.d.	100.2	n.d.	4.21E+14
Cumberland_CCAM	47.7	1.1	11.3	21.3	7.3	5.6	3.2	10.1	n.d.	100.9	n.d.	3.17E+14
Cumberland_Bowl	49.4	1.1	11.1	19.0	6.6	5.1	3.1	9	112.4	166.1	n.d.	4.71E+14
Cumberland_Bowl	45.0	0.8	7.8	17.6	16.7	3.8	2.1	8.8	n.d.	73.2	n.d.	4.70E+14
Cumberland_Bowl	3.4	0.2	0.5	5.4	2.2	29.8	0.1	5.9	n.d.	211.5	n.d.	3.85E+14
Cumberland_Bowl	44.8	1.0	9.6	19.5	9.0	5.1	2.7	8.4	46	109.8	n.d.	4.88E+14
Cumberland_Bowl	44.7	0.9	9.0	18.1	13.9	4.8	2.5	10.3	32.5	99.4	n.d.	5.13E+14
Cumberland_Bowl	47.9	0.9	10.0	19.3	8.6	4.9	3.0	10.2	30.8	123.6	n.d.	4.81E+14
Cumberland_Bowl	47.0	1.0	8.6	19.2	7.7	6.6	2.7	14	118.2	81.1	n.d.	4.71E+14
Cumberland_Bowl	43.4	0.8	8.3	18.5	16.3	4.5	2.4	8.7	n.d.	101.2	n.d.	5.45E+14
Cumberland_Bowl	50.3	0.9	8.5	20.3	10.0	3.7	3.7	14.7	34	89.5	n.d.	4.87E+14
Cumberland3	40.0	0.8	6.6	17.1	6.2	14.8	1.6	17.5	n.d.	101	n.d.	5.64E+14
Cumberland3	48.9	0.8	7.6	18.1	8.3	8.0	2.8	13.1	n.d.	95.1	n.d.	3.80E+14
Cumberland3	2.2	0.0	0.4	0.8	1.3	35.0	0.3	6.4	n.d.	372.1	n.d.	3.40E+14
Cumberland3	42.7	0.9	8.5	18.2	16.6	4.4	2.3	9.1	n.d.	101.2	n.d.	5.74E+14

Cumberland3	47.2	0.9	7.9	20.0	10.1	5.7	2.7	15	22.5	70.1	n.d.	4.95E+14
Cumberland3	45.0	1.1	9.3	21.4	7.5	4.9	2.6	10.2	n.d.	100.8	n.d.	6.09E+14
Cumberland3	45.8	1.1	10.0	20.2	7.2	6.1	2.8	11.9	63.9	140.3	n.d.	5.83E+14
Cumberland3	47.4	0.9	7.8	20.1	9.8	4.5	2.9	10.1	n.d.	75.4	n.d.	4.89E+14
Cumberland3	26.0	0.6	4.8	10.5	4.0	25.5	0.9	8.4	n.d.	102.2	n.d.	5.05E+14
CumberlandNew_RP	46.8	1.1	9.7	20.2	7.0	5.3	3.2	8.4	56.2	96.7	n.d.	4.93E+14
CumberlandNew_RP	46.8	1.2	10.1	20.7	6.6	5.4	3.0	8.1	39.2	166.2	n.d.	5.78E+14
CumberlandNew_RP	46.9	1.1	9.3	20.5	7.7	5.1	2.9	8.3	38.2	106.9	n.d.	5.05E+14
CumberlandNew_RP	47.0	1.1	11.1	19.8	6.7	5.9	3.1	8	41.8	123.7	n.d.	4.65E+14
CumberlandNew_RP	49.2	1.0	8.7	20.2	9.2	4.5	3.8	9.4	31.1	105.7	n.d.	4.25E+14
CumberlandNew_RP	45.4	1.2	10.1	20.9	6.9	5.7	3.0	10.8	40	135.7	n.d.	5.17E+14
CumberlandNew_RP	45.8	1.3	10.0	21.1	6.6	5.2	3.2	9.3	45.4	127.2	n.d.	5.11E+14
CumberlandNew_RP	46.6	1.3	10.6	20.9	6.0	5.0	3.0	7.6	55.5	147.4	n.d.	4.85E+14
CumberlandNew_RP	45.8	1.2	10.0	21.7	7.2	5.4	2.9	7.4	32.6	142.6	n.d.	5.44E+14
CumberlandNew_RP	46.9	1.0	10.1	20.1	8.1	5.6	2.9	7	34.2	108.5	n.d.	3.97E+14
CumberlandNew_RP	46.3	1.2	9.8	21.0	6.6	5.6	2.9	6.9	38.6	123.1	n.d.	5.30E+14
CumberlandNew_RP	45.9	1.2	9.7	21.0	7.1	5.1	2.8	7.8	n.d.	139.4	n.d.	5.81E+14
CumberlandNew_RP	45.2	1.0	8.2	20.7	8.7	5.4	2.8	7.2	n.d.	70.1	n.d.	4.45E+14
CumberlandNew_RP	46.5	1.1	9.1	20.5	7.5	6.0	2.9	7.2	n.d.	94.8	n.d.	5.13E+14
CumberlandNew_RP	46.9	1.1	10.6	21.0	6.8	5.6	2.8	8	n.d.	93.6	n.d.	4.24E+14
CumberlandNew_RP	46.8	1.1	10.0	20.4	6.9	6.2	2.7	6.6	31.2	146.6	n.d.	5.10E+14
Cumberland_DRT_RP	48.0	0.9	7.6	19.7	10.8	4.2	2.9	9.3	6.9	86.6	n.d.	5.42E+14
Cumberland_DRT_RP	48.3	1.0	10.8	18.4	6.9	5.1	3.6	9.8	44.5	103.8	n.d.	3.78E+14
Cumberland_DRT_RP	46.7	1.1	9.2	19.4	8.3	4.9	3.0	8.8	79.3	123.5	n.d.	5.81E+14
Cumberland_DRT_RP	48.8	1.0	10.5	18.9	7.7	5.5	3.1	9.3	84.2	140.2	n.d.	4.26E+14
Cumberland_DRT_RP	48.2	1.2	9.9	19.3	7.7	5.1	3.1	10.2	97.3	103.6	n.d.	3.92E+14
Cumberland_DRT_RP	48.3	1.0	10.8	19.5	7.3	5.8	3.0	9	104.5	145.8	n.d.	4.59E+14
Cumberland_DRT_RP	46.6	1.3	10.0	21.4	6.6	4.6	3.2	10.9	35.7	96.2	n.d.	3.92E+14
Cumberland_DRT_RP	48.0	1.2	10.3	21.3	7.0	5.0	3.0	13.1	n.d.	101.8	n.d.	4.07E+14
Cumberland_DRT_RP	48.4	1.0	10.2	18.3	8.1	5.6	3.0	11.2	23.7	118	n.d.	3.96E+14

Cumberland3_ccam	46.6	1.0	10.1	19.4	7.2	5.7	3.0	9.9	41.4	128.5	n.d.	5.23E+14
Cumberland3_ccam	18.0	0.5	4.2	11.5	2.9	27.2	0.8	4.9	24.2	192.3	n.d.	2.93E+14
Cumberland3_ccam	48.0	1.0	12.4	19.1	6.3	6.1	3.2	10.1	39.9	175.7	n.d.	4.75E+14
Cumberland3_ccam	46.1	1.2	10.0	20.6	6.9	5.8	2.8	9.6	36.7	175.7	n.d.	5.94E+14
Cumberland3_ccam	48.3	1.0	10.5	19.2	7.0	6.0	3.4	11.2	45.5	124.6	n.d.	4.42E+14
Cumberland3_ccam	47.5	1.1	11.2	20.2	6.5	6.4	3.1	11.7	34.8	168.4	n.d.	5.38E+14
Cumberland3_ccam	45.1	0.9	8.1	21.0	12.3	4.9	2.4	12	n.d.	97.7	n.d.	5.53E+14
Cumberland3_ccam	46.9	0.9	10.2	18.5	8.1	6.2	2.8	10.3	n.d.	124.6	n.d.	3.93E+14
Cumberland3_ccam	47.4	0.9	9.6	20.1	8.5	4.9	3.2	10.8	29.7	120.9	n.d.	5.27E+14
Drill Hole												
Cumberland_Hole	46.8	1.0	9.1	20.3	8.3	6.0	2.6	7.2	n.d.	83.1	n.d.	3.89E+14
Cumberland_Hole	47.1	0.9	9.3	20.0	8.3	5.6	2.9	8.1	28.3	89.7	n.d.	3.74E+14
Cumberland_Hole	46.6	1.0	8.8	20.4	8.5	5.2	3.0	7.8	n.d.	85.2	n.d.	3.58E+14
Cumberland_Hole	44.4	1.1	9.2	21.2	7.7	5.9	2.9	11	n.d.	80.3	n.d.	3.63E+14
Tailings												
CumberlandNew_RP	48.9	0.8	9.2	19.3	9.1	4.8	2.2	6.7	8.8	101	n.d.	4.39E+14
CumberlandNew_RP	47.2	0.8	8.9	19.4	8.3	5.5	2.2	5.5	n.d.	78.1	n.d.	3.13E+14
CumberlandNew_RP	47.9	0.8	9.2	20.0	8.2	5.8	2.1	5.4	n.d.	96.4	n.d.	3.59E+14
CumberlandNew_RP	47.5	0.8	9.2	19.9	8.2	4.9	2.1	5.5	n.d.	70	n.d.	3.15E+14
CumberlandNew_RP	46.8	0.7	9.4	19.6	8.3	5.5	2.1	8.3	n.d.	87	n.d.	2.77E+14
CumberlandNew_RP	47.1	0.7	9.4	19.8	8.4	5.2	2.1	8.1	n.d.	73	n.d.	3.16E+14
CumberlandNew_RP	47.1	0.7	9.1	20.0	8.2	5.4	2.2	11.2	n.d.	86.8	n.d.	3.14E+14
CumberlandNew_RP	48.4	0.7	9.6	19.2	8.2	5.8	2.3	12.6	n.d.	92.9	n.d.	5.17E+14
CumberlandNew_RP	49.6	0.8	9.8	20.2	9.0	5.0	2.2	7.2	n.d.	80.2	n.d.	5.07E+14
CumberlandNew_RP	49.1	0.8	9.7	19.6	8.2	5.0	2.4	6.2	28.6	119.1	n.d.	5.88E+13
CumberlandNew_RP_LL	47.6	0.8	9.1	18.7	9.0	6.0	2.0	7.6	n.d.	117.5	n.d.	1.98E+14
CumberlandNew_RP_LL	47.9	0.7	9.1	18.6	8.5	5.1	2.1	8.9	n.d.	105.3	n.d.	3.65E+14
CumberlandNew_RP_LL	47.3	0.8	9.0	18.8	8.5	5.1	2.0	4.5	n.d.	91.4	n.d.	3.80E+14
CumberlandNew_RP_LL	48.1	0.8	8.4	19.0	8.6	4.7	2.0	5.3	n.d.	114.8	n.d.	3.64E+14
CumberlandNew_RP_LL	49.3	0.8	9.2	19.2	8.7	5.3	2.1	6.5	35.7	125.6	n.d.	3.43E+14

CumberlandNew_RP_LL	47.3	0.7	8.9	19.0	8.5	5.2	2.1	11.7	n.d.	146.1	n.d.	3.83E+14
Dump Pile												
Dump_Pile	46.0	0.8	8.8	19.1	7.8	6.3	2.1	12	n.d.	70.1	n.d.	4.18E+14
Dump_Pile	45.1	0.8	8.8	19.7	7.9	6.2	2.2	10.2	7.1	79.8	n.d.	2.67E+14
Dump_Pile	45.4	0.8	9.4	20.9	7.0	5.6	2.6	6.7	42.6	29.2	n.d.	3.41E+14
Dump_Pile	47.0	0.8	10.1	21.0	6.6	6.1	2.9	31.9	69.6	14.7	n.d.	1.24E+14
Dump_Pile	46.9	0.8	10.3	21.4	6.3	6.2	3.2	8.6	n.d.	10.2	n.d.	2.82E+14
Dump_Pile	44.0	0.9	8.0	19.1	8.0	6.0	1.9	6.8	n.d.	n.d.	n.d.	9.32E+14
Dump_Pile	45.2	0.8	8.6	19.6	8.2	6.0	2.0	24.6	95.6	31.3	n.d.	5.45E+14
Dump_Pile	44.1	0.9	8.7	19.9	7.9	6.2	2.0	13	40.9	25.2	n.d.	7.46E+14
Dump_Pile	44.0	1.0	8.7	20.3	7.7	6.2	2.2	10.1	35.5	97.5	n.d.	8.00E+14
Dump_Pile	42.5	1.0	8.5	22.0	7.1	5.7	2.4	9	n.d.	2.4	n.d.	4.95E+14
Dump_Pile	45.1	0.9	7.8	18.8	8.9	5.8	1.8	8.4	n.d.	148.5	n.d.	7.91E+14
Dump_Pile	44.6	0.8	8.5	18.9	8.2	5.9	1.8	9.3	n.d.	267.5	n.d.	1.03E+15
Dump_Pile	45.9	0.8	8.6	19.5	8.7	5.9	1.9	6.5	n.d.	193.2	n.d.	8.91E+14
Dump_Pile	45.6	0.9	8.9	20.0	8.2	6.3	2.0	8.5	n.d.	113.3	n.d.	8.71E+14
Dump_Pile	46.4	0.8	9.5	20.9	7.6	5.9	2.4	8.6	n.d.	4.4	n.d.	7.50E+14

Windjana

Target	SiO_2	TiO_2	Al_2O_3	FeO_T	MgO	CaO	Na_2O	Li ppm	Rb ppm	Sr ppm	Ba ppm	Distance m	Spectrum Total
Surface													
Windjana	46.6	0.9	7.3	17.3	9.5	5.0	1.2	6.9	90	322.9	n.d.	2.40596	6.30E+14
Windjana	44.5	0.9	7.7	17.8	9.8	4.7	1.2	7.6	92.1	425.8	n.d.	2.40596	7.99E+14
Windjana	45.8	0.8	7.4	17.3	9.2	5.2	1.2	7.4	78.3	370.6	n.d.	2.40596	6.22E+14
Windjana	44.8	0.8	7.0	17.5	10.7	5.2	1.5	7.2	70.1	450.1	n.d.	2.40596	7.06E+14
Windjana	43.0	0.9	7.9	17.7	11.2	4.9	1.4	8.7	96	478.6	n.d.	2.40596	8.17E+14
Windjana	44.6	0.9	7.3	17.8	9.4	4.6	1.3	7.3	92.3	378.2	n.d.	2.42053	7.47E+14
Windjana	45.0	0.9	7.9	17.5	9.3	5.1	1.2	5.4	99.3	475.7	n.d.	2.42053	7.54E+14
Windjana	41.4	0.8	7.2	20.4	9.7	4.8	1.4	7	100	379.3	n.d.	2.42053	9.09E+14

Windjana	42.1	0.8	6.8	19.0	10.4	4.1	1.3	7.3	80.3	330.5	n.d.	2.42053	7.78E+14
Windjana	45.7	0.9	7.7	18.4	8.1	4.7	1.5	7.5	84.7	326.5	n.d.	2.42053	6.77E+14
Windjana	45.1	0.9	7.3	17.9	8.4	4.9	1.3	7.1	87	313.5	n.d.	2.42845	5.95E+14
Windjana	45.3	0.9	7.5	17.7	10.4	4.9	1.3	6.7	82.1	398.4	n.d.	2.42845	6.64E+14
Windjana	45.9	0.9	7.2	17.7	9.6	4.7	1.2	6.1	80.6	317.3	n.d.	2.42845	5.98E+14
Windjana	42.6	0.9	7.7	19.0	9.9	4.8	1.3	8	104.7	460.4	n.d.	2.42845	8.55E+14
Windjana	44.9	0.8	7.1	17.8	9.7	4.7	1.3	8.9	96.2	388.5	n.d.	2.42845	6.44E+14
Windjana	44.9	0.8	7.6	18.4	9.3	4.4	1.3	8.1	95	316.9	n.d.	2.43928	6.67E+14
Windjana	45.6	0.9	7.1	17.9	8.9	4.7	1.2	7.1	113.3	425.1	n.d.	2.43928	7.31E+14
Windjana	44.9	0.9	7.4	18.2	8.8	4.9	1.3	7.5	99.9	375.1	n.d.	2.43928	6.85E+14
Windjana	46.2	0.9	7.1	17.2	9.4	4.7	1.2	8.1	94.2	261.2	n.d.	2.43928	5.76E+14
Windjana	46.2	0.9	7.0	17.6	9.9	4.7	1.2	6.5	89.3	343.9	n.d.	2.43928	6.49E+14
Windjana	45.6	0.9	7.5	17.6	10.0	4.9	1.3	6.6	101.8	417.1	n.d.	2.44905	7.10E+14
Windjana	43.5	0.9	7.2	18.4	10.0	4.3	1.3	6.6	97.1	409.2	n.d.	2.44905	7.60E+14
Windjana	44.2	0.9	7.8	18.5	9.3	5.1	1.3	7.8	101.8	497.4	97	2.44905	8.17E+14
Windjana	45.4	0.9	7.7	17.8	10.1	4.8	1.4	6.4	91.3	444.1	n.d.	2.44905	6.96E+14
Windjana	44.8	0.9	6.8	18.6	9.5	4.8	1.2	8.3	89.3	330.2	n.d.	2.44905	6.56E+14
Windjana_drill _tailings	45.6	0.8	7.5	17.4	9.6	5.1	1.2	5.7	100.8	437.5	n.d.	2.46942	7.29E+14
Drill Hole													
Windjana_Mini_ Drill_Vertical	41.3	0.6	7.5	21.1	8.5	3.7	1.2	9.7	72.4	172.3	n.d.	2.38114	1.25E+14
Windjana_Mini_ Drill_Vertical	42.4	0.6	8.3	24.9	7.8	4.1	1.5	6.2	96.5	129.4	n.d.	2.38114	1.24E+14
Windjana_Mini_ Drill_Vertical	40.0	0.8	7.2	20.1	9.7	4.4	1.1	8.5	153.1	238.6	n.d.	2.39376	4.31E+14
Windjana_Mini_ Drill_Vertical	41.6	0.8	7.5	18.4	9.3	4.7	1.2	9	81.8	251	n.d.	2.39541	5.40E+14
Windjana_Mini_ Drill_Vertical	40.7	0.8	6.9	18.7	9.3	4.4	1.2	8.2	84.2	212.7	n.d.	2.39541	5.41E+14

Windjana_Mini_ Drill_Vertical	44.8	0.9	7.1	17.5	9.4	4.6	1.3	8.2	91.2	321.4	n.d.	2.39597	6.02E+14
Windjana_Mini_ Drill_Vertical	44.5	0.8	8.1	18.9	8.5	5.3	1.3	8.3	65.2	489.9	81.1	2.39597	6.04E+14
Windjana_Mini_ Drill_Vertical	43.3	0.7	7.7	19.4	8.8	4.6	1.1	6.5	106.6	225.4	n.d.	2.39597	3.59E+14
Windjana_Mini_ Drill_Horizontal	40.3	0.8	7.4	21.2	8.4	4.0	1.4	9	90.6	268	n.d.	2.37406	5.19E+14
Windjana_Mini_ Drill_Horizontal	41.3	0.7	7.6	20.6	8.9	4.1	1.2	7.1	50.1	246.9	60.8	2.37406	3.92E+14
Windjana_Mini_ Drill_Horizontal	40.9	0.7	7.4	20.1	8.6	4.3	1.2	7.7	53.3	246.7	n.d.	2.37406	4.36E+14
Windjana_Mini_ Drill_Horizontal	40.7	0.7	7.2	19.7	8.9	4.1	1.1	5.6	46.3	n.d.	68.6	2.37406	4.05E+14
Windjana_Mini_ Drill_Horizontal	41.2	0.7	6.9	20.0	9.1	3.9	1.0	6	176.8	228.8	n.d.	2.37406	3.89E+14
Windjana_Mini_ Drill_Horizontal	40.1	0.7	7.2	20.1	8.6	4.2	1.3	11.2	131.7	147.2	59.7	2.37406	3.10E+14
Windjana_Mini_ Drill_Horizontal	40.7	0.7	7.3	19.9	8.4	4.1	1.2	5.6	51.3	205.7	n.d.	2.37406	3.56E+14
Windjana_Mini_ Drill_Horizontal	39.9	0.6	7.2	21.0	8.6	4.0	1.4	7.1	44.6	137	n.d.	2.37406	3.10E+14
Windjana_drill _Hole_RMI	41.9	0.9	7.6	18.8	9.8	4.9	1.1	10.2	103.3	349.8	n.d.	2.42109	6.33E+14
Windjana_drill _Hole_RMI	40.6	0.8	7.1	18.7	11.4	4.5	1.3	8.6	92.8	317.9	n.d.	2.42109	6.46E+14
Windjana_drill _Hole_RMI	42.3	0.9	7.4	19.1	10.0	4.7	1.3	10	98.5	335.7	n.d.	2.42618	6.72E+14
Windjana_drill _Hole_RMI	43.3	0.9	7.3	18.5	10.0	4.9	1.3	8.4	96	353	n.d.	2.42618	6.06E+14

Windjana_drill_Hole_RMI	42.0	0.8	6.9	19.2	10.2	4.2	1.3	8.6	90.4	254.5	n.d.	2.41884	5.86E+14
Windjana_drill_Hole_RMI	43.6	0.9	7.0	19.1	8.4	4.4	1.2	8.3	110.2	346.9	n.d.	2.41884	6.03E+14
Windjana_drill_Hole_RMI	43.1	0.9	7.1	18.9	8.8	4.4	1.3	7.4	130.2	337.6	n.d.	2.4149	6.81E+14
Windjana_drill_Hole_RMI	44.0	0.8	7.8	18.7	9.7	4.7	1.1	6.3	75.5	391.4	n.d.	2.4149	6.63E+14
Windjana_drill_Hole_RMI	43.3	0.8	7.2	18.5	9.8	4.6	1.0	4.2	65	230.5	n.d.	2.41154	4.45E+14
Windjana_drill_Hole_RMI	42.5	0.8	7.6	19.4	9.2	4.5	1.1	6.8	148	248.9	n.d.	2.41154	4.94E+14
Tailings													
Windjana_drill_tailings	46.2	0.8	7.0	17.9	9.4	5.0	1.3	8.1	95.7	352.9	67.9	2.46942	6.19E+14
Windjana_drill_tailings	45.0	0.8	7.2	18.3	9.5	4.4	1.3	7.7	109.7	321.4	n.d.	2.46942	6.90E+14
Windjana_drill_tailings	44.9	0.8	6.8	17.9	9.8	4.6	1.3	5.5	85.2	320.5	n.d.	2.46942	6.63E+14
Windjana_drill_tailings	44.9	0.8	7.4	17.7	9.4	4.7	1.4	7.7	93.4	356	n.d.	2.46942	7.11E+14
Windjana_drill_tailings	45.5	0.9	7.7	18.0	10.2	4.7	1.2	9.3	88.2	372.6	n.d.	2.46942	7.20E+14
Windjana_drill_tailings	45.3	0.9	7.4	18.6	9.3	4.9	1.2	5.4	93.2	351.1	n.d.	2.47	7.46E+14
Windjana_drill_tailings	45.5	0.9	7.6	18.4	9.2	4.7	1.2	7.8	95.3	409.1	n.d.	2.47	7.32E+14
Windjana_drill_tailings	45.5	0.9	7.6	18.0	9.0	4.8	1.2	8.1	95.8	350.6	n.d.	2.47	7.03E+14
Windjana_drill	45.9	0.8	7.1	17.5	9.4	5.0	1.2	5	86.5	330.2	n.d.	2.47	6.27E+14

_tailings													
Windjana_drill _tailings2	43.2	0.7	7.1	20.2	9.1	3.6	1.1	10.3	56.7	230.5	n.d.	2.40707	4.28E+14
Windjana_drill _tailings2	45.1	0.8	7.7	19.9	10.5	4.7	1.1	7.5	n.d.	375.4	n.d.	2.40707	4.01E+14
Windjana_drill _tailings2	43.8	0.7	7.6	19.9	9.4	3.4	1.0	7.1	127.7	213.1	n.d.	2.40707	4.12E+14
Windjana_drill _tailings2	44.0	0.7	7.9	19.6	10.0	3.5	1.0	9.3	62.2	378.6	n.d.	2.42109	5.75E+14
Windjana_drill _tailings2	43.6	0.7	7.8	19.1	9.2	4.1	1.1	5.3	63.1	183.9	n.d.	2.42109	6.17E+14
Windjana_drill _tailings2	42.7	0.7	7.4	18.8	9.1	4.6	1.3	9.5	115.4	397.9	84.3	2.41603	5.69E+14
Windjana_drill _tailings2	42.7	0.8	7.6	19.6	8.7	4.8	1.2	8.1	84.7	447.3	n.d.	2.41434	6.94E+14
Windjana_drill _tailings2	41.5	0.8	6.6	18.3	10.1	4.3	1.2	7.8	70.2	364.1	n.d.	2.41434	6.32E+14
Windjana_drill _tailings2	41.4	0.7	7.2	20.1	9.4	3.7	1.0	8.4	66.5	391	n.d.	2.41434	5.55E+14
Dump Pile													
sol00704_Windjana _dump_pile	42.3	0.7	6.9	19.9	10.2	3.6	1.1	8	151.4	165.5	n.d.	2.2613	4.06E+14
sol00704_Windjana _dump_pile	43.7	0.7	6.9	19.8	10.2	3.8	1.2	10.5	57.1	135.4	n.d.	2.2613	4.19E+14
sol00704_Windjana _dump_pile	37.0	0.6	6.3	19.8	10.8	4.2	1.1	5.4	50.1	123.4	n.d.	2.2613	3.46E+14
sol00704_Windjana _dump_pile	42.2	0.7	6.7	20.0	10.4	3.6	1.1	8.9	n.d.	175.3	n.d.	2.26278	4.19E+14
sol00704_Windjana _dump_pile	43.7	0.7	6.1	19.5	9.7	3.2	1.2	7.6	51.6	169.8	n.d.	2.26278	4.33E+14

sol00704_Windjana_dump_pile	39.5	0.6	7.3	21.2	10.1	4.7	1.4	8.9	62.4	125.8	n.d.	2.26278	2.61E+14
sol00704_Windjana_dump_pile	43.2	0.7	6.9	20.2	9.6	3.7	1.2	7.6	49	158.4	n.d.	2.2613	4.35E+14
sol00704_Windjana_dump_pile	43.4	0.7	7.1	20.5	9.8	3.7	1.3	5.8	61.4	186	n.d.	2.2613	4.67E+14
sol00704_Windjana_dump_pile	37.4	0.6	7.8	25.5	11.5	4.9	1.2	n.d.	66	83.2	n.d.	2.2613	1.17E+14

Confidence Hills

Target	SiO_2	TiO_2	Al_2O_3	FeO_T	MgO	CaO	Na_2O	Li ppm	Rb ppm	Sr ppm	Ba ppm	Distance m	Spectrum Total
Drill Hole													
Confidence_Hills_Full_Drill_Hole	47.2	0.9	11.8	20.6	3.5	4.4	2.7	11.9	66.2	n.d.	n.d.	2.93089	3.23E+14
Confidence_Hills_Full_Drill_Hole	48.5	1.0	14.6	19.7	3.4	3.3	2.2	9	56.5	185.4	n.d.	2.93089	6.52E+14
Confidence_Hills_Full_Drill_Hole	50.1	1.0	12.4	20.8	3.7	3.7	2.7	11.7	51.5	218.9	n.d.	2.92514	6.07E+14
Confidence_Hills_Full_Drill_Hole	52.1	1.0	12.4	19.9	3.7	4.2	2.6	9.8	157.7	188.2	n.d.	2.92514	5.80E+14
Confidence_Hills_Full_Drill_Hole	50.2	1.0	12.5	20.1	3.7	4.6	2.5	9.6	118.7	157.9	n.d.	2.92514	6.29E+14
Confidence_Hills_Full_Drill_Hole	51.1	0.9	12.0	20.4	3.5	3.9	2.8	11.1	114.9	195.5	n.d.	2.92514	6.12E+14
Confidence_Hills_Full_Drill_Hole	48.9	0.9	14.0	20.0	3.6	4.2	2.7	10.3	52.7	135.1	n.d.	2.93007	6.19E+14

Confidence_Hills_ Full_Drill_Hole	48.8	1.0	11.5	19.7	3.7	5.1	3.0	10.8	87.3	145.7	n.d.	2.93007	6.81E+14
Confidence_Hills_ Full_Drill_Hole	50.5	1.0	12.6	20.4	3.7	3.2	3.1	11.4	119.9	165.9	n.d.	2.93007	6.05E+14
Confidence_Hills_ Full_Drill_Hole	48.1	1.0	13.8	17.7	3.2	3.2	2.7	9.1	51.3	150.5	n.d.	2.93007	8.86E+14
Tailings													
Panum	51.0	1.1	10.7	20.3	4.0	3.4	1.8	7.6	13.9	157	n.d.	2.89832	6.46E+14
Panum	52.3	1.1	9.8	20.6	3.7	3.0	1.8	6.2	21.8	162	n.d.	2.89832	6.19E+14
Panum	50.8	1.2	10.9	21.5	3.4	3.4	2.0	10	36.9	121.6	n.d.	2.89832	5.42E+14
Panum	51.0	1.1	10.5	20.4	3.7	3.6	1.9	10.5	65.4	164.1	n.d.	2.90559	6.25E+14
Panum	51.0	1.2	11.2	21.1	3.7	3.5	2.2	10.3	74.7	155	n.d.	2.90559	6.14E+14
Panum	50.3	1.1	10.4	21.2	3.6	3.3	2.0	10.4	n.d.	145.3	n.d.	2.90559	6.01E+14
Panum	50.5	1.2	10.7	21.0	3.7	3.4	1.8	10.4	86.4	165.2	n.d.	2.90559	6.65E+14
Panum	51.3	1.0	9.9	20.3	3.7	3.3	1.9	7.5	37	176.1	n.d.	2.89832	6.27E+14
Panum	52.3	1.1	10.4	20.6	3.6	3.1	2.1	10.2	73.7	252.7	n.d.	2.89832	7.20E+14
Panum	50.0	1.1	10.2	20.7	3.8	3.4	1.8	8.8	62.3	262.2	n.d.	2.89832	7.81E+14
Stovepipe_Wells	43.9	0.9	8.6	19.4	6.2	6.8	1.8	8	n.d.	141.3	n.d.	2.83297	6.65E+14
Stovepipe_Wells	43.8	1.0	8.0	18.8	6.9	6.8	1.7	7.4	25.9	116.4	n.d.	2.83297	5.82E+14

Stovepipe_Wells	43.8	0.9	7.8	19.0	5.9	5.9	1.5	9.5	66.5	166.9	n.d.	2.83297	6.24E+14
Stovepipe_Wells	50.5	1.1	10.4	20.9	4.6	3.7	2.0	7.4	84.4	177.6	n.d.	2.84379	6.41E+14
Stovepipe_Wells	51.6	1.1	10.3	20.5	4.5	3.6	2.0	7.6	58	160.3	n.d.	2.84379	6.40E+14
Stovepipe_Wells	50.9	1.1	10.7	20.4	4.5	3.9	2.0	8.2	65.5	139.8	n.d.	2.84379	6.19E+14
Stovepipe_Wells	49.1	1.0	11.6	19.9	4.3	5.0	2.0	10	80.1	210.8	n.d.	2.84379	6.67E+14
Stovepipe_Wells	51.7	1.1	9.6	21.2	4.2	2.5	2.0	6.2	13.4	154.9	n.d.	2.85391	5.44E+14
Stovepipe_Wells	51.5	1.1	10.7	21.5	4.0	3.0	2.3	12.3	91.9	130.2	n.d.	2.85391	5.97E+14
Stovepipe_Wells	50.7	1.2	10.8	20.9	4.6	3.5	1.9	7.2	58.5	202.9	n.d.	2.85391	8.84E+14
Paoha	44.2	0.9	8.3	18.7	7.6	6.3	1.7	10.7	n.d.	113.7	n.d.	2.83682	5.34E+14
Paoha	44.4	0.9	8.8	19.1	7.4	6.7	1.8	7.1	n.d.	125	n.d.	2.83682	5.94E+14
Paoha	43.3	0.9	8.0	19.2	7.7	6.5	1.6	5.2	n.d.	147.7	n.d.	2.83682	6.77E+14
Paoha	43.0	0.9	8.0	19.4	7.2	6.6	1.7	6.9	n.d.	139.6	n.d.	2.83682	6.75E+14
Paoha	43.0	1.0	8.6	19.4	7.1	6.4	1.8	7	n.d.	106.3	n.d.	2.83682	5.62E+14
Dump Pile													
confidence_hills_postsieve_dump_cc	49.9	1.1	11.5	18.8	5.4	5.1	2.4	10.9	110.4	189.4	n.d.		
confidence_hills_postsieve_dump_cc	49.7	1.0	11.7	21.8	4.3	3.4	2.4	8.6	91	122.3	n.d.		

confidence_hills_ postsieve_dump_cc	47.6	1.0	10.3	21.1	5.1	4.1	1.9	8.9	102	116. 8	n.d.	

Mojave

Target	SiO_2	TiO_2	Al_2O_3	FeO_T	MgO	CaO	Na_2O	Li ppm	Rb ppm	Sr ppm	Ba ppm	Distance m	Spectrum Total
Surface													
Mojave_Bedrock	54.1	0.87	17.5	12.6	4.8	5.1	3.45	18.5	80.8	181.3	-999	2.54186	3.86E+14
Mojave_Bedrock	51.8	0.95	15.5	15.6	4.4	4.9	3.19	15.2	69.3	158.6	-999	2.54186	4.63E+14
Mojave_Bedrock	51.1	0.89	16.9	15.8	4.9	5.9	3.19	16	80.7	248.5	-999	2.54186	5.73E+14
Mojave_Chunks	51.3	0.92	16.5	17.4	4.9	4.3	3.58	19.2	90	212.8	-999	2.53875	5.23E+14
Mojave_Chunks	51.5	0.9	16.8	17.4	4.7	4.8	3.72	19.4	96.7	123.7	-999	2.54996	3.00E+14
Mojave_Chunks	52.9	0.89	17.4	15.4	5	4.9	2.59	13.4	44.6	162.5	-999	2.53257	2.76E+14
Mojave2_FDH_ChemCam	48.1	0.79	13.9	15.9	4.9	7.7	2.76	11.5	36.8	150.7	-999	2.44444	5.38E+14
Mojave2_FDH_ChemCam	51	0.82	16.8	16.5	5	5	3.8	19	-999	244.3	-999	2.43471	5.40E+14
Tailings													
Mojave2_DTa	51.1	0.867	14.2	13.53	5.2	5.467	2.59	15.2	25.5	142.6	-999	2.45079	3.85E+14

	46.9	0.96	13.1	17.4		4.66	2.56			102.		2.4507	
Mojave2_DTa	7	7	3	3	5.7	7	7	11.8	31.9	5	-999	9	4.87E+14
	51.7	0.83	16.2	13.3	4.56	6.96				168.		2.4507	
Mojave2_DTa	3	7	3	3	7	7	3.19	13.6	53.5	3	-999	9	4.31E+14
	50.0	0.89			5.53		2.23			162.			
Mojave2_DTb	3	3	12.4	13.9	3	5.1	3	10.4	-999	2	-999	2.456	3.97E+14
	51.4			14.8	5.33	6.16	3.00			185.			
Mojave2_DTb	3	0.84	15.7	3	3	7	7	10.6	34.3	3	-999	2.456	4.50E+14
	52.5	0.92	11.4	13.4	4.96	3.96	3.17			169.			
Mojave2_DTb	3	7	3	3	7	7	3	14	38.7	6	-999	2.456	3.94E+14
Mojave2_MDH	43.5	0.72	14.5	19.8	4.73		2.77					2.5045	
_ChemCam	3	3	3	7	3	6.8	3	9.4	-999	94.2	-999	2	6.77E+14
Mojave2_MDH	51.8	0.92	16.8	16.1	4.23		3.88		102.	195.		2.5045	
_ChemCam	7	3	7	7	3	4.7	7	15.5	2	4	-999	2	5.14E+14
Mojave2_MDH	50.7	0.83	13.8	15.5		5.03	2.82					2.5105	
_ChemCam	7	7	7	7	4.7	3	7	8.9	35	130	-999	6	4.42E+14
Mojave2_FDH	50.7	0.95				4.13	2.39			142.		2.4398	
_ChemCam	7	7	11.4	15.1	5	3	3	9.4	-999	3	-999	5	4.30E+14
Dump Pile													
Mojave2_presie													
ve	47.4	1.33	11.7		4.53	4.33	1.74						
_dump	3	3	3	19.7	3	3	7	16.7	35.7	73.6	-999	2.4997	2.64E+14
Mojave2_post	53.3	1.00				3.53	3.30					2.6506	
_sieve_dump	3	3	16	15.4	4.8	3	3	16.2	64.5	160	-999	2	4.71E+14
Mojave2_post	53.4		16.3	13.7	4.46	5.66	3.12					2.6506	
_sieve_dump	3	1.02	3	3	7	7	3	15.9	87.9	184	-999	2	4.34E+14
Mojave2_post	54.8		15.1	14.6	4.66	4.23	3.04			213.		2.6506	
_sieve_dump	7	0.91	7	3	7	3	7	12.9	81.9	5	-999	2	4.44E+14

Telegraph Peak

Target	SiO_2	TiO_2	Al_2O_3	FeO_T	MgO	CaO	Na_2O	Li ppm	Rb ppm	Sr ppm	Ba ppm	Distance m	Spectrum Total
Surface													
Telegraph_Peak_ccam	49.4	1.17	12.7	17.9	2.3	6.7	3.16	6.6	68.6	153.2	n.d.	2.479	7.36E+14
Telegraph_Peak_ccam	50.5	1.26	13.4	18.8	2.6	5.1	3.25	7.8	86.5	178.7	n.d.	2.474	6.73E+14
Telegraph_Peak_ccam	54.2	1.17	11.5	19.5	2.7	4.3	3.01	10.1	83.7	118.8	n.d.	2.469	4.84E+14
Drill Hole													
Telegraph_Peak _drill_hole	51.6	1.25	13.5	19.6	3.7	4.1	3.35	6.2	103.8	137.6	241.7	2.29	4.42E+14
Telegraph_Peak _drill_hole	50.7	1.09	13.3	19.9	3.4	4.8	3.59	8.3	81	105.2	n.d.	2.29	4.56E+14
Telegraph_Peak _drill_hole	43.8	1.11	13.2	20.7	4.6	6.9	2.69	9.5	69.5	85.4	n.d.	2.29	4.87E+14
Telegraph_Peak _drill_hole_2	47.6	1.14	11.2	20.7	5	3.5	2.91	8	58.5	63	n.d.	2.293	4.36E+14
Telegraph_Peak _drill_hole_2	46.5	1.11	10.5	20.9	3.4	5.4	3.05	8.3	48.9	62.1	n.d.	2.298	4.75E+14
Telegraph_Peak _drill_hole_3	50.7	1.21	13.2	20	3.6	4.6	3.23	6.6	75	97.6	n.d.	2.29	4.57E+14
Telegraph_Peak _drill_hole_3	50.1	1.1	13.8	19.5	3.9	4.8	3.24	10.1	94.5	126.9	n.d.	2.299	4.30E+14
Telegraph_Peak _drill_hole_4	48	1.37	11.9	20.8	3.6	5	2.7	7.2	72.5	76.3	n.d.	2.297	5.39E+14
Telegraph_Peak _drill_hole_4	50.9	1.14	13.4	18.7	3.6	5.3	3.31	9.3	75.9	100.2	n.d.	2.297	4.14E+14
Telegraph_Peak _drill_hole_4	51.9	1.18	12.1	19.9	3.7	4.2	3.03	6.1	79.6	98.4	n.d.	2.297	4.34E+14
Telegraph_Peak	47.7	1.33	13.3	20.4	3.6	5.7	2.62	7.2	73.3	97	n.d.	2.297	5.38E+14

_drill_hole_4													
Telegraph_Peak _drill_hole_4	13.6	0.52	7.2	8.8	1.1	27.9	0.82	6.1	n.d.	n.d.	n.d.	2.297	3.49E+14
Telegraph_Peak _drill_hole_4	40.5	0.95	9.6	19.4	8	6.8	2.04	7.6	n.d.	67.7	n.d.	2.297	5.17E+14
Telegraph_Peak _drill_hole_4	46.4	1.26	12	21.1	5	3.8	2.98	10.2	69.1	55.2	n.d.	2.297	4.82E+14
Telegraph_Peak _drill_hole_4	49.4	1.35	12.9	20.5	3.4	4.3	3.18	9.5	71.6	77.9	n.d.	2.297	4.48E+14
Telegraph_Peak _drill_hole_4	48.3	1.12	11.4	20	5	4	2.87	8.2	65.6	66.6	n.d.	2.297	4.60E+14
Telegraph_Peak _drill_hole_4	31.8	0.73	10.3	14.9	2.6	17	1.44	4.9	n.d.	50.8	n.d.	2.297	4.36E+14
Telegraph_Peak _drill_hole_4	11.2	0.52	4	8.1	2	29.5	0.35	5.7	n.d.	64.8	n.d.	2.297	3.49E+14
Telegraph_Peak _drill_hole_4	49.3	1.26	12.3	20.6	4.2	5	2.84	7.1	74.3	82	n.d.	2.297	4.61E+14
Telegraph_Peak _drill_hole_4	47.5	1.3	12.1	20.1	3.6	4.5	3.05	9.6	74.7	71.5	n.d.	2.297	4.76E+14
Telegraph_Peak _drill_hole_4	46.1	1.25	11.8	20.9	4.6	4.4	2.89	11.9	82	69.3	n.d.	2.297	5.24E+14
Telegraph_Peak _drill_hole_4	46.2	1.28	10.5	21.3	5	3.9	2.67	13.3	75.9	56	n.d.	2.297	4.64E+14
Telegraph_Peak _drill_hole_4	33.5	0.82	10.2	15.5	2.7	16	1.56	8.2	n.d.	55.8	n.d.	2.297	4.28E+14
Dump Pile													
Telegraph_PK_ PreSieve_Dump	47.9	1.117	9.067	19.33	3.767	4.6	1.947	10.7	44.1	47	n.d.	2.343	2.36E+14
Telegraph_PK_ PreSieve_Dump	47.73	1.467	12.37	20	3.333	4.467	2.513	10.1	49.5	76	n.d.	2.351	3.89E+14

Telegraph_PK_ PreSieve_Dump	45.5	0.947	9.067	17	2.833	8.2	1.733	n.d.	n.d.	61.7	n.d.	2.348	2.26E+14

Buckskin

Target	SiO_2	TiO_2	Al_2O_3	FeO_T	MgO	CaO	Na_2O	Li ppm	Rb ppm	Sr ppm	Ba ppm	Distance m	Spectrum Total
Surface													
Buckskin	69.9	2.9	11.6	6.4	2.1	1.9	3.34	n.d.	n.d.	n.d.	n.d.	4.54181	1.78E+14
Buckskin	69.1	3.04	11.2	7.1	2.1	1.9	3.68	n.d.	n.d.	n.d.	n.d.	4.54181	1.90E+14
Buckskin	63.1	3.61	11.3	11.8	3.4	4.2	3.2	n.d.	n.d.	n.d.	n.d.	4.54181	1.69E+14
Blind_Gulch	72.1	2.55	10.1	4.4	1.8	2	1.82	6.9	94.1	210.3	n.d.	2.53011	2.78E+14
Blind_Gulch	72.3	2.36	9.6	5.1	2.2	1.9	1.83	7.3	140.6	168.4	n.d.	2.53011	2.63E+14
Blind_Gulch	73.5	2.38	9.3	4.6	1.9	1.7	1.84	8.7	121.4	180.9	n.d.	2.53011	2.81E+14
Blind_Gulch	64	3.28	9.1	7.6	2.4	6.1	1.83	8.6	71.5	179.7	n.d.	2.53504	3.37E+14
Blind_Gulch	72.1	2.34	9.8	4.9	2.2	1.9	1.99	6.8	40.2	177.1	n.d.	2.53504	2.80E+14
Blind_Gulch	70.3	2.51	9.9	6.2	2.1	2.1	1.78	5.8	84.7	176	n.d.	2.53504	3.08E+14
Blind_Gulch	67.9	2.55	10.4	6.5	2.8	2.3	2.82	8	42.4	507.5	892.1	2.53813	2.61E+14
Blind_Gulch	71.9	2.49	10	5.4	2.2	1.8	1.88	7.1	110.6	233.3	n.d.	2.53813	2.72E+14
Blind_Gulch	48.8	1.35	6.1	4.9	2.5	19.5	1.01	9	29.8	192.8	n.d.	2.53752	3.33E+14
Drill Hole													
Buckskin_Full _Drill_Hole_ccam	67.9	2.99	9.7	6.5	2.8	2.7	2.33	n.d.	n.d.	n.d.	n.d.	2.54933	1.94E+14
Buckskin_Full _Drill_Hole_ccam	64.5	7.08	9.6	14.3	3.2	1.5	2.45	n.d.	n.d.	n.d.	n.d.	2.54933	1.54E+14
Buckskin_Full _Drill_Hole_ccam	58.2	2.56	7.6	8	16.3	1.4		n.d.	n.d.	n.d.	n.d.	2.54933	1.66E+14
Buckskin_Full	63	1.89	8.5	7	10.5	1.3	1.79	n.d.	n.d.	n.d.	n.d.	2.57011	3.00E+14

_Drill_Hole_ccam													
Buckskin_Full _Drill_Hole_ccam	69.6	3.74	10.1	5.9	2.1	1.8	2.21	n.d.	n.d.	n.d.	n.d.	2.57011	2.95E+14
Buckskin_Full _Drill_Hole_ccam	67.3	2.98	10.2	7	4.3	1.9	2.28	n.d.	n.d.	n.d.	n.d.	2.57011	3.51E+14
Buckskin_Full _Drill_Hole_ccam	71.7	3.76	9.5	6.1	2.1	1.6	2.17	n.d.	n.d.	n.d.	n.d.	2.55434	2.94E+14
Buckskin_Full _Drill_Hole_ccam	43	1.74	5.5	6.6	2.2	21.4	0.9	n.d.	n.d.	n.d.	n.d.	2.55434	4.37E+14
Buckskin_Full _Drill_Hole_ccam	70.7	3.77	9.5	6.3	1.9	1.6	2.01	n.d.	n.d.	n.d.	n.d.	2.55434	3.07E+14
Buckskin_Full _Drill_Hole_ccam	70.7	3.83	9.4	6.3	2	1.6	2.09	n.d.	n.d.	n.d.	n.d.	2.56315	3.59E+14
Tailings													
Buckskin_Full_Drill_Hole _Tailings_ccam	56.3	6.0	6.5	12.3	5.4	3.8	1.7	8.5	12.3	164.9	n.d.	2.55937	3.82E+14
Buckskin_Full_Drill_Hole _Tailings_ccam	51.5	3.9	6.7	15.33	5.8	4.8	1.52	6.9	59.1	186.2	n.d.	2.55937	3.27E+14
Buckskin_Full_Drill_Hole _Tailings_ccam	55.1	6.0	6.1	12.0	5.5	3.9	1.48	n.d.	60	160.5	n.d.	2.55937	3.43E+14
Buckskin_Full_Drill_Hole _Tailings_ccam	56.7	8.4	6.1	11.1	4.9	3.0	1.8	10.5	n.d.	147.7	n.d.	2.55937	3.63E+14
Buckskin_Full_Drill_Hole _Tailings_ccam	56.1	7.9	5.8	11.4	5.2	3.7	1.5	7.7	n.d.	161.3	n.d.	2.55748	3.91E+14

Big Sky

Target	SiO_2	TiO_2	Al_2O_3	FeO_T	MgO	CaO	Na_2O	Li ppm	Rb ppm	Sr ppm	Ba ppm	Distance m	Spectrum Total
Surface													
Big_Sky	47.3	0.82	14.5	17.6	6.4	7.7	3.35	13.4	90.2	141.7	n.d.	2.65062	5.10E+14
Big_Sky	43.5	1.11	11	20.2	7.8	5	2.97	22.5	n.d.	98.2	n.d.	2.65062	6.08E+14
Big_Sky	43.5	1.52	7.1	19.7	12	4.9	2.08	12.2	n.d.	38	n.d.	2.65062	6.39E+14
Big_Sky	44	2.18	10.8	19.8	5.2	4.7	3.21	29.4	80.9	n.d.	n.d.	2.65062	7.01E+14
Big_Sky	41.1	0.96	8.5	19.7	9.6	8.8	2.19	18.7	11.3	97.3	n.d.	2.6513	6.38E+14
Drill Hole													
Big_Sky_Drill_Hole_ccam	43.3	0.85	12.1	21.2	6.7	6.4	2.54	11.8	n.d.	100.9	n.d.	2.68895	5.72E+14
Big_Sky_Drill_Hole_ccam	43.2	0.86	11.9	20.9	9.4	5.5	2.24	15.6	n.d.	87.7	n.d.	2.68895	5.29E+14
Big_Sky_Drill_Hole_ccam	40.5	0.77	10.3	20.1	8	8.8	2.31	18.4	n.d.	110.6	n.d.	2.68895	5.94E+14
Big_Sky_Drill_Hole_ccam	40.7	1.1	10.2	20.9	8.6	4.4	2.3	12.7	n.d.	79.1	n.d.	2.68895	5.94E+14
Big_Sky_Drill_Hole_ccam	43.5	0.82	13.1	20.5	8.3	5.3	2.23	16.7	27.7	81.2	n.d.	2.68895	7.08E+14
Big_Sky_Drill_Hole_ccam	41.8	0.87	11.6	21.1	7.6	6.1	2.28	14.8	n.d.	97.3	n.d.	2.68826	6.92E+14
Big_Sky_Drill_Hole_ccam	41.8	0.8	12.8	19.6	4.9	10.3	2.36	14.6	n.d.	137.9	n.d.	2.68826	6.86E+14
Big_Sky_Drill_Hole_ccam	38.8	1.19	9.1	19.6	6.8	9.2	2.12	14.5	n.d.	89.2	n.d.	2.68826	6.67E+14
Big_Sky_Drill_Hole_ccam	38.7	0.72	9.6	17.3	6.3	13.4	1.98	15.4	n.d.	114.7	n.d.	2.68826	5.82E+14
Big_Sky_Drill_Hole_ccam	39.1	1.4	8.9	18.1	5.8	12.3	1.79	12.6	n.d.	151.6	n.d.	2.69104	7.06E+14
Tailings													
Big_Sky_tailings_ccam	41.9	1.0	12.6	19.4	5.5	7.5	2.1	11.9	n.d.	80.1	n.d.	2.6841	2.28E+14
Big_Sky_tailings_ccam	40.9	1.0	12.3	19.4	5.4	7.7	2.2	7.5	n.d.	59.3	n.d.	2.6841	2.57E+14
Big_Sky_tailings_ccam	42.0	1.0	12.4	19.2	5.3	7.6	2.2	12.7	n.d.	70.1	n.d.	2.6841	2.89E+14
Big_Sky_tailings_ccam	41.4	1.0	12.3	19.6	5.2	7.4	2.2	6.5	n.d.	68.9	n.d.	2.6841	3.34E+14
Big_Sky_tailings_ccam	41.2	1.0	12.1	20.2	5.4	7.4	2.2	7	n.d.	84	n.d.	2.68272	4.01E+14

Greenhorn

Target	SiO_2	TiO_2	Al_2O_3	FeO_T	MgO	CaO	Na_2O	Li ppm	Rb ppm	Sr ppm	Ba ppm	Distance m	Spectrum Total
Surface													
Greenhorn_ccam	80.9	1.89	1.4	5	1.6	0.2	1.04	3.9	n.d.	18.8	n.d.	2.43928	2.43E+14
Greenhorn_ccam	69.2	1.45	2.3	10.5	2.8	8.4	1.16	2.4	n.d.	117.6	n.d.	2.43928	3.16E+14
Greenhorn_ccam	63	2.08	0.3	12.8	2.9	10	0.99	2.4	n.d.	108.6	n.d.	2.43928	4.62E+14
Greenhorn_ccam	71.9	1.41	4.4	8	2.6	5.5	0.73	5.1	116.2	72.3	n.d.	2.43243	2.70E+14
Greenhorn_ccam	76.7	1.93	0.1	7.2	3.9	0.6	1.04	1.5	n.d.	17.1	n.d.	2.43243	3.41E+14
Greenhorn_ccam	77.2	2.19	2.2	6.4	2.2	0.7	0.88	0.7	n.d.	54.5	n.d.	2.43243	2.59E+14
Greenhorn_ccam	80.8	1.96	2.8	4.5	1.7	0.1	0.91	1.4	n.d.	14.8	n.d.	2.42788	2.42E+14
Greenhorn_ccam	71.7	4.89	0.3	15.7	2.4	1.3	1.37	0.6	n.d.	499.2	1176	2.42788	4.54E+14
Greenhorn_ccam	48.6	0.67	2.4	7	2.8	20.4	1.17	2.3	n.d.	96.8	n.d.	2.42788	3.03E+14
Greenhorn_ccam	53.8	0.75	3.5	8.2	2.8	16.4	1.28	11.5	n.d.	115.3	n.d.	2.42448	3.43E+14
Greenhorn_ccam2	68.3	1.55	3.7	17.5	3.9	3.9	1.29	2.7	n.d.	91.2	n.d.	2.40317	3.48E+14
Greenhorn_ccam2	74.9	2.15	3.9	12.4	1.9	2.3	1.64	1.5	30.8	33	n.d.	2.40317	2.84E+14
Greenhorn_ccam2	64.6	3.2	3.8	20.4	2.4	2.4	2.23	1.6	34.4	61.6	n.d.	2.40317	4.21E+14
Greenhorn_ccam2	63	2.19	3.5	18.8	2.5	4.7	1.46	2	n.d.	64.6	n.d.	2.40317	4.60E+14
Greenhorn_ccam2	55.4	1.55	5.9	21.5	2.5	5.5	2.03	3.6	n.d.	124.9	n.d.	2.40151	4.26E+14
Drill Hole													
Greenhorn_Drill_Hole_1	50.2	0.99	6.1	13.1	2.3	13.6	1.32	n.d.	n.d.	n.d.	n.d.	2.40317	3.92E+14
Greenhorn_Drill_Hole_1	46.4	0.74	8.5	10.2	1.6	17.7	1.7	n.d.	n.d.	n.d.	n.d.	2.4121	3.85E+14
Greenhorn_Drill_Hole_1	60.2	1.63	4.7	16.4	2.6	8.2	1.5	n.d.	n.d.	n.d.	n.d.	2.4121	4.48E+14
Greenhorn_Drill_Hole_1	51.2	2.06	4.2	16.5	2.2	10.5	1.65	n.d.	n.d.	n.d.	n.d.	2.4121	4.85E+14
Greenhorn_Drill_Hole_1	57	2.35	5.9	18.2	3	5.4	2.48	n.d.	n.d.	n.d.	n.d.	2.4121	5.42E+14
Greenhorn_Drill_Hole_1	67.5	2	7.2	18.4	3.1	1.7	2.84	n.d.	n.d.	n.d.	n.d.	2.4093	4.66E+14
Greenhorn_Drill_Hole_1	49.4	0.92	4.2	12.8	2.5	16.8	1.15	n.d.	n.d.	n.d.	n.d.	2.4093	4.56E+14
Greenhorn_Drill_Hole_1	54.5	1.28	6.7	17	2.5	9.6	1.85	n.d.	n.d.	n.d.	n.d.	2.4093	5.08E+14
Greenhorn_Drill_Hole_1	49.1	0.93	3.7	14.7	3.2	15	1.4	n.d.	n.d.	n.d.	n.d.	2.4093	4.57E+14

Greenhorn_Drill_Hole_1	69.2	2.33	5.2	18.2	3.2	0.8	2.36	n.d.	n.d.	n.d.	n.d.	2.40763	4.79E+14
Greenhorn_Drill_Hole_2	53.5	1.24	8.4	13.4	2.3	11.9	1.61	n.d.	n.d.	n.d.	n.d.	2.41266	4.04E+14
Greenhorn_Drill_Hole_2	53.7	1.19	9	13.8	2.3	11	2.18	n.d.	n.d.	n.d.	n.d.	2.41266	4.16E+14
Greenhorn_Drill_Hole_2	45.6	1.26	6.8	16.4	2	13.1	1.67	n.d.	n.d.	n.d.	n.d.	2.41266	5.56E+14
Greenhorn_Drill_Hole_2	60	2.4	3.3	19.5	4.4	4.1	1.46	n.d.	n.d.	n.d.	n.d.	2.41266	5.00E+14
Greenhorn_Drill_Hole_2	41.6	0.99	5.5	17.1	2.1	14.2	1.47	n.d.	n.d.	n.d.	n.d.	2.40986	5.31E+14
Greenhorn_Drill_Hole_2	46.5	2.47	5.1	16.3	2.2	5.7	1.84	n.d.	n.d.	n.d.	n.d.	2.40986	6.20E+14
Greenhorn_Drill_Hole_2	54.2	0.89	9.2	12.2	2.4	11.1	2.46	n.d.	n.d.	n.d.	n.d.	2.40986	4.32E+14
Greenhorn_Drill_Hole_2	70	1.14	4.8	14.7	6	1.9	2.12	n.d.	n.d.	n.d.	n.d.	2.40986	4.01E+14
Greenhorn_Drill_Hole_2	65.4	1.5	6.3	18.7	2.4	3.8	2.19	n.d.	n.d.	n.d.	n.d.	2.40707	5.39E+14
Tailings													
Greenhorn_Drill_Hole _RMI_Tailings	47.1	1.3	5.9	17.7	2.2	10.6	1.9	3.8	n.d.	63.7	n.d.	2.42109	3.40E+14
Greenhorn_Drill_Hole _RMI_Tailings	47.2	1.5	6.1	17.1	2.3	9.7	2.0	3	n.d.	78.1	n.d.	2.42109	2.64E+14
Greenhorn_Drill_Hole _RMI_Tailings	47.6	1.4	5.7	17.8	2.4	9.4	2.1	2.5	n.d.	60.7	n.d.	2.42109	2.71E+14
Greenhorn_Drill_Hole _RMI_Tailings	44.1	1.4	6.0	17.8	2.3	12.2	1.9	5	n.d.	105.5	n.d.	2.42109	3.49E+14
Greenhorn_Drill_Hole _RMI_Tailings	45.1	1.2	5.4	16.7	2.3	12.3	1.5	2.1	n.d.	94.9	n.d.	2.40428	3.69E+14
Dump Pile													
Greenhorn_postsieve_dump	46.5	1.1	6.9	18.2	2.8	10.3	1.6	9.9	107.1	178	n.d.	2.64322	5.71E+14
Greenhorn_postsieve_dump	47.2	1.2	6.8	18.1	2.8	9.7	1.7	5.5	100.5	112.9	n.d.	2.64322	6.75E+14
Greenhorn_postsieve_dump	46.3	1.1	6.8	17.9	2.7	10.9	1.5	6.6	104.5	93.9	n.d.	2.64322	5.06E+14
Greenhorn_postsieve_dump	48.3	1.1	7.0	17.6	2.8	10.8	1.7	6.8	116.1	99.2	n.d.	2.64322	3.35E+14
Greenhorn_postsieve_dump	47.5	1.3	7.2	18.5	2.9	10.3	1.7	5.1	113.6	103.6	n.d.	2.6372	3.72E+14

Lubango

Target	SiO_2	TiO_2	Al_2O_3	FeO_T	MgO	CaO	Na_2O	Li ppm	Rb ppm	Sr ppm	Ba ppm	Distance m	Spectrum Total
Surface													
Okahao	60.9	0.77	20.8	2.1	1.2	5.6	6.32	7.7	75.4	653.7	n.d.	2.99138	2.62E+14
Okahao	55.1	1.37	6.3	17.8	2.7	6	2.38	2.4	n.d.	156.1	n.d.	2.99138	4.68E+14
Okahao	57.3	1.45	9.1	14.6	3	9.1	2.23	6.2	89.6	114.7	n.d.	2.99138	3.67E+14
Okahao	54.9	0.82	9.5	12.9	3.9	11.8	2.3	5.4	n.d.	167	n.d.	2.99138	3.16E+14
Okahao	66.2	2.05	5.2	10.6	4.7	8.7	1.52	9.1	25.8	147.5	n.d.	2.99138	3.61E+14
Okahao	66.1	1.25	5.4	12.4	2.8	9.1	2.06	3.7	n.d.	115.5	n.d.	2.99138	2.75E+14
Okahao	70.1	0.89	3.6	8.7	5.3	9.2	1.77	6.7	n.d.	221	n.d.	2.99138	2.35E+14
Okahao	76.1	1.53	5.4	6.8	3.9	1.6	2.66	7.4	n.d.	79.8	n.d.	2.99138	1.73E+14
Okahao	70.8	2.02	6.9	14.3	3.2	3.7	2.5	3.3	n.d.	81.6	n.d.	2.99138	2.30E+14
Okahao	54.9	0.86	9	12	3.7	12.6	1.98	n.d.	n.d.	176.1	n.d.	3.00776	3.47E+14
Drill Hole													
Lubango_drill_hole_1	68.2	1.62	7.1	6.5	3.8	6	1.46	n.d.	n.d.	n.d.	n.d.	2.79125	3.37E+14
Lubango_drill_hole_1	70.8	2.02	3.6	5.6	3	7.2	1.06	n.d.	n.d.	n.d.	n.d.	2.79125	3.02E+14
Lubango_drill_hole_1	61.1	0.79	4.4	2.1	2.5	15.7	0.65	n.d.	n.d.	n.d.	n.d.	2.79125	2.59E+14
Lubango_drill_hole_1	63.1	1.19	8.7	7.4	3.2	9.5	2.09	n.d.	n.d.	n.d.	n.d.	2.79125	3.38E+14
Lubango_drill_hole_1	54.2	0.86	10.2	5.5	2.3	14.9	2.36	n.d.	n.d.	n.d.	n.d.	2.79125	3.37E+14
Lubango_drill_hole_1	53.6	1.18	2.9	11.2	5.8	13.7	0.86	n.d.	n.d.	n.d.	n.d.	2.79125	4.67E+14
Lubango_drill_hole_1	48	1.12	3.3	15.1	2.8	14.4	0.96	n.d.	n.d.	n.d.	n.d.	2.78975	5.30E+14
Lubango_drill_hole_1	59.4	2.24	5.2	7	3.5	10.8	1.48	n.d.	n.d.	n.d.	n.d.	2.78975	3.33E+14
Lubango_drill_hole_1	51.7	0.75	3.2	11.4	5.9	14.1	1.06	n.d.	n.d.	n.d.	n.d.	2.78975	4.02E+14
Lubango_drill_hole_1	71.9	2.25	5.8	6	3.1	4.3	1.95	n.d.	n.d.	n.d.	n.d.	2.78975	3.08E+14

Lubango_drill_hole_1	68.9	1.41	4.3	6	4	7.3	1.25	n.d.	n.d.	n.d.	n.d.	2.78975	3.46E+14
Lubango_drill_hole_1	60.1	2.51	3.1	10.6	4	9.9	1.48	n.d.	n.d.	n.d.	n.d.	2.78975	3.84E+14
Lubango_drill_hole_1	47.1	0.86	1.1	7.5	3	21.8	0.6	n.d.	n.d.	n.d.	n.d.	2.78975	3.95E+14
Lubango_drill_hole_1	64.9	1.68	8.9	5.8	2.9	8	2.72	n.d.	n.d.	n.d.	n.d.	2.78975	3.39E+14
Lubango_drill_hole_1	59.3	0.97	9.7	5.1	2.3	11.8	2.4	n.d.	n.d.	n.d.	n.d.	2.78975	3.24E+14
Lubango_drill_hole_1	59.5	0.81	10.5	4.5	2.9	11.4	2.11	n.d.	n.d.	n.d.	n.d.	2.78975	3.13E+14
Lubango_drill_hole_1	74.4	2.14	4.4	6.3	3	3.2	1.94	n.d.	n.d.	n.d.	n.d.	2.78975	2.98E+14
Lubango_drill_hole_1	75.2	1.9	5.8	5.8	2.9	2.1	2.17	n.d.	n.d.	n.d.	n.d.	2.78975	2.68E+14
Lubango_drill_hole_1	58.2	1.37	3	8.9	3.8	12.7	1.15	n.d.	n.d.	n.d.	n.d.	2.78975	3.36E+14
Tailings													
Lubango_Tailings_LIBS	50.9	2.3	3.4	12.9	3.4	11.5	0.9	2.5	n.d.	111.2	n.d.	2.75801	3.27E+14
Lubango_Tailings_LIBS	49.5	2.2	4.0	12.8	3.5	11.7	0.9	1.8	n.d.	126.9	n.d.	2.75801	3.60E+14
Lubango_Tailings_LIBS	50.0	2.3	3.3	12.7	3.3	11.7	0.9	1.5	n.d.	96	n.d.	2.75801	3.27E+14
Lubango_Tailings_LIBS	52.1	3.7	4.3	13.6	3.3	10.7	1.4	n.d.	n.d.	66.6	n.d.	2.75801	3.54E+14
Lubango_Tailings_LIBS	50.7	2.9	3.1	13.6	3.3	11.8	1.1	7.4	n.d.	98.7	n.d.	2.75801	4.33E+14
Lubango_Tailings_LIBS	52.4	3.7	4.7	12.9	3.3	10.7	1.4	6.2	n.d.	159.9	n.d.	2.75801	4.98E+14
Lubango_Tailings_LIBS	49.9	3.7	4.6	14.4	3.3	11.2	1.6	5.1	n.d.	66.8	n.d.	2.75801	2.94E+14
Lubango_Tailings_LIBS	50.4	3.7	4.4	13.3	3.1	12.0	1.5	3.9	n.d.	95	n.d.	2.75801	2.85E+14
Lubango_Tailings_LIBS	52.0	2.7	2.6	13.8	3.7	10.7	0.9	3.4	n.d.	108.2	n.d.	2.77268	4.22E+14
Dump Pile													
Lubango_postsieve_1337	53.7	1.9	6.3	17.4	4.0	9.1	1.7	12.2	n.d.	176.4	n.d.	3.72836	5.68E+14
Lubango_postsieve_1337	53.8	2.1	6.5	16.5	3.6	9.7	1.8	5.5	n.d.	67.9	n.d.	3.72836	2.96E+14
Lubango_postsieve_1337	50.8	2.4	6.1	17.9	3.5	9.1	1.8	3.9	n.d.	94.7	n.d.	3.72836	2.21E+14

Lubango_postsieve_133 7	53.4	2.5	6.8	17.7	3.5	9.1	2.1	9.2	n.d.	96.2	n.d.	3.72836	3.19E+14
Lubango_postsieve_133 7	52.6	1.9	5.8	17.2	4.0	10.4	1.6	11.9	n.d.	85	n.d.	3.75105	4.26E+14

Okoruso

Target	SiO_2	TiO_2	Al_2O_3	FeO_T	MgO	CaO	Na_2O	Li ppm	Rb ppm	Sr ppm	Ba ppm	Distance m	Spectrum Total
Surface													
Okoruso	43.9	1.21	9.7	18.4	9.5	6.5	2.68	12	n.d.	110.4	n.d.	2.6206	7.71E+14
Okoruso	42.9	1.29	10.8	19.5	7.3	6.9	3.21	12.3	n.d.	116.9	n.d.	2.6206	7.54E+14
Okoruso	44	1	11.9	19.4	7.6	6.5	2.95	14.4	n.d.	127.5	n.d.	2.6206	7.13E+14
Okoruso	45.4	0.74	6.2	20.2	15.6	3.6	1.88	25.1	n.d.	44.2	n.d.	2.62721	6.65E+14
Okoruso	44.1	1	9.2	20.2	8.4	4.9	2.94	11.4	n.d.	100.7	n.d.	2.62721	6.55E+14
Okoruso	43	0.98	11.8	21.2	5.5	6.7	3.09	10.9	n.d.	150.1	n.d.	2.62721	7.14E+14
Okoruso	41.9	0.84	7.8	19.8	7.3	8.5	2.43	13.6	n.d.	56	n.d.	2.63386	5.89E+14
Okoruso	48.8	0.91	15.1	16.5	6.4	5.5	4.35	10.6	39.3	189	n.d.	2.63386	4.98E+14
Okoruso	41.1	0.83	10.3	23.4	5.2	5.2	3.62	7.7	n.d.	47.9	n.d.	2.63453	5.74E+14
Omatako	45.1	0.85	13.1	19.4	7	4.8	2.72	12.4	n.d.	97.8	n.d.	2.53504	5.45E+14
Omatako	46.4	0.88	13.1	19.4	7.1	3.9	2.73	11.3	32.4	78.8	n.d.	2.53504	5.03E+14
Omatako	42.9	1.1	12.2	21.1	5.7	4.6	2.82	12.3	n.d.	99.3	n.d.	2.53504	6.78E+14
Omatako	43.5	1.07	11.8	20.7	6.1	4.3	3.04	11.5	n.d.	123	n.d.	2.53566	6.34E+14

Omatako	43.6	0.97	11.4	20.7	6.6	4.9	2.73	13	n.d.	98.7	n.d.	2.53566	6.31E+14
Omatako	45.9	0.86	13.5	19.1	6.9	5	2.8	13	n.d.	86.6	n.d.	2.53566	5.31E+14
Omatako	43.2	0.91	14	20.5	6.3	5.4	2.85	11.3	38.3	91.9	n.d.	2.5369	6.33E+14
Omatako	43.8	0.9	12.8	20.3	6.5	6.2	2.64	12.7	n.d.	99.3	n.d.	2.5369	6.38E+14
Omatako	44.3	1	12.4	20	7.3	5.4	2.77	12	n.d.	87.8	n.d.	2.5369	5.64E+14
Omatako	42.1	0.91	11.1	19.6	5.8	7.8	2.67	12.3	n.d.	106.5	n.d.	2.5369	6.59E+14
Drill Hole													
Okoruso_drill_hole_ccam_2	42.9	1.02	10	20.4	7.4	6	2.47	n.d.	n.d.	n.d.	n.d.	2.6292	5.60E+14
Okoruso_drill_hole_ccam_2	42.9	0.8	10	20.2	6.7	7.6	2.39	n.d.	n.d.	n.d.	n.d.	2.6292	4.55E+14
Okoruso_drill_hole_ccam_2	42.4	0.78	9.1	20.8	7.7	6.3	1.87	n.d.	n.d.	n.d.	n.d.	2.63053	4.88E+14
Tailings													
Okoruso_tailings_LIBS	44.1	0.9	9.9	19.1	7.1	6.6	2.3	7.8	n.d.	65.2	n.d.	2.62854	3.92E+14
Okoruso_tailings_LIBS	43.7	0.9	10.1	19.7	6.6	7.1	2.2	9.5	n.d.	73.4	n.d.	2.62854	4.34E+14
Okoruso_tailings_LIBS	44.0	0.9	10.4	20.8	6.7	6.3	2.4	10	n.d.	75.7	n.d.	2.62854	5.14E+14
Okoruso_tailings_LIBS	44.5	0.9	9.9	20.7	7.0	6.5	2.3	11.7	n.d.	112.8	n.d.	2.63253	6.22E+14
Okoruso_tailings_LIBS	42.3	1.0	9.1	21.2	6.9	6.0	2.1	14.2	n.d.	71.5	n.d.	2.63253	5.77E+14
Okoruso_tailings_LIBS	42.1	0.9	8.7	20.8	7.2	5.9	2.1	10.5	74.7	58.6	n.d.	2.63253	5.28E+14
Okoruso_tailings_LIBS	43.9	0.9	9.8	20.9	7.2	6.0	1.9	10.9	n.d.	74.7	n.d.	2.6312	6.82E+14

Okoruso_tailings_LIB S	43.3	0.8	10.0	19.7	7.4	6.6	2.0	9	n.d.	84.9	n.d.	2.6312	4.57E+14
Okoruso_tailings_LIB S	43.5	0.9	10.2	20.0	6.9	6.4	2.4	9.8	n.d.	56.6	n.d.	2.6312	4.56E+14
Okoruso_tailings_LIB S	43.5	0.9	10.0	20.3	7.4	5.9	2.1	7.3	21.5	66.9	n.d.	2.62522	4.50E+14
Okoruso_tailings _APXS_LIBS	44.4	0.9	9.4	20.3	7.7	5.8	2.0	12.2	n.d.	76.4	n.d.	2.60355	5.10E+14
Okoruso_tailings _APXS_LIBS	44.4	0.9	9.8	20.7	7.4	6.1	2.2	8.9	n.d.	73.3	n.d.	2.60355	4.20E+14
Okoruso_tailings _APXS_LIBS	43.8	1.0	9.5	20.9	7.8	5.7	2.2	8.9	n.d.	93.5	n.d.	2.60355	8.01E+14
Okoruso_tailings _APXS_LIBS	43.9	1.0	10.6	21.1	7.2	6.0	2.2	15.9	n.d.	42	n.d.	2.6029	5.74E+14
Okoruso_tailings _APXS_LIBS	42.7	1.0	9.5	21.1	7.2	5.9	1.9	6.3	n.d.	149. 3	n.d.	2.6029	4.92E+14
Okoruso_tailings _APXS_LIBS	43.3	0.9	9.1	21.2	7.2	5.6	2.1	9.8	n.d.	82.9	n.d.	2.6029	5.47E+14
Okoruso_tailings _APXS_LIBS	43.5	0.9	9.6	20.8	7.0	6.0	2.2	12.6	n.d.	79.9	n.d.	2.6016	5.16E+14
Okoruso_tailings _APXS_LIBS	44.5	1.0	10.0	21.1	7.1	5.8	2.4	9.4	n.d.	68	n.d.	2.6016	5.80E+14
Okoruso_tailings _APXS_LIBS	44.1	1.0	9.9	20.7	7.2	6.1	2.1	9	n.d.	88.3	n.d.	2.6016	5.06E+14
Okoruso_tailings _APXS_LIBS	43.8	0.9	9.0	21.0	7.5	5.5	2.0	11.5	n.d.	43.8	n.d.	2.59965	4.27E+14
Dump Pile													
Okoruso_presieve _dump_ccam	43.9	0.9	9.0	20.1	7.1	5.7	2.0	9.9	n.d.	56.4	n.d.	2.35789	4.15E+14
Okoruso_presieve	44.4	0.9	9.5	20.3	7.0	5.4	2.1	8.6	n.d.	67.2	n.d.	2.35789	3.84E+14

_dump_ccam													
Okoruso_presieve _dump_ccam	44.2	0.9	8.6	20.6	7.1	5.3	1.9	9.3	n.d.	54	n.d.	2.35789	3.52E+14
Okoruso_presieve _dump_ccam	44.2	0.9	8.8	20.1	6.9	5.3	2.0	7.2	n.d.	76.4	n.d.	2.35842	3.79E+14
Okoruso_presieve _dump_ccam	44.1	0.9	9.3	20.2	6.9	5.6	2.2	8.2	n.d.	68.5	n.d.	2.35842	3.77E+14
Okoruso_presieve _dump_ccam	43.0	0.9	9.4	20.5	6.8	5.8	2.0	9.1	n.d.	84.6	n.d.	2.35842	4.00E+14
Okoruso_presieve _dump_ccam	44.3	0.9	9.3	20.8	6.8	5.7	2.1	7.8	n.d.	68.2	n.d.	2.36003	3.96E+14
Okoruso_presieve _dump_ccam	44.4	0.9	10.1	20.4	7.3	5.7	2.1	8.5	9.6	84.8	n.d.	2.36003	3.83E+14
Okoruso_presieve _dump_ccam	45.2	0.9	9.7	20.6	7.0	5.3	2.1	7.8	n.d.	50.7	n.d.	2.36003	3.65E+14
Okoruso_presieve _dump_ccam	43.9	0.9	9.6	20.9	6.9	5.5	2.1	8.1	33.6	66.8	n.d.	2.36272	3.94E+14
Okoruso_postsieve _dump_pile_ccam	44.5	1.0	10.1	19.2	6.8	6.3	2.1	3.8	72.8	175.8	n.d.	2.47235	4.57E+14
Okoruso_postsieve _dump_pile_ccam	44.3	0.9	9.7	19.9	7.1	5.8	2.0	7.1	45.2	101.2	322.8	2.47235	6.76E+14
Okoruso_postsieve _dump_pile_ccam	44.9	0.9	9.7	19.5	7.0	6.3	2.0	4	71	124.1	n.d.	2.47235	4.61E+14
Okoruso_postsieve _dump_pile_ccam	44.3	0.9	9.8	20.2	6.8	5.9	2.3	8	61.9	147.8	n.d.	2.47235	4.08E+14
Okoruso_postsieve _dump_pile_ccam	44.2	0.9	9.7	19.6	7.3	6.2	2.0	5.2	53.7	124.1	338.5	2.48714	5.01E+14

Oudam

Target	SiO_2	TiO_2	Al_2O_3	FeO_T	MgO	CaO	Na_2O	Li ppm	Rb ppm	Sr ppm	Ba ppm	Distance m	Spectrum Total
Surface													
Otiiha	46.6	0.8	9.0	19.7	8.6	1.8	2.3	4.6	72.1	105.9	n.d.	2.23595	5.90E+14
Otiiha	53.0	1.0	11.9	17.6	6.8	2.3	2.5	7.8	85.4	192.1	n.d.	2.23595	4.97E+14
Otiiha	52.5	1.0	11.2	20.1	5.2	2.2	2.6	7.6	72.9	280.9	n.d.	2.23595	5.82E+14
Otiiha	51.6	0.9	11.5	19.9	5.7	2.4	2.7	4.3	77.6	260.2	n.d.	2.23595	5.77E+14
Otiiha	51.7	0.9	10.2	20.2	6.2	2.1	2.8	9.1	79.5	254.8	n.d.	2.23836	6.26E+14
Oudam_tailings _ccam_2	51.7	1.0	8.7	19.8	4.6	1.9	2.1	3.5	120.3	109.3	n.d.	2.22015	4.24E+14
Oudam_tailings _ccam_2	51.6	1.0	9.9	20.6	3.7	2.5	2.4	3.3	112.8	143.8	n.d.	2.22015	4.01E+14
Oudam_tailings _ccam_2	49.6	1.0	10.4	20.7	4.7	2.8	2.0	3.1	105.4	214.6	n.d.	2.22015	4.63E+14
Oudam_tailings _ccam_2	51.2	1.0	9.8	21.0	4.2	2.3	2.1	3.1	71.7	182.5	n.d.	2.22015	4.68E+14
Tailings													
Oudam_tailings _ccam_2	52.1	0.9	8.5	18.0	5.6	3.2	1.6	3.9	83.2	104.8	n.d.	2.22015	4.05E+14
Dump Pile													
Oudam_presieve_ dump_ccam	52.9	1.0	9.5	17.5	5.3	3.4	1.7	7	40.3	59.7	n.d.	2.4659	2.86E+14
Oudam_presieve_ dump_ccam	52.7	1.0	9.7	18.4	5.3	3.5	1.8	4.8	63.7	57	n.d.	2.4659	3.06E+14
Oudam_presieve_ dump_ccam	52.4	1.0	9.7	18.2	5.3	3.6	1.8	10.2	n.d.	71.3	n.d.	2.4659	3.12E+14
Oudam_presieve_ dump_ccam	52.1	1.0	10.2	18.4	5.6	4.0	1.7	6.7	115.8	75	n.d.	2.4659	3.71E+14
Oudam_presieve_ dump_ccam	52.2	1.0	9.9	19.0	5.3	3.6	1.7	6.4	n.d.	66.8	n.d.	2.46942	2.72E+14

Marimba

Target	SiO_2	TiO_2	Al_2O_3	FeO_T	MgO	CaO	Na_2O	Li ppm	Rb ppm	Sr ppm	Ba ppm	Distance m	Spectrum Total
Surface													
Marimba	55.9	0.96	10	17.5	5.3	1.4	2.38	11.7	103.6	108.4	n.d.	2.53628	5.32E+14
Marimba	51.4	0.88	10.5	17.1	4.2	5.4	2.29	11.1	98.1	109.9	n.d.	2.53628	4.75E+14
Marimba	53.4	0.99	10.9	20.2	4.6	1.6	2.67	11.9	84.4	144.3	n.d.	2.53628	6.29E+14
Marimba	50.6	0.84	10.5	18.9	4.1	4.3	2.35	11.6	91.4	95.8	n.d.	2.5369	4.95E+14
Marimba	29.6	0.65	5.7	11.7	1.9	22.4	0.99	8.6	n.d.	137	n.d.	2.5369	6.21E+14
Marimba	50.7	1	12.3	18.9	4.1	4.9	2.39	8.4	71.3	175.5	n.d.	2.5369	6.36E+14
Marimba	49.4	0.93	9.9	17.7	3.4	3	2.28	8.9	84.2	154.6	n.d.	2.5369	6.04E+14
Marimba	54.2	1	12.1	19.4	4.4	2	2.72	8.9	80.4	205.9	n.d.	2.5369	5.50E+14
Marimba	34.3	0.75	5.5	14.3	2.9	17.7	1.16	14.5	39.9	124	n.d.	2.5369	5.16E+14
Marimba	31.2	0.71	5.4	11.5	2.1	21	1.09	7.8	36.7	127.9	n.d.	2.53628	5.68E+14
Marimba2_ccam	53.5	0.94	10.3	20.6	4.3	1.6	2.06	13	102.4	128.5	n.d.	2.57584	4.70E+14
Marimba2_ccam	54.2	0.98	9.7	19.8	4.5	1.6	2.24	11.5	86.2	124.5	n.d.	2.57584	4.28E+14
Marimba2_ccam	54.2	0.99	10.4	19.3	4.8	1.7	2.33	12.2	74	102.2	n.d.	2.57584	4.14E+14
Marimba2_ccam	49.8	0.89	10	20.1	4.1	4.4	2.06	12.5	76.6	90.6	n.d.	2.57584	4.39E+14
Marimba2_ccam	48.7	0.9	9.1	19.5	4.6	4.1	2.24	10.8	122.5	92.9	n.d.	2.57584	4.28E+14
Marimba2_ccam	54.1	0.91	9.7	18.8	5.5	1.7	2.24	11.3	88.3	n.d.	n.d.	2.57584	3.97E+14
Marimba2_ccam	48.7	0.89	8.8	19.5	5	5.4	2.02	10	72.8	98.5	n.d.	2.57584	4.22E+14
Marimba2_ccam	53.1	0.95	9.2	21.1	4.3	1.4	2.36	11.1	84.4	80.9	n.d.	2.57584	4.07E+14
Marimba2_ccam	52.9	0.9	9.5	20.6	4.4	1.4	2.45	10.8	80.4	88.2	n.d.	2.57584	3.87E+14
Marimba2_ccam	55	0.94	9.5	20.6	4.2	1.5	2.74	12.1	n.d.	96	n.d.	2.56694	3.89E+14
Drill Hole													
Marimba_Drill_Hole_1420_ccam	47.4	0.86	9.5	17.7	3.8	9.7	1.77	9	76	139	n.d.	2.51969	6.13E+14
Marimba_Drill_Hole_1420_ccam	55.9	0.95	9.5	17.8	4.9	1.7	2.11	9.6	112.2	n.d.	n.d.	2.51969	3.50E+14

Marimba_Drill_Hole_1420_ccam	32.9	0.68	6.6	12.9	2.1	19.7	0.97	8.9	n.d.	104.1	n.d.	2.51969	4.27E+14
Marimba_Drill_Hole_1420_ccam	44.8	0.88	8.4	19.7	4.2	7.4	1.77	14.1	67.6	84.6	n.d.	2.51969	6.26E+14
Marimba_Drill_Hole_1420_ccam	52.8	0.98	10.1	20.3	4.9	1.6	2.59	18.9	111.8	125.6	n.d.	2.53196	6.62E+14
Marimba_Drill_Hole_1420_ccam	53.9	1.04	10.7	18.9	5.5	1.6	2.56	17.2	130.4	122.5	n.d.	2.53196	5.85E+14
Marimba_Drill_Hole_1420_ccam	53.6	1.07	10.8	19	5.5	1.8	2.69	17.6	106.7	133.6	n.d.	2.53196	6.35E+14
Marimba_Drill_Hole_1420_ccam	53.8	0.87	9.5	19.2	5.3	1.5	3.1	17.9	145.2	86.4	n.d.	2.53196	4.37E+14
Marimba_Drill_Hole_1420_ccam	53.9	0.9	9.5	19.2	6.2	1.4	2.25	15.6	88.7	82.6	n.d.	2.53196	5.06E+14
Marimba_Drill_Hole_1420_ccam	20.1	0.62	3.5	10.1	1.9	27.1	0.63	9.2	26.9	142.7	n.d.	2.53504	6.26E+14
Dump Pile													
sol1427_Marimba_presieve_dump	46.23	0.85	7.73	20.90	4.10	4.10	1.20	6	62.3	92.4	n.d.	2.26872	4.17E+14
sol1427_Marimba_presieve_dump	45.80	0.94	7.43	20.90	4.30	4.30	1.27	7.2	69.1	69.7	n.d.	2.26872	3.62E+14
sol1427_Marimba_presieve_dump	46.70	0.90	7.70	20.67	4.30	3.93	1.21	9	117.1	67.6	n.d.	2.26872	3.14E+14

Quela

Target	SiO_2	TiO_2	Al_2O_3	FeO_T	MgO	CaO	Na_2O	Li ppm	Rb ppm	Sr ppm	Ba ppm	Distance m	Spectrum Total

Surface													
Quela_DRT_ccam	45.4	0.84	8.5	18.8	4	10.8	1.79	13.3	64.7	155.6	n.d.	2.54123	5.80E+14
Quela_DRT_ccam	54.7	0.93	11.4	20	4.7	2.4	2.89	7.2	78.2	163.3	n.d.	2.54123	5.11E+14
Quela_DRT_ccam	51.4	0.89	10.3	19.8	4.5	6.2	2.31	8	64.4	181.4	145.4	2.54123	5.74E+14
Quela_DRT_ccam	52.2	0.87	11.3	19.7	4.3	4.4	2.79	7.3	91.9	145.6	n.d.	2.54186	4.90E+14
Quela_DRT_ccam	37.5	0.75	6.5	15.1	3.9	17.1	1.33	10.5	48.4	117	n.d.	2.54186	5.47E+14
Quela_DRT_ccam	46.4	0.89	9.7	18.5	3.8	10.2	1.94	10.5	60	154.6	n.d.	2.54186	6.35E+14
Quela_DRT_ccam	54.5	0.95	12.2	20	4.8	2.8	2.84	7.5	79.8	183.5	n.d.	2.54186	4.94E+14
Quela_DRT_ccam	43.1	0.82	8.4	17.9	4	13.3	1.63	14.7	n.d.	169	n.d.	2.54186	6.33E+14
Quela_DRT_ccam	46.4	0.87	8.9	18.3	4.2	11.2	1.63	7.6	49.2	160.3	n.d.	2.54186	4.81E+14
Quela_DRT_ccam	53.3	0.97	11.3	21.8	4.8	2.6	2.64	7.2	80.2	188.4	n.d.	2.54186	6.08E+14
Drill Hole													
Quela_Drill_ Hole_CCAM	29.1	0.58	7.6	12.2	1.6	23.2	1.03	9.7	n.d.	48.7	n.d.	2.53937	1.03E+14
Quela_Drill_ Hole_CCAM	42.5	0.77	9.6	22.8	2.7	8.6	2.01	14.2	110	83.4	n.d.	2.53937	2.00E+14
Quela_Drill_ Hole_CCAM	47.8	0.87	10.1	20.8	4	3.9	2.48	11.9	130.6	104.5	n.d.	2.53937	2.04E+14
Quela_Drill_ Hole_CCAM	45.6	0.84	9.5	21.3	3.7	6.1	2.16	10.8	102.3	97.4	n.d.	2.53937	2.53E+14
Quela_Drill_ Hole_CCAM	35.8	0.71	8.2	17.1	1.8	15.2	1.51	15	126.2	114.1	n.d.	2.53937	2.97E+14
Quela_Drill_ Hole_CCAM	44	0.8	9	21.3	3.3	7	2.02	10.4	109.3	104.3	n.d.	2.53937	2.80E+14
Quela_Drill_ Hole_CCAM	48.9	0.9	9.8	19.7	4.3	2.9	2.37	12	92.7	121.1	n.d.	2.53937	2.91E+14
Quela_Drill_ Hole_CCAM	47.9	0.99	10	19.7	4.1	4	2.29	10.3	149.7	112.9	n.d.	2.53937	3.46E+14
Quela_Drill_ Hole_CCAM	51.6	0.95	10.7	19.7	4.1	3.4	2.72	12.9	71.8	163.3	n.d.	2.55559	5.30E+14

Quela_Drill_ Hole_CCAM_1	32.1	0.72	6.9	14.2	2.3	17.8	1	n.d.	n.d.	n.d.	n.d.	2.54248	4.64E+14
Quela_Drill_ Hole_CCAM_1	45.8	0.88	9.4	19.5	3.9	7.8	1.89	n.d.	n.d.	n.d.	n.d.	2.54248	4.90E+14
Quela_Drill_ Hole_CCAM_1	51.9	1.08	11.3	20.4	4.1	3.8	2.42	n.d.	n.d.	n.d.	n.d.	2.54248	5.76E+14
Quela_Drill_ Hole_CCAM_1	53.1	0.9	11.5	19.9	4.1	2.6	2.85	n.d.	n.d.	n.d.	n.d.	2.54248	4.84E+14
Quela_Drill_ Hole_CCAM_1	40.7	0.78	8.2	16.9	3	13	1.53	n.d.	n.d.	n.d.	n.d.	2.53566	5.43E+14
Quela_Drill_ Hole_CCAM_1	51.2	0.99	10.7	20.3	4.2	2.8	2.68	n.d.	n.d.	n.d.	n.d.	2.53566	5.10E+14
Quela_Drill_ Hole_CCAM_1	38.4	0.76	7.4	16.3	2.9	14.8	1.35	n.d.	n.d.	n.d.	n.d.	2.53566	5.81E+14
Quela_Drill_ Hole_CCAM_1	54.1	1.1	11.5	20.1	4.4	2.7	2.65	n.d.	n.d.	n.d.	n.d.	2.53566	5.76E+14
Quela_Drill_ Hole_CCAM_1	46.9	0.86	9.2	18.7	5	6.3	2.34	n.d.	n.d.	n.d.	n.d.	2.53566	5.49E+14
Quela_Drill_ Hole_CCAM_1	51.5	0.98	10.3	19.7	4.8	2.6	2.78	n.d.	n.d.	n.d.	n.d.	2.53504	5.24E+14
Tailings													
Quela_Drill_ Tailings_ccam_1	45.9	1.0	9.3	21.2	4.3	5.6	2.2	7.1	65.6	57.3	n.d.	2.51969	3.04E+14
Quela_Drill_ Tailings_ccam_1	43.5	0.9	8.3	20.7	4.2	7.7	1.4	6.4	n.d.	61.2	n.d.	2.51969	2.34E+14
Quela_Drill_ Tailings_ccam_1	41.8	0.9	8.4	19.9	3.8	9.1	1.3	9.4	n.d.	81.3	n.d.	2.51969	2.82E+14
Quela_Drill_ Tailings_ccam_1	42.3	0.9	7.4	19.8	3.8	8.3	1.3	7	32.7	60.1	n.d.	2.51969	3.05E+14
Quela_Drill_	40.6	0.9	7.6	19.7	3.8	9.8	1.2	4.6	n.d.	59.1	n.d.	2.5203	3.01E+14

Tailings_ccam_1

Sebina

Target	SiO_2	TiO_2	Al_2O_3	FeO_T	MgO	CaO	Na_2O	Li ppm	Rb ppm	Sr ppm	Ba ppm	Distance m	Spectrum Total
Surface													
Sebina_ccam	41.8	0.82	9.5	15.2	3.1	15.1	1.74	20.5	45.7	244	n.d.	2.44963	7.82E+14
Sebina_ccam	48.5	0.91	11.1	17.3	4.1	8	2.4	13.9	59.9	155	n.d.	2.44963	5.08E+14
Sebina_ccam	50.2	0.95	11.1	17.9	4.5	6.6	2.32	16	78.4	163.3	n.d.	2.44963	5.23E+14
Sebina_ccam	41.3	0.77	8.1	16	3.3	14.8	1.13	17.4	44.4	161.3	n.d.	2.45194	5.57E+14
Sebina_ccam	29.6	0.63	5.8	11.6	2.2	23.8	0.81	23.3	34.8	202.4	n.d.	2.45194	7.09E+14
Sebina_ccam	45.9	0.88	11.2	17.1	5.2	9.1	2	18.7	51.8	202.4	n.d.	2.45194	6.83E+14
Sebina_ccam	40	0.85	8.3	16.5	3.2	14.7	1.46	20.5	47.7	224.7	n.d.	2.45542	7.89E+14
Sebina_ccam	33.2	0.67	6.1	12.2	3.2	22.3	0.96	n.d.	39.3	204.2	n.d.	2.45542	6.16E+14
Sebina_ccam	48.9	0.96	10.7	17.2	4.2	7.8	2.13	12.8	150.3	181.4	n.d.	2.4531	5.26E+14
Sebina_Drill_Hole_ccam	38.8	0.78	7.4	15.5	2.6	14.3	1.18	14.4	29.9	141.3	n.d.	2.45716	5.77E+14
Drill Hole													
Sebina_Drill_Hole_ccam	36.3	0.71	7.4	14.1	2.3	16.6	1.13	13.8	n.d.	131.5	n.d.	2.4589	4.83E+14

Sebina_Drill_Hole_ccam	42.7	0.83	9.2	16	2.7	12.7	1.57	11.6	127.4	133	n.d.	2.4589	5.19E+14
Sebina_Drill_Hole_ccam	49.9	0.87	10	19.1	4.7	3.4	2.27	15.4	64.5	111.1	n.d.	2.45368	4.25E+14
Sebina_Drill_Hole_ccam	49.7	0.93	9.3	19.3	4.5	4.9	2.11	15.4	170.2	135.9	n.d.	2.45368	4.30E+14
Sebina_Drill_Hole_ccam	40.5	0.8	7.6	15.4	3	13.2	1.51	13.1	n.d.	122.1	n.d.	2.45368	4.56E+14
Sebina_Drill_Hole_ccam	44.2	0.81	8.2	16.8	3.4	10.6	1.7	15.7	128.9	115.5	n.d.	2.45368	4.23E+14
Sebina_Drill_Hole_ccam	54.9	0.95	11.5	18.7	5.1	2.1	2.51	17.4	109.7	196	n.d.	2.45368	4.97E+14
Sebina_Drill_Hole_ccam	20.6	0.59	4.6	9.7	0.7	28.6	0.54	11.8	n.d.	178.7	n.d.	2.45368	8.18E+14
Sebina_Drill_Hole_ccam	43.9	0.86	9.4	17.2	3.5	11.1	1.53	12	95.7	180.4	n.d.	2.45368	6.93E+14

Appendix D

Chapter 3 Data Tables

Coordinates of Rock Samples

Sample	Location	Latitude	Longitude
Qc_stream_cobble	Redondo Peak	35°51'45.26"N	106°31'55.97"W
Qvdm_float_rhyolite	Cerro del Medio	35°53'9.53"N	106°28'18.09"W
Qvdm4_boulder	Cerro del Medio	35°53'11.50"N	106°28'17.20"W
Qvdms_outcrop_1	Cerro del Medio	35°52'46.90"N	106°27'32.90"W
Qvdms_outcrop_2	Cerro del Medio	35°52'29.10"N	106°26'50.50"W
Qvdm_stream_cobble	Cerro del Medio	35°52'25.80"N	106°26'44.80"W
Qvdm_stream_cobble_sediment	Cerro del Medio	35°52'25.80"N	106°26'44.80"W
Qvdms_outcrop	Cerro del Medio	35°52'27.41"N	106°26'36.60"W
Qvdms_outcrop_sediment	Cerro del Medio	35°52'27.41"N	106°26'36.60"W
Qvsm_float_rhyolite	South Mountain	35°50'48.20"N	106°31'14.10"W
Qvsm3_outcrop_altered	South Mountain	35°50'49.90"N	106°31'19.70"W
Qbt_outcrop_1	Redondo Peak	35°51'4.80"N	106°32'11.50"W
Qbt_outcrop_2	Redondo Peak	35°51'4.80"N	106°32'11.50"W
Qc_float_altered	Redondo Peak	35°51'11.20"N	106°32'9.20"W
Qc_float	Redondo Peak	35°51'25.40"N	106°32'4.30"W
Qbt_outcrop_3	Redondo Peak	35°53'7.40"N	106°30'34.60"W
Qc_altered	Redondo Peak	35°53'6.40"N	106°30'21.30"W
Qbt_float	Redondo Peak	35°53'12.00"N	106°30'18.10"W

XRD Patterns

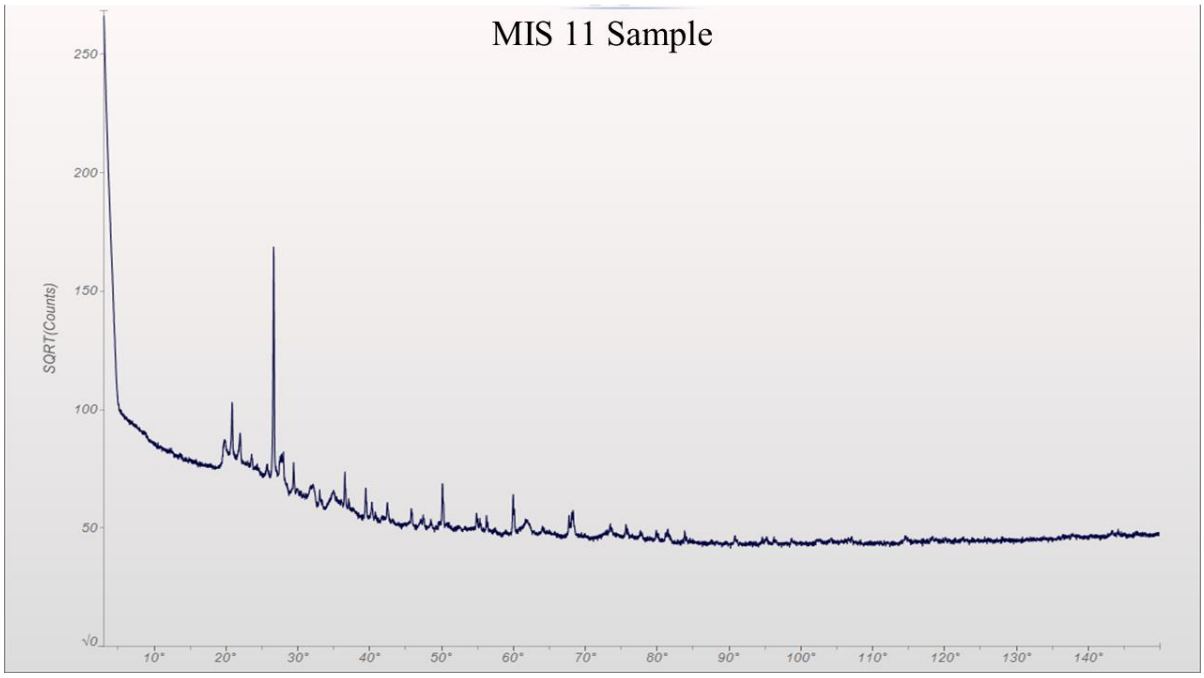

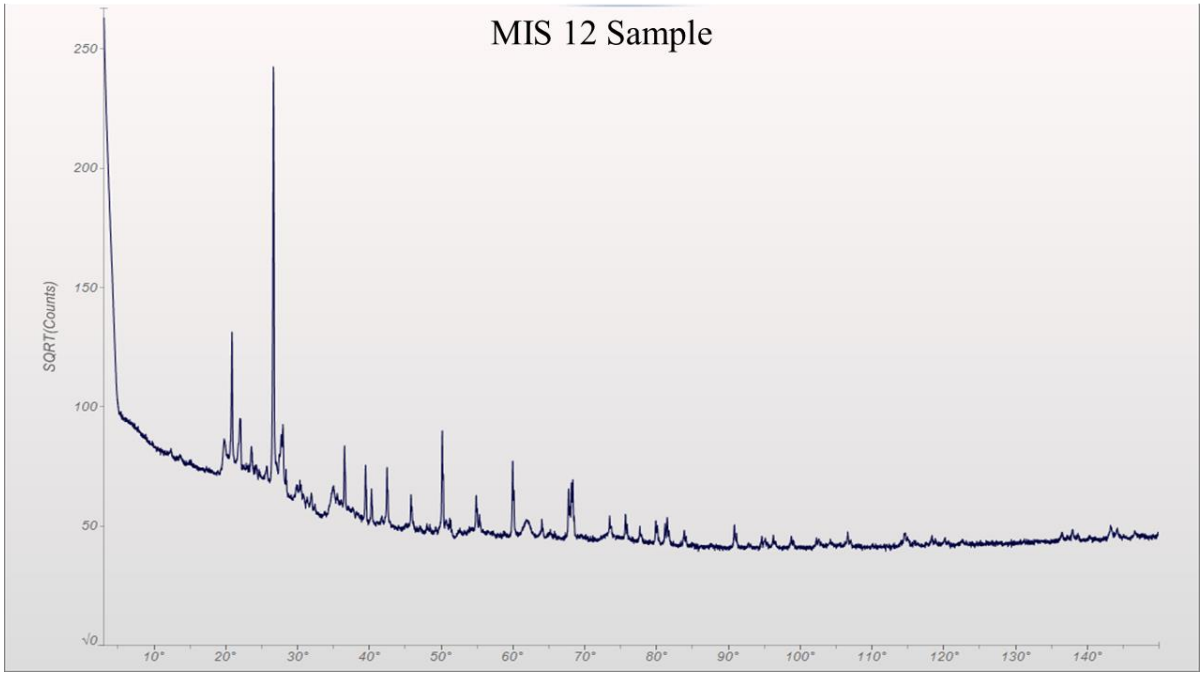

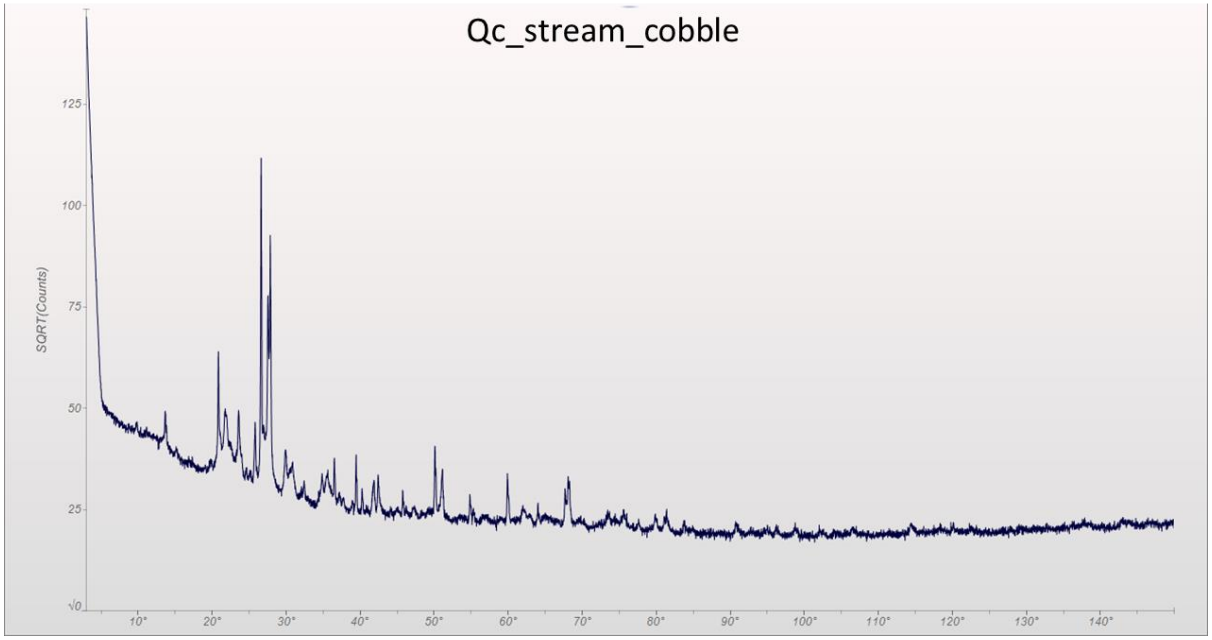
Qc_stream_cobble
SQRT(Counts)
125
100
75
50
25
√0
10°
20°
30°
40°
50°
60°
70°
80°
90°
100°
110°
120°
130°
140°

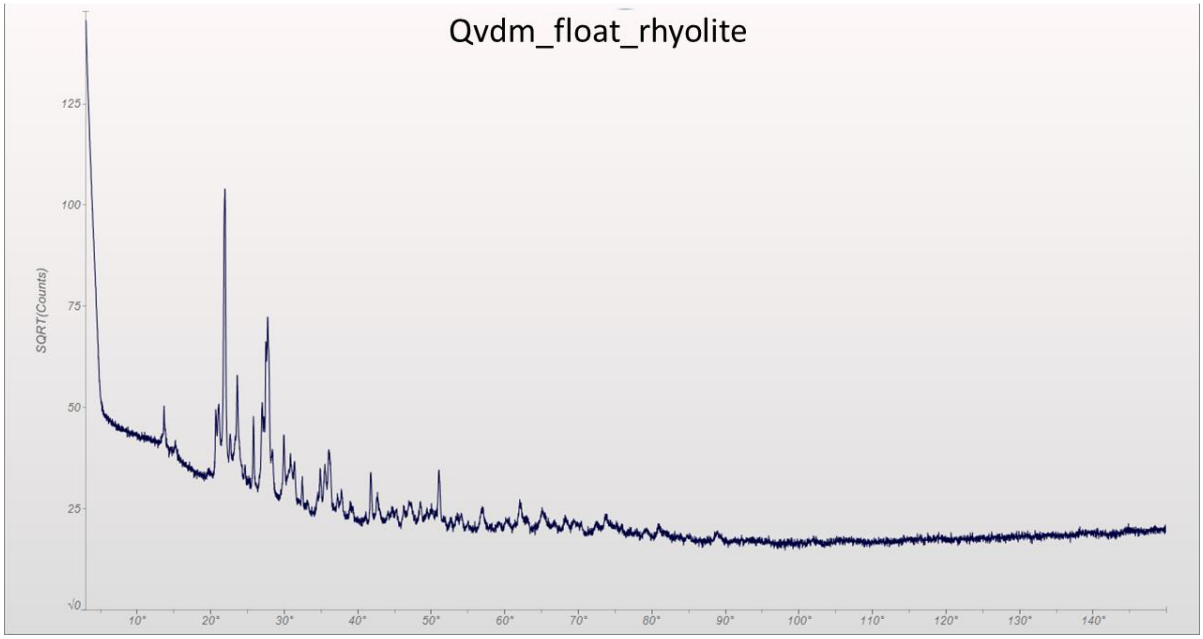
Qvdm_float_rhyolite
SQRT(Counts)
125
100
75
50
25
√0
10°
20°
30°
40°
50°
60°
70°
80°
90°
100°
110°
120°
130°
140°

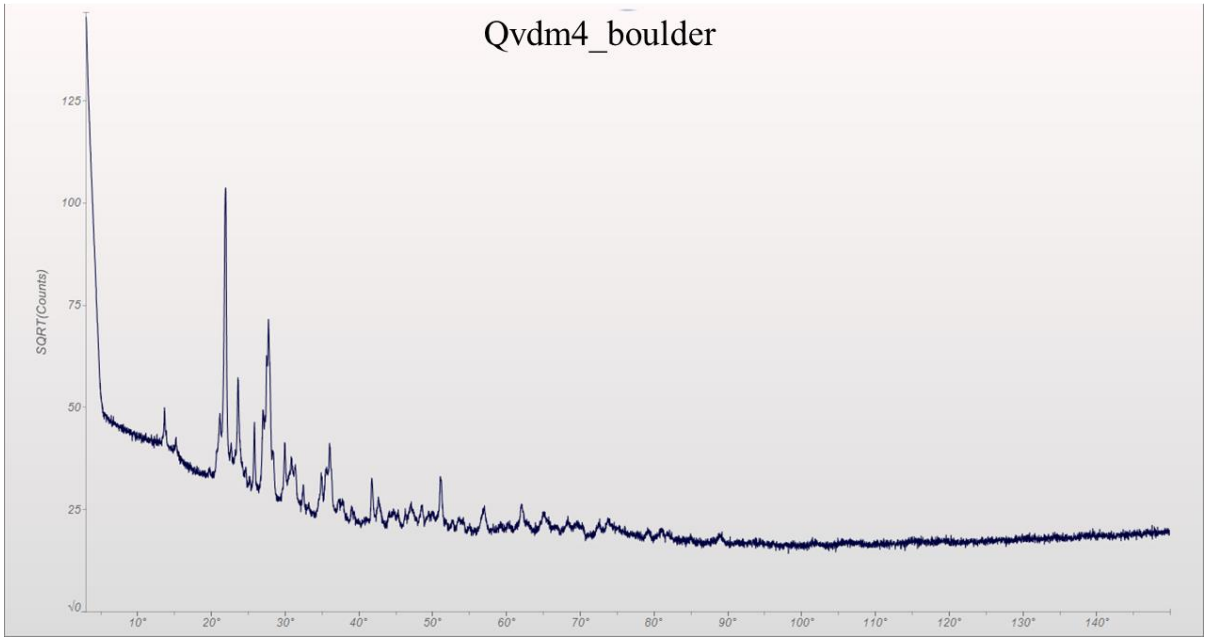
Qvdm4_boulder
SQRT(Counts)
125
100
75
50
25
√0
10°
20°
30°
40°
50°
60°
70°
80°
90°
100°
110°
120°
130°
140°

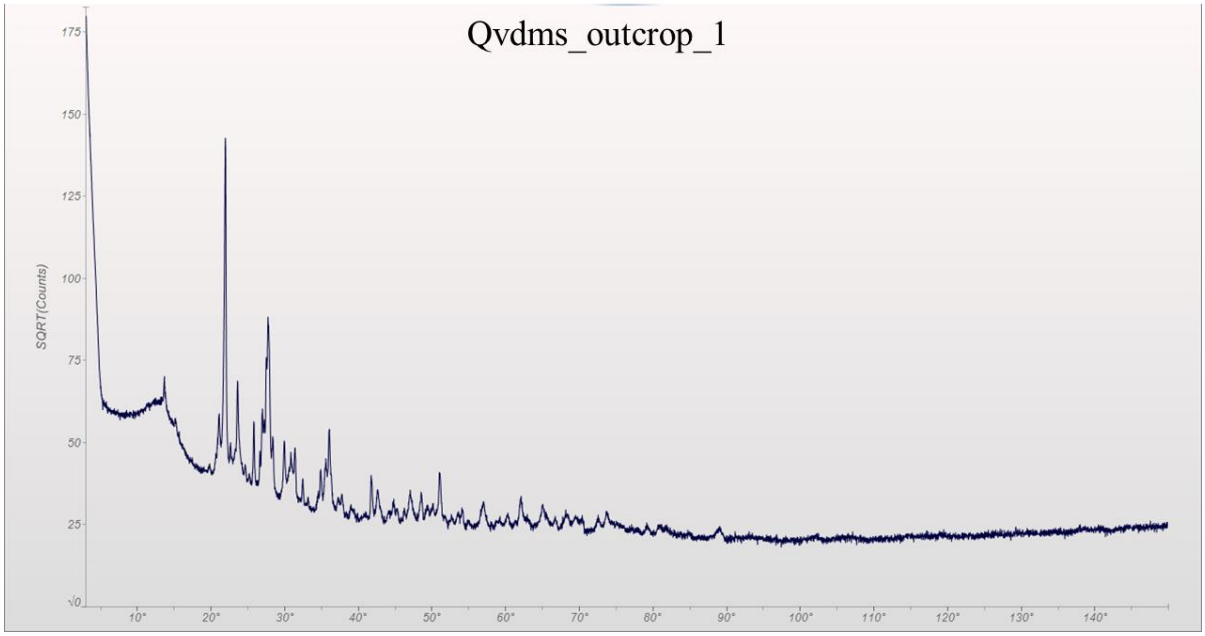
Qvdms_outcrop_1
SQRT(Counts)
175
150
125
100
75
50
25
√0
10°
20°
30°
40°
50°
60°
70°
80°
90°
100°
110°
120°
130°
140°

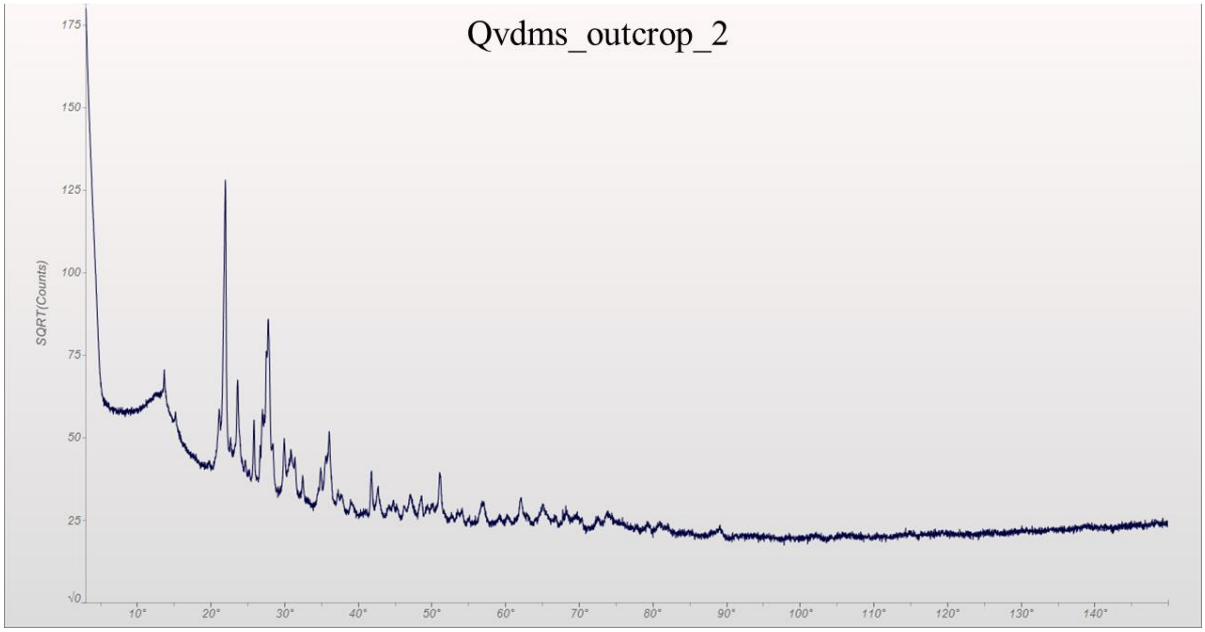
Qvdms_outcrop_2
SQRT(Counts)
175
150
125
100
75
50
25
√0
10°
20°
30°
40°
50°
60°
70°
80°
90°
100°
110°
120°
130°
140°

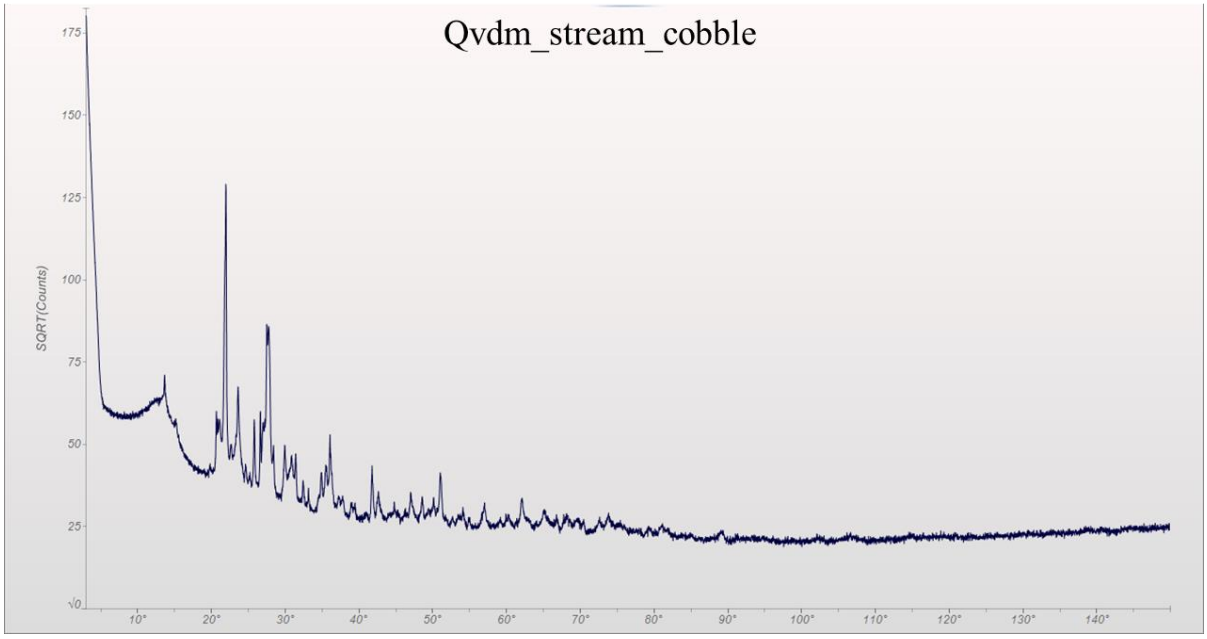
Qvdm_stream_cobble
SQRT(Counts)
175
150
125
100
75
50
25
√0
10°
20°
30°
40°
50°
60°
70°
80°
90°
100°
110°
120°
130°
140°

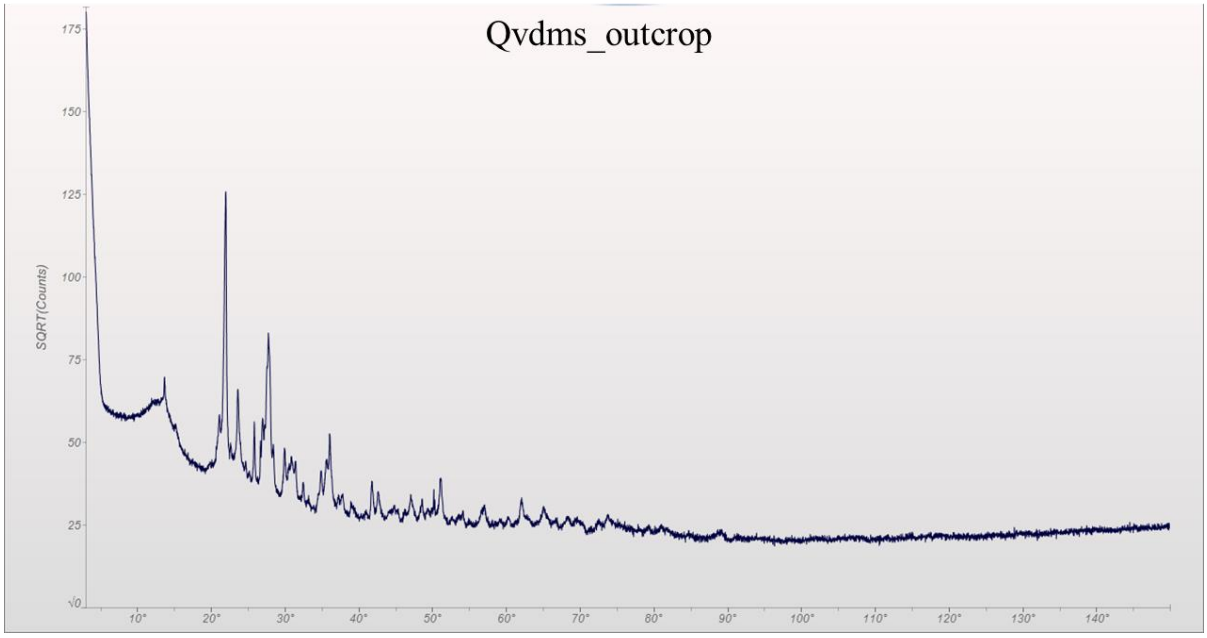
Qvdms_outcrop
SQRT(Counts)
175
150
125
100
75
50
25
√0
10°
20°
30°
40°
50°
60°
70°
80°
90°
100°
110°
120°
130°
140°

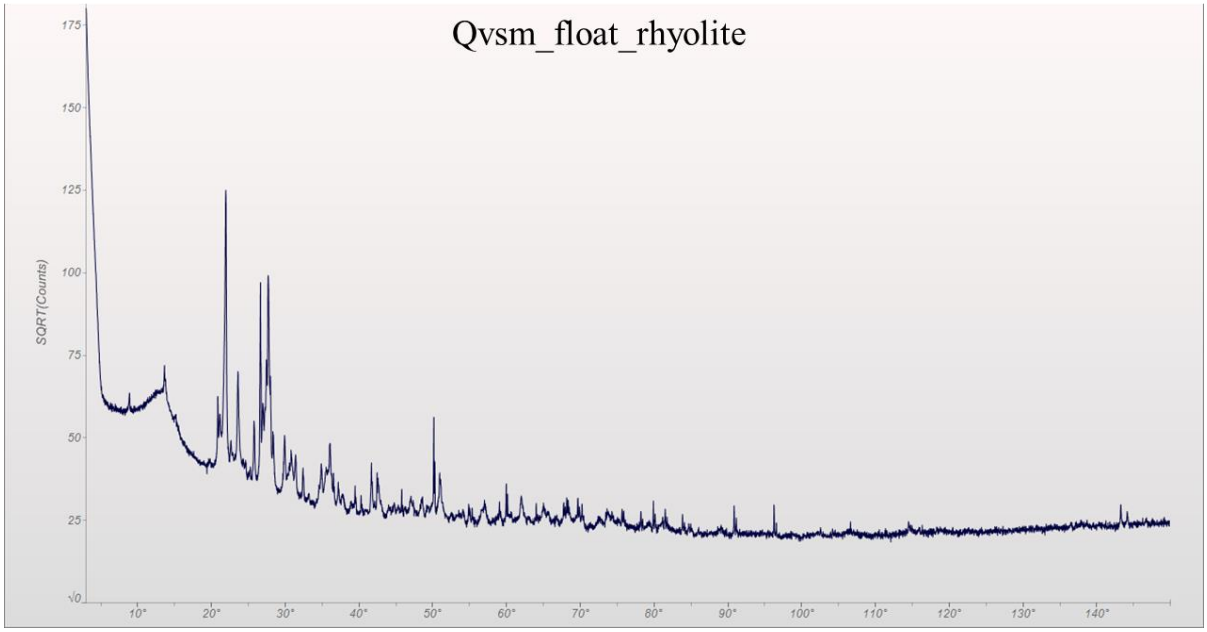
Qvsm_float_rhyolite
SQRT(Counts)
175
150
125
100
75
50
25
√0
10°
20°
30°
40°
50°
60°
70°
80°
90°
100°
110°
120°
130°
140°

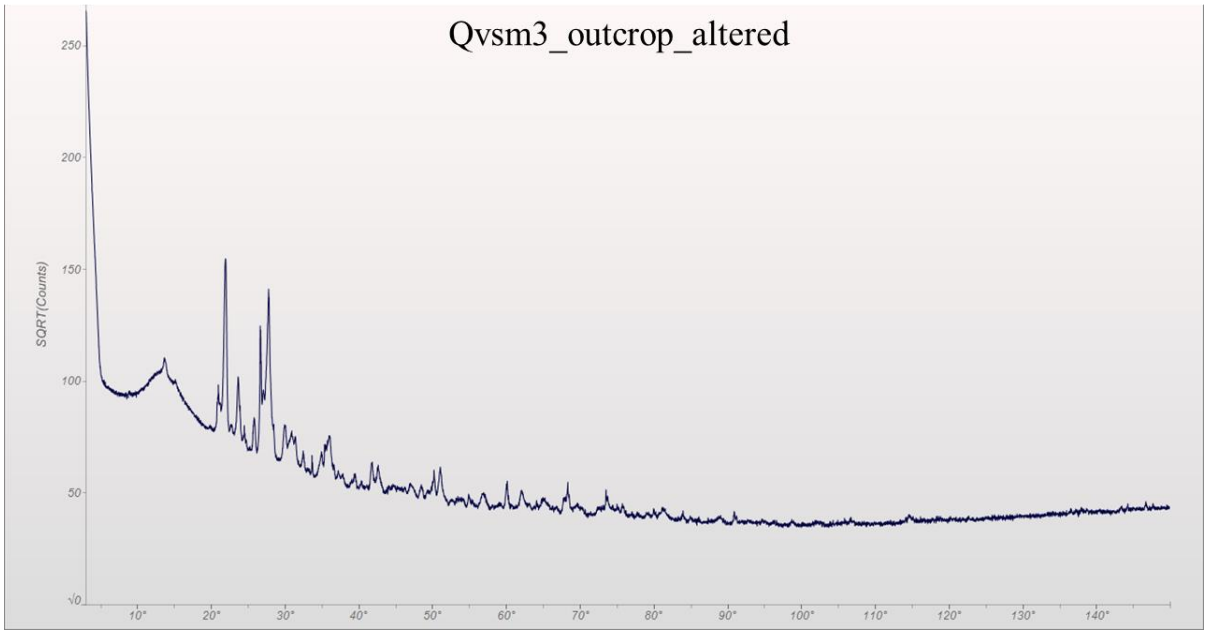
Qvsm3_outcrop_altered
SQRT(Counts)
250
200
150
100
50
√0
10°
20°
30°
40°
50°
60°
70°
80°
90°
100°
110°
120°
130°
140°

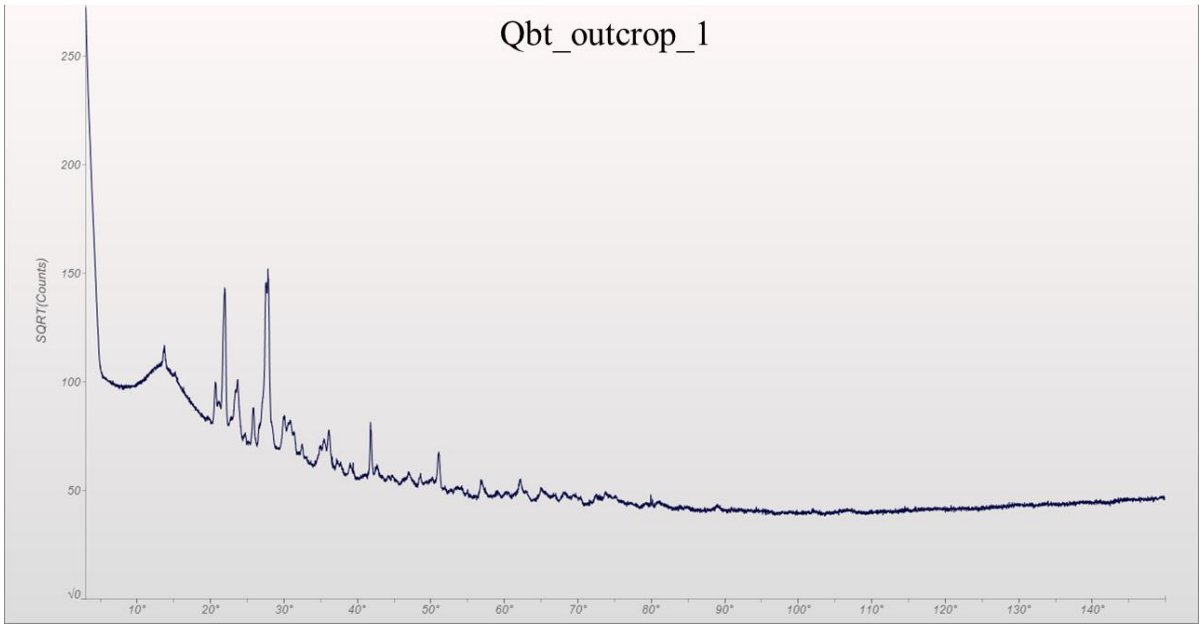
Qbt_outcrop_1
SQRT(Counts)
250
200
150
100
50
√0
10°
20°
30°
40°
50°
60°
70°
80°
90°
100°
110°
120°
130°
140°

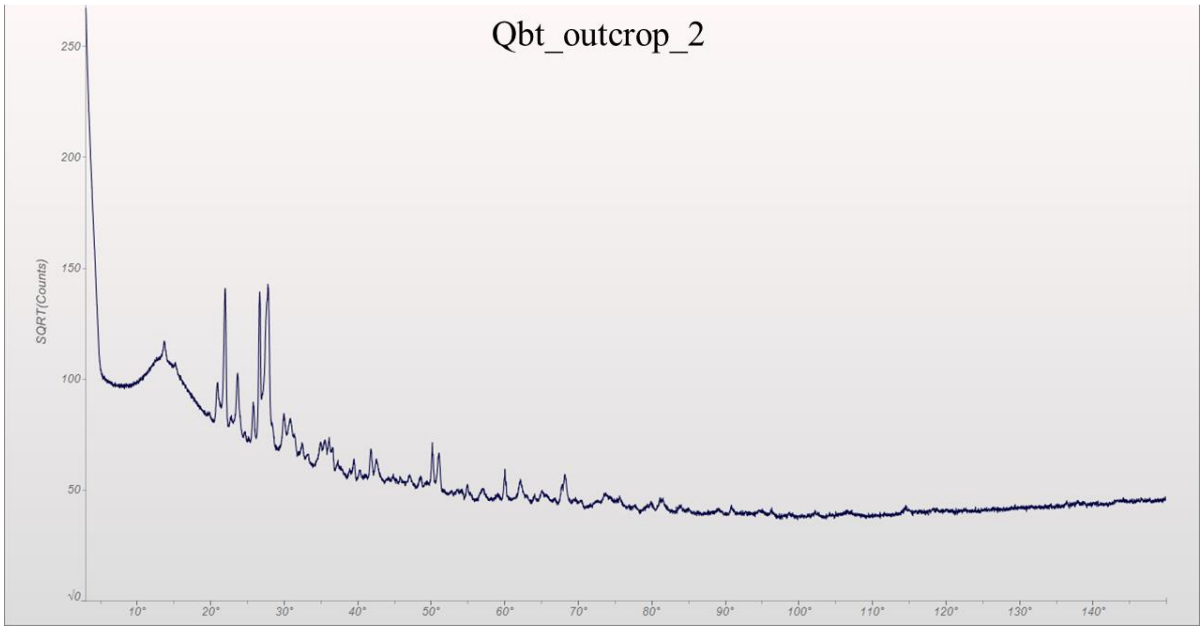
Qbt_outcrop_2
SQRT(Counts)
250
200
150
100
50
√0
10°
20°
30°
40°
50°
60°
70°
80°
90°
100°
110°
120°
130°
140°

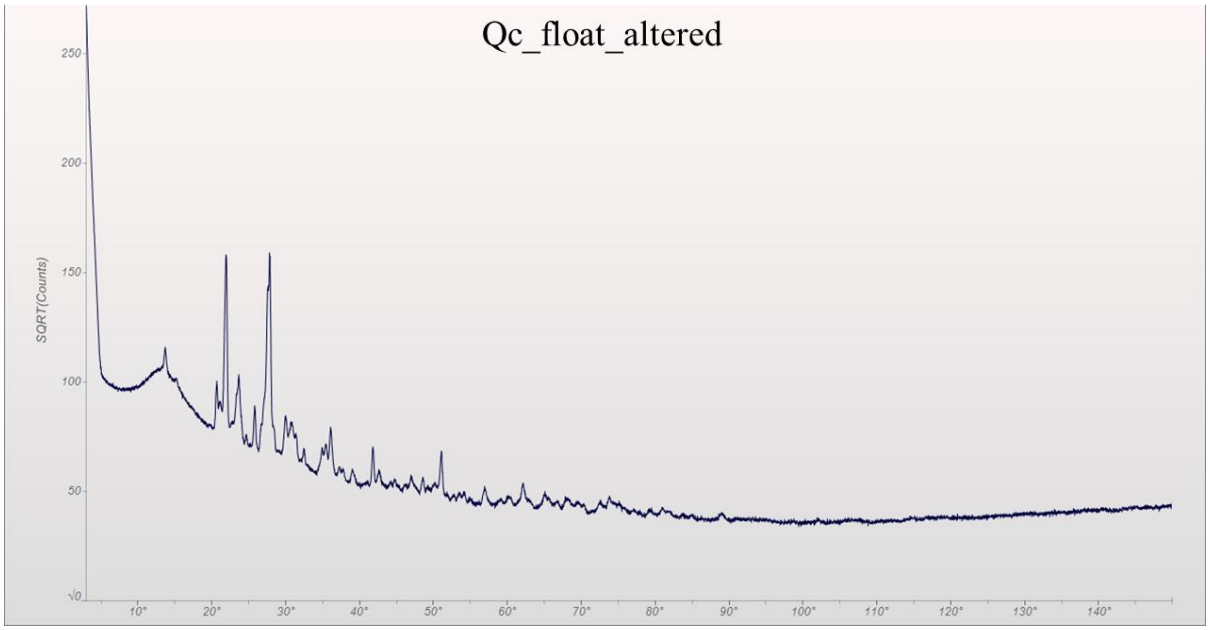
Qc_float_altered
SQRT(Counts)
250
200
150
100
50
√0
10°
20°
30°
40°
50°
60°
70°
80°
90°
100°
110°
120°
130°
140°

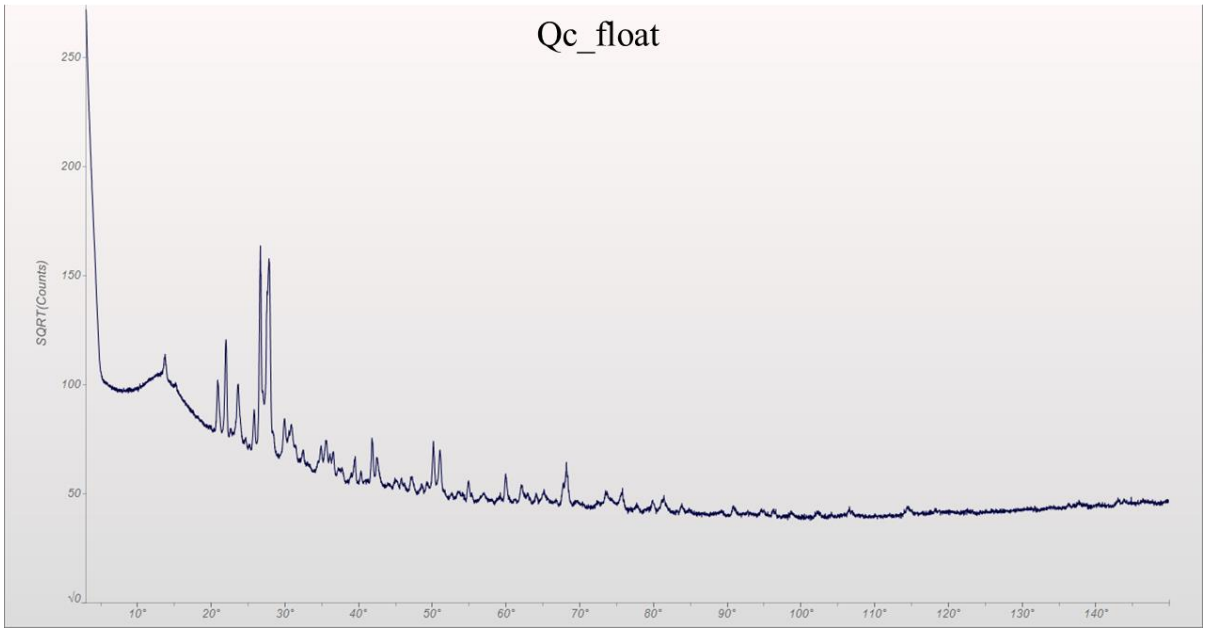
Qc_float
SQRT(Counts)
250
200
150
100
50
√0
10°
20°
30°
40°
50°
60°
70°
80°
90°
100°
110°
120°
130°
140°

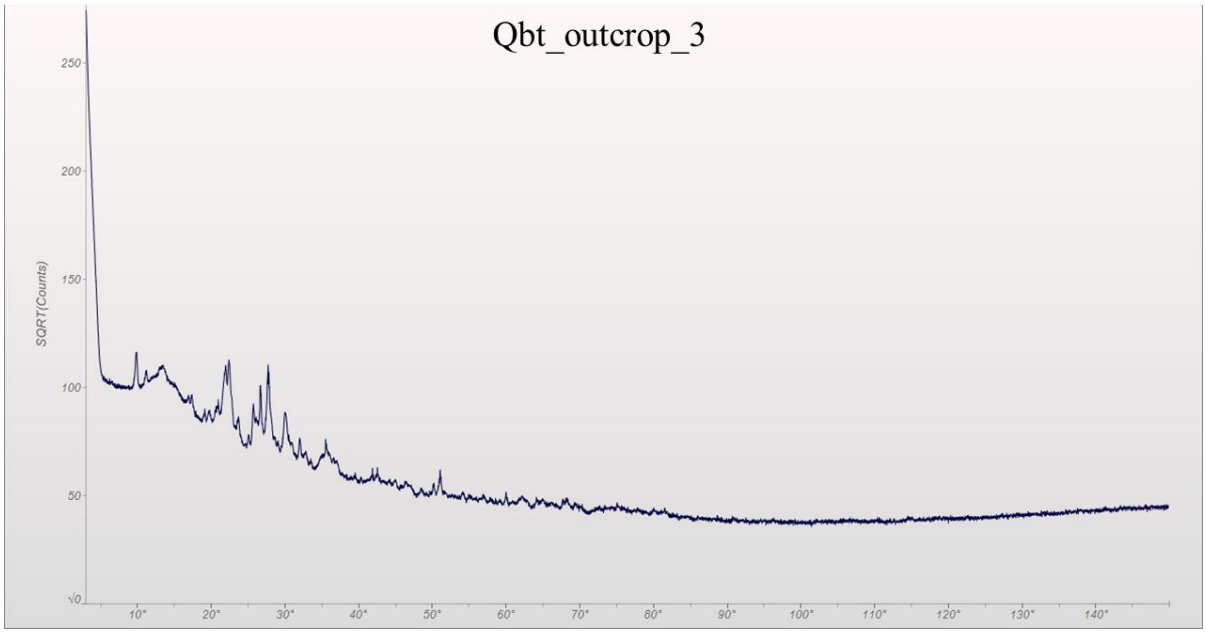
Qbt_outcrop_3
SQRT(Counts)
250
200
150
100
50
√0
10°
20°
30°
40°
50°
60°
70°
80°
90°
100°
110°
120°
130°
140°

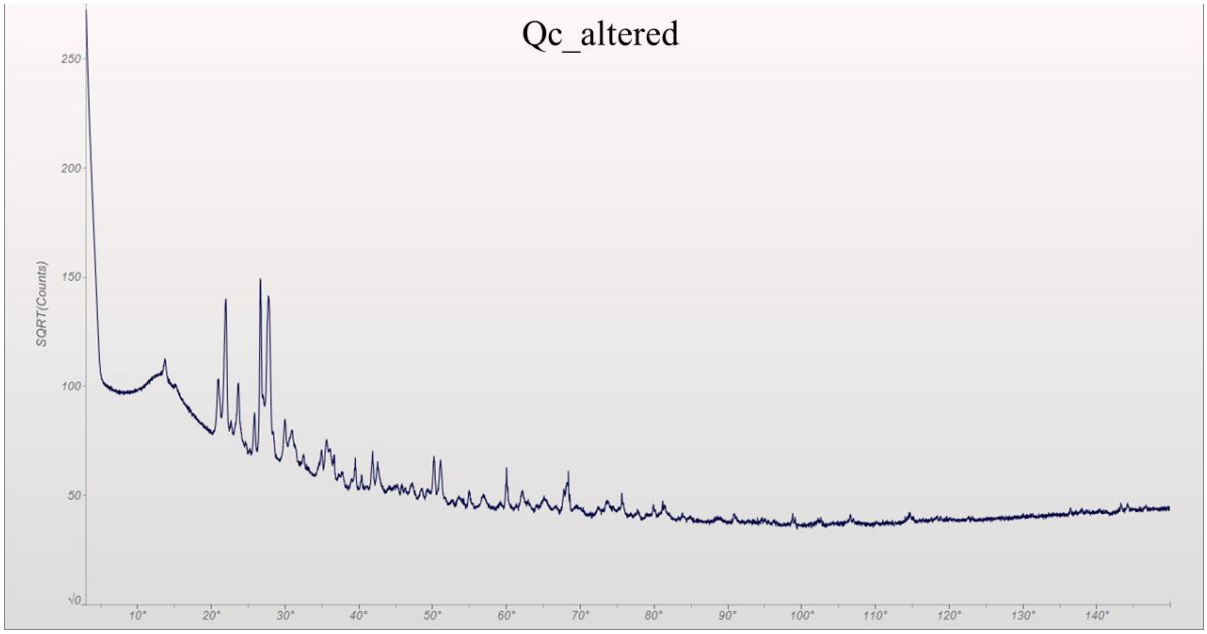
Qc_altered
SQRT(Counts)
250
200
150
100
50
√0
10°
20°
30°
40°
50°
60°
70°
80°
90°
100°
110°
120°
130°
140°

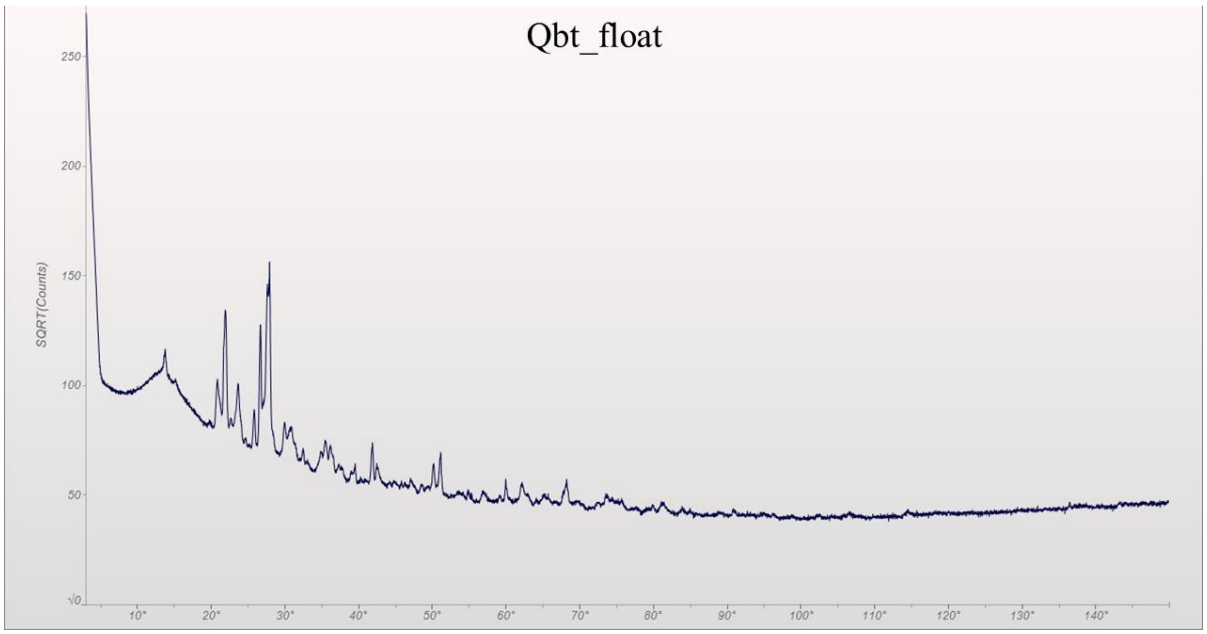
Qbt_float
SQRT(Counts)
250
200
150
100
50
√0
10°
20°
30°
40°
50°
60°
70°
80°
90°
100°
110°
120°
130°
140°

Appendix E

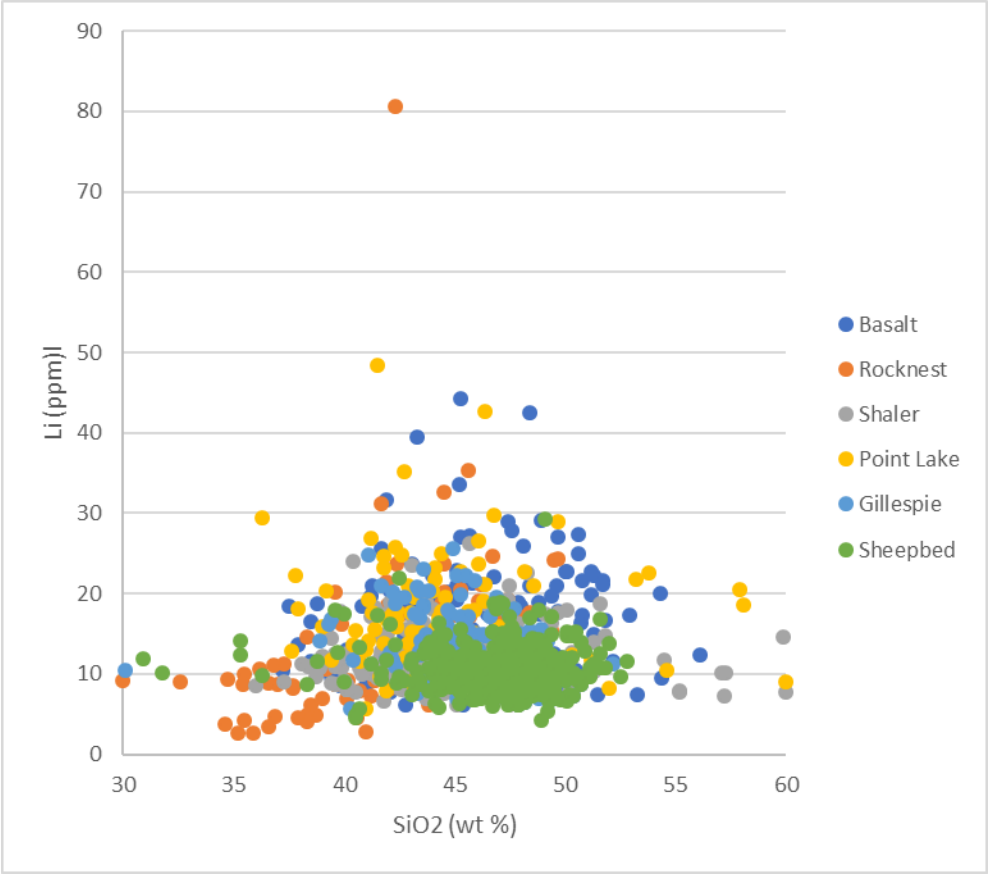
90
80
70
60
50
40
30
20
10
0
Li (ppm)]
30
35
40
45
50
55
60
SiO2 (wt %)
Basalt
Rocknest
Shaler
Point Lake
Gillespie
Sheepbed

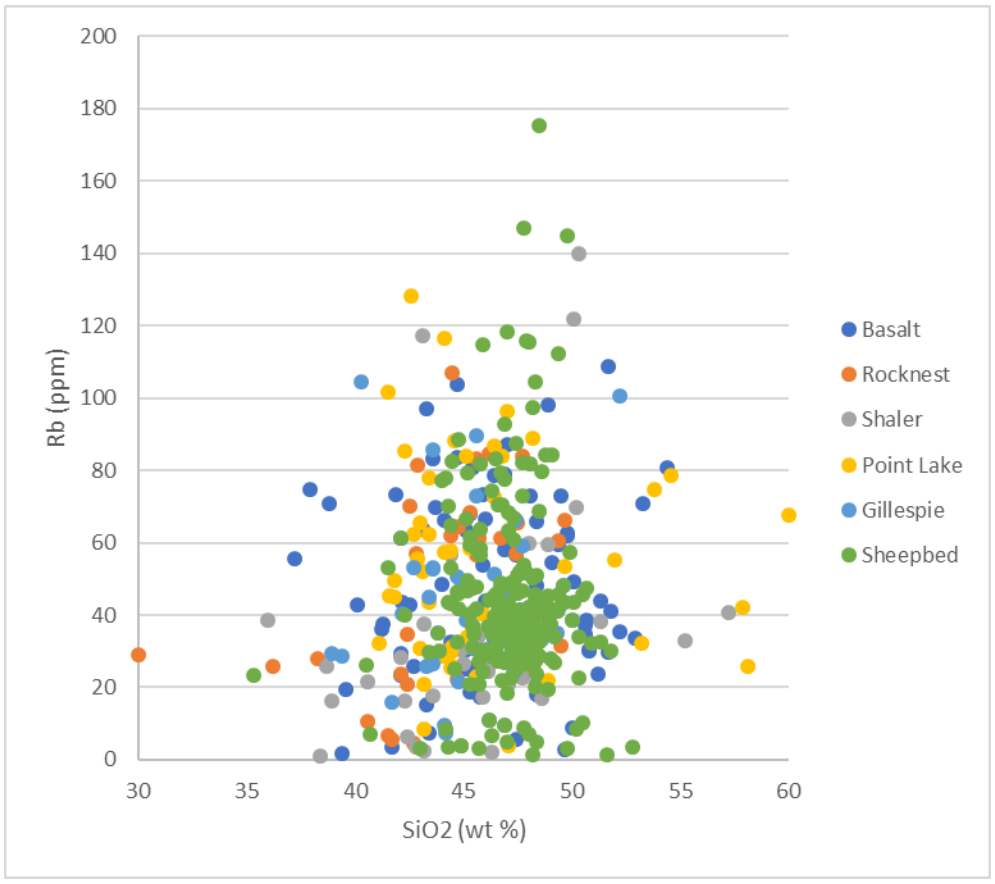
200
180
160
140
120
100
80
60
40
20
0
Rb (ppm)
30
35
40
45
50
55
60
SiO2 (wt %)
Basalt
Rocknest
Shaler
Point Lake
Gillespie
Sheepbed

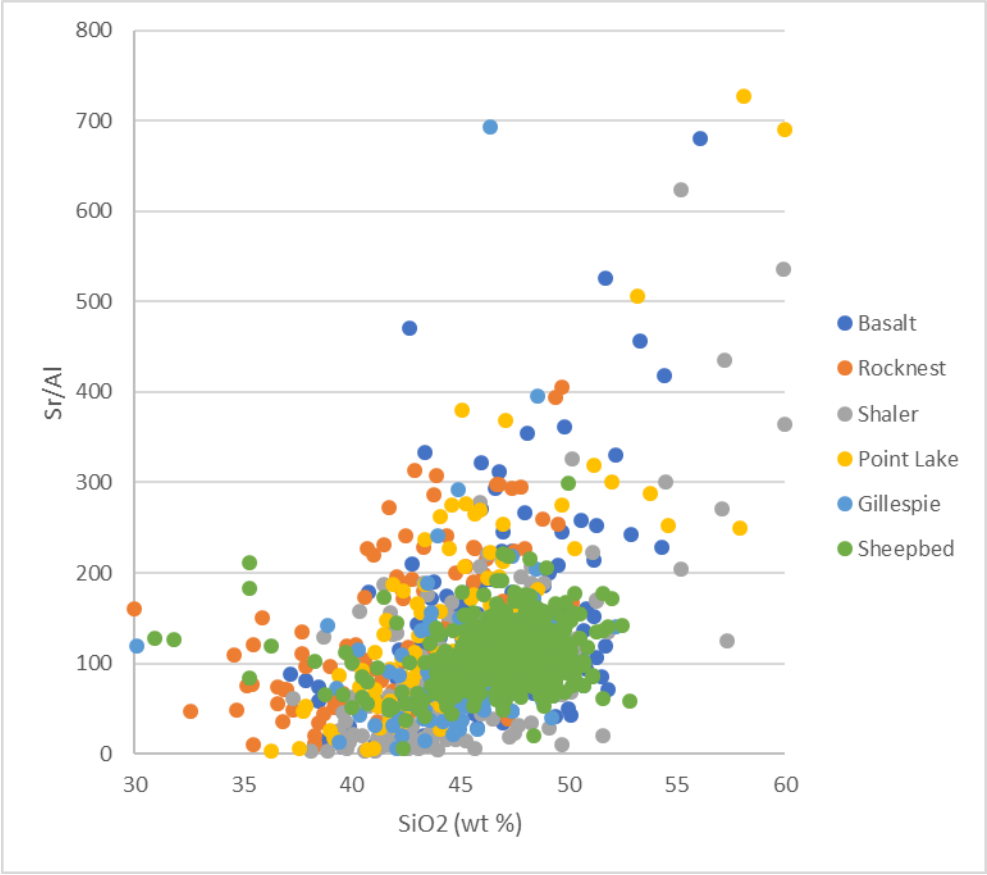
800
700
600
500
400
300
200
100
0
Sr/Al
30
35
40
45
50
55
60
SiO2 (wt %)
Basalt
Rocknest
Shaler
Point Lake
Gillespie
Sheepbed

Appendix F

Chapter 4 Data Tables

Rocknest Target	SiO_2	TiO_2	Al_2O_3	FeO_T	MgO	CaO	Na_2O	K_2O	Li (ppm)	Rb (ppm)	Sr (ppm)
Rocknest3	43.9	2.09	9.2	27.1	4	2.5	3.31	0.95	13.9	n.d.	307
Rocknest3	43.3	2.13	8.7	26.8	4	2.7	3.54	1.19	16.1	n.d.	228.9
Rocknest3	47.8	1.67	12.5	19.7	3.4	6.4	3.72	1.38	17.3	32	294.4
Rocknest3	44.8	2.04	9.7	21.6	3.9	7.2	3.14	1.06	17.1	64.4	200.2
Rocknest3	46.8	2.42	11.3	22.2	3.5	3.5	3.36	1.11	17.2	40.9	297.5
Rocknest7	47.7	0.91	9.3	18.8	5.6	6.2	2.82	0.78	9.4	83.8	82.6
Rocknest7	47.2	0.71	7.7	19.4	12.8	6.2	1.82	0.17	16.9	n.d.	38.9
Rocknest7	46	0.74	9.6	16.7	12.1	5.9	2.59	0.38	9.4	n.d.	120.2
Rocknest7	47	0.96	9.6	19.1	7.4	5.8	2.09	0.31	11.3	n.d.	85.7
Rocknest7	48	0.99	11.5	19.8	4.7	6.2	3.81	0.36	10.2	n.d.	88.6
Pearson	42.6	1.95	7.6	31.8	3.3	1.8	3.24	1.28	17.4	n.d.	118.1
Pearson	42.6	2.17	6.5	29.2	3.1	2	2.87	1	12.3	n.d.	42.3
Pearson	41.9	1.18	5.8	23.1	4	9.6	2.3	0.82	21.4	n.d.	69.9
Pearson	27.3	1.06	6.4	31.7	2	15	1.78	0.72	19.7	31.6	120.9
Pearson	38.5	2.42	7.2	34.1	2.6	1.7	2.83	0.73	6.2	n.d.	34.1
Pearson	42.7	1.61	5.8	27.8	5	3.3	2.6	0.61	12.1	4.6	31.9
Pearson	41.4	1.87	7	30.8	2.8	3.1	2.97	1.09	9.1	n.d.	81.3
Pearson	30	1.13	7.6	27.9	1.9	16	2.2	0.78	9.2	29	159.8
Pearson	38.3	1.83	8	27.7	3.4	6	3.13	0.8	14.6	n.d.	8.2
Pearson_1	37.3	2.39	7.1	29.6	3.7	1.8	2.81	1.08	11.2	n.d.	47.9
Pearson_1	39	2.93	6.7	33.2	2.5	1.9	2.6	0.86	6.9	n.d.	96
Pearson_1	38.7	2.72	7.5	31.5	2.2	1.8	2.98	1.17	4.8	n.d.	44.6

Pearson_1	47.4	1.42	9	23.4	4.4	3	3.52	1.19	19.3	24.1	117.8
Pearson_1	39.6	1.84	6.3	31.8	2.9	3.7	2.64	0.81	8.7	n.d.	53.5
Pearson_1	44.7	2.45	7.2	31.3	3.2	0.5	2.62	0.86	8.5	22.3	37.5
Pearson_1	43.6	1.77	9.1	26.2	3.9	4.5	2.82	0.76	12	n.d.	74.2
Pearson_1	43.3	1.92	8.1	30.1	3.2	2.4	3	0.97	10.8	n.d.	180.2
Pearson_1	39.2	1.7	7.8	33.2	3.3	4.1	2.78	0.73	10.6	n.d.	50.7
Snare	46.2	1.2	8.5	22.9	4.1	2.2	3.22	1.1	21.2	84.7	215.6
Snare	46.1	1.32	9	22.5	3.3	3.4	3.15	1.15	19	28.9	198.5
Snare	42.4	1.62	8.2	25.7	2.7	4.7	2.98	1.04	10.4	34.8	172.2
Snare	44.5	1.57	7.6	23.3	3.5	2.4	3.06	1.05	23.7	106.9	151.7
Snare	41.5	2.07	8.9	25.8	2.5	3.8	3.14	0.99	11.3	6.8	231.8
Rocknest6	38.3	1.4	8.5	30.5	3.9	6	2.71	0.63	4	n.d.	11.5
Rocknest6	35.5	1.57	8.6	34.4	3.3	4.5	2.84	0.78	10	n.d.	9.8
Rocknest6	36.6	1.29	9.4	34.5	3.3	3.4	3.02	0.79	8.8	n.d.	55
Rocknest6	40.6	1.2	9.9	26.1	3.5	6	3.18	0.91	4.6	n.d.	103.7
Rocknest6	41.2	1.19	8.7	23.7	4	7.1	3.3	0.82	7.2	n.d.	35.7
Rocknest6	38.3	1.34	8	27.1	3.8	5.7	2.59	0.45	4.9	27.8	19.5
Rocknest6	40.1	1.34	11.2	36.1	2.8	2.8	4.04	0.94	6.9	n.d.	20.7
Rocknest6	36.2	1.65	9	39.1	3	3.3	3.07	0.65	10.6	25.7	n.d.
Rocknest6	40.2	1.31	8.6	28.2	3.4	3.3	2.9	0.55	9.1	n.d.	120.1
Zephyr	43.4	1.32	7	20.6	5.1	6.4	2.21	0.56	13.6	n.d.	54.4
Zephyr	49.4	1.87	10.4	19.9	3.4	3.5	3.34	1.34	15.4	60.6	394.3
Zephyr	45.6	1.39	8.5	21.6	6.4	3.2	2.53	0.58	15	n.d.	74.1
Zephyr	49.5	2.83	9.2	19.9	4.1	3.4	3.99	1.91	24.2	31.4	254.1
Zephyr	44.5	2.87	7.4	20.4	4.4	3.2	3.16	1.2	20.1	n.d.	147.4
Zephyr	45.6	2.28	8.3	21.3	4.8	3.4	3.41	1.47	35.3	83.3	189.9
Zephyr	43.5	0.89	9.3	18.8	7.5	6.7	1.84	0.13	11.2	n.d.	87.9
Zephyr	43.4	1.56	7.9	21.1	5.5	4.5	2.1	0.54	10.5	n.d.	98.3
Zephyr	43.8	0.95	9.1	18.3	7.4	7.3	2.04	0.27	9.5	n.d.	111.4
Peg	48.8	1.6	12.7	20	3.2	3.9	3.7	1.26	12	n.d.	260

Peg	47.4	1.66	12.1	21.7	3.2	4	4.09	1.77	12.6	n.d.	95.8
Peg	46.5	2.2	13.4	22.5	2.9	3.7	4.21	1.77	12.9	n.d.	81.1
Peg	39.8	2.15	9.2	24.4	3.2	7	2.56	0.68	12.4	n.d.	119.1
Peg	46.2	1.46	9.2	20.2	3.7	6.6	2.98	0.85	10	n.d.	108.3
Peg	48.4	1.76	9.7	21.5	3.9	3.1	3.86	1.75	17.7	n.d.	80.9
Peg	50.2	1.31	11.1	19.5	4.2	7.4	3.68	1.4	9.1	n.d.	166.9
Peg	47	1.98	9.9	20.3	3.3	4	3.41	1.27	9	n.d.	168.9
Peg	48	1.67	11.8	21.7	3.2	4.2	4.21	1.28	8.7	24.6	227.2
Rocknest3_DP	46.7	1.74	11.8	20.7	3.6	6.2	3.32	1.12	24.7	61.2	297.8
Rocknest3_DP	49.7	1.38	14.5	19.7	3.4	4.6	3.96	1.42	24.3	66.2	405.5
Rocknest3_DP	44.4	1.5	11.7	21.2	3.6	7	3.78	1.36	18.7	61.9	240.8
Rocknest3_DP	47.4	1.56	12.7	19.9	3.5	5.7	3.85	1.42	16.6	56.9	294.2
Rocknest3_1	42.1	1.93	9.7	27.7	3.3	4.2	2.99	1.11	8.6	23.7	195.4
Rocknest3_1	42.1	2.05	8.2	31.4	2.7	2.4	2.98	0.95	8.3	n.d.	191.8
Rocknest3_1	40.7	1.86	9.6	29.8	3.1	3.7	2.95	0.94	7.9	n.d.	227.4
Rocknest3_1	41.7	1.22	10.4	25.9	6	4.9	2.7	0.78	31.2	5.5	271.9
Rocknest3_1	42.4	1.62	10.2	29.5	4.4	2.6	2.83	0.58	23.7	20.7	188.3
Rocknest3_1	43.8	1.55	11	27.5	2.7	2.8	2.98	0.79	6.2	n.d.	286
Rocknest3_1	39.6	0.95	8.1	26.6	4.7	9	2.75	0.67	20.1	n.d.	66.5
Rocknest3_1	42.4	1.49	8.3	28.8	3.7	3.8	2.78	0.6	19.6	n.d.	102.4
Rocknest3_1	40.6	1.56	10.2	30.6	3.3	4.3	2.72	0.57	11.7	10.5	173.1
Rocknest3_1	39.2	1.58	9.2	32.7	3.3	3	2.79	0.55	15.7	n.d.	59.9
Rocknest3_2	42	2.33	8.2	27.3	3.5	3.9	2.91	0.86	18.6	n.d.	135.1
Rocknest3_2	42.5	2.29	9.8	25.1	2.9	4.8	3.51	1.42	12.3	70.2	240.7
Rocknest3_2	45.7	2.13	10.9	22.5	3.4	5	3.44	1.31	17.1	61.4	227.4
Rocknest3_2	45.3	2.3	10.2	23.3	3.7	4.7	3.26	1.28	20.5	68.3	207.4
Rocknest3_2	47.5	1.74	11.5	19.8	3.4	6.6	3.67	1.48	18.6	65.4	224.2
Rocknest3_2	44.5	1.82	8.3	24.3	5.7	4.9	2.87	0.89	32.6	31.1	144.5
Rocknest3_2	45.6	1.66	11.4	21.3	3.9	6.4	3.67	1.35	15.2	56.8	228
Rocknest3_2	42.3	2.31	9.8	28.4	2.9	2	3.31	0.85	80.6	n.d.	181.8

Rocknest3_2	42.9	2.02	12.5	28	2.2	2.3	3.78	1.36	10.8	81.4	313.2
Rocknest3_2	42.8	1.76	11	28.5	2.9	2.9	3.55	1.44	11.6	57	192.8
Rocknest6a	37.9	1.16	10.4	28.9	3.1	4.3	3.21	0.74	4.6	n.d.	96.9
Rocknest6a	39.9	0.95	10.3	25.2	4	7.5	2.9	0.59	16.2	n.d.	108.7
Rocknest6a	32.6	1.06	9.1	32.1	2.6	7.8	3	0.72	9	n.d.	46.4
Rocknest6a	37.7	1.13	10.4	30.3	3.1	5.4	2.85	0.58	8.6	n.d.	110.6
Rocknest6a	34.6	1.21	10.4	33	2.7	2.4	2.92	0.55	3.8	n.d.	109.9
Rocknest6a	37	1.03	9.7	28.7	3.2	6.1	3.42	0.84	8.7	n.d.	70.8
Rocknest6a	34.7	1.16	8.8	33.5	3.2	5.5	2.78	0.61	9.4	n.d.	48.8
Rocknest6a	35.5	1.23	9	31.9	2.8	3.7	2.49	0.45	4.3	n.d.	121
Rocknest6a	37.7	1.14	10.1	30.1	2.7	4.1	3.06	0.73	8.2	n.d.	134.8
Rocknest6b	36.9	1.32	9.3	29.3	3.6	6.1	3.1	0.79	4.7	n.d.	71.6
Rocknest6b	29.1	0.83	8.5	30	2	14.2	1.84	0.42	11.1	n.d.	160.7
Rocknest6b	35.2	1.31	8.6	32.5	3	4.4	2.68	0.6	2.7	n.d.	74.7
Rocknest6b	41	1.51	11.1	24.8	3	4.7	2.77	0.62	2.8	n.d.	220.3
Rocknest6b	35.4	1.23	9.6	31.5	4	7	2.91	0.63	8.7	n.d.	77.4
Rocknest6b	35.9	1.44	9.9	37.2	2.7	2.7	2.87	0.67	2.7	n.d.	151
Rocknest6b	36.6	1.69	9.3	36.3	2.7	2.3	3.26	0.75	3.5	n.d.	73.3
Rocknest6b	36.8	1.21	9.5	32.9	2.8	6	3.28	0.71	11.1	n.d.	36.3
Rocknest6b	41.1	0.96	8.9	20	6.5	7.3	1.82	0.18	10.8	n.d.	93
Rocknest_3_Top1	36.8	1.24	5.2	29.3	7.1	5.9	1.9	0.17	n.d.	n.d.	n.d.
Rocknest_3_Top1	41	1.35	8.1	28.8	3.6	3.6	2.75	0.62	n.d.	n.d.	n.d.
Rocknest_3_Top1	39.8	1.28	6.6	27.2	4.3	5.8	2.63	0.43	n.d.	n.d.	n.d.
Rocknest_3_Top1	45.2	1.51	11	25.3	3.3	2.6	3.16	0.79	n.d.	n.d.	n.d.
Rocknest_3_Top1	44.9	1.59	10.9	25.5	2.8	2.1	3.82	1.17	n.d.	n.d.	n.d.
Rocknest_3_Top1	34	1.32	6.6	34.5	4.2	3.3	2.47	0.33	n.d.	n.d.	n.d.
Rocknest_3_Top1	37.9	1.27	7.9	30.6	4.7	3.9	2.5	0.39	n.d.	n.d.	n.d.
Rocknest_3_Top1	40.5	1.44	9	32	3.4	4.3	3.12	0.66	n.d.	n.d.	n.d.
Rocknest_3_Top1	44	1.25	9.4	24.9	3.5	4.2	2.95	0.63	n.d.	n.d.	n.d.
Rocknest_3_Top1	43	1.5	9.3	27.5	3.8	4.1	3.04	0.77	n.d.	n.d.	n.d.

Rocknest_3_Top1	39	1.68	7.3	34.7	3.4	2.8	2	0.39	n.d.	n.d.	n.d.
Rocknest_3_Top1	42.3	1.35	8.3	28.8	4.1	6.8	3.01	0.68	n.d.	n.d.	n.d.
Rocknest_3_Top1	41.2	1.58	6.6	30.9	4.1	5.8	3.04	0.78	n.d.	n.d.	n.d.
Rocknest_3_Top1	41.5	1.5	9.3	32.4	3.2	3.2	2.87	0.77	n.d.	n.d.	n.d.
Rocknest_3_Top1	32.2	1.97	7.2	43	2.8	1.3	1.74	0.27	n.d.	n.d.	n.d.
Rocknest_3_Top1	43.3	0.98	11.4	24	4.9	4.3	2.97	0.34	n.d.	n.d.	n.d.
Rocknest_3_Top1	39.8	0.8	9.7	19	8	7.7	2.02	0.28	n.d.	n.d.	n.d.
Rocknest_3_Top1	45.7	1.31	15.5	20.6	4.8	8	3.66	0.5	n.d.	n.d.	n.d.
Rocknest_3_Top1	50.1	0.73	16.1	16.8	7.3	8.3	3.67	0.8	n.d.	n.d.	n.d.
Rocknest_3_Top1	43	0.88	10.9	20.7	7.1	7.5	2.47	0.56	n.d.	n.d.	n.d.

Shaler

Target	SiO_2	TiO_2	Al_2O_3	FeO_T	MgO	CaO	Na_2O	K_2O	Li (ppm)	Rb (ppm)	Sr (ppm)
Stanbridge	49.1	0.69	5.5	21.5	16.9	4.4	1.82	0.26	17.4	n.d.	29.2
Stanbridge	45.7	0.81	5.7	20.7	11.3	9.6	1.49	0.21	26.2	n.d.	5.8
Stanbridge	46.4	0.98	8.2	19.7	11.1	5.5	2.43	0.62	18.8	n.d.	65.4
Stanbridge	51.3	1.07	12.4	19.6	7.3	3.2	2.98	0.9	13.9	n.d.	168.6
Stanbridge	47.8	1.01	11	20.2	8.8	4.1	2.98	0.74	16.4	n.d.	195.5
Port_Radium_1	49.2	0.83	9.6	17.8	7.5	7.7	2.37	0.81	11.3	n.d.	84.2
Port_Radium_1	45.2	1.17	7.7	20.4	8.2	4	2.68	0.68	12.6	31.3	104.5
Port_Radium_1	47.5	0.91	9.3	18.6	7.8	7.3	2.69	0.5	8.9	n.d.	84.8
Port_Radium_1	43.2	1.28	9.5	24	7	3.6	2.79	0.84	13.8	n.d.	100.2
Port_Radium_1	43.7	0.8	7.7	22.8	12.5	4.4	2.66	0.62	19	28.7	16.2
Rove	42.5	1.12	9.5	22.5	7.8	6	2.19	0.63	n.d.	n.d.	n.d.
Rove	44.1	1.06	8.5	23	10.2	5	2.23	0.68	n.d.	n.d.	n.d.
Rove	44.3	1.5	13.6	20.4	3.8	8	3.6	1.43	n.d.	n.d.	n.d.
Rove	41.4	0.9	10.3	20.1	7	7.8	2.59	0.47	n.d.	n.d.	n.d.
Rove	40.5	1.69	9.1	27.1	7.5	3.1	2.29	0.99	n.d.	n.d.	n.d.
Rove	41.4	1.33	9.5	28.8	7.6	3.6	2.91	0.83	n.d.	n.d.	n.d.

Rove	43.6	1.17	7.5	21.5	13.4	2.7	1.84	0.79	n.d.	n.d.	n.d.
Rove	40.6	0.94	8	22.6	11.3	4.5	1.87	0.54	n.d.	n.d.	n.d.
Rove	43.9	0.84	7.9	23.5	12	4.9	2.34	0.5	n.d.	n.d.	n.d.
Rove	50.5	0.82	11.9	20.3	5.4	7.2	2.83	1.4	n.d.	n.d.	n.d.
Rove	39.7	1.3	7.6	23.7	10.5	3.3	1.8	0.42	n.d.	n.d.	n.d.
Rove	47.4	0.98	10.3	21.6	9.6	5.1	2.26	1.05	n.d.	n.d.	n.d.
Rove	38.5	0.89	6.9	23.7	12.9	4.2	1.98	0.38	n.d.	n.d.	n.d.
Rove	41.8	1.32	7.5	22.8	11.3	3.2	2.08	0.64	n.d.	n.d.	n.d.
Rove	45.4	0.89	7.3	21.9	9	8.6	2.05	0.61	n.d.	n.d.	n.d.
Rove	45.3	1.17	8.3	20.8	7.6	6.9	2.31	1.05	n.d.	n.d.	n.d.
Rove	39.4	0.81	6.9	22.3	10.4	6.3	1.84	0.41	n.d.	n.d.	n.d.
Rove	42.5	0.88	9	20	7.9	7.1	1.91	0.3	n.d.	n.d.	n.d.
Ramah	47.1	0.91	8.7	21.1	9.1	5	3.02	1.06	13.1	20.8	82.5
Ramah	50.3	1.04	11.5	20.1	5.4	6	2.99	1.65	12.7	140	113.2
Ramah	50.1	1.07	10	20.5	6.4	7.1	2.96	2.39	17.9	121.8	67.5
Ramah	47.4	0.95	10.6	21	9.7	3.4	2.66	1.08	19.3	n.d.	87.6
Ramah	51.8	0.98	11	21.4	7.7	3.8	2.63	1.63	14.7	n.d.	134.8
Michigamme	40	0.79	7.7	20.3	10.3	4.8	1.9	0.35	9.2	n.d.	62.3
Michigamme	42.7	0.9	8.5	21.3	8.1	6.4	2.08	0.58	8.2	n.d.	31.8
Michigamme	49.4	0.85	10.5	20.1	8	6.5	2.89	0.97	16.4	n.d.	77.9
Michigamme	44.2	1.04	9.2	21.5	9.8	5	2.16	0.59	10.6	n.d.	90
Michigamme	42.5	1.2	8.1	22.7	12.7	2.8	2.02	0.61	8.3	n.d.	19.9
Michigamme	57.3	0.76	15	17.7	6.5	4	3.82	2.25	10.1	n.d.	125.3
Michigamme	46.4	1.01	11.9	21	8.1	5.6	2.66	0.91	10.5	n.d.	72.1
Michigamme	44.5	1.46	10.1	21.9	5.8	4.9	2.36	0.97	12.3	n.d.	70.9
Michigamme	46.5	0.98	10.1	22.4	8	4.5	2.71	1.11	8.6	n.d.	38.7
Michigamme	43.9	1.18	11.9	23.7	6.8	5.9	3.03	1.06	12.2	n.d.	42.5
Michigamme	44.8	1.15	8.4	22.5	11.3	3.6	2.44	0.94	9.7	n.d.	15.1
Michigamme	47.1	0.82	10.8	22.7	9.2	5	2.8	1.08	13.2	n.d.	81.9
Michigamme	44.2	1.45	10.6	23.2	6.8	4.6	3	1.07	9.3	n.d.	74.5

Michigamme	46.9	2.76	15.8	21.2	3.8	1.8	4.19	2.18	7	n.d.	215.4
Michigamme	47.7	0.89	10.8	21.6	8.6	7	2.57	0.95	15.6	22.5	31.1
Michigamme	51.1	1.27	14.8	21.2	6.1	3.5	3.3	1.73	9.8	n.d.	222.4
Michigamme	47.5	1.04	7.4	19.8	6.4	12.4	2.16	0.96	20.9	30.6	23.4
Michigamme	48.6	0.68	14.3	17.4	6.7	8.5	3.15	0.72	7.9	16.9	131.4
Michigamme	42.8	1.01	8.4	22.8	8.6	7.2	2.39	0.69	15.6	3.5	30.5
Michigamme	45.4	1.31	12.3	21.3	5.9	6.2	2.77	0.92	10	n.d.	75.7
Piling	43.1	1.1	7.3	21.2	9.5	3.8	1.97	0.42	10.7	n.d.	14.7
Piling	41.3	1.47	6.8	22.7	9.1	3.6	2.01	0.43	9.9	n.d.	7.5
Piling	43.2	1.4	8.3	22	8.6	2.5	1.86	0.67	9.3	2.6	75.9
Piling	40.1	3.29	7.8	25	7	3.2	1.92	0.57	8	n.d.	51.3
Piling	43.7	0.91	7.8	21.7	10.9	4.2	1.68	0.45	9.4	n.d.	22.7
Piling	43.5	0.87	6.9	21.6	10.5	6.2	2	0.41	12.7	n.d.	9.1
Piling	51.3	0.81	12	21.2	7.7	3.2	2.58	1.57	10.3	38.3	169.9
Piling	46	1.01	10.2	20.5	9	3.4	2.5	0.87	9.4	n.d.	44.1
Piling	41.1	1.07	9.6	29.2	7.1	3.8	2.79	0.7	10.2	n.d.	3.5
Gogebic	45.6	1.14	8.8	21.4	10	3.7	2.7	0.79	14.6	n.d.	84.6
Gogebic	42.6	1	8.5	21.2	8.1	7.9	2.1	0.36	12.5	n.d.	69.1
Gogebic	40.1	1.4	5.9	20.1	17.5	1.7	1.3	0.13	12.5	n.d.	n.d.
Gogebic	40.1	0.94	6.9	20.5	7.5	9.9	1.58	0.21	8.7	n.d.	21
Gogebic	44.8	1.49	10.3	18.9	5.9	8.9	2.68	0.81	n.d.	n.d.	23.9
Gogebic	39.6	1.34	9.2	24.1	6	6	2.75	0.78	8.7	n.d.	45.1
Gogebic	49.7	0.72	9.6	18.4	7.4	12	2.53	0.88	17.6	n.d.	10.6
Gogebic	40.7	1.6	8.3	25.1	9.5	3.3	1.96	0.28	10.7	n.d.	59.6
Gogebic	45	1.03	10.7	21	7.6	6.3	3.03	0.96	14.7	26.5	133.8
Saglek	50.4	1.15	13.1	20	4.4	4.7	3.63	1.05	7.2	n.d.	127.8
Saglek	46.7	1.05	10.4	21.2	8.1	4.9	2.67	0.54	11	n.d.	100.2
Saglek	49.7	0.85	9.7	18.8	7.3	7.4	2.57	0.55		n.d.	65.8
Saglek	47.5	1.79	11.9	18.4	3.7	4	3.42	1.08	6.2	n.d.	159.1
Saglek	39.4	1.02	5	21	8	9.7	1.2	0.11	8.8	n.d.	25.1

Saglek	47.7	1.14	8.6	22	10	2.3	2.84	0.77	11.8	n.d.	130.3
Saglek	47	1.2	10.5	20.5	8.6	1.9	3.39	0.86	8.2	n.d.	148.6
Saglek	57.1	0.77	22.2	2.1	0.9	7.3	6.41	0.74	10.2	n.d.	270.8
Saglek	47.3	0.73	8.9	17.7	7.4	9.9	1.87	0.44	12.9	n.d.	18.2
Rusty_Shale	48.3	1.1	15.1	20	5.3	7.5	4.05	1.75	22.6	n.d.	34.8
Rusty_Shale	41.7	1.36	8.1	25.3	10.4	2.9	2.45	0.74	17.5	n.d.	9.4
Rusty_Shale	44.6	1.5	11.6	25.3	7.1	2.8	3.91	1.43	13.7	n.d.	51.2
Rusty_Shale	43.6	1.62	9.8	26	9.1	4	3.02	1.03	16.4	17.8	22.6
Rusty_Shale	42.3	2.36	8.6	32	5.9	2.3	2.94	0.72	9.9	n.d.	
Rusty_Shale	43.3	1.26	10.9	25.8	8.8	3.5	3.5	1.11	11.4	n.d.	17.5
Rusty_Shale	45.8	1.21	16.1	24.5	5.1	4	4.56	1.41	10.6	n.d.	88.7
Rusty_Shale	42	1.34	12.1	27.4	5.5	5.3	3.6	1.01	15	n.d.	35.5
Rusty_Shale	41.7	1.41	11.4	27.9	5.4	5.4	3.62	1.25	11.7	n.d.	17.4
Rusty_Shale	44.6	1.43	17	23.8	5.5	5.9	4.51	1.28	15.2	n.d.	81.9
Montaigne	46.1	0.88	8.3	19.9	9.6	5.8	2.29	0.67	10.2	25.4	70.3
Montaigne	48	0.99	11.3	20.6	7.1	4.2	2.57	0.66	7.2	n.d.	151.5
Montaigne	41.9	0.95	6	21.9	14.9	2.8	1.9	0.35	10.4	n.d.	27.3
Montaigne	43.9	1.38	8.1	21	5.5	6.1	2.39	0.66	8.3	n.d.	
Montaigne	41.9	1.59	8	21.8	4.9	3.4	2.53	0.71	9.8	n.d.	131.8
Montaigne	43.5	1.2	9	21.1	6.3	5.7	2.27	0.69	13.9	n.d.	175.9
Montaigne	43.6	0.92	8.2	22.2	9.7	4.6	2.1	0.47	14.7	n.d.	50
Montaigne	38.1	0.83	4.5	21.6	17.9	2.1	1.41	0.3	11.2	n.d.	2.9
Montaigne	41.9	1.36	6.7	21.7	9.9	3.8	2.05	0.55	12.6	n.d.	28.9
Montaigne	42	1.03	6.9	21	13.7	3.3	2.18	0.48	11.6	n.d.	50.5
Montaigne	45.3	0.87	10.4	20.7	8.9	4.6	2.84	0.67	10.9	n.d.	122.1
Montaigne	46.1	1.15	11	21.2	6.3	4	2.98	0.9	9.8	24.5	138.1
Montaigne	47.4	0.8	9.4	19.1	8	5.9	3.11	0.91	7.5	n.d.	75.1
Montaigne	48.3	1.11	8	20.3	9	5.1	2.74	0.5	10	n.d.	207.5
Montaigne	42.6	1.23	8.9	21.7	7.9	4.6	2.6	0.71	9.6	n.d.	67.3
Montaigne	43.2	0.92	7.5	21.8	11.2	4	2.18	0.61	12.4	n.d.	66.6

Double_Mer	40.4	0.89	8.4	22.4	6.9	6.1	2.24	0.37	24	n.d.	157.2
Double_Mer	42.4	0.81	9.3	19.1	7.8	7.3	2.36	0.27	13.2	n.d.	75.9
Double_Mer	40.8	1.45	10.1	21.4	4.8	8.5	2.13	0.18	10	n.d.	53.2
Double_Mer	47.3	0.97	8	21.9	10.2	4.2	2.67	0.98	12.1	n.d.	119
Double_Mer	46.5	0.89	12.3	18.9	6.4	7.2	2.58	0.32	12.8	n.d.	158.3
Double_Mer	48	1.12	12.8	20.1	4.7	6.8	3.47	0.66	8.7	60	108.1
Double_Mer	44	0.92	7.6	23.1	13.5	2.3	2.55	0.75	18.1	n.d.	4.1
Double_Mer	44.4	0.84	7	22.4	13.7	4.2	2.46	0.62	13.7	n.d.	15.7
Double_Mer	54.5	0.86	16.6	18.2	6.5	3.9	3.31	1.02	11.7	n.d.	300.6
Aillik	42.3	0.81	7.5	21.7	12.2	4.7	2.14	0.21	9.4	16.1	39.6
Aillik	45.9	0.82	10.2	20.2	6.9	7.9	2.78	0.47	9.5	n.d.	127.4
Aillik	42.7	0.85	8.7	21.9	10.9	4.4	2.34	0.27	10.8	n.d.	102.7
Aillik	41.8	0.96	8.3	21.8	6.8	7	2.53	0.33	10.4	n.d.	n.d.
Aillik	43.6	0.79	7.6	20.5	8	8.6	2.12	0.34	12	n.d.	41.9
Aillik	42.7	0.76	6.4	21.9	13.7	5.2	1.98	0.21	11.9	n.d.	19.8
Aillik	38.9	0.94	5.5	22.5	13.2	4.8	1.69	0.14	10.7	16.4	3.5
Aillik	41.7	0.83	6.4	22.3	14	4.5	2.03	0.23	10.8	n.d.	22.7
Aillik	39.4	0.7	6.3	22.4	16.2	3.6	1.99	0.18	14.5	n.d.	19.4
Eqalulik	60	0.75	19.1	7	2.3	4.2	6.11	1.75	7.7	n.d.	364.5
Eqalulik	36	1	4.5	23.8	12	6.9	1.54	0.08	8.5	38.7	n.d.
Eqalulik	44.5	0.84	7.8	20.4	8.2	7.9	2.46	0.3	7.6	n.d.	61.5
Eqalulik	45.1	1.03	10	21.4	8.9	6	2.17	0.25	6.1	n.d.	71.6
Eqalulik	42.4	0.94	8.4	21.7	6.8	8.6	2.32	0.36	9.9	n.d.	n.d.
Eqalulik	38.4	0.98	5.8	23.4	12.2	5.2	1.74	0.13	10.9	0.9	n.d.
Eqalulik	43.7	1.17	11	27	8	3.9	2.97	0.62	6.9	n.d.	n.d.
Eqalulik	42.6	0.84	8.5	23.4	11.9	4.2	2.54	0.43	8	n.d.	5.7
Eqalulik	40.5	1.27	7.4	22.9	7.1	6.6	2.22	0.28	7.7	n.d.	20.3
Cartwright	43.9	1.17	9	20.5	7	8.7	1.92	0.39	12.8	n.d.	37.9
Cartwright	41.5	1.33	6.6	20.5	12.7	3.9	1.71	0.3	9.5	n.d.	13.1
Cartwright	47.5	1.01	11.8	19.3	5.4	8.2	2.6	0.82	11.7	n.d.	123.5

Cartwright	39.6	1.13	7.2	21	9.2	6.1	1.82	0.41	10.9	n.d.	7.8
Cartwright	45.3	1.23	11.1	21.1	6.5	5.2	2.97	1.11	8.7	n.d.	95.9
Cartwright	45.7	1.35	13.7	20.9	5.8	4.5	3.4	1.25	13.3	34.3	139.8
Fabricius_Cliffs	44.6	1	10.8	20.4	7.2	7.8	2.38	0.43	11.9	n.d.	105.6
Fabricius_Cliffs	42.1	0.85	10.5	22.4	6.7	8.5	2.64	0.39	18.9	n.d.	44.8
Fabricius_Cliffs	39.8	0.85	8.8	24.6	8.8	6	2.32	0.3	17.8	n.d.	5.7
Fabricius_Cliffs	41.4	0.91	11.5	24.1	6.1	7.3	2.89	0.49	18.3	n.d.	25.2
Fabricius_Cliffs	39.9	1.17	9.9	30.5	6.5	6	2.33	0.27	10.8	n.d.	12.3
Steep_Rock	41.7	0.99	9.2	22.8	8.7	5.8	2.45	0.65	12.4	n.d.	42.2
Steep_Rock	46	0.95	13.1	20.9	6	6.5	2.97	0.96	10.8	n.d.	147.7
Steep_Rock	39.6	1.03	6.5	22.3	11	6.1	1.81	0.26	12.6	n.d.	n.d.
Steep_Rock	43.1	1.18	10.2	21.8	5.1	7.7	2.43	0.89	17.1	n.d.	5.5
Steep_Rock	40.6	1.14	10.5	28.1	7.2	4.1	2.69	0.69	11.6	21.6	2.4
Steep_Rock	37.3	1.31	9.6	28.2	6.1	5	2.57	0.81	9	n.d.	60.8
Steep_Rock	43.2	1.13	9	21.9	6.5	6.2	2.55	0.76	15.1	n.d.	107.9
Steep_Rock	44	1.02	10.9	23	8.2	3.8	2.81	0.95	8.4	n.d.	90.1
Steep_Rock	41.2	1.15	9.3	22.4	6.4	9.1	2.22	0.59	17.2	n.d.	16.9
Steep_Rock	43.2	0.77	9.5	19.4	7.6	9.9	2.32	0.47	15.9	37.4	49.8
Steep_Rock	59.9	0.75	19.6	3.8	1.4	5.1	6.8	2.06	14.6	n.d.	536
Steep_Rock	39	1.39	7.8	25.2	9.2	4.3	1.95	0.38	12.2	n.d.	n.d.
Steep_Rock	42.7	1.12	8.5	21.8	10	4.4	2.28	0.56	12.4	n.d.	33.3
Steep_Rock	45.3	0.96	9.4	21.2	8.9	6.7	2.54	0.69	15.2	n.d.	15
Steep_Rock	43.8	1.25	11.6	21.9	6.1	6.1	2.34	0.63	11.3	n.d.	30.2
Steep_Rock	39.7	1.08	8.8	24.6	8.6	3.5	2.41	0.65	11.9	n.d.	35
Steep_Rock	44.8	0.88	9.8	21.7	9.1	5	2.48	0.81	9	n.d.	45.3
Steep_Rock	40.1	1.59	10.6	27	6.8	2.4	2.86	1.06	8.1	n.d.	99.3
Steep_Rock	46.3	1.04	13.6	20	4.5	6.9	3.58	1.58	14.1	2	100.5
Steep_Rock	46.5	1.03	10.2	21.2	8.1	3.7	3.14	1.06	13.5	n.d.	146.8
Camp_Island	41.5	0.99	8.1	22	11.2	3.1	2.64	0.63	11.5	n.d.	186.7
Camp_Island	41.7	0.98	8.1	19.8	6.2	9.3	2.2	0.6	12.9	n.d.	64.5

Camp_Island	50.2	0.85	14.9	17.8	4.8	6	4.14	1.34	7.8	69.9	325.9
Camp_Island	44.4	0.93	11.2	19.2	5	8.8	2.94	0.93	12.4	56.7	154.2
Camp_Island	48.3	0.88	12.2	19.4	7	4.5	2.97	1.31	8.3	31.9	188.5
Howells	42.4	0.97	9	20.1	6.5	7.3	2.68	0.87	9.3	6.5	72
Howells	51.6	0.65	6.7	16.6	9.4	11	1.76	0.52	18.7	n.d.	20.6
Howells	44.8	1.23	11.1	20.4	4.9	6.8	2.71	0.79	8.1	n.d.	149.2
Howells	43.3	1.49	9.9	21.2	5.7	4.3	2.75	0.9	8.7	n.d.	189
Howells	42.1	1.32	9.1	21.3	6.7	5.7	2.53	0.87	10.4	28.3	133.7
Howells	43.1	1.49	10.8	21	5.1	6.2	2.79	0.93	10.4	n.d.	103.4
Howells	46.3	0.98	10.2	21.2	6.2	6.1	3.04	1.28	13.6	n.d.	221.5
Howells	45.9	1.16	9.7	21.4	8	2.6	2.82	1.03	13.7	n.d.	206.9
Howells	44.1	1.19	8.2	21.2	12.2	2.9	2.22	0.65	13.2	n.d.	117.9
Howells	41.6	0.88	6.8	21.9	9	6.4	1.95	0.25	14.7	n.d.	28
Howells	43.3	1.31	8	21	12.4	2.4	2.37	0.67	12.9	n.d.	103.5
Howells	42.8	1.27	8.9	20.9	6.6	5.2	2.26	0.76	9.7	n.d.	63.9
Howells	44.9	1.28	9.4	20.8	7.7	3.9	2.47	0.79	8.9	30.3	68
Howells	43.8	0.84	8.1	20.3	8.8	7.2	2.03	0.61	14.3	n.d.	20.3
Howells	43.1	0.71	4.9	21.8	7.5	9.4	1.28	1.24	23.6	117.1	9.1
Howells	44.6	0.95	10.2	21.8	9.8	4.1	2.11	0.43	13.7	n.d.	167.7
Howells	45.9	1.29	10	21.1	8.3	1.9	3.23	1.05	10.8	17.5	277.9
Howells	55.2	1.09	18.9	13.7	1.7	5	4.83	1.27	7.9	32.9	623.8
Howells	38.7	1.61	8.8	23.6	6.5	4.4	2.51	0.76	9.6	25.8	128.5
Howells	45.4	1.02	9.1	22	5.4	8.1	2.65	1.01	13.5	n.d.	59.5
Howells	55.2	0.87	14.5	17.6	4.8	3.9	3.88	1.2	7.8	n.d.	204.7
Howells	48.9	1.07	11.1	21.4	5.2	5.9	2.78	0.93	10.1	59.4	188.3
Howells	46.1	1.14	10.2	20.7	6.5	4.4	2.76	0.85	10.2	n.d.	148.3
Howells	57.2	0.96	17.6	15.5	3.1	2.4	5.28	2.2	7.3	40.6	435
Howells	41.8	2.2	10.2	25.9	3.3	2.6	3.24	1.32	6.6	n.d.	156.3

Point Lake

Target	SiO_2	TiO_2	Al_2O_3	FeO_T	MgO	CaO	Na_2O	K_2O	Li (ppm)	Rb (ppm)	Sr (ppm)
Acasta	42.2	0.96	7.5	19.7	9.4	8.8	1.99	0.37	17.5	n.d.	27.3
Acasta	45.9	1.25	10.9	20.7	5.1	6.1	3.28	0.8	8.2	n.d.	121.4
Acasta	45.1	1.21	11.4	20.8	5.4	5	2.94	0.65	14.7	n.d.	130.2
Acasta	44	1.43	11.3	22.8	5.7	4.9	2.6	0.62	20.3	28.8	110.7
Acasta	42.9	1.73	11.3	25.9	4.6	3.2	3.11	0.97	13.8	n.d.	111.9
Acasta	41.3	1.26	9.1	26.2	7.1	3	4.12	0.32	17.6	n.d.	28.6
Acasta	46.1	1.04	11.1	20.9	5.8	6	3.02	0.7	23.7	n.d.	77.7
Acasta	44.3	1.1	10	22.8	6.9	4.3	3	0.65	15.5	n.d.	76.8
Acasta	40.4	1.69	8.3	26.6	5.9	3.7	2.26	0.53	13.7	n.d.	73.5
Amagok	43.4	1.4	11.9	21.4	4.9	7	2.88	0.88	15.3	77.9	187.6
Amagok	42.6	1.48	10.2	22.5	6	7	2.4	0.77	24.8	128.2	62.5
Amagok	44.6	1.39	13.9	21.9	5.5	3.8	3.29	1.14	17.9	88.2	274.4
Amagok	41.2	1.5	9.4	23.2	7.8	5.8	1.85	0.36	26.9	n.d.	52.4
Amagok	47	1.31	13.9	20.5	5.2	5.6	3.79	1.25	15.9	96.5	254.4
Amagok	44.1	1.11	9.5	21.2	8	5.2	2.42	0.66	15.6	116.7	27
Amagok	44.1	1.26	10.6	22.8	8.7	2	3.14	1.13	21.8	n.d.	54.5
Amagok	46.3	1.21	12	20.4	5.8	7.2	3.38	0.83	19.1	36	194.6
Amagok	41.4	1.08	8.4	21	10.1	5.4	1.71	0.3	15.5	n.d.	53.2
Bell_Island_1	27.6	0.55	4.7	9.2	4.8	24.4	1.67	0.16	5.4	n.d.	171.2
Bell_Island_1	58.1	0.72	15.6	5	2.9	2.5	5.94	1.2	18.6	25.8	727.1
Bell_Island_1	46.1	0.98	6.7	19.4	12.4	1.8	2.49	0.5	26.5	n.d.	102
Bell_Island_1	60	0.81	16.6	6.7	2.3	2.2	5.08	1.34	9	67.5	690.2
Bell_Island_1	53.2	0.71	16.1	11.3	5.6	4.9	4.64	1.03	21.8	32.3	506.8
Bell_Island_1	37.8	1.09	8	22.3	10.5	2.8	2.04	0.6	22.3	n.d.	46.6
Bell_Island_1	50.3	0.84	11.3	18.2	6.4	5.2	3.37	0.89	12.3	n.d.	227.4
Bell_Island_1	48.2	0.84	9.5	17.4	6.5	5.7	3.67	1.09	22.8	88.9	104.9
Bell_Island_1	45.9	1.06	10.8	19.6	5.9	5.3	3.38	0.83	14.3	40.2	269.6

Ingraham	47	1.34	12	19.7	4.8	6.2	3.12	0.72	11	n.d.	212.3
Ingraham	51.2	0.99	18.1	15.8	3.2	7.8	4.58	0.82	11.8	n.d.	319
Ingraham	44.6	1.13	8.3	21.2	7.8	6.3	2.58	0.49	19.5	n.d.	39.8
Ingraham	45.6	1.16	10.4	20.9	6.7	6.5	2.67	0.63	17.8	23.1	175.8
Ingraham	45.5	1.5	12.1	21.1	5	6	3.44	0.95	14.3	n.d.	172
Ingraham	41.9	1.24	9.1	22.1	5.8	9.6	2.65	0.58	16.9	n.d.	51.7
Ingraham	47.1	1.52	16.4	21	3.7	5.4	4.18	1.21	7.9	3.7	368.3
Ingraham	45.7	1.63	13.4	21.5	5.2	4.9	3.18	0.86	12.8	n.d.	265.7
Ingraham	41	2.05	13.9	31.4	4	3.6	3.28	0.93	5.6	n.d.	6
Kapvik	42.4	1.19	9.7	25.1	7.2	5.2	2.98	0.87	16.8	n.d.	85.9
Kapvik	44.4	1.18	11.5	21.6	7.5	4.9	3.11	1.07	15	29.7	106.5
Kapvik	45.9	0.9	10.2	19.6	7.3	8.3	2.94	0.97	17.9	n.d.	97.4
Kapvik	45.2	1.1	11.6	20.6	5.8	7.5	3.13	0.96	13.9	n.d.	129.5
Kapvik	45.9	1.15	12.4	20.5	6.4	5.9	2.92	0.77	15.1	n.d.	121.5
Kapvik	41.1	0.92	10.3	18.2	4.9	13.9	2.53	0.72	19.2	n.d.	111.6
Kapvik	44.7	1.41	13.5	20.9	5	7.4	3.07	0.91	10.6	n.d.	112.9
Kapvik	44.5	1.23	12.6	21.8	6.4	6.6	2.79	0.68	17	31.3	62.9
Kapvik	42.8	1.69	13	27.9	5.7	4.4	3.54	1.12	12.1	n.d.	81.5
Knob_Lake	54.6	0.61	25.6	1.6	1.1	4.2	9.91	2.19	10.4	78.6	252.9
Knob_Lake	43.2	1.65	14.9	28.5	4.2	3.2	4.01	1.51	19.5	20.7	99.3
Knob_Lake	42.4	1.25	13.3	25.5	5.1	6	3.48	1.17	15.8	n.d.	46
Knob_Lake	36.3	1.99	8.6	26.1	4.8	10.6	2.23	0.42	29.4	n.d.	3.7
Knob_Lake	57.9	0.73	20.4	6.2	3.7	1.1	6.32	2.91	20.5	42	249.9
Knob_Lake	39	1.38	8.9	29.3	6.8	4.2	2.52	0.62	15.8	n.d.	25.2
Knob_Lake	48.6	1.08	18.3	20.1	4.8	5.9	4.38	1.68	20.9	39.6	182.1
Knob_Lake	48.9	1.24	19.2	20.8	3.6	3.5	4.83	1.74	12	22	140.4
Knob_Lake	43.4	1.02	10.4	21.7	6.6	7.4	2.81	0.89	14.5	62.4	55.1
Athole_Point	39.4	2.1	9.7	29.5	5.3	2.7	2.87	0.77	11.8	n.d.	87
Athole_Point	40.7	1.27	8.8	25.4	6.6	6.6	2.19	0.5	11.6	n.d.	4.5
Athole_Point	41.8	1.27	9.3	24.4	7.5	6.1	2.55	0.62	23.2	n.d.	57.7

Athole_Point	43	2.12	13.9	26.9	4.4	4	3.76	1.28	9	30.9	166
Athole_Point	44.4	1.13	11.3	22.5	6.4	5.9	3.1	1.09	17.8	25.3	70.3
Athole_Point	41.1	1.82	11.3	27.3	5.6	5.9	3.27	1.05	14.1	32.3	70.5
Athole_Point	41.5	1.68	16.7	22.7	3	8.2	3.87	1.61	48.4	101.7	132.4
Athole_Point	42.3	1.77	14	23.8	5.1	6	3.32	1.14	25.8	85.4	105.1
Athole_Point	44.4	1.25	13.9	22.9	5.7	6.6	3.38	1.41	24.9	57.7	66.3
Balboa	43.2	1.23	9.2	21.7	5.8	5.3	3.26	0.91	8.1	8.6	155.8
Balboa	45.1	1.36	11.4	20.4	3.9	4.6	3.1	0.74	13.3	83.8	380.1
Balboa	45.2	1.01	11.2	20.8	4.9	6.7	3.5	1.04	12	33.9	206.9
Balboa	46.8	1.22	11.2	22	7.2	3	2.74	0.78	29.8	83.8	195.1
Balboa	44.5	1.06	10.6	20.5	5.7	7.9	2.79	0.66	9.5	26	226.6
Balboa	46.4	0.95	10.2	21	7.4	4.9	3.05	1.06	21.1	86.8	222.3
Balboa	43	0.84	7.1	18.9	7.2	10.9	2.1	0.58	17.6	65.6	91.1
Balboa	44.3	1.01	7.9	22.5	6.5	6.2	2.75	0.96	17	29.2	50.6
Balboa	46.4	1	10.6	20.8	6.6	5.3	2.97	1.11	42.6	72.5	163.9
LeRoux	43.6	1.11	9.2	23.2	7.8	4.2	3.42	0.46	n.d.	n.d.	n.d.
LeRoux	41.3	0.93	7.8	22.9	9.3	4.3	2.54	0.33	n.d.	n.d.	n.d.
LeRoux	41.5	0.99	8	25.2	7.3	5.4	3.24	0.25	n.d.	n.d.	n.d.
LeRoux	45.2	1	9.7	22.2	7.3	6.1	3.68	0.38	n.d.	n.d.	n.d.
LeRoux	42.6	1.1	9.7	25.7	6.9	4.4	3.28	0.37	n.d.	n.d.	n.d.
LeRoux	43.7	0.8	9.5	24.3	6.3	5.6	4.41	0.46	n.d.	n.d.	n.d.
LeRoux	37	0.89	8.7	22.4	5.6	11.2	2.48	0.34	n.d.	n.d.	n.d.
LeRoux	43.3	1.46	9.1	33.2	5.5	4	3.8	0.65	n.d.	n.d.	n.d.
Measles_Point	52	0.91	17.3	18.2	3.1	3.8	5.47	1.71	8.3	55.3	300.6
Measles_Point	53.8	0.95	16.7	16.9	3.8	1.7	5.26	1.56	22.6	74.6	287.4
Measles_Point	41.8	1.13	9.5	21.3	7.6	4.5	2.44	0.6	24.6	49.4	94.4
Measles_Point	40.5	1.51	8.4	21.5	5.6	6.7	2.11	0.6	15.4	n.d.	92.6
Measles_Point	41.8	0.91	9.4	21.2	7.7	7.4	2.14	0.59	13.8	44.8	38.5
Measles_Point	41.6	1.19	9.8	22	5.6	5.6	2.73	0.72	9.6	45.3	147.8
Measles_Point	41	0.84	9	21.6	10.5	5	2.38	0.43	13	n.d.	60.7

Measles_Point	41.9	1.74	9	22.7	6	2.4	2.81	0.82	7.9	n.d.	187.7
Balboa_2	45.3	1.28	12.3	21.1	4.8	4.8	3.41	1.05	22.7	58.4	276.5
Balboa_2	44.1	1.27	12.9	22	5.3	3.8	4.13	1.34	14.1	57.4	262.5
Balboa_2	43.4	1.27	11.5	21.7	4.7	4.8	3.69	1.28	8.3	43.6	236.3
Balboa_2	42.9	1.14	10.2	21.4	7	5	2.59	0.88	20.9	55.7	n.d.
Balboa_2	44.1	1.14	9.7	21.5	8	3.6	2.86	0.89	23.2	n.d.	156.9
Balboa_2	42.7	0.99	8.9	22	10	4.1	2.6	0.97	35.2	62.3	59.6
Balboa_2	42.4	1.11	10.5	21.8	6.4	4.7	3.02	0.93	17.9	n.d.	180.2
Balboa_2	49.7	0.98	12.9	20.1	5.5	5.2	3.5	1.09	28.9	53.4	275.6
Balboa_2	43.1	1.25	11.2	21.2	5.3	5.4	2.93	0.92	15.3	52.1	130.4
Nancroix	37.9	0.8	6.7	22.6	12.9	4.6	2.67	0.46	18.1	n.d.	52.6
Nancroix	39.2	0.93	6.6	21.3	14.2	5	1.56	0.34	20.3	n.d.	17.4
Nancroix	47.5	1.38	10.6	19.8	5	5	2.66	0.6	10.2	35.1	164.1
Nancroix	37.6	1.07	6.6	24.2	9.9	5.9	1.99	0.53	12.9	n.d.	5.7
Nancroix	46.6	0.92	11.2	20.1	7.1	6.3	3.11	0.75	11	n.d.	146.5
Croteau	44.3	1.04	9.7	22.7	6.2	3.6	3.14	0.85	n.d.	n.d.	n.d.
Croteau	44.8	0.95	8.5	21	6.2	7.7	2.44	0.72	n.d.	n.d.	n.d.
Croteau	42.1	1.09	7.4	21.7	7.4	5	2.01	0.63	n.d.	n.d.	n.d.
Croteau	43.5	1.02	8.9	21.5	6.9	5.7	2.63	0.73	n.d.	n.d.	n.d.
Croteau	46.7	0.82	8.8	20.9	11	3.9	2.74	0.71	n.d.	n.d.	n.d.
Croteau	40.7	0.8	8	20.2	8.3	6.6	1.67	0.2	n.d.	n.d.	n.d.
Croteau	39.6	0.81	8.3	20.4	8	6.8	1.8	0.21	n.d.	n.d.	n.d.
Croteau	40.9	0.88	8.5	20.8	7.9	6.6	2.02	0.32	n.d.	n.d.	n.d.
Croteau	47.3	1.02	9.8	21.3	5.6	5.8	2.95	0.6	n.d.	n.d.	n.d.

Gillespie Lake

Target	SiO_2	TiO_2	Al_2O_3	FeO_T	MgO	CaO	Na_2O	K_2O	Li (ppm)	Rb (ppm)	Sr (ppm)
Kikerk	43.7	1.15	10.5	21	5.8	7.6	2.6	0.61	14.9	n.d.	155.9
Kikerk	41.9	1.09	8.3	21.4	5.7	6.6	2.38	0.66	11.9	n.d.	30.7

Kikerk	39.4	0.9	5	20.7	10.5	9.6	1.33	0.15	16.9	28.5	13.2
Kikerk	40.4	1.25	7.6	23.5	6.4	5.2	1.89	0.45	11.8	n.d.	43.3
Kikerk	40.3	1.55	11	27.6	4.1	3	2.99	1.08	5.7	104.5	115.2
Kahochella	43.4	1.18	8.2	20.6	6.5	7.1	2.46	0.6	12.4	n.d.	65.4
Kahochella	43.5	1.11	7.9	21.1	9	5.9	2.27	0.36	14.2	n.d.	91
Kahochella	43.3	0.82	7.6	19.2	11	8.1	1.95	0.33	20.8	n.d.	44
Kahochella	43.6	1.07	9.5	20.4	7.4	7.2	2.46	0.52	18.6	85.8	84.9
Kahochella	42.2	1.1	8	22.2	9	6.4	1.75	0.23	20.2	n.d.	39.9
Crest	38.9	0.69	8.3	14.6	5.8	16.8	1.73	0.21	14.2	29.3	142.1
Crest	45.8	0.88	8.5	20.1	10.8	6.5	2.38	0.21	9.3	n.d.	57.3
Crest	45.1	1.01	8.1	20.9	12.6	3.3	2.29	0.19	7	38.5	37
Crest	48.8	0.81	9	19.7	12.5	4.5	2.11	0.45	7	n.d.	57.7
Crest	44.1	0.89	8.4	20.2	11.4	7.3	1.82	0.1	9.1	9.5	64.8
Crest	45.5	0.9	8.9	20.2	12.3	4.7	2.26	0.15	9.8	n.d.	68.5
Crest	43.3	1.18	7.7	21	11.3	4	2.27	0.22	7.6	26	37.8
Crest	45	1.09	7.4	21.1	13.1	3.7	2.15	0.19	10.3	n.d.	27.4
Gillespie_Lake_1	45.8	1.02	10.6	19.5	8.4	6.1	2.93	0.45	14.6	n.d.	126.4
Gillespie_Lake_1	46.8	0.96	8.8	20.6	10.7	5.4	2.28	0.28	14.7	n.d.	67.9
Gillespie_Lake_1	44.9	1.56	10.5	21	5.4	6.3	3.29	1.12	14.7	49.5	292.8
Gillespie_Lake_1	48.9	0.81	9.9	19.1	10.7	5.6	3.17	0.5	15.5	n.d.	73.8
Gillespie_Lake_1	46.1	0.9	6	21.4	15	3.3	1.98	0.26	14.9	n.d.	48.6
Gillespie_Lake_1	46.3	1.05	12.5	21.2	7	5.8	2.97	0.37	14.9	n.d.	118.3
Gillespie_Lake_1	39.3	1.46	9.3	21.2	5.6	7.6	3.03	0.46	16.2	n.d.	72.2
Gillespie_Lake_1	45.7	1.07	12.2	20.3	6.6	6.1	3.27	0.45	12.7	n.d.	136.2
Gillespie_Lake_1	47.5	0.94	12	21.1	7.3	5.7	2.99	0.53	14.8	40.8	80.9
Gillespie_Lake_2	46.3	0.93	10	19.5	9.2	6.3	2.59	0.24	11.9	n.d.	75.6
Gillespie_Lake_2	48.6	0.88	13.2	17.9	6.6	7.8	3.3	0.62	11.8	34.9	121.8
Gillespie_Lake_2	30.1	0.65	5.5	13.6	4.4	21.2	0.89	0.04	10.5	n.d.	119.2
Gillespie_Lake_2	45.3	1.25	10.4	19.9	8.1	6.3	2.63	0.23	14.6	n.d.	95.3
Gillespie_Lake_2	44.8	0.78	7	18.9	9.3	9.4	2.11	0.25	14.3	n.d.	27.6

Gillespie_Lake_2	46.7	0.91	8.7	19.4	9.5	6.4	2.53	0.29	11.8	35.2	68.6
Gillespie_Lake_2	45	1.18	13.4	18.8	6.1	6.7	3.52	0.32	13.2	n.d.	150.2
Gillespie_Lake_2	45.8	0.87	6.9	20.1	10.5	6.8	2.17	0.13	14.2	n.d.	27.2
Gillespie_Lake_2	45.4	1.16	9.6	20.9	9.7	5.3	2.35	0.21	10.3	n.d.	94.3
Laddie	42.3	0.99	6.7	23.6	8.4	1.9	1.9	0.24	11	n.d.	19.8
Laddie	45.6	1	11.5	19.8	6.9	5.9	2.78	0.65	15	72.9	143.4
Laddie	52.2	0.86	13.5	17.6	6.5	4.1	3.67	1.86	11.3	100.6	140.1
Laddie	42.2	0.84	7.3	27.1	5.5	2.9	1.93	0.29	11.8	40.3	86.4
Laddie	43.4	0.85	6.9	19.3	11.1	8.9	1.66	0.53	20.3	45.1	48.1
Laddie	45.6	1.1	8.3	19.9	10	4.7	2.47	0.89	17.2	89.7	92.3
Laddie	46.4	0.91	9.6	20.7	9.2	4.4	2.6	0.54	14.8	51.2	66.3
Laddie	47.3	0.93	9.3	19.4	8.9	5.1	2.78	0.55	13.9	24	78.7
Laddie	47.4	0.85	9.4	18.9	9.7	7.5	2.48	0.53	17.7	66.3	66.1
Kipalu	41.7	0.77	8.2	17.9	8.9	11.4	1.48	0.05	21	16	91
Kipalu	45.6	1.03	7.9	20	12	5.3	2.02	0.1	15.6	n.d.	75.1
Kipalu	45.3	1.11	10.9	19.4	7.8	7.2	2.48	0.22	11	n.d.	113.9
Kipalu	48.9	0.83	11.5	18.2	9	5.8	2.89	0.31	9.4	n.d.	156.5
Kipalu	41.1	0.73	5.7	20	12.5	10	1.24	0.06	24.8	n.d.	31.5
Kipalu	47	0.97	9.8	19.6	9.8	6.4	2.3	0.2	11.7	n.d.	50.9
Kipalu	47.6	0.9	9.7	19.4	9.5	6.2	2.45	0.27	10.4	n.d.	92.8
Kipalu	46	1.02	9.7	19.4	9.3	5.9	2.4	0.18	8.6	n.d.	90.9
Kipalu	47.9	0.78	9.7	19.8	12.8	4.1	2.86	0.47	15	n.d.	91.9
Lucas_Creek	49.3	0.95	11.4	19.7	9	5	2.94	0.83	10.6	35	148.2
Lucas_Creek	47.2	0.81	8.1	20.8	11.3	6.3	2.31	0.39	14.1	29.4	120.7
Lucas_Creek	43.2	0.76	4.4	19.5	11.4	11	1.45	0.07	17.5	n.d.	136.2
Lucas_Creek	43.5	1.13	10.6	19.1	7	6.2	2.89	0.24	9.6	n.d.	188.1
Lucas_Creek	46.2	1.04	7.5	20.7	12.3	4.8	2.01	0.24	10.6	n.d.	69.8
Nanok	47.2	0.96	10.4	20.6	7.6	5.8	3.74	0.45	12.4	n.d.	97.1
Nanok	46	1.14	7.3	21.3	11.3	4	2.5	0.34	10.1	n.d.	61.9
Nanok	43.6	1.43	10.6	20.5	6.1	5.6	2.81	0.25	9.5	n.d.	145.6

Nanok	46.1	0.9	9	20.3	10.2	5.4	2.96	0.45	13	n.d.	56.3
Nanok	46.8	0.97	10.4	21.4	8.4	6	2.96	0.39	11.8	n.d.	131.7
Nanok	47.9	0.99	10.2	20.8	7.9	6	3.06	0.35	10.7	n.d.	133.2
Nanok	48.3	0.98	11.5	19.6	6.7	6.7	3.54	0.73	11.5	42.9	119.4
Nanok	46.4	1.3	8.1	20.2	9	3.7	2.97	0.35	11.4	n.d.	99.1
Nanok	45.3	1.16	10.3	21	6.9	5.4	3.45	0.52	8.6	n.d.	138.6
Jolliffe	44.9	0.86	8.9	21.3	8.5	8.4	2.48	0.53	25.6	n.d.	53.8
Jolliffe	45.5	1.07	12.3	22	6.6	5.7	3.63	0.79	22.3	30.9	119.9
Jolliffe	43.8	1.19	10.1	23.2	6.5	5.3	3.48	0.78	20.3	34.9	131.4
Jolliffe	45.1	0.97	11	20	8.6	5.8	2.84	0.59	14.7	n.d.	99.5
Jolliffe	42.3	1.22	9.4	21.1	11	5.4	2.15	0.29	18.7	n.d.	108.8
Jolliffe	48.4	0.82	12.2	18.8	9	6.2	2.87	0.47	15.4	n.d.	171.9
Jolliffe	45.9	0.88	8.8	21.2	10.8	5.5	2.55	0.45	21.6	n.d.	67.3
Jolliffe	45.1	1.09	8.3	21.1	10	5.3	2.67	0.59	22.2	n.d.	82.3
Jolliffe	45.3	1.28	8.8	21	9.7	4.9	2.74	0.56	19.9	n.d.	63.6
Jolliffe	46.9	0.84	10.3	19.3	8.9	7.6	2.66	0.57	19.6	46.6	81.6
Nanok2	48.6	0.95	12.6	18.4	8.1	5.8	2.67	0.16	11	n.d.	395.9
Nanok2	45.5	0.69	7.7	17.4	11	8.3	1.73	0.12	10	n.d.	109.3
Nanok2	46.4	1.08	10.1	19.9	8.7	6.2	2.52	0.62	11.9	31.4	693.6
Nanok2	44	1.18	8.6	21.3	8.8	5.1	2.26	0.15	9.9	n.d.	241.1
Nanok2	47.7	0.85	9.2	19.8	10.1	6.6	2.24	0.27	15.1	n.d.	119.3
Nanok2	47.4	0.97	12.8	19.7	6.8	7.1	3.03	0.25	12.8	29.1	218.1
Nanok2	47.8	1.22	7.8	21.8	10.7	4.9	2.4	0.28	12	n.d.	111.9
Nanok2	46.6	0.94	8.9	19.9	7.6	9.2	2.14	0.31	17.2	n.d.	85
Nanok2	48.5	1.51	11.6	20.5	7.5	5.4	3.19	0.61	9.1	40.4	203.7
Nanok2	48.6	0.99	10.4	20.8	8.1	5.9	3.08	0.53	12.6	33.2	120.1
Doublet	47.7	0.83	12.8	19.4	10	3.2	2.65	0.62	18.1	59	66.6
Doublet	45.3	0.89	10.4	19.7	10.6	4.3	2.38	0.39	17.2	n.d.	52.4
Doublet	44.8	0.96	10.7	20.3	9.8	5	2.34	0.53	17.5	21.6	33.7
Doublet	47.4	0.87	10.6	19	10.8	4.2	3.03	0.63	10.1	34.8	47.1

Doublet	42.7	0.93	10.3	19.7	10.2	5.9	1.98	0.32	19.6	53.2	55.6
Doublet	43.6	1.17	9.8	19.6	11.1	3.7	2.16	0.35	18.3	52.8	67.4
Doublet	43.6	0.98	11.4	20.2	9.9	4.7	2.13	0.49	23	53	65.6
Doublet	43.6	1.04	8.5	19.9	12.3	2.7	2.75	0.24	9.9	26.5	37.3
Doublet	44.2	0.98	8.2	20.3	10.9	6.2	2.09	0.3	13.4	7.4	36.3
Doublet	43.4	0.97	7.9	19.8	13.4	5.4	1.75	0.3	17	n.d.	14.4
Mugford	49.2	0.97	9.7	20.4	13.1	2.8	1.64	0.12	14.2	n.d.	39.3
Mugford	44.7	1.14	9.4	20.7	13.8	2.3	2.04	0.34	18	n.d.	22.1
Mugford	42.1	0.8	7.5	20.8	13.1	5.2	2.17	0.04	12.7	n.d.	6.4
Mugford	43.4	1.07	9	20.8	11.9	2.9	1.82	0.31	12.8	26.3	n.d.
Mugford	44.7	0.89	10.7	19.1	11.9	4.5	2.12	0.5	15.8	50.7	59.8
Rae	49	0.91	10.3	18.3	8.7	5.2	3.49	0.63	7.9	n.d.	127.4
Rae	49.4	0.83	8.3	19.6	12.3	3.7	3.18	0.68	11.1	41.6	90.8
Rae	47.4	0.98	9.5	19.2	8.9	5	3.26	0.61	6.6	n.d.	132.3
Rae	46.5	1.09	10.1	19.6	8.3	5.7	3.13	0.54	7.1	45.5	118.1
Rae	46.7	1	9.8	19.8	9.2	5.1	3.16	0.55	8.1	n.d.	127.5
Rae	46.2	1.01	9.2	19.2	9.1	5.8	3.07	0.5	9.8	10.9	117.4
Rae	47.9	1.03	10	19.2	8.3	5.1	3.29	0.61	6.1	51.6	138.1
Rae	48.8	0.9	9.6	18.3	8.4	5.1	3.69	0.67	8.1	n.d.	98.4
Rae	46.2	0.91	9.9	19.3	8.9	6.3	2.98	0.41	11.8	n.d.	120.2
Iqqittuq	50.7	0.77	7.5	19	13.8	3.3	2.66	0.49	8.7	n.d.	75.4
Iqqittuq	48	0.96	11.1	18.7	8.1	6.1	3.3	0.53	10.2	42.3	141.7
Iqqittuq	49.7	0.86	7.8	19.7	13.8	3.6	2.69	0.48	9.9	n.d.	96.1
Iqqittuq	48.1	0.99	11.5	18.9	8.4	5.4	3.53	0.6	12.1	33.8	166
Iqqittuq	50.4	0.78	8.7	20	12.9	3.5	2.81	0.54	10.2	n.d.	100.7
Iqqittuq	46.1	1.05	10.4	21.4	8.8	4.9	3.08	0.48	11.2	n.d.	97.5
Iqqittuq	48.7	0.79	9.1	20.5	10.1	6.4	2.61	0.47	12	n.d.	64.4
Iqqittuq	46.9	1.01	10.4	21.5	8.3	5.9	3.03	0.61	11.3	9.5	77.6
Iqqittuq	47.3	1.01	11.4	19.6	7.9	5.7	3.35	0.62	13.8	34.7	108.6
Bylot	47.2	1.03	10.1	18.8	8.2	5	3.35	0.6	7.6	48.7	115.1

Bylot	49.6	0.89	10.3	17.6	8.4	5.3	3.47	0.72	7.2	48	120.8
Bylot	46.7	0.9	9.8	19.2	10.9	4.5	2.98	0.5	7.7	33.2	123
Bylot	48.2	1.01	10.6	18.5	8.6	5.2	3.34	0.59	6.5	37.6	134.4
Bylot	50.4	0.88	8.5	19.6	10.6	4.2	2.79	0.48	7.3	n.d.	78.5
Bylot	49.3	0.85	7.1	19.8	14	3.2	2.54	0.48	6.6	n.d.	64.6
Bylot	46.3	0.98	9.3	19	8.7	5.3	3.17	0.56	8.7	35.2	97.9
Bylot	46.4	1	10	18.7	8.2	6	3.23	0.6	8.2	n.d.	124.9
Bylot	47.1	1.03	10.1	19.4	8.8	4.8	3.25	0.65	8.9	34.3	136.8
Rae	48	0.95	10.5	18.6	8.5	5.6	3.32	0.57	10	n.d.	153.4
Rae	50	0.78	9.4	19.2	11.7	3.9	3.37	0.8	9.2	38.5	110.8
Rae	48.2	0.87	11.5	18.7	7.9	6.5	3.37	0.59	8.6	40.4	173.8
Rae	46.7	0.9	9.1	19.2	9.2	5.6	3.35	0.55	11.2	41.1	108.8
Rae	46.2	0.96	10.4	19.6	8.2	6.1	3.31	0.58	9.6	30.3	136
Rae	46.9	0.93	10.4	19.1	8.6	5.8	3.41	0.56	8.8	39.5	131.2
Rae	48.5	0.87	12.2	18.9	8	5.9	3.49	0.65	7.2	28.8	161.3
Rae	48.1	0.87	11.3	18.6	8.6	5.6	3.49	0.64	8.3	36.5	140.9
Rae	48.3	0.92	10.5	19.2	8.6	5.3	3.34	0.54	8	n.d.	148.7

Sheepbed

Target	SiO_2	TiO_2	Al_2O_3	FeO_T	MgO	CaO	Na_2O	K_2O	Li (ppm)	Rb (ppm)	Sr (ppm)
Sheepbed	48.8	1.07	11	19.2	8.3	6.1	2.88	0.56	14.3	n.d.	120.1
Sheepbed	48.5	1.37	12.5	19.8	7.6	5.8	3.3	0.74	14.4	35.8	n.d.
Sheepbed	50.5	1.02	12.5	18.7	7.4	6.9	3.17	0.71	15.3	45.8	154.4
Sheepbed	50.3	1.05	12.1	18.1	7.6	6.8	3	0.67	12	22.8	177.5
Sheepbed	48.4	1.12	14.4	19.8	6.7	6.7	3.57	1.03	10.9	n.d.	126.7
Sheepbed	48.1	1.16	13.9	19.7	6.9	6.7	3.45	0.88	12.8	n.d.	171.7
Sheepbed	48.2	1.42	13.8	20	6.4	5.8	3.67	1.15	13.7	50.2	152
Sheepbed	48.4	1.3	13.4	19.9	6.8	6.1	3.52	0.92	10.7	51	144
Sheepbed	46.9	1.4	14	20.1	6.6	6.3	3.49	0.94	18.1	27	129.7

Beachrock	46.3	1.04	9.5	20.5	8.7	5.1	2.62	0.38	7.1	n.d.	127.8
Beachrock	46.6	0.95	9	19.9	8.9	5.2	2.9	0.42	10.7	32.6	82.1
Beachrock	45.7	1.01	9.3	20.3	8.5	5.5	2.71	0.37	9.4	n.d.	91
Beachrock	46.5	0.96	9.9	19.5	8.6	6.2	2.83	0.38	10.3	n.d.	82.4
Beachrock	46.3	0.97	9.5	20	8.5	5.8	2.62	0.3	10.4	n.d.	96.1
Beachrock	46.4	0.97	9.1	20	8.9	5.6	2.68	0.29	9.2	n.d.	92.3
Beachrock	46.7	0.93	10.4	19.2	8.8	6.4	2.73	0.33	10.4	n.d.	116.1
Beachrock	46.6	0.94	8.6	19.5	9.4	6.5	2.4	0.25	11.7	n.d.	66.9
Beachrock	46.9	0.97	10	20.6	7.9	5.6	2.93	0.44	9.2	n.d.	89.4
Belcher	46.2	0.87	10.2	19.3	9	6.2	3.12	0.46	10.3	n.d.	90.4
Belcher	46.7	0.89	10.2	19	9	6.5	2.89	0.31	9.1	n.d.	83.6
Belcher	46.3	0.9	10.5	19.6	8.4	6.3	2.97	0.41	8.9	n.d.	88.9
Belcher	45.9	0.89	9.6	19.7	8.8	6.3	2.98	0.39	11	n.d.	66.2
Belcher	46.8	0.91	10.5	19.5	8.9	6.1	3.1	0.48	13.4	n.d.	88
Belcher	47.6	0.87	10.6	18.6	8.9	6.7	2.84	0.39	8.9	n.d.	n.d.
Belcher	45.7	0.92	9.7	19.4	8.9	6.6	2.97	0.35	10.7	3.2	78.5
Belcher	46.6	0.9	10.8	18.6	9	6.2	3.28	0.49	11.2	27.4	92.2
Belcher	46.9	0.88	9.5	18.2	9.4	6.6	3	0.42	8	n.d.	108.2
Flaherty	44.9	0.92	9.7	19.5	7.7	5.9	2.97	0.35	9.8	3.8	89.7
Flaherty	45.3	0.93	9	19.5	8.5	5.6	2.79	0.29	7.8	n.d.	75.9
Flaherty	44.2	0.97	9.2	20	7.3	6	2.71	0.49	8	8.6	90.1
Flaherty	45.3	0.88	9.1	19.3	8.6	6.1	2.99	0.4	11.9	20.7	70.3
Flaherty	44.8	0.82	8.6	19.5	11	5.5	2.74	0.54	10.4	88.7	64.4
Richardson	41.9	0.8	8.1	18.7	12.2	5.8	2.53	0.27	11.8	n.d.	51
Richardson	41.7	0.83	8.4	19.1	11.6	5.9	2.47	0.26	9.3	n.d.	48.8
Richardson	43.2	0.81	8.4	18.9	12.6	5.2	2.52	0.31	8.9	n.d.	54.7
Richardson	42.5	0.83	8.4	19.4	9.9	6.4	2.9	0.35	9.7	n.d.	55
Richardson	41.7	0.89	8.5	20.2	10.3	5.5	2.97	0.36	10.1	n.d.	53.9
Flaherty_2	45.7	0.88	9.9	19.3	8.2	6	3.01	0.48	11	27.1	77
Flaherty_2	45.2	0.94	9.9	20.5	8.1	5.8	2.96	0.41	10.6	n.d.	82.8

Flaherty_2	43	0.91	9.1	19.7	8.4	6.1	3.09	0.39	11.2	3.1	66.5
Flaherty_2	45.1	0.95	10.2	20.5	8.1	5.6	3.02	0.43	9.7	n.d.	89.9
Flaherty_2	44.5	0.96	10.8	20.3	7	6.1	2.99	0.5	9.9	n.d.	93.1
Richardson_2	44.3	0.83	11.5	22.4	8.3	5	3.31	0.44	14.8	3.5	110.5
Richardson_2	11.7	0.57	1.1	9	4	24.9	0.52	0.02	5.6	n.d.	166.5
Richardson_2	44.6	0.77	9.5	20.8	12.1	4.9	3.1	0.49	14.9	n.d.	43.5
Rackla	45.2	1.01	9.8	20	7.9	7.1	2.6	0.36	7.9	n.d.	122.8
Rackla	45.7	0.82	8.4	19	9.2	7.7	2.62	0.43	11.4	20.9	71.8
Rackla	45.3	1.09	9.9	20.5	7.3	6.5	2.75	0.38	10.7	n.d.	124.8
Rackla	47.5	0.89	10.7	19.5	8	5.7	3.16	0.59	11.5	29.7	117.9
Rackla	46.8	0.97	8.6	20.7	8.1	4.9	2.87	0.59	11.1	34.7	77.3
Rackla	47.2	0.87	9	19.5	9	5.7	2.85	0.46	10.5	n.d.	77.3
Rackla	46.5	0.92	9.1	20.2	8.4	5.6	2.74	0.51	8.9	30.3	93.3
Rackla	48	0.84	8.8	19.7	9.2	5.9	2.83	0.46	10.8	n.d.	89.9
Rackla	47.4	0.92	10.8	20.6	7.6	5.9	2.9	0.53	12.7	29	82.6
Bonnet_Plume	48.8	0.89	11.5	18.3	9.4	5.5	2.98	0.51	9.5	n.d.	85.7
Bonnet_Plume	48.1	1.08	10.8	20.1	8.7	5.2	3.25	0.64	8.5	n.d.	77.1
Bonnet_Plume	48.3	1.17	10.5	20.2	8.9	4.7	3.26	0.63	9.5	27.4	74.6
Bonnet_Plume	47.6	1.11	9.4	19.8	9.1	5.3	2.84	0.49	7.7	38.8	76.8
Bonnet_Plume	44.2	0.95	12.2	19.3	6.7	7.7	2.86	0.44	8.6	n.d.	88.9
Bonnet_Plume	50.5	0.79	13.6	19.3	8.2	6.8	3.58	0.7	9.3	10.3	128.2
Bonnet_Plume	46.7	1.05	10.8	19.8	8.7	6.1	3.11	0.6	15.2	n.d.	99.5
Bonnet_Plume	47.1	1.27	9.9	20.5	7.9	5.3	3.31	0.74	13.3	n.d.	99.8
Bonnet_Plume	49.8	1.08	8.4	19.7	13	3.5	2.2	0.29	6.8	n.d.	67.8
Haig	46.4	1.26	10.3	20	8.3	5.3	3.05	0.59	11.3	39.6	124.2
Haig	47.2	1.13	10.7	20	8.5	5.6	3.05	0.61	18.7	n.d.	119.4
Haig	46.7	1.07	10.9	20.3	8.5	5.2	3.06	0.57	11.4	40.7	147.9
Haig	48.3	1.01	11.7	19.6	8.7	5.8	3.12	0.58	10.1	31.5	133.1
Haig	48.9	0.94	11.2	19.4	9	5.9	3.14	0.5	9.1	n.d.	146.3
Hay_Creek	47.1	1.13	10.2	18.7	6.8	6	3.11	0.64	10.1	68.3	110.6

Hay_Creek	46.9	1.17	10.1	18.3	7.1	6.1	2.96	0.57	11.8	77.6	116.5
Hay_Creek	45.8	0.84	8.9	17.4	10.5	7.7	2.29	0.4	6.8	81.8	120.4
Hay_Creek	45.3	0.99	9.5	18.6	9	5.8	2.8	0.41	9.9	59.4	119.8
Hay_Creek	46.8	1.21	9.7	18.8	7.3	6.1	2.92	0.52	9.8	70.3	106
Hay_Creek	47.4	1.1	9.5	18.8	7.5	6.3	2.82	0.52	7.6	87.4	133.8
Hay_Creek	47.7	1.06	10.2	18.4	7.3	6.1	3.04	0.49	9.5	82.1	144.9
Hay_Creek	46.8	1.08	9.5	18.9	8.1	5.3	2.55	0.47	10.2	21.9	136.9
Hay_Creek	44.5	0.92	8	18.3	13.1	5.3	2.5	0.44	9.5	n.d.	75.1
Hayhook	46.3	1.23	11	20.1	7.7	5.6	3.21	0.52	11	6.7	144.8
Hayhook	44.5	1.53	10.2	20.5	7.2	5.3	2.9	0.51	11.3	82.4	103.1
Hayhook	47.7	0.95	9.6	19.6	10.7	5.8	2.64	0.38	15.3	n.d.	66.4
Hayhook	36.3	0.75	7.5	14.9	5.7	17.5	1.5	0.17	9.8	n.d.	119.9
Hayhook	46.4	1.3	10.1	19.9	7.4	5.5	2.93	0.46	10.4	n.d.	101.2
Hayhook	47.8	1.02	10.6	19.5	7.7	6.4	2.94	0.47	9.6	n.d.	100.3
Hayhook	47.4	1.07	10.1	19.4	9.3	5.3	2.88	0.51	10	27.7	101
Hayhook	48.7	1.01	11.5	18.8	7.9	6	2.89	0.45	8.7	n.d.	134.8
Hayhook	48.6	1.02	12.1	19.6	7.6	6	3.3	0.53	12.2	n.d.	141.2
Hudson_Bay	43.4	1.17	8.5	20.5	9.5	5.3	2.38	0.35	9.2	29.8	41.6
Hudson_Bay	47.8	1.13	10.9	20.6	8.7	5.3	3.15	0.63	11.9	n.d.	103.2
Hudson_Bay	47.2	1.1	10	19.9	8.6	5.3	3.04	0.62	10.4	n.d.	115.5
Hudson_Bay	47.2	1.08	10.1	19.6	8.6	5.9	2.77	0.38	11	n.d.	110.4
Hudson_Bay	47.9	1.11	10.6	19.5	8.3	5.7	3.02	0.54	11.6	32.4	118.2
Hudson_Bay	48	0.99	10.2	19	8.6	6.1	2.95	0.47	11.5	29.2	85.7
Hudson_Bay	48.6	1	10.5	19	9	5.7	2.85	0.49	9.3	34.4	100.7
Hudson_Bay	47.7	1	10.7	18.7	9	6.7	2.68	0.42	13.7	n.d.	103.2
Hudson_Bay	47.6	1.07	10.8	19.7	8.6	5.9	2.86	0.47	12.7	n.d.	101.8
Quartet	48.8	1.29	11.7	20.3	8.6	4.8	3.33	0.71	13	43.7	122.2
Quartet	49.1	1.13	11	20.7	8.9	4.7	3.44	0.64	13.5	84.3	128.4
Quartet	51.6	0.9	11.1	18.7	10.1	4.8	3.49	0.65	12.5	n.d.	136.5
Quartet	49.9	1.08	11.4	20	9	4.7	3.45	0.81	12.1	57.2	141.9

Quartet	47.7	1.08	9.9	19	9.5	4.8	3.31	0.75	14.4	73	80.1
Quartet	50.9	0.88	10.7	18.3	10.2	5.4	3.11	0.58	12.9	32.2	118.1
Quartet	48.3	1.1	10.9	18.8	9.1	6.3	3.15	0.49	11.7	20.3	111.5
Quartet	47.7	1.14	13	20.4	7.3	6.6	3.62	0.68	11.1	n.d.	86.5
Hay_Creek_ND	43.8	1.3	9.1	20.6	7.1	5.2	2.57	0.37	7.9	34.9	75.3
Hay_Creek_ND	47.3	1.18	10.8	19.3	6.6	5.8	3.29	0.77	9.8	67	144.8
Hay_Creek_ND	48.5	1.13	9.6	19.7	6.9	5.9	3.16	0.69	9.6	68.8	108.6
Hay_Creek_ND	47.3	1.03	10.8	18.4	8.1	5.7	3.27	0.63	10.9	61	146.5
Hay_Creek_ND	45.7	0.95	7.6	19.6	13.4	4.6	2.79	0.38	10.5	n.d.	59.9
Hay_Creek_ND	47.3	1.14	10.2	20	7.1	5.9	3.14	0.59	13	48.7	87
Hay_Creek_ND	47.8	1.2	10.9	20.7	6.9	5.2	3.16	0.67	10	147	109.5
Hay_Creek_ND	47.1	1.05	10.1	20.2	8.3	6	3.07	0.67	11.7	63.3	83.3
Hay_Creek_ND	48.5	1.09	10.8	19.4	7.2	5.8	3.38	0.62	11.5	175.5	137.2
Quartet_ND	48.1	1.09	10.7	20.6	9.6	4.8	3.19	0.67	10.1	40.3	96
Quartet_ND	49.3	0.99	10.2	20	9.8	5.5	2.97	0.43	10.8	n.d.	112.2
Quartet_ND	47	0.79	9.5	19.9	10.9	5.5	2.72	0.32	13.5	n.d.	87.3
Quartet_ND	49.2	1.01	10.3	20	9.6	5	3.27	0.54	9.1	n.d.	129.9
Quartet_ND	49.8	0.97	10.2	19.9	9.9	4.7	3.14	0.46	10.2	3.3	92.9
Quartet_ND	49.4	0.92	9.4	19.9	10.4	5.3	3.05	0.48	12.1	n.d.	79.8
Quartet_ND	49.1	0.95	9	19.6	14.5	5.3	2.48	0.27	11.8	n.d.	107.1
Quartet_ND	49.3	0.99	9.9	19.4	10.4	5.1	2.92	0.49	11.1	41.2	105.1
Selwyn	44.4	1.23	10.1	20.2	7.9	6.4	2.8	0.5	13.7	64.7	99.4
Selwyn	45.1	1.22	10	20.2	8.2	5.6	2.92	0.56	11.9	66.7	106.4
Selwyn	46.3	1.07	9.7	20.7	8.4	5.7	3.1	0.59	12.1	74.5	113.8
Selwyn	46	0.93	11	19.7	9	6.3	2.89	0.38	12.2	n.d.	138.7
Selwyn	45.6	0.8	8.1	19.8	11.6	4.6	2.8	0.54	12.8	n.d.	52.1
Selwyn	42.3	1.21	9.2	20.9	8	5.5	2.94	0.5	13.6	39.9	68.6
Selwyn	44.4	1.25	10.2	20.7	7.8	5.2	3.35	0.61	14.6	43.1	74.2
Selwyn	39.6	0.74	8.3	17.5	7.3	13.8	1.82	0.19	18	n.d.	65.5
Selwyn	45.3	0.91	11.5	19.2	8.3	8	2.58	0.49	15.5	61.5	124.5

John_Klein	47.1	1.08	14.3	21.3	7.4	4.6	3.94	0.5	18.9	n.d.	75.6
John_Klein	49.1	0.58	10.4	21.3	15.1	2.5	3.32	0.22	29.2	n.d.	103.7
John_Klein	50.7	0.57	10	20.5	18.3	2.7	2.98	0.2	14	n.d.	n.d.
John_Klein	50.1	0.79	13.1	19.7	10.4	5.9	3.54	0.45	6.6	n.d.	113.1
John_Klein	48.9	0.93	11.4	19.6	8.2	4.5	2.7	0.39	4.2	19.5	52.6
Selwyn	43.1	1.42	7.2	21.3	9.3	5.5	2.22	0.25	11.9	n.d.	60.3
Selwyn	45.8	1.15	11	18.9	8.2	6.2	2.99	0.47	10.4	58.5	140.2
Selwyn	45.2	1.22	10.2	19.1	8.4	5.9	3.06	0.47	11.2	79.3	152.6
Selwyn	43.3	1.04	8	20	7.9	5	3.04	0.55	10.3	n.d.	59.3
Selwyn	44.4	1.24	10.4	18.8	7.9	6.1	3.19	0.52	12.8	53.2	107.3
Selwyn	45.2	1.18	10.9	18.8	7.9	6.3	3.03	0.53	10.5	46.8	153.7
Selwyn	48.1	0.78	7.7	18.5	13.5	4.1	2.77	0.43	12.2	n.d.	103.6
Selwyn	44.3	1.05	10.7	19.3	7.6	6	3.26	0.64	12.8	70	110.4
Selwyn	44.7	1.17	10.3	19.5	8.1	6.1	2.91	0.47	12.9	46.4	136.4
Selwyn	45.6	1.11	10.3	19.4	8	5.6	3.01	0.59	12.7	58.1	155.4
Selwyn	42.1	0.95	9.1	18.5	7.8	9.5	2.64	0.34	16.2	61.2	144.6
Selwyn	41.5	0.9	9.1	17.9	7.3	11.5	2.14	0.31	17.3	53	173.1
Selwyn	44.1	0.87	9.5	18.2	8.5	8.1	2.75	0.4	13.1	n.d.	132.1
Selwyn	28	0.67	6.1	13	3.5	21.9	1.06	0.08	8.6	n.d.	119.5
Selwyn	40.7	0.62	5.8	16.2	9	13.8	1.32	0.15	13.3	n.d.	79.8
Selwyn	44	1.33	10	19.7	8.7	5.4	2.94	0.44	9.9	77.3	131.7
Selwyn	45.9	0.98	9.6	19.3	10.5	5.4	2.8	0.44	13.3	24.4	120.3
Selwyn	46.7	1.03	13.2	18.5	6.9	6.7	3.54	0.41	15.2	n.d.	191.6
Selwyn	43.9	1.23	8.5	19.4	8.6	6.3	2.54	0.35	12.7	n.d.	66.5
Selwyn	49	0.9	14.4	18.2	6.6	6.2	3.44	0.36	11.4	n.d.	205.3
Selwyn	44.2	1.29	10.1	20.2	8.5	5.5	2.81	0.42	11.9	77.8	109.1
Selwyn	44.6	0.95	10.3	20.2	8.5	5.6	3.04	0.58	12	25.2	94
Selwyn	46.4	1.15	9.7	19.8	9.1	5.9	2.83	0.44	11.5	n.d.	121.1
Selwyn	30.9	0.81	6.5	14.2	4.3	23.1	1.28	0.09	11.9	n.d.	128.2
Selwyn	35.3	0.71	8	13.5	4.7	21.5	1.82	0.27	12.4	23.5	182.4

Selwyn	43.9	0.83	11.7	18	6.4	11.2	2.92	0.53	12.9	30	138.4
Selwyn	47.4	0.76	13.2	17.6	7.7	7	2.86	0.27	6.8	n.d.	122.8
Selwyn	45.4	0.86	13.6	19.4	7.4	7	3.64	0.64	14.2	31.1	88.2
Mavor	43.6	0.91	9	19.6	8.9	6.8	2.49	0.46	12.5	n.d.	122.1
Mavor	50	0.79	15.6	17.1	5.9	6.2	3.74	0.39	10.1	n.d.	299.5
Mavor	45.1	1.07	10.8	18.5	8.1	5.9	2.65	0.25	9.5	n.d.	178.1
Mavor	48	1.05	8.8	20.4	9.6	4.9	2.45	0.41	10.5	n.d.	103.4
Mavor	47.2	1.06	9.4	19.7	9.8	5.1	2.68	0.42	8.3	n.d.	103.9
Mavor	47.3	1.02	10.6	20.8	8.9	5.3	2.82	0.4	11.3	n.d.	125.6
Mavor	46.7	1.23	9.2	21.3	9.2	4.5	2.75	0.51	10.4	n.d.	123.4
Nastapoka	48.2	0.95	9.1	20.4	10.9	4.6	2.91	0.62	9.4	31	215.2
Nastapoka	47.8	1.01	8.5	20.4	11.1	4.6	2.65	0.48	8	28.2	90.1
Nastapoka	47.7	1.01	9.1	20.4	10.6	4.2	3.05	0.63	7.4	46.9	133.9
Nastapoka	47.8	0.97	9.8	19.7	10.9	4.8	2.89	0.48	8.9	n.d.	108.3
Nastapoka	47.8	1.03	9.8	20.3	10.3	4.4	3.15	0.64	9.8	33.6	92.4
Nastapoka	47.7	0.94	9.8	20.2	10.5	4.7	3	0.56	9.2	n.d.	77.9
Nastapoka	48.5	0.86	11.5	19.8	9.8	5.7	3.16	0.5	9.5	n.d.	84.6
Nastapoka	46.9	0.98	9.7	20.9	10	4.6	2.97	0.45	9.2	n.d.	66.5
Nastapoka	45.7	1.14	9.6	19.7	9.5	5.3	2.9	0.49	11.1	n.d.	104.9
Cape_Smith	47	1.28	11.5	20.3	7.4	6.5	3.06	0.59	12.9	37.9	109
Cape_Smith	49.4	0.89	13.4	18.3	8	8.3	3.16	0.61	14.9	n.d.	102.7
Cape_Smith	47.5	1.07	11.4	20.4	7.9	6.4	3.26	0.71	17.1	30.6	70
Cape_Smith	51.8	1.02	13.2	19.1	7.7	6.5	3.33	0.64	10.8	30	140
Cape_Smith	48.4	1.15	13.5	20.1	7	6.2	3.71	0.93	10.9	5.1	131.9
Cape_Smith	48.7	0.92	13.2	19.9	7.2	7.3	3.44	0.64	13	n.d.	131.5
Cape_Smith	52.5	0.96	9.5	20.5	10.8	4.7	3.18	0.65	9.6	n.d.	142.1
Cape_Smith	51.6	0.97	13.4	18.7	8.3	7.4	3.21	0.48	16.9	n.d.	176.8
Cape_Smith	48.2	0.87	15	19.5	7.3	8.3	3.59	0.58	13.6	1.5	101.3
Kootenay	44.9	0.94	8.2	20.6	10.7	5.1	2.44	0.35	10.1	3.9	72.5
Kootenay	46.4	1.18	9.7	20.6	7.8	5.4	2.76	0.46	11.1	n.d.	97.9

Kootenay	46.4	1.12	9.8	20.8	7.7	5.5	2.74	0.48	11.1	n.d.	126.2
Kootenay	43.8	1.39	9.9	20.3	7.4	5.1	2.86	0.56	10.7	n.d.	103.5
Kootenay	46.6	1.24	10.2	20.5	7.3	5.6	2.82	0.46	12.1	n.d.	96.2
Kootenay	44.8	1.22	9.4	20.7	7.6	5.1	2.75	0.66	12	41.7	91.8
Kootenay	44.5	1.02	9	19.4	9.2	6	2.33	0.35	12.3	n.d.	59.1
Kootenay	46.1	1.16	10.2	20.9	7.7	5.5	2.75	0.45	10.1	n.d.	107.3
Kootenay	47.3	0.95	9.5	19	9.2	5.6	2.72	0.43	10.7	n.d.	108.4
John_Klein_RP2	48.5	1.03	10.8	18.1	8.3	6.1	3.07	0.56	10.8	32.4	129.3
John_Klein_RP2	50.7	0.82	8.7	18.6	14.8	3.7	2.29	0.42	8.9	n.d.	98.2
John_Klein_RP2	47	1.18	10.7	19.6	8.2	5.6	3.15	0.62	9.7	38.4	135.9
John_Klein_RP2	44.3	1.13	9.6	20	8	6.8	3.3	0.26	16.3	n.d.	72.6
John_Klein_RP2	49.3	0.93	12.3	18.8	7.9	6.2	3.15	0.43	12.5	n.d.	105.2
John_Klein_RP2	47.1	0.8	7.2	19.1	16.5	3.8	1.68	0.21	9.7	n.d.	59.8
John_Klein_RP2	48.3	1.04	11.3	18.3	8.6	5.8	3.1	0.53	11.3	33.6	119.6
John_Klein_RP2	47.5	1.13	11.3	19.3	7.9	6	3.03	0.5	11	40.8	178.9
John_Klein_RP2	45.4	1.14	11.5	19.6	8.2	6.3	3	0.44	12.3	n.d.	98.8
John_Klein_RP3	45.8	0.97	7.6	19.2	11.7	4	2.4	0.34	10.7	n.d.	110.3
John_Klein_RP3	47	1.09	12.4	18.5	7	6.3	3.35	0.6	9.5	18.5	221.6
John_Klein_RP3	47.2	1.07	11.8	19	7.1	6.6	3.25	0.63	9.8	28.3	217.9
John_Klein_RP3	42.5	0.65	8.3	19.5	18.8	2.7	1.99	0.05	21.9	n.d.	37
John_Klein_RP3	48.4	0.58	7.2	18.5	18.5	3.2	1.6	0.05	17	n.d.	20
John_Klein_RP3	49.4	0.64	6.9	19	17.4	2.3	2.68	0.16	17.1	n.d.	70
John_Klein_RP3	35.3	0.83	7.5	15.6	5.9	16.5	1.73	0.1	n.d.	n.d.	211.3
John_Klein_RP3	47.8	0.92	11.4	17.8	7.6	6.8	3.31	0.32	9	9	130.1
John_Klein_RP3	47.8	0.98	11.2	18.6	7.2	6.4	3.32	0.38	8.9	n.d.	123.4
DT_RP5_STG	47.5	0.98	14.1	18.6	7.5	6.7	3.49	0.59	12.6	28.3	137
DT_RP5_STG	51.3	0.81	11.7	18.8	10.5	4.6	3.43	0.66	11.2	32.7	134.8
DT_RP5_STG	49.9	0.9	12.4	17.9	8.8	6.4	3.32	0.53	11.3	n.d.	167.3
DT_RP5_STG	49.2	0.91	12.5	18	8.6	6.4	3.4	0.59	12.5	27	136.9
DT_RP6	50.1	0.93	13.5	19.8	8.2	7	3.09	0.48	15.2	n.d.	121.4

DT_RP6	50.2	0.86	14.1	19.2	9.3	6.5	3.33	0.44	11.8	n.d.	155.8
DT_RP6	50.1	0.95	13.4	18.7	8.1	6.5	3.31	0.57	14.7	43.6	147.2
DT_RP6	48.9	1.05	11.8	19.7	8.4	5.8	3.3	0.67	12.8	45.3	157.7
Wernecke_1	48.1	0.97	11.4	18.3	7.9	5.8	3.25	0.68	10.8	n.d.	162.7
Wernecke_1	48.1	1	12.1	17.9	7.3	5.9	3.53	0.74	9.7	81.7	160.6
Wernecke_1	49.8	0.96	12.3	17.8	7.6	5.4	3.51	0.82	10.2	144.7	136.2
Wernecke_1	48.5	1.07	11.9	18.9	7.2	5.5	3.43	0.84	9.9	42.2	154.6
Wernecke_1	49	1	10.9	19	7.7	5.6	3.17	0.69	7.8	41.1	115.8
Wernecke_1	49.6	0.9	10.9	18.3	8.3	5.7	3.19	0.67	9.1	n.d.	113.2
Wernecke_1	49.2	0.98	10.3	18.7	8	5.2	3.37	0.74	8.3	34	130.6
Wernecke_1	49.6	0.95	10.4	18.4	7.9	5.4	3.48	0.73	9.2	n.d.	126.1
Wernecke_1	48.6	0.91	12.5	18.1	7.8	6	3.45	0.71	9.2	34.8	150.7
Wernecke_1	47.6	1.18	9.6	20.1	8.3	4.6	3.18	0.67	8	52	148
Wernecke_1	47.3	0.96	10.2	18.9	7.8	6.4	3.23	0.71	9.9	32.9	106.2
Wernecke_1	48	0.99	11.6	18.7	8.2	5.6	3.22	0.67	11.2	115.4	137.5
Wernecke_1	47.8	0.97	10.4	18.2	7.9	5.7	3.41	0.79	10.9	36.1	120.2
Wernecke_1	48.5	0.93	11.2	18.7	8.4	5.5	3.32	0.7	11.8	n.d.	141.4
Wernecke_1	48.3	1.04	10	19.5	8.5	4.9	3.22	0.73	9	n.d.	93
Wernecke_1	48.3	1.02	10.4	19.1	8.4	5.3	3.32	0.77	9	n.d.	128.6
Wernecke_1	48.7	0.99	11.2	19.2	8.3	5.5	3.16	0.65	9	43.6	154.4
Wernecke_1	47.8	0.96	10.9	19.4	8	5.8	3.12	0.58	10.6	n.d.	134.7
Cumberland	47.6	1.08	10.8	19.4	7.3	5.8	3.24	0.66	8.2	41.3	126.7
Cumberland	47.8	0.99	8.6	18.8	9	5	3.02	0.47	7.3	n.d.	62.5
Cumberland	46.7	1.01	9.1	18.9	8.3	6.1	2.95	0.41	6.9	n.d.	84.5
Cumberland	44.6	0.95	9.8	18.6	8.5	6.8	2.82	0.42	11	n.d.	79.4
Cumberland	45.7	1.18	10.9	19.9	7.4	5.6	3.08	0.48	9.4	n.d.	130.2
Cumberland	48.4	1	9.7	19.9	8.3	5.3	3.13	0.47	7.8	n.d.	102.4
Cumberland	48.4	1.07	10.2	20	7.4	5.3	3.15	0.5	7.2	n.d.	121.5
Cumberland	49.5	0.91	8	20.4	11.4	3.2	3.47	0.37	8.3	n.d.	n.d.
Cumberland	48.9	0.95	9.3	19.8	10.2	5	2.76	0.45	8.3	36.3	95.7

Cumberland	47.5	1.04	11.4	19.4	6.6	7.1	3.19	0.56	10.1	36.3	138.7
Cumberland	51.6	0.87	8.2	19.9	11.3	3.7	3.49	0.3	10.8	1.3	60.5
Cumberland	47	1.09	11	19.6	7.1	5.9	3.06	0.49	7.2	4.8	121.5
Cumberland	47.5	1.08	10.4	20.1	7.7	5.3	3.18	0.62	8.9	46.2	108
Cumberland	50.2	0.91	8.2	20.1	12.5	3.7	2.36	0.3	7.5	8.4	75.7
Cumberland	46.7	1.06	10.7	20.1	8.2	5.2	2.91	0.45	11.9	n.d.	104.2
Cumberland	47.3	1.09	11.1	19.8	7.1	6.2	3.05	0.53	9.6	32.4	133.8
seward_1	40	0.73	8.1	19.5	7.6	7.2	1.63	0.17	9	n.d.	51
seward_1	42.4	0.62	9.9	21.6	9.3	4.6	2.34	0.33	8.8	n.d.	6.1
seward_1	40.5	0.76	8.7	18.9	8.3	7.1	1.9	0.23	4.6	26.1	63
seward_1	31.8	0.63	5.4	12.6	3.7	24.6	0.89	0.14	10.1	n.d.	126.3
seward_1	45.2	0.73	7.5	18	16.6	3.4	2.04	0.5	8.5	49.7	78.9
seward_1	46.3	1.03	10.6	19.4	7.1	6.3	2.82	0.55	10.8	35.9	150.8
seward_1	46.6	0.9	10.4	18.4	9.4	5.7	2.91	0.63	10.3	n.d.	103.2
seward_1	45.2	0.96	9.8	19	11.1	5.1	2.74	0.51	6.3	n.d.	136.3
seward_1	46.9	1.12	10.3	19.5	7.6	5.7	3.2	0.77	9.2	41	121
seward_1	41.2	0.88	7.9	18.2	9	9.6	2.08	0.39	11.2	n.d.	94.9
seward_1	48.9	0.83	7.1	19.4	14.5	3.3	2.14	0.46	10.5	n.d.	68.8
seward_1	46.9	1.11	11.2	19.7	6.9	5.7	3.24	0.67	12.1	92.9	191.5
seward_1	48	0.93	10.7	19.2	8.1	5.7	3.08	0.67	8.8	32.3	163.1
seward_1	48.6	0.89	10.7	18.5	8.1	6.1	3.27	0.62	9.1	79.7	155.7
Kazan	48.1	0.97	9.4	18.9	8.7	5.3	2.97	0.56	10.1	33.6	91.8
Kazan	46.7	1.1	10	20.5	8	4.7	3.03	0.74	9	48.9	110.3
Kazan	47.1	1.03	10.3	19.4	7.2	5.9	2.84	0.59	12	32.7	134.8
Kazan	43.1	0.92	7.8	21.8	6.5	4	2.48	0.29	7.5	n.d.	50
Kazan	45.6	1.33	10.8	20.5	7	5.4	2.94	0.53	8.8	47.7	142.6
Kazan	48.7	1.06	10.5	19.1	7.2	5.6	3.08	0.66	12.2	40	158.9
Kazan	47.5	1.23	10.5	20	6.8	5.2	3.22	0.73	9	50.9	n.d.
Kazan	45.6	1.17	10.9	19.5	7.8	5.4	3.11	0.59	9.7	41.6	114.8
Kazan	46.2	1.16	10.5	20.3	7.8	5	2.97	0.57	10.7	44.4	99.4

Kazan	50.7	1.01	9.6	19.5	8.2	4.6	3.11	0.55	9.6	47.4	102.4
Kazan	48.4	1.06	11.2	19.9	7.1	5.6	3.22	0.62	9.1	n.d.	136.6
Kazan	49.4	0.99	8.3	19.7	10.7	3.5	3.18	0.62	12.3	45.7	96.1
Kazan	50	1.04	9.2	19.1	9.7	5.1	3.04	0.47	9.8	n.d.	98.7
Kazan	49.9	0.92	9.3	20.4	10.1	4	3.5	0.61	9.8	n.d.	88.9
Kazan	45.4	1.01	8.7	20.7	10.6	4.3	2.48	0.45	9.1	37.1	94.5
Kazan	35.3	1.27	6.6	19.3	5.2	13.9	1.67	0.2	14.1	n.d.	83.2
Kazan	48.3	0.98	7.9	20.7	10.4	4.2	3.02	0.52	10.3	n.d.	75.6
Kazan	45.1	1.08	9.2	18.8	7.8	5.5	2.32	0.33	8.5	n.d.	119.8
Kazan	45.4	1.1	11.2	19.5	7.5	5.8	2.99	0.57	10.6	36.7	123.3
Kazan	46.5	1.2	9.8	20.6	7.8	4.7	3.09	0.69	9.5	n.d.	124.6
Kazan	44.3	1.46	8.7	21	8	5.1	2.77	0.64	10.1	43.5	114.1
Kazan	47.4	1.19	10.5	20.2	7.2	5.4	3.19	0.74	11.2	45.9	125.2
Kazan	48.8	1.12	9.4	19.3	7.5	4.7	3.1	0.62	9.7	36	81
Kazan	47.6	1.02	9.2	19.1	8.2	5.7	2.27	0.31	9.6	n.d.	86.3
Fury	47.9	0.9	11.8	18.1	7.4	6.4	3.33	0.63	7	116	171.2
Fury	47	0.98	10.5	18.5	7.7	6.6	3.22	0.64	10.3	n.d.	132.3
Fury	46.9	0.92	10.5	18.9	8.2	6.3	3.08	0.57	8.5	43.1	159.4
Fury	40.5	0.7	7.7	16.4	18.1	3.9	1.98	0.27	4.9	n.d.	84.8
Fury	48.4	0.94	10.1	18.6	11	4.7	2.86	0.44	11.3	n.d.	73.8
Fury	46.5	1.23	9.3	20.1	6.9	5.5	3.2	0.67	8	83.2	105.4
Fury	48.2	1.07	9.7	19.7	7.4	5.4	3.15	0.64	7.7	n.d.	108.6
Fury	46.6	1.15	9.8	20.6	7	5.5	3.15	0.64	8.6	n.d.	95.8
Rae	49	0.91	10.3	18.3	8.7	5.2	3.49	0.63	7.9	n.d.	127.4
Rae	49.4	0.83	8.3	19.6	12.3	3.7	3.18	0.68	11.1	41.6	90.8
Rae	47.4	0.98	9.5	19.2	8.9	5	3.26	0.61	6.6	n.d.	132.3
Rae	46.5	1.09	10.1	19.6	8.3	5.7	3.13	0.54	7.1	45.5	118.1
Rae	46.7	1	9.8	19.8	9.2	5.1	3.16	0.55	8.1	n.d.	127.5
Rae	46.2	1.01	9.2	19.2	9.1	5.8	3.07	0.5	9.8	10.9	117.4
Rae	47.9	1.03	10	19.2	8.3	5.1	3.29	0.61	6.1	51.6	138.1

Rae	48.8	0.9	9.6	18.3	8.4	5.1	3.69	0.67	8.1	n.d.	98.4
Rae	46.2	0.91	9.9	19.3	8.9	6.3	2.98	0.41	11.8	n.d.	120.2
Iqqittuq	50.7	0.77	7.5	19	13.8	3.3	2.66	0.49	8.7	n.d.	75.4
Iqqittuq	48	0.96	11.1	18.7	8.1	6.1	3.3	0.53	10.2	42.3	141.7
Iqqittuq	49.7	0.86	7.8	19.7	13.8	3.6	2.69	0.48	9.9	n.d.	96.1
Iqqittuq	48.1	0.99	11.5	18.9	8.4	5.4	3.53	0.6	12.1	33.8	166
Iqqittuq	50.4	0.78	8.7	20	12.9	3.5	2.81	0.54	10.2	n.d.	100.7
Iqqittuq	46.1	1.05	10.4	21.4	8.8	4.9	3.08	0.48	11.2	n.d.	97.5
Iqqittuq	48.7	0.79	9.1	20.5	10.1	6.4	2.61	0.47	12	n.d.	64.4
Iqqittuq	46.9	1.01	10.4	21.5	8.3	5.9	3.03	0.61	11.3	9.5	77.6
Iqqittuq	47.3	1.01	11.4	19.6	7.9	5.7	3.35	0.62	13.8	34.7	108.6
Bylot	47.2	1.03	10.1	18.8	8.2	5	3.35	0.6	7.6	48.7	115.1
Bylot	49.6	0.89	10.3	17.6	8.4	5.3	3.47	0.72	7.2	48	120.8
Bylot	46.7	0.9	9.8	19.2	10.9	4.5	2.98	0.5	7.7	33.2	123
Bylot	48.2	1.01	10.6	18.5	8.6	5.2	3.34	0.59	6.5	37.6	134.4
Bylot	50.4	0.88	8.5	19.6	10.6	4.2	2.79	0.48	7.3	n.d.	78.5
Bylot	49.3	0.85	7.1	19.8	14	3.2	2.54	0.48	6.6	n.d.	64.6
Bylot	46.3	0.98	9.3	19	8.7	5.3	3.17	0.56	8.7	35.2	97.9
Bylot	46.4	1	10	18.7	8.2	6	3.23	0.6	8.2	n.d.	124.9
Bylot	47.1	1.03	10.1	19.4	8.8	4.8	3.25	0.65	8.9	34.3	136.8
Rae	48	0.95	10.5	18.6	8.5	5.6	3.32	0.57	10	n.d.	153.4
Rae	50	0.78	9.4	19.2	11.7	3.9	3.37	0.8	9.2	38.5	110.8
Rae	48.2	0.87	11.5	18.7	7.9	6.5	3.37	0.59	8.6	40.4	173.8
Rae	46.7	0.9	9.1	19.2	9.2	5.6	3.35	0.55	11.2	41.1	108.8
Rae	46.2	0.96	10.4	19.6	8.2	6.1	3.31	0.58	9.6	30.3	136
Rae	46.9	0.93	10.4	19.1	8.6	5.8	3.41	0.56	8.8	39.5	131.2
Rae	48.5	0.87	12.2	18.9	8	5.9	3.49	0.65	7.2	28.8	161.3
Rae	48.1	0.87	11.3	18.6	8.6	5.6	3.49	0.64	8.3	36.5	140.9
Rae	48.3	0.92	10.5	19.2	8.6	5.3	3.34	0.54	8	n.d.	148.7
Thelon	47.1	1.14	10.1	19.6	7.4	5.6	2.84	0.57	7.6	43.3	113.3

Thelon	46.9	1.04	9.7	19.3	8.9	5.6	2.41	0.41	9.3	n.d.	119.4
Thelon	45.9	1.35	10.3	19.1	7	5.7	3.16	0.71	9.5	n.d.	109.4
Thelon	45.8	1.15	9.6	20.1	7	6.5	2.76	0.56	11.5	56.5	112.1
Thelon	46.5	1.06	9.3	19.5	10.2	5	2.8	0.56	9.3	29.5	153.9
Thelon	43.9	1.11	7.9	18.8	7.2	8.6	2.4	0.42	13.9	n.d.	89.6
Thelon	46.9	1.09	10.5	19.5	7.3	5.7	3.14	0.66	11.4	43.3	146.3
Thelon	46.8	1.06	8.4	19.5	8.9	4.2	3.13	0.68	7.9	n.d.	72.4
Thelon	47.8	1.23	10.3	19.9	7	5.7	3.06	0.56	10.9	53.7	114.4
Drillhole_CCAM	46	0.97	9	18.8	9.1	5.9	2.9	0.45	11.4	30.5	79
Drillhole_CCAM	47	1.09	9.4	19.6	8.7	5.2	2.91	0.49	9.1	n.d.	128
Drillhole_CCAM	46.2	1	9.2	19.6	8.4	5.3	3.18	0.6	7	n.d.	91.5
Drillhole_CCAM	45.3	1.19	8.8	20.2	8.3	5.1	3	0.49	8.7	40.4	118.9
Drillhole_CCAM	45.9	1.09	9.6	19.4	8.2	5.2	3.17	0.58	6.8	30.2	97.4
Drillhole_CCAM	47.4	1.02	10	19.3	9	5.3	2.92	0.44	6.2	n.d.	98.2
Drillhole_CCAM	38.8	0.65	5.5	17.6	9.2	13.6	1.39	0.2	11.5	n.d.	66
Drillhole_CCAM	45.2	0.92	8.4	20	9	6.2	2.18	0.29	9.7	n.d.	85.5
Drillhole_CCAM	38.3	0.66	7	16.3	6.6	13.6	1.18	0.06	8.7	n.d.	102.1
Drillhole_CCAM	44.4	0.71	8.3	18.7	9.1	5.9	2.03	0.16	8.1	n.d.	52.1
Ruth	46.3	1.15	10.8	20.7	7.2	5.1	3.17	0.65	11.7	28.6	106
Ruth	45.3	1.24	9.6	20.7	7.4	5	3.1	0.68	12.1	n.d.	96.1
Ruth	43.7	1.33	9.3	20.9	6.9	5.1	3.06	0.69	13.3	n.d.	75.2
Ruth	45.5	1.25	10.2	21.2	6.8	5.2	3.36	0.72	14	34.8	89.2
Ruth	45.4	1.34	9.6	20.8	7.9	5.1	3	0.61	11.8	47.3	101.9
Ruth	46.3	1.17	10.7	20.7	7.5	5.3	3.15	0.62	11.5	28.5	122
Ruth	48.3	0.94	9.9	20.5	9.8	4.7	3.17	0.56	13.7	34.6	106.2
Ruth	47.3	1.01	10.6	20.8	8	5.2	3.24	0.68	13.8	30.7	148.5
Ruth	51.1	0.93	9.6	20.1	8.5	5.3	3.22	0.51	10.8	n.d.	85.9
Ruth	47	1.24	10.5	21.2	7.3	5.2	3.24	0.65	12.7	32.7	138.7
Ruth	47.4	1.11	9.9	21	8.5	5.3	2.95	0.58	11	25.2	126.7
Ruth	48.8	0.96	10.3	20.3	8	5.6	3.12	0.6	11.1	n.d.	126.4

Ruth	46.7	1.03	11.6	20.3	7.6	5.7	3.02	0.48	11.1	35.8	165.7
Ruth	49.8	1	8.5	20.6	9.5	4.6	3.05	0.43	10.3	n.d.	98
Ruth	47.5	1.03	9.6	20.7	8.7	5.5	2.74	0.48	13	n.d.	116.4
Ruth	47.2	0.99	8.1	20.9	13.7	3.4	2.55	0.47	14.6	n.d.	n.d.
Ruth	46.1	1	10.4	20	10.7	5.1	2.84	0.58	11.8	n.d.	138.8
Ruth	46.2	0.98	9.2	20.1	12.2	4.9	2.66	0.46	10.6	n.d.	126.5
Ruth	48.7	0.95	9.4	19.3	11.7	4.5	2.99	0.59	8.8	n.d.	103.4
Ruth	47.7	1.01	10	21.6	9.5	4.3	2.9	0.58	10.7	n.d.	106.1
Cumberland_CCAM	48.3	1.08	10.7	20.3	7.1	5.7	3.27	0.51	10	n.d.	108.7
Cumberland_CCAM	48.4	0.95	10	19.2	8.3	5.2	3.16	0.48	10.9	n.d.	85.1
Cumberland_CCAM	47.5	1.05	11.5	20.1	7.3	6.4	3.22	0.5	11.4	n.d.	129.1
Cumberland_CCAM	46.8	1.05	11.8	20.4	7.8	6.2	3.07	0.48	18.7	n.d.	100.2
Cumberland_CCAM	47.7	1.11	11.3	21.3	7.3	5.6	3.18	0.5	10.1	n.d.	100.9
Kazan_CCAM	44.3	0.95	8.5	19.7	15.3	4.4	2.28	0.3	5.8	n.d.	59.2
Kazan_CCAM	47.6	1.21	11.5	21.4	6.8	5.2	2.92	0.46	15.8	n.d.	137.1
Kazan_CCAM	48.8	1.11	12.1	20.5	7.3	5.3	3.48	0.76	17.9	42.3	138.2
Kazan_CCAM	52	0.88	13.2	19.5	9.2	6.7	2.51	0.3	13.8	n.d.	171.9
Kazan_CCAM	52.8	0.83	11.3	21	9.8	4.5	3.44	0.64	11.6	3.5	57.7
Cumberland_Bowl	49.4	1.08	11.1	19	6.6	5.1	3.08	0.66	9	112.4	166.1
Cumberland_Bowl	45	0.82	7.8	17.6	16.7	3.8	2.1	0.32	8.8	n.d.	73.2
Cumberland_Bowl	44.8	1.03	9.6	19.5	9	5.1	2.74	0.54	8.4	46	109.8
Cumberland_Bowl	44.7	0.86	9	18.1	13.9	4.8	2.5	0.51	10.3	32.5	99.4
Cumberland_Bowl	47.9	0.94	10	19.3	8.6	4.9	3	0.64	10.2	30.8	123.6
Cumberland_Bowl	47	0.99	8.6	19.2	7.7	6.6	2.73	0.52	14	118.2	81.1
Cumberland_Bowl	43.4	0.84	8.3	18.5	16.3	4.5	2.36	0.45	8.7	n.d.	101.2
Cumberland_Bowl	50.3	0.92	8.5	20.3	10	3.7	3.66	0.64	14.7	34	89.5
Cumberland3	40	0.82	6.6	17.1	6.2	14.8	1.63	0.3	17.5	n.d.	101
Cumberland3	48.9	0.8	7.6	18.1	8.3	8	2.8	0.5	13.1	n.d.	95.1
Cumberland3	42.7	0.85	8.5	18.2	16.6	4.4	2.27	0.34	9.1	n.d.	101.2
Cumberland3	47.2	0.85	7.9	20	10.1	5.7	2.65	0.54	15	22.5	70.1

Cumberland3	45	1.14	9.3	21.4	7.5	4.9	2.62	0.48	10.2	n.d.	100.8
Cumberland3	45.8	1.1	10	20.2	7.2	6.1	2.81	0.58	11.9	63.9	140.3
Cumberland3	47.4	0.89	7.8	20.1	9.8	4.5	2.92	0.44	10.1	n.d.	75.4
Cumberland_Hole	40.7	0.91	8.3	19.4	8.4	6.8	2.14	0.26	5.7	6.9	55.8
Cumberland_Hole	44.1	0.9	8.1	20.3	8.7	6	2.28	0.33	6.3	n.d.	n.d.
Cumberland_Hole	46.6	0.91	9.2	19.5	8.3	6.5	2.73	0.4	8.7	n.d.	92
Cumberland_Hole	46.3	1	8.8	20.1	8.2	5.6	2.95	0.42	10.1	n.d.	82.8
Cumberland_Hole	45.6	0.99	8.3	20.4	8.6	5.8	2.47	0.31	8.8	n.d.	74.4
Cumberland_Hole	47.7	0.88	7.9	20.7	11.4	4.1	2.27	0.3	9.6	n.d.	68.5
Cumberland_Hole	46.8	1.01	9.1	20.3	8.3	6	2.59	0.35	7.2	n.d.	83.1
Cumberland_Hole	47.1	0.94	9.3	20	8.3	5.6	2.94	0.43	8.1	28.3	89.7
Cumberland_Hole	46.6	1	8.8	20.4	8.5	5.2	3	0.46	7.8	n.d.	85.2
Cumberland_Hole	44.4	1.08	9.2	21.2	7.7	5.9	2.91	0.44	11	n.d.	80.3
Cumberland_DRT_RP	48	0.88	7.6	19.7	10.8	4.2	2.92	0.46	9.3	6.9	86.6
Cumberland_DRT_RP	48.3	1.02	10.8	18.4	6.9	5.1	3.62	0.76	9.8	44.5	103.8
Cumberland_DRT_RP	46.7	1.07	9.2	19.4	8.3	4.9	2.98	0.61	8.8	79.3	123.5
Cumberland_DRT_RP	48.8	0.96	10.5	18.9	7.7	5.5	3.11	0.67	9.3	84.2	140.2
Cumberland_DRT_RP	48.2	1.22	9.9	19.3	7.7	5.1	3.09	0.73	10.2	97.3	103.6
Cumberland_DRT_RP	48.3	1.01	10.8	19.5	7.3	5.8	2.98	0.53	9	104.5	145.8
Cumberland_DRT_RP	46.6	1.3	10	21.4	6.6	4.6	3.15	0.78	10.9	35.7	96.2
Cumberland_DRT_RP	48	1.16	10.3	21.3	7	5	3.02	0.7	13.1	n.d.	101.8
Cumberland_DRT_RP	48.4	0.97	10.2	18.3	8.1	5.6	2.95	0.6	11.2	23.7	118
Duluth	49.5	0.98	12.8	19.5	7.1	6.1	3.33	0.55	6.9	n.d.	154
Duluth	48.9	0.94	12.8	19.2	7.6	6.1	3.54	0.55	7.4	n.d.	151.3
Duluth	49	0.97	12.3	19.3	7.1	6.4	3.44	0.63	9.5	37.5	131.7
Duluth	49.3	0.9	12.2	19	7.1	6.9	3.49	0.61	12.1	41	133.7
Duluth	48.5	0.98	12.4	19.7	6.8	6.3	3.26	0.59	8.1	n.d.	122.9
Cumberland3_ccam	46.6	0.99	10.1	19.4	7.2	5.7	3.04	0.64	9.9	41.4	128.5
Cumberland3_ccam	48	0.99	12.4	19.1	6.3	6.1	3.2	0.68	10.1	39.9	175.7
Cumberland3_ccam	46.1	1.18	10	20.6	6.9	5.8	2.83	0.6	9.6	36.7	175.7

Cumberland3_ccam	48.3	0.98	10.5	19.2	7	6	3.39	0.74	11.2	45.5	124.6
Cumberland3_ccam	47.5	1.06	11.2	20.2	6.5	6.4	3.12	0.64	11.7	34.8	168.4
Cumberland3_ccam	45.1	0.86	8.1	21	12.3	4.9	2.43	0.42	12	n.d.	97.7
Cumberland3_ccam	46.9	0.91	10.2	18.5	8.1	6.2	2.83	0.5	10.3	n.d.	124.6
Cumberland3_ccam	47.4	0.93	9.6	20.1	8.5	4.9	3.15	0.61	10.8	29.7	120.9
Sibley	51.1	0.76	8.5	18.5	11.6	3.2	4.09	0.48	9.6	n.d.	87.2
Sibley	45.4	0.83	10.8	17.9	13.2	5.2	2.88	0.51	9.7	n.d.	124.4
Sibley	49.7	1.04	12.9	19.1	6.7	6.1	3.49	0.78	10.7	43.7	138.4
Sibley	49	0.95	13	20	6.9	6.2	3.2	0.59	9.8	28.1	136.2
Sibley	47.1	1.03	11.9	20.1	6.9	6.2	2.84	0.45	10	n.d.	157.1
Mesabi	45.9	1.04	9.9	20.5	7.6	5.2	3.06	0.62	7.8	114.8	91.1
Mesabi	46.6	0.97	9.8	19.6	7.9	5.8	3.04	0.63	n.d.	70.4	88.4
Mesabi	46.8	1.03	10	21	7.8	5.3	2.99	0.61	8	43.8	122.2
Mesabi	46.7	1.01	8.6	21.1	8.1	4.8	2.63	0.48	7.5	n.d.	59.6
Mesabi	46.7	1.04	8.7	20.7	8	4.9	2.91	0.56	6	37.8	88.5
Mesabi	46.7	1.03	8.8	20.5	8.1	5.4	2.74	0.48	7.1	47.9	94.3
Mesabi	47.9	0.94	8.5	19.6	8.2	5.6	2.6	0.37	6.1	26.6	77.3
Mesabi	49.2	0.87	8.7	19.6	9.5	5.3	2.26	0.28	5.4	n.d.	73.7
Mesabi	47	0.82	7.7	21.2	13.6	4.4	2.15	0.35	10.9	n.d.	48.8
Cape_Strawberry	46.8	1.21	8.9	21	8.3	5	2.91	0.53	7.6	43	92.6
Cape_Strawberry	48.1	0.98	10	19.8	8.2	6.1	3.09	0.57	10	35.3	119.5
Cape_Strawberry	47.3	1	9.8	19.9	7.6	6.3	3.12	0.65	11.1	48.1	103.2
Cape_Strawberry	48	0.96	10.2	20.3	8.7	5.9	2.86	0.54	8.2	34	130.9
Cape_Strawberry	47.8	1.06	11.2	20	7.5	5.6	3.27	0.6	8.8	31.5	118.3
Cape_Strawberry	47.6	1.07	11.1	20.5	7.4	5.5	3.29	0.61	8	37.8	136.6
Cape_Strawberry	47.2	1.05	11.5	20.9	7.2	5.9	2.75	0.4	8.4	n.d.	113.9
Cape_Strawberry	46.7	1.15	9.4	22.4	8.1	5	2.62	0.47	10.2	36	95.6
Cape_Strawberry	39.7	0.75	6.3	19.9	6.2	12.9	1.75	0.18	12.7	n.d.	111.9

Veins

Target	SiO_2	TiO_2	Al_2O_3	FeO_T	MgO	CaO	Na_2O	K_2O	Li (ppm)	Rb (ppm)	Sr (ppm)
Measles_Point	1.4	0	0.5	2.7	3.1	33.6	0.92	0.03	5.1	n.d.	345.7
Crest	21.8	0.33	4	7.3	3.1	28.2	1.05	0.01	6.8	n.d.	101.6
Richardson_2	18.1	0.55	3.6	8.2	3.5	28.3	0.6	0.05	6.5	n.d.	218.7
Richardson_2	13.6	0.53	2.7	8.7	3.9	26.4	0.6	0.02	4.6	n.d.	182.4
Quartet	27.5	0.61	3.2	11.2	4.4	28.1	0.7	0.04	9.3	n.d.	193.2
Quartet_ND	0.9	0	0.8	3.9	1.2	37	0.2	0	7.3	n.d.	186.9
Selwyn	22	0.37	4.1	9.1	3.3	30.2	0.65	0.03	9.9	n.d.	194.7
Selwyn	14.9	0.31	3.3	4.7	2.2	33.2	0.46	0.02	9.4	n.d.	225.2
Mavor	6.2	0.2	0.6	5.3	3	32.3	0.25	0.01	6.4	n.d.	254.1
Mavor	0.2	0	0.3	0.1	1	38.3	0.04	0	7	n.d.	195.7
DT_RP6	33.8	0.55	8.2	11.1	4.8	30.8	1.29	0.09	11.4	n.d.	195.9
seward_1	0.1	0	0.4	2.1	0.9	37.8	0.11	0	6.8	n.d.	125.8
Kazan	0	0	0.4	2.1	0.8	39.8	0.09	0	8.1	n.d.	471.9
Fury	9.3	0.56	1.6	8.6	2.9	27.8	0.35	0.01	5.6	n.d.	196.7
Ruth	0.9	0	0.3	2.1	1.3	34.7	0.03	0	7.4	n.d.	286.2
Ruth	20.9	0.64	4.9	10.7	3.1	31.5	0.74	0.05	8.4	n.d.	340.1
Ruth	21.7	0.52	2.1	7.4	3.2	27.1	0.52	0.03	6.5	n.d.	157.8
Ruth	21.9	0.61	3.6	11	3.3	31.1	0.67	0.05	8.3	n.d.	202.9
Ruth	5	0.2	0.6	7	3.6	30.2	0.22	0.01	6	n.d.	191.6
Cumberland_Bowl	3.4	0.2	0.5	5.4	2.2	29.8	0.14	0.01	5.9	n.d.	211.5
Cumberland3	2.2	0	0.4	0.8	1.3	35	0.27	0.01	6.4	n.d.	372.1
Cumberland3	26	0.58	4.8	10.5	4	25.5	0.85	0.09	8.4	n.d.	102.2
Cumberland3_ccam	18	0.54	4.2	11.5	2.9	27.2	0.84	0.05	4.9	24.2	192.3

Float Rocks

Target	SiO_2	TiO_2	Al_2O_3	FeO_T	MgO	CaO	Na_2O	K_2O	Li (ppm)	Rb (ppm)	Sr (ppm)
Watterson	40.8	1.31	7	29.7	2.6	7.1	2.91	0.64	18.4	n.d.	178.3
Watterson	48	0.84	7.9	30.8	2.2	0.7	2.87	0.9	18.5	n.d.	266.2
Watterson	43.8	0.91	9	28.9	4.3	3	2.33	0.33	19.4	n.d.	189.9
Watterson	43	1.3	5.5	34.1	2.8	2.4	2.39	0.45	19.1	n.d.	142.8
Watterson	41	1.49	8.2	36.1	2.4	0.9	3.01	0.9	8.6	n.d.	n.d.
Watterson	48.1	0.84	8.6	24.1	2.8	4.4	3.57	0.87	25.9	73	355.1
Watterson	39.9	0.95	5.5	29.8	2.3	5.8	2.91	0.35	12.6	n.d.	30.4
Watterson	51.3	0.65	8.4	19.2	2.7	5.4	4.26	0.7	22.2	43.9	252.9
Watterson	38.5	1.42	6.7	31.7	2.6	6.1	2.23	0.34	16.5	n.d.	58.6
Watterson	46.8	0.7	7.9	23.3	2.7	4.8	3.2	0.8	22.1	47.7	312.2
Gunflint	43.6	1.6	7.4	21.4	8.4	4.6	2.57	1.46	15.3	83.4	121
Gunflint	42.1	1.19	8.3	21.5	7.4	5.9	1.88	0.44	7.8	29.2	83.6
Gunflint	46.9	1.14	7.9	21.8	9.2	5.4	2.46	1.23	12.9	79.1	223.4
Gunflint	46	1.23	8.3	21.3	10.1	4.7	2.31	1.38	12.8	66.6	270.2
Gunflint	44.4	1.78	7.3	20.9	9.1	3.9	2.39	1.48	11.8	32.4	173.8
Gunflint	45.8	1.33	7.2	20.6	9.9	5.1	2.45	1.33	15.1	17.4	154.9
Gunflint	45.8	1.17	5.9	21.5	10.7	6.1	2.39	0.69	21.3	n.d.	78.5
Gunflint	46.6	1.41	8.3	21.2	10	5.4	2.34	1.11	14.2	n.d.	293.4
Gunflint	45.1	1.41	7.2	20.8	11.6	4	2.36	0.77	19.3	25.2	163.8
Gunflint	47.4	0.98	6.4	20.8	14.4	3.5	2.6	1.05	29	n.d.	148.1
Pisolet	41.9	1.65	9.6	23.3	7	4.7	2.85	0.96	31.7	73.3	140.5
Pisolet	45.3	0.96	7.5	20.5	13.7	3.7	2.7	0.68	44.3	25	n.d.
Pisolet	43.3	1.39	10.5	20	6.6	5.8	3.17	1.51	39.4	97.2	133.1
Pisolet	45.2	1.24	8.9	20.5	11	3.2	3.07	0.99	33.5	n.d.	113.4
Pisolet	45.3	1.62	9.5	21	7.1	5	3.05	1.15	15.4	68	174.2
Pisolet	43.2	1.69	8.8	20.8	7.1	5.8	2.73	1.11	17.6	n.d.	120.7
Pisolet	45.7	1.05	7.7	20.6	12.8	5.1	2.46	0.7	27.2	n.d.	43.4

Pisolet	51.7	1.25	17.9	14.9	3.6	5.5	4.4	1.93	21.2	108.7	525.9
Pisolet	44.7	1.56	10.3	21	6.6	5.3	2.9	1.37	19.9	83.6	100.8
Ikpiarjuk	47	0.97	17.8	23	6	1.3	4.5	1.05	18.5	87.3	34.8
Ikpiarjuk	51.2	1.2	23.6	10.2	1.6	3.3	7.95	1.46	19.9	n.d.	151.4
Ikpiarjuk	54.3	0.95	23.9	6.8	1.1	3.2	8.72	1.99	20	n.d.	228.4
Ikpiarjuk	50	0.74	17.9	12.3	4.1	12.7	5.18	1.44	22.7	8.9	49.1
Ikpiarjuk	37.5	3.54	11.3	29.6	3.9	6.2	3.51	0.58	18.5	n.d.	n.d.
Blackhead	54.4	0.85	20.1	11.3	1.2	3.9	7.68	2.18	9.5	80.7	417.9
Blackhead	45.3	1	17.9	20.6	2	6.3	5.28	1.24	9.5	25	76.4
Blackhead	47.4	1.37	16.5	20.9	2.6	3.6	4.37	1.58	12.3	n.d.	224.3
Blackhead	48.8	0.75	16.6	16.9	3.9	9.9	4.9	0.94	17.5	n.d.	89.3
Blackhead	39.8	1.29	9.5	22.7	5	7	3.01	0.79	8.5	n.d.	57.2
Blackhead	42.8	1.62	11.6	23.4	2.4	4.2	4.05	0.87	6.1	n.d.	210.5
Blackhead	37.2	0.71	9.5	15	3.4	18.7	2.47	0.8	10.4	55.6	88.5
Blackhead	48.8	0.79	16.1	18.6	4.2	7.8	5.66	1.15	18.9	n.d.	n.d.
Blackhead	50.1	0.74	16.4	15.9	4.9	6.7	5.29	0.98	22.8	49.1	43
Fleur_de_Lys	44.4	2.17	9.1	20.2	3.7	8.6	3.28	0.41	14.8	n.d.	59.3
Fleur_de_Lys	46.4	1.87	11.8	19.6	3.1	7.9	3.64	0.51	14.2	78.7	87.6
Fleur_de_Lys	50.5	1.58	11.4	18.4	3.7	7	3.83	0.51	10.4	n.d.	98.8
Fleur_de_Lys	51.5	1.68	14.8	16.3	2.5	7.6	3.85	0.55	7.5	n.d.	85.3
Fleur_de_Lys	43.9	1.4	11.1	19.7	3.2	7.8	3.16	0.4	13.9	n.d.	66.2
Aztec	43.7	2.63	14.1	23.2	3.2	3.7	3.96	1.04	11.7	69.6	171.5
Aztec	45.4	1.47	17.5	21	1.9	5.1	4.78	1.14	6.1	80.6	132.9
Aztec	48.9	0.86	17.8	16.2	1.5	6.7	6.4	1.31	29.1	98.2	185.9
Aztec	37.9	2.08	11.2	25.7	2.7	7.3	3.31	1.09	13.7	74.9	81.1
Aztec	53.3	0.8	18.9	13	1.1	5.9	6.59	1.16	7.5	70.7	456.1
Tully	44.7	1.26	10.5	20.3	8.1	4.5	2.77	0.97	20.2	103.6	161.8
Tully	50.6	0.9	17.5	13.7	4.5	10.4	3.16	1.47	25	37.1	257.8
Tully	47.4	1.06	12.7	15.6	5.4	10.5	2.41	1.02	10.3	5.8	47.4
Tully	52.9	0.94	16.9	17.7	6.6	3.4	4.17	1.42	17.3	33.5	242.2

Tully	67.2	1.09	17.2	5.5	2.9	1.9	5.07	0.54	17.6	n.d.	17
Limekiln	47	2	11.2	20.8	3.2	5.9	3.7	1.61	11.1	45.4	245.6
Limekiln	45.9	2.1	8.8	22.4	4.1	5.2	3.52	1.67	13.6	53.7	187.8
Limekiln	42.2	1.85	8.8	29.1	3.3	4.8	3.36	1.05	11.6	43.7	115.5
Limekiln	46.4	2.32	8.8	19.8	3.5	5.9	3.62	1.34	7.8	33.2	193.4
Limekiln	49.1	1.71	10	18.8	3.9	5.9	4.07	1.52	12.3	54.5	200.2
Pyramid_Hills	38.8	1.05	6.1	18.9	10.7	5.4	2.56	0.36	18.8	71	14.1
Pyramid_Hills	41.1	0.97	4.8	19.8	12.5	3.8	1.87	0.74	10.8	n.d.	10.1
Pyramid_Hills	44.1	1.18	5.8	19	10.1	4.8	2.29	1.48	14.9	66.1	128.5
Pyramid_Hills	43.1	1.09	6.3	19.6	9	5.4	2.1	1.01	23.7	63.8	64.8
Pyramid_Hills	42.7	1.3	4.9	19.5	11.5	5.6	1.8	1.36	14.7	26	471
Johnnie	45.8	0.8	8.6	19.6	11.3	6.9	2.68	0.76	15.5	n.d.	27.9
Johnnie	41.3	0.86	8.4	24.5	13.1	2.9	2.38	0.99	21	37.6	56.7
Johnnie	40.1	1.42	7.5	28.3	10.2	4.4	2.5	0.86	13	42.8	60
Johnnie	45.1	1.02	9.1	21.7	11.5	3.4	2.73	1.15	20.9	30.3	76.9
Johnnie	42.1	1.89	9.5	27.8	6.7	4.2	2.99	0.91	11.9	23.5	37.7
South_Park2	39.6	0.87	5.1	19.2	13.4	5.5	1.73	0.19	9.6	19.4	7.5
South_Park2	39.4	0.87	6.5	18.9	10.9	6.3	1.73	0.23	9.7	1.7	19.1
South_Park2	44.3	1.02	8.5	18.5	6.1	6.8	2.99	0.51	7.8	n.d.	92.8
South_Park2	43.7	0.89	6.8	19.4	12.9	3.1	2.37	0.32	13.5	n.d.	n.d.
South_Park2	42.6	0.73	8.4	17.8	10.2	6.9	2.73	0.61	11.3	n.d.	60.9
Skidoo	50.8	1.05	9.6	20.4	6.1	4.6	3.29	0.87	17.3	30.4	160.8
Skidoo	47.6	0.96	10.1	19.4	7.3	6.8	2.99	0.78	27.9	41.3	76.1
Skidoo	41.7	2.58	5.1	23.8	9.7	2	2.28	0.64	25.6	3.6	10.2
Skidoo	44	2.09	7.4	21.5	5.9	4.5	2.88	1.02	22.2	48.5	112.5
Skidoo	45.3	1.77	9.7	21.2	5.1	5.3	3.06	1.22	27.1	47.7	121
Skidoo	48.4	0.94	9.4	18.7	6	11.4	3.08	0.73	17.2	20.7	n.d.
Skidoo	41.2	2.04	5.6	22.9	6.1	5.8	2.37	0.86	19.7	36	33.4
Skidoo	49.4	1.04	12.1	20.3	5.8	3.5	3.49	0.76	19.7	59.5	41.1
Skidoo	48.4	1.16	10.9	20.7	6.4	6.8	3.77	1.25	21	n.d.	79.4

Skidoo	43.3	1.66	10	23.4	7.1	5.9	3.41	1.17	17.6	15.3	20
Chocolate_Sundae_Mountain	46	1.43	14.4	21	4.2	7.1	4.09	1.31	13	44	321.5
Chocolate_Sundae_Mountain	49.8	1.5	16.8	18.8	3.4	5.8	4.4	2.33	12.1	61.9	361.5
Chocolate_Sundae_Mountain	48.4	1.58	9.7	21.4	8	3.6	3.16	1.91	42.5	48.3	66.5
Chocolate_Sundae_Mountain	50.6	1.92	9.9	20.7	8.6	1.4	3.32	1.8	27.3	34.6	110.2
Chocolate_Sundae_Mountain	49.7	1.3	13.6	20.7	7.7	3.7	4.03	1.41	27.1	n.d.	246
Chocolate_Sundae_Mountain	45.3	1.56	9.7	20.8	9	5.7	3.11	1.15	20.3	18.7	91.9
Chocolate_Sundae_Mountain	48.4	1.93	9.6	20.6	9.5	1.6	3.12	1.05	14.1	18.2	93.1
Chocolate_Sundae_Mountain	50.7	1.25	13	18.3	6.9	7.7	3.57	1.4	16.4	38.5	135.6
Chocolate_Sundae_Mountain	48.2	1.56	9.4	19.8	8.5	7.1	2.74	1.1	17.7	26.7	112.9
Chocolate_Sundae_Mountain	46.5	1.39	9.4	18.8	7.8	9.8	2.54	0.83	17.5	n.d.	72.7
Thimble	46.9	1.14	11.7	20.5	5	5.7	3.88	1.84	16.1	58.1	91.4
Thimble	49.5	1.15	17.3	18.6	3.9	4.1	5.14	1.75	12.5	72.8	208.8
Thimble	47.4	1.33	13	19.2	4.3	6.8	4.69	1.71	10.2	56.6	178.5
Thimble	52.2	1.35	20.3	16.6	3.6	3	6.29	1.77	11.6	35.3	330.8
Thimble	45.9	1.14	9.7	19.8	6.5	7	2.93	1.28	13.7	73.3	108
Thorndike	51.8	1.48	8.4	20	5.1	3.6	3.32	0.83	16.7	40.9	71
Thorndike	50.8	2.05	7.9	20.4	5	2.9	3.2	0.84	21.6	30.2	93.3
Thorndike	51.7	1.74	8.4	20.1	4.8	3.4	3.12	0.84	21.6	29.8	118.6
Thorndike	49.8	2.3	8.8	17.3	3.5	3.9	3.72	1.12	7.8	62.8	112.4

Thorndike	48.4	1.56	9.4	17.3	3.2	6.8	3.4	1.24	10.6	65.7	121.8
Keeler_Canyon	49.6	1.25	18.2	16.2	5	9.1	3.97	0.49	21	n.d.	129.5
Keeler_Canyon	51.3	1.53	12.9	17.8	7.1	6.6	3.69	0.6	14.9	n.d.	107.1
Keeler_Canyon	49.7	1.83	11.8	19.4	7.3	6.7	3.01	0.3	17.8	2.7	161.4
Keeler_Canyon	47.9	1.79	7.9	19.8	9.9	7.1	2	0.16	18.9	n.d.	94.8
Keeler_Canyon	51.2	1.12	13	19	7.7	4.1	4.01	0.66	22.7	23.6	213.5
Warm_Spring	42.5	0.98	8.4	18.9	14.1	1.7	3.19	0.21	18.2	42.7	5.3
Warm_Spring	56.1	0.77	18.8	6.9	1.1	4.5	5.53	2.71	12.4	n.d.	680.9
Warm_Spring	45.6	0.88	9.5	19.1	7.3	4.7	2.74	1.39	11.9	33.6	187.5
Warm_Spring	43.7	0.66	4.5	15.4	8.3	13.7	1.56	0.08	20.1	n.d.	10.2
Warm_Spring	42.1	0.99	8.4	19.5	9.3	4.8	2.62	1.04	20.3	61.3	61.4
Warm_Spring	45.1	0.82	10.5	18.1	10.2	2.3	3.15	1.24	22.9	63.4	127.4
Warm_Spring	43.4	0.92	8.5	18	13.8	2.7	2.76	1.06	15.1	7.3	332.9
Warm_Spring	44.1	0.82	8	19.1	12.6	3.2	2.65	0.95	19.8	n.d.	40.8
Warm_Spring	38.5	2.71	7.8	21.8	5.9	4.9	2.17	0.99	11.6	n.d.	73.2